# ADVANCES IN OSCILLATING REACTIONS

EDITED BY: Zeljko Dimitrije Cupic, Annette F. Taylor, Dezso Horvath, Marek Orlik and Irving Robert Epstein

PUBLISHED IN: Frontiers in Chemistry

frontiers Research Topics

# frontiers

**Frontiers eBook Copyright Statement**

The copyright in the text of individual articles in this eBook is the property of their respective authors or their respective institutions or funders. The copyright in graphics and images within each article may be subject to copyright of other parties. In both cases this is subject to a license granted to Frontiers.

The compilation of articles constituting this eBook is the property of Frontiers.

Each article within this eBook, and the eBook itself, are published under the most recent version of the Creative Commons CC-BY licence. The version current at the date of publication of this eBook is CC-BY 4.0. If the CC-BY licence is updated, the licence granted by Frontiers is automatically updated to the new version.

When exercising any right under the CC-BY licence, Frontiers must be attributed as the original publisher of the article or eBook, as applicable.

Authors have the responsibility of ensuring that any graphics or other materials which are the property of others may be included in the CC-BY licence, but this should be checked before relying on the CC-BY licence to reproduce those materials. Any copyright notices relating to those materials must be complied with.

Copyright and source acknowledgement notices may not be removed and must be displayed in any copy, derivative work or partial copy which includes the elements in question.

All copyright, and all rights therein, are protected by national and international copyright laws. The above represents a summary only. For further information please read Frontiers' Conditions for Website Use and Copyright Statement, and the applicable CC-BY licence.

ISSN 1664-8714
ISBN 978-2-88966-922-6
DOI 10.3389/978-2-88966-922-6

## About Frontiers

Frontiers is more than just an open-access publisher of scholarly articles: it is a pioneering approach to the world of academia, radically improving the way scholarly research is managed. The grand vision of Frontiers is a world where all people have an equal opportunity to seek, share and generate knowledge. Frontiers provides immediate and permanent online open access to all its publications, but this alone is not enough to realize our grand goals.

## Frontiers Journal Series

The Frontiers Journal Series is a multi-tier and interdisciplinary set of open-access, online journals, promising a paradigm shift from the current review, selection and dissemination processes in academic publishing. All Frontiers journals are driven by researchers for researchers; therefore, they constitute a service to the scholarly community. At the same time, the Frontiers Journal Series operates on a revolutionary invention, the tiered publishing system, initially addressing specific communities of scholars, and gradually climbing up to broader public understanding, thus serving the interests of the lay society, too.

## Dedication to Quality

Each Frontiers article is a landmark of the highest quality, thanks to genuinely collaborative interactions between authors and review editors, who include some of the world's best academicians. Research must be certified by peers before entering a stream of knowledge that may eventually reach the public - and shape society; therefore, Frontiers only applies the most rigorous and unbiased reviews.
Frontiers revolutionizes research publishing by freely delivering the most outstanding research, evaluated with no bias from both the academic and social point of view. By applying the most advanced information technologies, Frontiers is catapulting scholarly publishing into a new generation.

## What are Frontiers Research Topics?

Frontiers Research Topics are very popular trademarks of the Frontiers Journals Series: they are collections of at least ten articles, all centered on a particular subject. With their unique mix of varied contributions from Original Research to Review Articles, Frontiers Research Topics unify the most influential researchers, the latest key findings and historical advances in a hot research area! Find out more on how to host your own Frontiers Research Topic or contribute to one as an author by contacting the Frontiers Editorial Office: frontiersin.org/about/contact

# ADVANCES IN OSCILLATING REACTIONS

Topic Editors:
**Zeljko Dimitrije Cupic,** University of Belgrade, Serbia
**Annette F. Taylor,** The University of Sheffield, United Kingdom
**Dezso Horvath,** University of Szeged, Hungary
**Marek Orlik,** University of Warsaw, Poland
**Irving Robert Epstein,** Brandeis University, United States

**Citation:** Cupic, Z. D., Taylor, A. F., Horvath, D., Orlik, M., Epstein, I. R., eds. (2021). Advances in Oscillating Reactions. Lausanne: Frontiers Media SA. doi: 10.3389/978-2-88966-922-6

# Table of Contents

frontiers in Chemistry

EDITORIAL
published: 28 April 2021
doi: 10.3389/fchem.2021.690699

# Editorial: Advances in Oscillating Reactions

*Željko D. Cupić[1]*, Annette F. Taylor[2], Dezso Horváth[3], Marek Orlik[4] and Irving R. Epstein[5]*

*[1] Institute of Chemistry, Technology and Metallurgy, University of Belgrade, Belgrade, Serbia, [2] Department of Chemical and Biological Engineering, The University of Sheffield, Sheffield, United Kingdom, [3] Department of Applied and Environmental Chemistry, University of Szeged, Szeged, Hungary, [4] Laboratory of Electroanalytical Chemistry, Faculty of Chemistry, University of Warsaw, Warsaw, Poland, [5] Department of Chemistry, Brandeis University, Waltham, MA, United States*

**Keywords: non-linear dynamics, oscillating reactions, chemical computing, chaos, chemical oscillation**

## Editorial on the Research Topic

## Advances in Oscillating Reactions

Numerous processes in physical chemistry and related sciences take place in a cyclic fashion, with time-periodic variations in concentrations widely known as oscillatory or oscillating reactions. Such processes have been explored as non-linear phenomena, but their potential in various applications became recognized only recently. Self-oscillating gels were developed to be used as components of micro devices (actuators) or to achieve controlled periodic drug delivery. Attempts were made to use oscillating reactions in detecting traces of CO in the air by special sensor technology. Also, a wide spectrum of analytical applications of oscillatory reactions was developed, with unexpected robustness and high sensitivity toward evaluation of pharmaceutically active compounds. Advantages of fuel cells in which electrocatalytic oxidations occur in an oscillating regime have also been reported.

The growth in applications of oscillatory reactions to a wide range of different areas has been enabled by new experimental techniques for both detection of exotic dynamic states and control of complex systems far from equilibrium. Also, new insights have been achieved in understanding the physical and chemical mechanisms underlying the extraordinary properties of such processes.

In the work by von Boehn and Imbihl, photoemission electron microscopy and low-energy electron microscopy were used to study the surface dynamics of ultrathin vanadium oxide layers epitaxially grown on Rh(111) and Rh(110) single crystal surfaces during catalytic methanol oxidation. Movement and coalescence of neighboring $VO_x$ islands was observed, as well as phase separation inside the vanadium oxide islands, resulting in a substructure consisting of a reduced core and an outer oxidized ring, leading to periodic phase transitions and simultaneous size oscillations.

Shklyaev et al. determine how externally imposed flows affect chemical oscillations that are generated by two enzyme-coated patches within a fluid-filled millimeter-sized channel. An analytical model and simulations show that the distance between the enzyme-coated patches dictates the existence of chemical oscillations within the channel.

Li et al. generated both chemical oscillation and mechanical oscillation on lyotropic liquid crystalline gels, in which a Ru catalyst was embedded. Small fibers of gel were fabricated to achieve a macroscopically oscillatory bending–unbending transition driven by the Belousov–Zhabotinsky reaction.

Kurin-Csörgei et al. present results on new perborate oscillators. They successfully replaced $H_2O_2$ with $NaBO_3$ in two oscillating reaction systems resulting in new ones: the $BO_3^-$ –$S_2O_3^{2-}$-Cu(II) and the $BO_3^-$ –$SCN^-$-Cu(II) systems. Experimental measurements are supported by numerical simulations.

OPEN ACCESS

***Edited and reviewed by:***
*Malgorzata Biczysko, Shanghai University, China*

****Correspondence:***
*Željko D. Cupić*
*zcupic@ihtm.bg.ac.rs*

***Specialty section:***
*This article was submitted to Physical Chemistry and Chemical Physics, a section of the journal Frontiers in Chemistry*

***Received:*** *03 April 2021*
***Accepted:*** *09 April 2021*
***Published:*** *28 April 2021*

***Citation:***
*Cupić ŽD, Taylor AF, Horváth D, Orlik M and Epstein IR (2021) Editorial: Advances in Oscillating Reactions. Front. Chem. 9:690699. doi: 10.3389/fchem.2021.690699*

In the paper by Bubanja et al., intermittent forms of chaos are generated in the Bray-Liebhafsky oscillatory reaction, as a function of the specific flow rate in the CSTR. Chaotic complexity was observed in the vicinity of the critical control parameter value, between two extreme values for which periodic oscillations were observed. Although extremely hard to control, this type of dynamics has once more been confirmed as a robust phenomenon with a deterministic origin.

In the paper by Maria, glycolytic oscillations in *Escherichia coli* cells are subjected to *in silico* analysis to obtain a validated model useful for potential application. The model can be used to evaluate cellular metabolic fluxes, opening the possibility to re-design the cell metabolism *in silico* in order to obtain GMOs with industrial or medical applications.

The work of Fulczyk et al. provides an overview of studies on the hampering effect of heavy water ($D_2O$) on the spontaneous oscillatory peptidization of selected proteinogenic α-amino acids. The experiments were carried out with the use of high-performance liquid chromatography, mass spectrometry, and scanning electron microscopy. These techniques were chosen to demonstrate spontaneous oscillatory peptidization of α-amino acids in the absence of $D_2O$ and the hampering effect of $D_2O$ on peptidization.

An extraordinarily important field for potential applications of oscillating reactions is chemical computing. Therefore, several authors have contributed to this issue with their results in this area. Muzika et al. examine dynamical switching among discrete Turing patterns in arrays of mass-coupled reaction cells. Carefully chosen transitions between discrete Turing patterns and uniform oscillations using precisely targeted perturbations were used to design chemical computing devices. Furthermore, computer simulations were used in the paper by Gorecki and Bose to explore the efficiency of chemical computing performed by a small network of three coupled chemical oscillators. The network was optimized to recognize the white and red regions of the Japanese flag. Finally, Perez-Mercader and Dueñas-Diez demonstrate that all physically realizable computing automata can be represented/assembled/built in the laboratory using oscillatory chemical reactions, and illustrate their implementation with the example of a programmable LBA Turing machine using the Belousov-Zhabotinsky oscillatory chemistry. Their device is capable of recognizing words in a Context Sensitive Language and rejecting words outside the language.

We hope that this overview of the latest work on non-linear dynamics in chemistry will inspire especially young researchers to further research in this fascinating field.

## AUTHOR CONTRIBUTIONS

All authors listed have made a substantial, direct and intellectual contribution to the work, and approved it for publication.

**Conflict of Interest:** The authors declare that the research was conducted in the absence of any commercial or financial relationships that could be construed as a potential conflict of interest.

*Copyright © 2021 Cupić, Taylor, Horváth, Orlik and Epstein. This is an open-access article distributed under the terms of the Creative Commons Attribution License (CC BY). The use, distribution or reproduction in other forums is permitted, provided the original author(s) and the copyright owner(s) are credited and that the original publication in this journal is cited, in accordance with accepted academic practice. No use, distribution or reproduction is permitted which does not comply with these terms.*

frontiers in Chemistry

PERSPECTIVE
published: 30 June 2020
doi: 10.3389/fchem.2020.00541

# The Hampering Effect of Heavy Water ($D_2O$) on Oscillatory Peptidization of Selected Proteinogenic α-Amino Acids

*Agnieszka Fulczyk[1], Eliza Łata[1], Ewa Talik[2], Teresa Kowalska[1]* and Mieczysław Sajewicz[1]*

[1] Institute of Chemistry, University of Silesia, Katowice, Poland, [2] Department of Physics of Crystals, University of Silesia, Katowice, Poland

We present an overview of our studies on the hampering effect of heavy water ($D_2O$) on spontaneous oscillatory peptidization of selected proteinogenic α-amino acids. The investigated set of compounds included three endogenous and two exogenous species. The experiments were carried out with use of high-performance liquid chromatography (HPLC), mass spectrometry (MS) and scanning electron microscopy (SEM). These techniques were chosen to demonstrate spontaneous oscillatory peptidization of α-amino acids in an absence of $D_2O$ (HPLC) and the hampering effect of $D_2O$ on peptidization (HPLC, MS and SEM). The HPLC analyses were carried out at 21 ± 0.5°C with each α-amino acid freshly dissolved in the binary liquid mixture of organic solvent + $H_2O$, 70:30 (v/v) or in pure $D_2O$ for several dozen hours or several hours, respectively. The analyses with use of MS and SEM were carried out, respectively, after 7 days and 1 month of sample storage period in the darkness at 21 ± 0.5°C and for these experiments, each α-amino acid was dissolved in the liquid mixture of organic solvent + X, 70:30 (v/v), where X: $H_2O$ + $D_2O$ in volume proportions from 30:0 to 0:30. The results obtained with use of HPLC, MS and SEM point out to the strong hampering effect of $D_2O$ on the oscillations and peptidization yields, yet the dynamics of these processes significantly depends on chemical structure of a given α-amino acid.

**Keywords: spontaneous oscillatory peptidization, proteinogenic α-amino acids, soluble peptides, insoluble peptides, $D_2O$**

OPEN ACCESS

***Edited by:***
*Zeljko Dimitrije Cupic, University of Belgrade, Serbia*

***Reviewed by:***
*Katarina Novakovic, Newcastle University, United Kingdom*
*Zivoslav Lj Tesic, University of Belgrade, Serbia*

****Correspondence:***
*Teresa Kowalska*
*teresa.kowalska@us.edu.pl*

***Specialty section:***
*This article was submitted to Physical Chemistry and Chemical Physics, a section of the journal Frontiers in Chemistry*

***Received:*** *14 April 2020*
***Accepted:*** *26 May 2020*
***Published:*** *30 June 2020*

***Citation:***
*Fulczyk A, Łata E, Talik E, Kowalska T and Sajewicz M (2020) The Hampering Effect of Heavy Water ($D_2O$) on Oscillatory Peptidization of Selected Proteinogenic α-Amino Acids. Front. Chem. 8:541. doi: 10.3389/fchem.2020.00541*

## SPONTANEOUS OSCILLATORY PEPTIDIZATION OF PROTEINOGENIC α-AMINO ACIDS AND OTHER STRUCTURALLY RELATED COMPOUNDS

Our research on spontaneous oscillatory processes in organic chemistry has started with an observation that the thin-layer chromatographic (TLC) runs of ibuprofen resulted in an irreproducible retardation factor ($R_F$) which was, however, confined to the two borderlines (Sajewicz et al., 2005a). Although ibuprofen is regarded as structurally stable and indestructible in the binary organic-aqueous solvents, irreproducibility of retardation factor ($R_F$) was clearly related to the length of its storage period in solution. Later, an analogical phenomenon was observed with other profen drugs (Sajewicz et al., 2005b, 2006a,b, 2007; Marczak et al., 2006), α-hydroxy acids

(Sajewicz et al., 2008a, 2009) and α-amino acids (Sajewicz et al., 2008b,c). Common structural denominator was that all these compounds were chiral low molecular weight carboxylic acids. Soon it became evident that the borderlines of the retardation factor ($R_F$) values were those characterizing pure (+)- and pure (–)-enantiomer, and the phenomenon was the oscillatory chiral inversion (Sajewicz et al., 2008a,c, 2009).

Based on general knowledge of reaction mechanisms, it was understood that the elementary steps of chiral inversion proceed *via* the non-chiral intermediary products and their presence was demonstrated in the experiment performed with use of the high-performance liquid chromatography (HPLC) employing chiral stationary phase dedicated to the enantioseparation of α-amino acids (Sajewicz et al., 2014b). As the test analytes, two enantiomers of phenylglycine (Phg) were used and separation thereof was carried out for the period of 44 h. After 6 h, two separate chromatographic peaks of L-PhG and D-Phg coalesced into one and the coalescence period lasted 12 h. After that time, the single coalesced peak split to again give two peaks of L-PhG and D-Phg. This process was monitored with use of the DAD detector and a clear difference was observed between the identical UV spectra valid for L-PhG and D-Phg on the one hand, and the UV spectrum of the coalesced peak on the other. The latter one was ascribed to the non-chiral intermediary product(s) and its relative longevity (12 h) was regarded as striking and noteworthy. Our discovery of spontaneous oscillatory chiral inversion was approved by some other researchers as a reasonable justification of their own striking and quite unexpected results (e.g., Rincon et al., 2009; Stich et al., 2013).

Proteinogenic α-amino acids as the smallest "bricks" of all living matter seem the most important species undergoing oscillatory chiral inversion. Soon it became clear that α-amino acids undergo oscillatory peptidization as well. The main analytical tool to monitor this phenomenon was the non-chiral HPLC system and we focused on signals originating from the monomeric (i.e., non-peptidized) α-amino acids and their oscillatory concentration changes in the function of time, due to the peptidization–depeptidization process. We published a number of reports on this phenomenon which was also theoretically modeled, and the most important papers are (Sajewicz et al., 2010, 2014a; Godziek et al., 2016; Maciejowska et al., 2016). Up to our best knowledge, there had never been any earlier report neither on spontaneous peptidization of α-amino acids under such mild external conditions (dissolution at ambient temperature in an organic aqueous solvent), nor on oscillatory nature of this process. All our investigations were inspired by an interest in chemical evolution preceding biological one, in which spontaneous peptidization of α-amino acids might have played a significant role.

## $D_2O$ IN BIOCHEMICAL STUDIES AND THE AIM OF OUR RESEARCH PROJECT

With an improved availability of $D_2O$ in the thirties of the twentieth century, its influence on animals and plants has become investigated and a slowdown effect on life processes was recognized, in extreme cases resulting in an organism's death (Harvey, 1934; Lewis, 1934; Katz et al., 1962). Current experiments with $D_2O$ largely focus on its apoptotic effect on cancer cells (Takeda et al., 1998; Hartmann et al., 2005). All these results instigated our interest in an impact of $D_2O$ on the dynamics of spontaneous oscillatory peptidization and peptidization yields with selected endogenous (L-Cys, L-Pro, and L-Ala) and exogenous (L-Met and L-Hyp) α-amino acids as the smallest building blocks of all living matter.

## EFFECT OF $D_2O$ ON SPONTANEOUS OSCILLATORY PEPTIDIZATION

Five α-amino acids (L-Cys, L-Met, L-Pro, L-Hyp, and L-Ala) were dissolved in the binary liquid mixture of the organic solvent + $H_2O$, 70:30 (v/v) (where organic solvent: acetonitrile or methanol) and due to oscillatory peptidization-depeptidization process, the monomer concentrations of these compounds underwent spontaneous oscillatory changes. These changes were recorded with use of the non-chiral HPLC and graphically presented in supplementary materials of papers (Fulczyk et al., 2018, 2019a,b, 2020a,b) as time series, together with the corresponding plots of the Fourier-transformed data. From Fourier transformation it came out that with two endogenous species (L-Cys and L-Pro) the circadian rhythm of the oscillatory concentration changes occurs as equal to ca. 24 and ca. 20.8 h, respectively, and with two exogenous species (L-Met and L-Hyp) no periodicity of oscillations is observed. With the third endogenous species (L-Ala), the oscillatory pattern is still different. After two initial and not periodic oscillations lasting for ca.10 h, the investigated system reaches a steady state.

Dissolution of the investigated α-amino acids in pure $D_2O$ results in full inhibition of oscillatory peptidization, as confirmed by HPLC. Differentiation of peptidization dynamics and peptide yields becomes visible only, when proportions of $D_2O$ in solution stepwise change. Mass spectrometry (MS) and scanning electron microscopy (SEM) were used to record differences in the hampering effect of $D_2O$ on dynamics of peptidization and peptide yields depending of proportions of heavy water in solution.

Apart from considering the investigated compounds as belonging to two groups of endogenous and exogenous α-amino acids, they can also be viewed as three structural entities: two sulfur atom containing species (L-Cys, L-Met), two pyrrolidine ring and secondary amino group containing species (L-Pro, L-Hyp), and the simplest endogenous α-amino acid, L-Ala. First, let us reflect on the mass spectrometric results. As mass spectrometric technique used in this study was applicable to monitoring liquid samples alone, the obtained mass spectra provided information on changing contents of soluble lower molecular weight peptides depending on proportions of $D_2O$ in solution. For each α-amino acid considered, mass spectra were recorded after 7 days sample storage period in the darkness at 21 ± 0.5°C, in presence of 0, 5, 10, 20, 30, and 100% $D_2O$. The obtained MS results were originally published in papers (Fulczyk et al., 2018, 2019a,b, 2020a,b). It was shown that with increasing proportions of $D_2O$ in solution, L-Cys and L-Met produce growing yields of soluble lower peptides. With L-Pro,

the yields of soluble lower peptides are decreasing up to 10% $D_2O$, but then with higher amounts of $D_2O$ these yields start gradually growing. With L-Hyp and L-Ala, the decreasing yields of soluble lower peptides are observed in pace with growing proportions of $D_2O$ in solution. It can be concluded that the response of five investigated α-amino acids to changing quantitative proportions of $D_2O$ in solution depends on chemical structure of individual species rather than on belongingness to the endogenous/exogenous category, or on structural similarity of species (although a similar trend is observed with two sulfur atom containing α-amino acids, i.e., L-Cys and L-Met). **Figure 1** briefly illustrates an impact of selected proportions of $D_2O$ on the yields of soluble lower peptides upon the examples of L-Cys, L-Pro, and L-Ala.

Now let us consider the results originating from the scanning electron microscopy. For each α-amino acid under the discussion, scanning electron micrographs were recorded after 1 month sample storage period in the darkness at 21 ± 0.5°C, in presence of 0, 5, 10, 20, 30, and 100% $D_2O$. As this technique was applicable to solid samples alone, basic information which can be derived from the obtained micrographs focuses on changing yields of insoluble higher peptides, depending on proportions of $D_2O$ in solution. The obtained results unequivocally demonstrate that irrespective of the α-amino acid considered, in the presence of $D_2O$ in solution the hampering effect on peptidization process is observed and consequently, the yields of higher insoluble peptide drastically lower. Apparently, the higher is the $D_2O$ proportion in solution, the stronger pronounced is the hampering effect. For each species, a series of photographs was taken at different magnifications to best illustrate regularities and trends of this inhibitory effect and they were published in papers (Fulczyk et al., 2018, 2019a,b, 2020a,b). In **Figure 2**, we present selected micrographs valid for L-Cys, L-Met, and L-Pro, which illustrate an impact of the growing proportions of $D_2O$ on formation of insoluble higher peptides. They also allow a comparison of different structural forms of peptides derived from each individual α-amino acid. Peptides derived from L-Cys are spherical and gather in greater and spongy-looking structures. Peptides derived from L-Met are the flat, elongated laminas with sharp edges, and peptides derived from L-Pro resemble the 3D starry-looking objects of different sizes. All these micrograph series collected in **Figure 2** provide convincing evidence that the increasing proportions of $D_2O$ in solutions really result in diminishing yields of higher insoluble peptides.

## CONCLUSIONS

The starting point of our research project was demonstration with use of the non-chiral HPLC that all investigated proteinogenic (endogenous and exogenous) α-amino acids

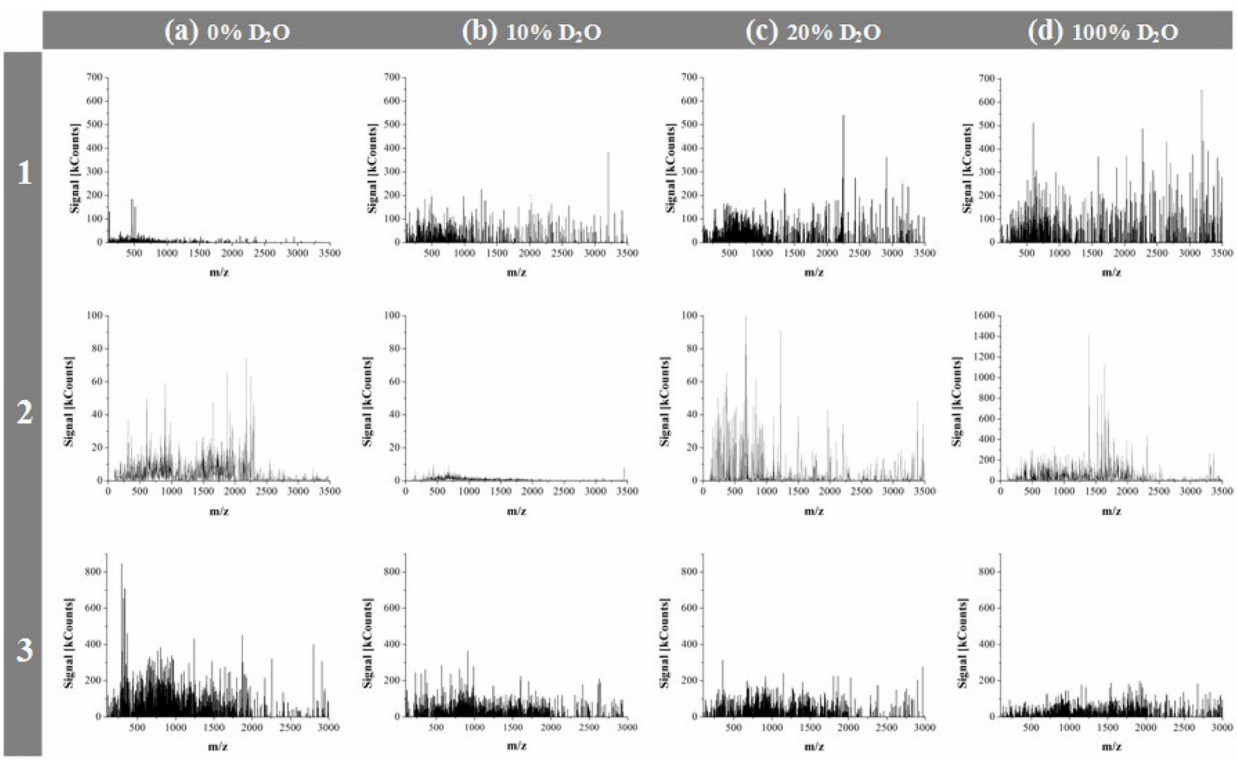


**FIGURE 1 |** Mass spectra recorded for L-Cys (1), L-Pro (2), and L-Ala (3), respectively, dissolved in organic solvent + X, 70:30 (v/v), where X: the binary mixture of $H_2O$ + $D_2O$ in the changing volume proportions; **(a)** 0% $D_2O$; **(b)** 10% $D_2O$; **(c)** 20% $D_2O$, and **(d)** 100% $D_2O$. Organic solvent: ACN (L-Cys), or MeOH (L-Pro and L-Ala); [adapted from Figures in Fulczyk et al. (2018, 2019a, 2020a)].

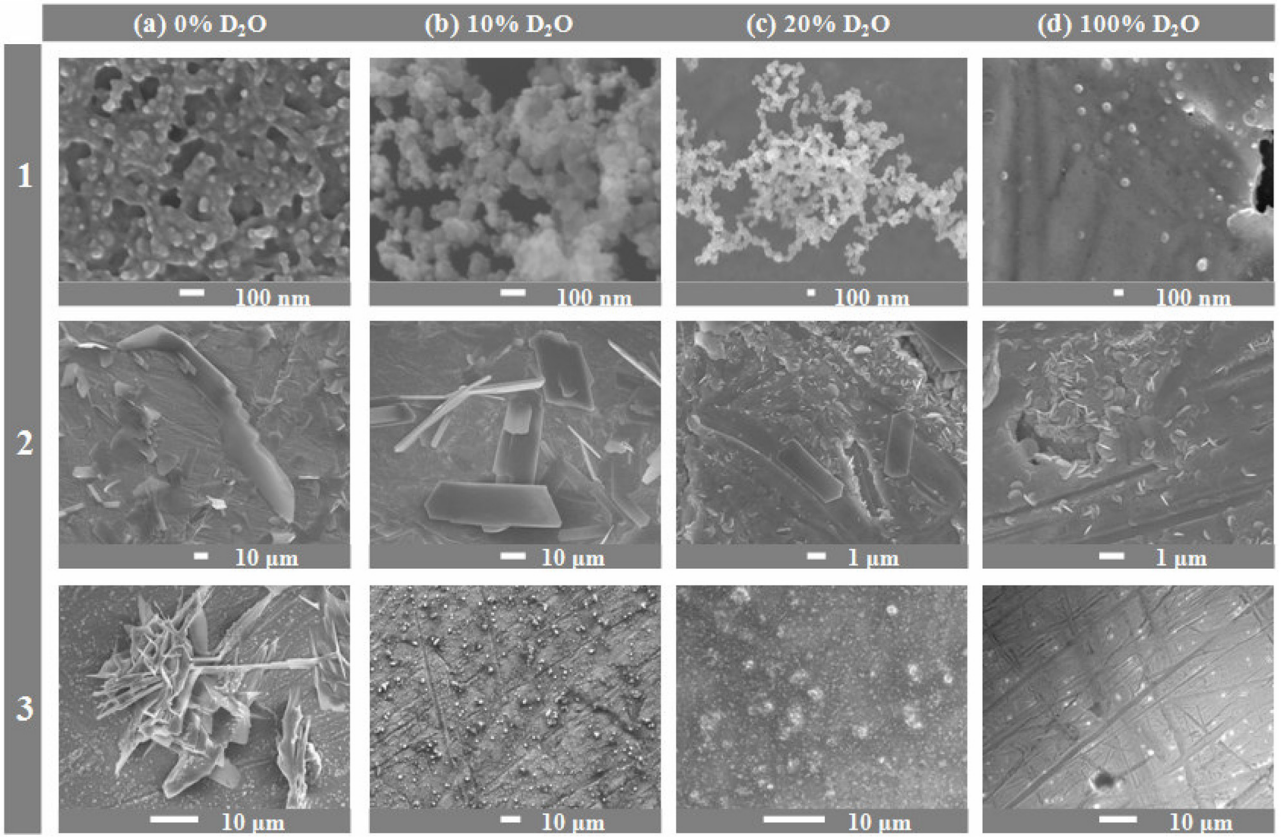


**FIGURE 2 |** Scanning electron micrographs recorded for L-Cys (1), L-Met (2), and L-Pro (3), respectively, dissolved in organic solvent + X, 70:30 (v/v), where X: the binary mixture of $H_2O + D_2O$ in the changing volume proportions; **(a)** 0% $D_2O$; **(b)** 10% $D_2O$; **(c)** 20% $D_2O$, and **(d)** 100% $D_2O$. Organic solvent: ACN (L-Cys and L-Met), or MeOH (L-Pro). Magnifications of individual micrographs: $(a_1) \times 100{,}000$; $(a_2) \times 550$; $(a_3) \times 1{,}900$; $(b_1) \times 100{,}000$; $(b_2) \times 1{,}000$; $(b_3) \times 750$; $(c_1) \times 30{,}000$; $(c_2) \times 7{,}500$; $(c_3) \times 2{,}500$, $(d_1) \times 37{,}000$; $(d_2) \times 10{,}000$; $(d_3) \times 1{,}500$ [partially adapted from Figures in Fulczyk et al. (2018, 2019a,b)].

dissolved in an organic-aqueous solvent yet in an absence of $D_2O$ undergo spontaneous oscillatory peptidization. Then we focused on the impact of $D_2O$ on spontaneous oscillatory peptidization process carried out either in pure heavy water, or in the mixture of organic solvent, $H_2O$ and $D_2O$. With use of scanning electron microscopy (SEM), it was shown that $D_2O$ hampers formation of insoluble higher peptides with all investigated species and this effect is monotonously dependent on proportions of $D_2O$ in solution. With use of mass spectrometry (MS), it was shown though that $D_2O$ affects formation of the soluble lower peptides in a less straightforward manner. With L-Cys and L-Met, growing proportions of $D_2O$ in solution result in growing yields of respective lower soluble peptides. With L-Hyp and L-Ala, growing proportions of $D_2O$ in solution result in declining yields of respective peptides. Response of L-Pro to proportions of $D_2O$ in solution is non-monotonous. Initially, growing proportions of $D_2O$ in solution result in the declining yields of the lower soluble peptides, but for the $D_2O$ proportions above 10% these yields rather unexpectedly start growing. Within the framework of the adopted research project, we disclosed individual patterns of spontaneous oscillatory peptidization in an absence of heavy water and also inhibition of this process with $D_2O$ under the assumed working conditions for three endogenous and two exogenous α-amino acids.

Summing up, even if the research perspective outlined in this study is currently absent from consciousness of scientific community worldwide or underestimated by many (partially due to serious limitations of effective analytical tools), we firmly believe in purposefulness of carrying out similar research even on a much larger scale, simply because we can see its relevance to a wide spectrum of diverse scientific disciplines spanned between evolutionary history of life and contemporary medicine.

## DATA AVAILABILITY STATEMENT

The original contributions presented in the study are included in the article/supplementary materials, further inquiries can be directed to the corresponding author/s.

## AUTHOR CONTRIBUTIONS

All authors equally contributed to preparation of the submitted manuscript.

## REFERENCES


Fulczyk, A., Łata, E., Dolnik, M., Talik, E., Kowalska, T., and Sajewicz, M. (2018). Impact of $D_2O$ on peptidization of L-cysteine. *React. Kinet. Mech. Catal.* 125, 555–565. doi: 10.1007/s11144-018-1469-y

Fulczyk, A., Łata, E., Talik, E., Dolnik, M., Kowalska, T., and Sajewicz, M. (2020a). Impact of $D_2O$ on peptidization of L-alanine. *React. Kinet. Mech. Catal.* 43, 745–750. doi: 10.1007/s11144-020-01783-y

Fulczyk, A., Łata, E., Talik, E., Kowalska, T., and Sajewicz, M. (2019a). Impact of $D_2O$ on peptidization of L-proline. *React. Kinet. Mech. Catal.* 128, 599–610. doi: 10.1007/s11144-019-01681-y

Fulczyk, A., Łata, E., Talik, E., Kowalska, T., and Sajewicz, M. (2019b). Impact of $D_2O$ on peptidization of L-methionine. *React. Kinet. Mech. Catal.* 126, 939–949. doi: 10.1007/s11144-019-01538-4

Fulczyk, A., Łata, E., Talik, E., Kowalska, T., and Sajewicz, M. (2020b). Impact of $D_2O$ on peptidization of L-hydroxyproline. *React. Kinet. Mech. Catal.* 129, 17–28. doi: 10.1007/s11144-019-01711-9

Godziek, A., Maciejowska, A., Talik, E., Wrzalik, R., Sajewicz, M., and Kowalska, T. (2016). On spontaneously pulsating proline-phenylalanine peptide microfibers. *Curr. Protein Pept. Sci.* 17, 106–116. doi: 10.2174/1389203717021602091215 13

Hartmann, J., Bader, Y., Horvath, Z., Saiko, P., Grusch, M., Illmer, C., et al. (2005). Effects of heavy water ($D_2O$) on human pancreatic tumor cells. *Anticancer Res.* 25, 3407–3411.

Harvey, E. N. (1934). Biological effects of heavy water. *Biol. Bull.* 66, 91–96. doi: 10.2307/1537322

Katz, J. J., Crespi, H. L., Czajka, D. M., and Finkel, A. J. (1962). Course of deuteriation and some physiological effects of deuterium in mice. *Am. J. Physiol.* 203, 907–913. doi: 10.1152/ajplegacy.1962.203.5.907

Lewis, G. N., (1934). The biology of heavy water. *Science* 79, 151–153. doi: 10.1126/science.79.2042.151

Maciejowska, A., Godziek, A., Talik, E., Sajewicz, M., Kowalska, T., and Epstein, I. R. (2016). Spontaneous pulsation of peptide microstructures in an abiotic liquid system. *J. Chromatogr. Sci.* 54, 1301–1309. doi: 10.1093/chromsci/bmw073

Marczak, W., Kowalska, T., Bucek, M., Piotrowski, D., and Sajewicz, M. (2006). Effect of dilution on compressibility of naproxen in acetonitrile studied by ultrasonic method. *J. Phys.* 137, 219–222. doi: 10.1051/jp4:2006137045

Rincon, A. G., Guzman, M. I., Hoffmann, M. R., and Colussi, A. J. (2009). Optical absorptivity versus molecular composition of model organic aerosol matter. *J. Phys. Chem. A* 113, 10512–10520. doi: 10.1021/jp904644n

Sajewicz, M., Dolnik, M., Kowalska, T., and Epstein, I. R. (2014a). Condensation dynamics of *L*-proline and *L*-hydroxyproline in solution. *RCS Adv.* 4, 7330–7339. doi: 10.1039/C3RA46921B

Sajewicz, M., Gontarska, M., and Kowalska, T. (2014b). HPLC/DAD evidence of the oscillatory chiral conversion of phenylglycine. *J. Chromatogr. Sci.* 52, 329–333. doi: 10.1093/chromsci/bmt033

Sajewicz, M., Gontarska, M., Kronenbach, D., and Kowalska, T. (2008a). Investigation of the spontaneous oscillatory *in vitro* chiral conversion of L-(+)-lactic acid. *Acta Chromatogr.* 20, 209–225. doi: 10.1556/AChrom.20.2008.2.6

Sajewicz, M., Gontarska, M., Kronenbach, D., Leda, M., Kowalska, T., and Epstein, I. R. (2010). Condensation oscillations in the peptidization of phenylglycine. *J. Syst. Chem.* 1:7. doi: 10.1186/1759-2208-1-7

Sajewicz, M., Gontarska, M., Wojtal, Ł., Kronenbach, D., Leda, M., Epstein, I. R., et al. (2008c). Experimental and model investigation of the oscillatory transenantiomerization of L-α-phenylalanine. *J. Liq. Chromatogr. Relat. Technol.* 31, 1986–2005. doi: 10.1080/10826070802197578

Sajewicz, M., Kronenbach, D., Gontarska, M., Wróbel, M., Pietka, R., and Kowalska, T. (2009). TLC in search for structural limitations of spontaneous oscillatory in-vitro chiral conversion. α-hydroxybutyric and mandelic acids. *J. Planar. Chromatogr. Modern TLC* 22, 241–248. doi: 10.1556/JPC.2009.1001

Sajewicz, M., Kronenbach, D., Staszek, D., Wróbel, M., Grygierczyk, G., and Kowalska, T. (2008b). Experimental investigation of the oscillatory transenantiomerization of L-tyrosine. *J. Liq. Chromatogr. Relat. Technol.* 31, 2006–2018. doi: 10.1080/10826070802197693

Sajewicz, M., Pietka, R., Drabik, G., and Kowalska, T. (2006a). On the mechanism of oscillatory changes of the retardation factor ($R_F$) and the specific rotation $[\alpha]_D$ with selected solutions of *S*-(+)-naproxen. *J. Liq. Chromatogr. Relat. Technol.* 29, 2071–2082. doi: 10.1080/10826070600759934

Sajewicz, M., Pietka, R., Pieniak, A., and Kowalska, T. (2005b). Application of thin-layer chromatography (TLC) to investigate oscillatory instability of the selected profen enantiomers in dichloromethane. *J. Chromatogr. Sci.* 43, 542–548. doi: 10.1093/chromsci/43.10.542

Sajewicz, M., Gontarska, M., Kronenbach, D., Wojtal, Ł., Grygierczyk, G., and Kowalska, T. (2007). Study of the oscillatory *in vitro* transenantiomerization of the antimers of flurbiprofen and their enantioseparation by thin-layer chromatography (TLC). *Acta Chromatogr.* 18, 226–237.

Sajewicz, M., Pietka, R., Kuś, P., and Kowalska, T. (2006b). On the gelation of profens as a property causing their oscillatory transenantiomerization. *Acta Chromatogr.* 16, 181–191.

Sajewicz, M., Pietka, R., Pieniak, A., and Kowalska, T. (2005a). Application of thin-layer chromatography (TLC) to investigating oscillatory instability of the selected profen enantiomers. *Acta Chromatogr.* 15, 131–149.

Stich, M., Blanco, C., and Hochberg, D. (2013). Chiral and chemical oscillations in a simple dimerization model. *Phys. Chem. Chem. Phys.* 15, 255–261. doi: 10.1039/C2CP42620J

Takeda, H., Nio, Y., Omori, H., Uegaki, K., Hirahara, N., Sasaki, S., et al. (1998). Mechanisms of cytotoxic effects of heavy water (deuterium oxide: D2O) on cancer cells. *Anticancer Drugs* 9, 715–725. doi: 10.1097/00001813-199809000-00007


**Conflict of Interest:** The authors declare that the research was conducted in the absence of any commercial or financial relationships that could be construed as a potential conflict of interest.

*Copyright © 2020 Fulczyk, Łata, Talik, Kowalska and Sajewicz. This is an open-access article distributed under the terms of the Creative Commons Attribution License (CC BY). The use, distribution or reproduction in other forums is permitted, provided the original author(s) and the copyright owner(s) are credited and that the original publication in this journal is cited, in accordance with accepted academic practice. No use, distribution or reproduction is permitted which does not comply with these terms.*

frontiers in Chemistry

ORIGINAL RESEARCH
published: 23 July 2020
doi: 10.3389/fchem.2020.00618

# Effects of an Imposed Flow on Chemical Oscillations Generated by Enzymatic Reactions

*Oleg E. Shklyaev, Victor V. Yashin† and Anna C. Balazs**

*Department of Chemical Engineering, University of Pittsburgh, Pittsburgh, PA, United States*

Using analytical and computational models, we determine how externally imposed flows affect chemical oscillations that are generated by two enzyme-coated patches within a fluid-filled millimeter sized channel. The fluid flow affects the advective contribution to the flux of chemicals in the channel and, thereby, modifies the chemical reactions. Here, we show that changes in the flow velocity permit control over the chemical oscillations by broadening the range of parameters that give rise to oscillatory behavior, increasing the frequency of oscillations, or suppressing the oscillations all together. Notably, simply accelerating the flow along the channel transforms time-independent distributions of reagents into pronounced chemical oscillations. These findings can facilitate the development of artificial biochemical networks that act as chemical clocks.

**Keywords: chemical oscillations, enzymatic reactions, fluid flow, surface-bound enzymes, microfluidic channels**

OPEN ACCESS

***Edited by:***
*Irving Robert Epstein, Brandeis University, United States*

***Reviewed by:***
*Baptiste Blanc, Brandeis University, United States*
*Olga Kuksenok, Clemson University, United States*

***Correspondence:**
*Anna C. Balazs*
*balazs@pitt.edu*

**†ORCID:**
*Victor V. Yashin*
*orcid.org/0000-0002-9991-0877*

***Specialty section:***
*This article was submitted to Physical Chemistry and Chemical Physics, a section of the journal Frontiers in Chemistry*

***Received:*** *07 May 2020*
***Accepted:*** *12 June 2020*
***Published:*** *23 July 2020*

***Citation:***
*Shklyaev OE, Yashin VV and Balazs AC (2020) Effects of an Imposed Flow on Chemical Oscillations Generated by Enzymatic Reactions. Front. Chem. 8:618. doi: 10.3389/fchem.2020.00618*

## INTRODUCTION

Oscillating chemical reactions in living systems are known to regulate circadian rhythms, varieties of metabolic processes, the transcription of DNA and other important biological functions (Novak and Tyson, 2008; Lim et al., 2013). Within the small-scale dimensions of a biological cell, the diffusion of chemicals is sufficient to ensure the homogeneous mixing of the reagents and therefore, the chemical oscillations are solely functions of time (Elowitz and Leibler, 2000; Novak and Tyson, 2008; Lim et al., 2013; Shum et al., 2015). On a larger spatial scale, when the diffusive homogenization cannot be considered instantaneous, the combination of non-linear chemical reactions and diffusive transport gives rise to chemical Turing patterns (Turing, 1952) and traveling chemical waves (Prigogine and Lefever, 1968). The behavior of the spatio-temporal pattern formation can be adequately described by coupled reaction-diffusion equations. The introduction of an externally imposed flow, however, will modify the chemical fluxes produced by the reaction-diffusion processes and hence, will not only alter the dynamics of the system, but could also provide an effective means of regulating the oscillatory behavior within the solution. Here, we probe how an externally imposed flow affects the chemical oscillations due to coupled enzymatic reactions within a fluid-filled, millimeter sized channel and show that characteristic features of the oscillatory behavior are highly sensitive to the velocity of the applied flow fields.

The chemical oscillations in our systems result from interactions between two enzyme-coated patches, which are localized on the bottom wall of a fluidic chamber. These enzymatic reactions involve two steps. The product of the first enzymatic reaction acts as a promoter for the second reaction. On the other hand, the product of the second reaction acts as an inhibitor for the first. These promoting and inhibiting signals enable the system to exhibit both the positive and negative feedback loops that enable the chemical oscillations. The imposed pressure-driven flow will affect the transport of the reactants between the enzyme-coated patches and hence can alter oscillatory

behavior produced by the feedback loops. We also anticipate that the overall dynamic behavior and chemical oscillations in this system will depend on the relative positions of the catalyst patches within the channel.

In order to test the above hypotheses, we analyze the properties of two distinct examples. In the first example, the promotor and inhibitor enzymes are placed in a periodically alternating pattern; with this assumption, we can model the system within a single, periodic unit cell. In the second example, the enzymes are localized at two specific points within an infinitely long pipe. To study these cases, we develop a one-dimensional analytic model for the behavior of chemical phenomena within a long and narrow channel. To validate the 1D model, we compare the predictions from this analytic model to computer simulations of chemical oscillations occurring within two-dimensional channels. The results of both modeling approaches reveal that the distance between the catalytic patches dictates the existence of the chemical oscillations. Furthermore, the speed of the imposed fluid flows can promote or suppress the chemical oscillations in the system. In particular, we show that the imposed flow can enlarge the region in phase space where the chemical oscillations are stable and increase the frequency of the oscillations.

## THEORETICAL MODEL

We consider a mixture of chemicals transported along a narrow channel, which has a rectangular cross-section of size $L_y \times L_z$, and a long-axis pointing in x-direction, as shown in **Figure 1A**. The solution contains a number of reactants, but only the two key species, $A$ and $B$, are essential for producing chemical oscillations in the system. Specifically, in the presence of a flowing solution that contains the substrate $S$, the immobilized enzymes $E_1$ and $E_2$ (see **Figure 1A**) catalyze the chemical reactions $S \xrightarrow{E_1} A$ and $S + A \xrightarrow{E_2} B$. In addition to the latter reactions, the species $A$ and $B$ undergo deactivation over time. We assume that the concentrations of the reactant substrate $S$ are constant (Prigogine and Lefever, 1968), and neglect the reverse reactions. Experimentally, this system could be realized in a continuous flow reactor. It is important to note that our theoretical model does not provide an explicit description of all chemical transformations possible in the system. Instead, we design a minimal model that takes into account only the processes that involve the two key reactant species, $A$ and $B$.

The chemical transformations of the reagents $A$ and $B$ can be viewed as a simplified model of the biosynthesis of glutathione that occurs as a two-step process (Jez and Cahoon, 2004; Jez et al., 2004) in all living organisms. During the first step, glutamate-cysteine ligase (GCL) catalyzes production of γ-glutamylcystein from glutamate, cysteine, and ATP. At the second step, glutathione synthetase (GS) catalyzes the formation of glutathione from γ-glutamylcystein, glycine, and ATP. The two-step process (Jez and Cahoon, 2004; Jez et al., 2004) can be expressed as

$$\text{L-glutamate} + \text{L-cysteine} + \text{ATP} \xrightarrow{\text{GCL}} \gamma\text{-glutamylcysteine} + \text{ADP} \quad (R1)$$

$$\gamma\text{-glutamylcysteine} + \text{glycine} + \text{ATP} \xrightarrow{\text{GS}} \text{glutathione} + \text{ADP} \quad (R2)$$

In the living cells, there are mechanisms that maintain concentrations of chemicals within certain range necessary for proper functioning. To mimic the self-regulation in the biological process, we assume that γ-glutamylcystein promotes the production of glutathione, while glutathione inhibits the production of γ-glutamylcystein. Identifying chemicals $A$ and $B$ with γ-glutamylcystein and glutathione, respectively, and the enzymes GCL and GS with E1 and E2, respectively, we use Michaelis-Menten type reaction rates to realize the proposed regulation mechanism. The substrate for the reaction contains a mixture of all the other components including L-glutamate, L-cystein, glycine, ATP, and ADP; this allows us to represent the reactions (R1) and (R2) as $S \xrightarrow{E_1} A$ and $S + A \xrightarrow{E_2} B$. Note, that unlike the cell environment where the enzymes GCL and GS are mixed throughout the solution, in our case the enzymes are immobilized at the two surfaces, allowing us to spatially separate the two chemical reactions and, ultimately, generate chemical oscillations.

We note, however, that the proposed reaction scheme is a model that enables us to study the response of chemical oscillations to the advective chemical flux. Because the latter response depends on the relative contribution of the diffusive and advective fluxes, which transport chemicals throughout the solution, the effect should apply to a range of catalytic reactions that promote chemical oscillations by localized catalysts.

The behavior of the system, characterized by the concentrations $C^A$ and $C^B$ of the reagents $A$ and $B$, and the fluid velocity $\mathbf{u} = (u_x, u_y, u_z)$, can be described by the continuity, Navier-Stokes (in the Boussinesq approximation Chandrasekhar, 1961), and reaction and diffusion equations

$$\nabla \cdot \mathbf{u} = 0, \tag{1}$$

$$\partial_t \mathbf{u} + (\mathbf{u} \cdot \nabla)\mathbf{u} = -\frac{1}{\rho}\nabla p + \nu \nabla^2 \mathbf{u}, \tag{2}$$

$$\partial_t C^j + (\mathbf{u} \cdot \nabla) C^j + \gamma^j C^j = D^j \nabla^2 C^j, \quad j = A, B. \tag{3}$$

Here and in what follows, $\partial_y$ is the derivative with respect to a variable $y$, $\nabla$ is the spatial gradient operator, $\rho$ is the density of solution, $\nu$ is the kinematic viscosity, $\gamma^j$ is the deactivation (decay) rate constant, and $D^j$ is the diffusivity of respective reactants $C^j$, $j = A, B$. We assume that the fluid flow with the

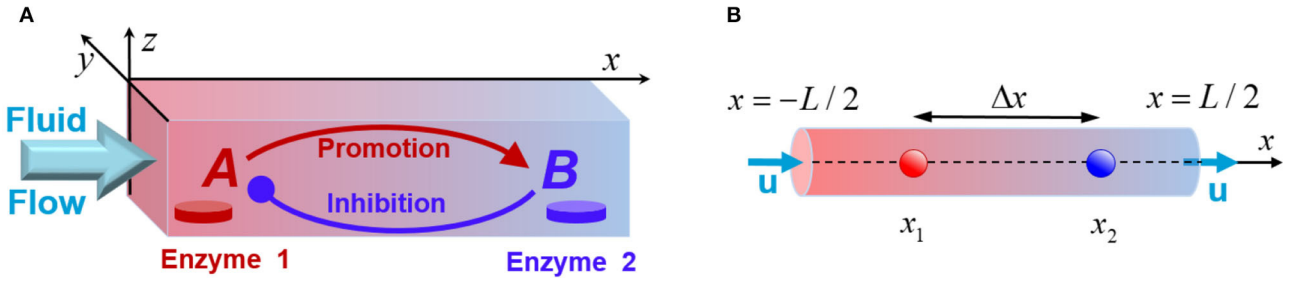


**FIGURE 1 | (A)** Schematic of a fluidic channel that supports chemical oscillations promoted by the enzyme-coated patches, Enzyme 1 and Enzyme 2. The patches initiate transformations of the reactants *A* (red) and *B* (blue), and the fluid flow modifies the chemical kinetics. **(B)** The quasi-1D model of the system that models a channel with the longitudinal size *L* being much greater than the transversal dimensions.

velocity $\mathbf{u} = (u, 0, 0)$ in the $x$-direction along the channel is generated by the pressure gradient $\nabla p = (f, 0, 0)$ created by an external fluidic pump. For simplicity, we assume that the system is uniform in the $y$-direction and develop a 2D model descibed by $x$ and $z$ spatial variables.

The chemical reactions, which occur due to the enzyme-coated patches localized on the bottom wall of the channel at $z = 0$ (see **Figure 1A**), are introduced through the boundary conditions:

$$\left\{z = 0,\ x_1 - \frac{\delta x}{2} \le x \le x_1 + \frac{\delta x}{2}\right\}:$$
$$-D^A \partial_z C^A = k_1 \sigma_1 F_1(C^B), \quad D^B \partial_z C^B = 0, \tag{4}$$

$$\left\{z = 0,\ x_2 - \frac{\delta x}{2} \le x \le x_2 + \frac{\delta x}{2}\right\}:$$
$$-D^A \partial_z C^A = k_2 \sigma_2 F_2(C^A), D^B \partial_z C^B = k_2 \sigma_2 F_2(C^A). \tag{5}$$

Here, the patch $\alpha$, where $\alpha = 1, 2$, is centered at $x_\alpha$ and coated with the enzyme $\alpha$, at a surface density of $\sigma_\alpha$. Each patch has length $\delta x$. The enzymes are characterized by the reaction rate constants $k_\alpha$. The functions $F_1(C^B)$ and $F_2(C^A)$ describe the concentration dependence of the inhibited and promoted reactions, respectively, and are chosen to mimic those for the glutathione biosynthesis pathway (Jez and Cahoon, 2004; Jez et al., 2004):

$$F_1(C^B) = \frac{1}{1 + (C^B/K^B)^{n_1}}, \quad F_2(C^A) = \frac{(C^A/K^A)^{n_2}}{1 + (C^A/K^A)^{n_2}}, \tag{6}$$

where $K^B$ and $K^A$ are the respective inhibition and dissociation constants. As seen from Equations (4) to (6), the rate of production of the chemical $A$ decreases with an increase in the concentration $C^B$ (inhibition), whereas an increase in $C^A$ increases the rate of production of $B$ until saturation (promotion). Note that the reaction rates in Equations (4)–(6) are taken to be dependent on the cooperativity parameters (Hill coefficients) $n_\alpha > 0$, $\alpha = 1, 2$. Cooperativity of the enzymatic reactions is known to affect the dynamic regimes that could exist in the system (Elowitz and Leibler, 2000; Shum et al., 2015).

Finally, for the solid walls that bound the channel at $z = 0$, and $z = H$, we require zero velocity at the walls and zero flux of the reagent concentrations normal to the walls

$$\mathbf{u}(z = 0) = \mathbf{u}(z = H) = \mathbf{0},$$
$$\partial_z C^j(x, z = 0, t) = \partial_z C^j(x, z = H, t) = 0. \tag{7}$$

For periodic boundary conditions in the $x$-direction, we set:

$$x: \quad \mathbf{u}(0) = \mathbf{u}(L_x), \quad C^j(0) = C^j(L_x). \tag{8}$$

To simplify the analysis, we reduce the number of model parameters by setting $D^A = D^B = D$, $\gamma^A = \gamma^B = \gamma$, $\sigma_1 = \sigma_2 = \sigma$, and $K^A = K^B = K$. Assuming that our solution is aqueous, we take $\nu = 10^{-6}\mathrm{m^2 s^{-1}}$ and $\rho = 10^3 \mathrm{kg\,m^{-3}}$. We use the glutathione diffusion coefficient (Jin and Chen, 2000) $D = 0.67 \times 10^{-9}\mathrm{m^2 s^{-1}}$ to characterize the diffusivity of both reagents $A$ and $B$. The deactivation rate $\gamma$ sets a time and distance (Shklyaev et al., 2020) over which the diffusing reagents turn unto products in the substrate, which we do not model explicitly. To obtain chemical oscillations in a system with a millimeter characteristic length scale, we set $\gamma = 10^{-3}\mathrm{s^{-1}}$. The reaction rates of glutamate-cysteine ligase (Jez et al., 2004) (GCL) and glutathione synthetase (Jez and Cahoon, 2004) (GS) were taken as $k_1 = 114\,\mathrm{s^{-1}}$, and $k_2 = 3954\mathrm{s^{-1}}$, respectively. The inhibition and dissociation constants $K^B$ and $K^A$ both were set to $K = 3.383 \times 10^{-2}\mathrm{mol\,m^{-3}}$, which is of the same order of magnitude as the dissociation constants (Jez and Cahoon, 2004) for ATP glycine, and $\gamma$-glutamylcystein participating in the reaction Equation (R2). We chose the smallest equal cooperativity parameters $n_1 = n_2 = 3$ that support the chemical oscillations controlled by the non-linear Hill-type functions presented in Equation (6). Finally, we fix the ratio of the reaction rates $k_1\sigma_1/k_2\sigma_2 = const \approx 0.0288$, and use $k_1\sigma_1$ as an independent variable to identify the domain of chemical oscillations and the corresponding values of the enzyme concentrations $\sigma$. Note that we obtain enzyme surface densities $\sigma \sim 10^{-7}\mathrm{mol\,m^{-2}}$, which are available through current fabrication techniques.

In what follows, we investigate the behavior of the system controlled by the distance between the enzyme-coated patches $\Delta x = x_2 - x_1$; reaction rates $k_1\sigma_1$ and $k_2\sigma_2$, which regulate the

kinetics of the chemical transformations; and the imposed fluid velocity $u$, which controls the flux of the chemicals $D\partial_x C^j + uC^j$. For this purpose, the system behavior is characterized by the group of parameters $(\Delta x, k_1\sigma_1, u)$.

## QUASI 1D APPROXIMATION

When the transversal dimensions $L_y$ and $L_z$ of the channel are much smaller than the characteristic longitudinal scale $L_x$ as schematically shown in **Figure 1A**, the problem can be reduced to a quasi-one-dimensional system described by a single coordinate $x$ (**Figure 1B**). In this approximation, the externally imposed fluid flow that transports the solution along the channel is characterized by a constant velocity $u$. Appropriate averaging of Equation (3) under the boundary conditions given by Equations (4) and (5) yields the following set of one-dimensional (1D) reaction-diffusion equations:

$$\partial_t C^A + u\partial_x C^A + \gamma C^A = D\partial_x^2 C^A + \frac{k_1\sigma_1}{H}F_1\delta(x-x_1) - \frac{k_2\sigma_2}{H}F_2\delta(x-x_2), \quad (9)$$

$$\partial_t C^B + u\partial_x C^B + \gamma C^B = D\partial_x^2 C^B + \frac{k_2\sigma_2}{H}F_2\delta(x-x_2). \quad (10)$$

The non-linear terms describing the chemical reactions pass from the boundary conditions (Equations 4 and 5), to the right-hand sides of the above 1D equations. We also assume that the spatial extent of the enzyme-coated patches, $\delta x$, is much smaller than the length of the channel, $L_x$. Therefore, the location the catalytic patches within the channel and their characteristics are introduced in Equations (8) and (9) by the terms with $\delta$ -functions. Finally, the equations are complemented with the periodic boundary conditions

$$x: \quad C^j(0) = C^j(L_x), \quad j = A, B \quad (11)$$

For concreteness, we analyze two representative configurations of the channel with specific locations of the enzyme-coated patches. First, we consider an infinite array of alternating enzyme-coated patches distributed equidistantly along an infinite channel. In this case, we solve the problem within a periodic unit cell of length $L_x$ with the neighboring enzyme-coated patches separated by a distance $x_2 - x_1 = L_x/2$ (see **Figure 1B**). This configuration of the system possesses a symmetry with respect to the velocity reversal from $u$ to $-u$. In the second case, we consider only two enzyme-coated patches (1 and 2) separated by a distance $x_2 - x_1$ and placed within an infinite channel, $L_x \to \infty$. This configuration does not have the degeneracy with respect to the sign change of the fluid velocity. For the both of cases under consideration, we demonstrate that below certain critical values of the reaction rates $k_1\sigma_1$ there exists a time independent solution, whereas the chemical oscillations are possible above the threshold. To find the domain of the oscillatory regime, we solve a relevant stability problem.

## BASE STATE SOLUTION

The equations (Equations 9–11), permit the existence of a time-independent base state, which is governed by the following 1D equations:

$$D\partial_x^2 C_0^A - u\partial_x C_0^A - \gamma C_0^A = -\frac{k_1\sigma_1\delta(x-x_1)}{1+(C_0^B/K^B)^{n_1}} + \frac{k_2\sigma_2\delta(x-x_2)}{1+(C_0^A/K^A)^{-n_2}}, \quad (12)$$

$$D\partial_x^2 C_0^B - u\partial_x C_0^B - \gamma C_0^B = -\frac{k_2\sigma_2\delta(x-x_2)}{1+(C_0^A/K^A)^{-n_2}}. \quad (13)$$

The solution of Equations (12) and (13) could be presented in a compact form in terms of the Green's function $G(x, x_0)$ as

$$C_0^A(x) = \frac{k_1\sigma_1 G(x,x_1)}{1+(C_0^B(x_1)/K^B)^{n_1}} - \frac{k_2\sigma_2 G(x,x_2)}{1+(C_0^A(x_2)/K^A)^{-n_2}}, \quad (14)$$

$$C_0^B(x) = \frac{k_2\sigma_2 G(x,x_2)}{1+(C_0^A(x_2)/K^A)^{-n_2}}. \quad (15)$$

The Green's function $G(x, x_0)$ is given by the equation

$$G(x,x_0) = \mathrm{e}^{V\xi_0(x-x_0)}\begin{cases} c_1\mathrm{e}^{\xi(x-x_0)} + c_2\mathrm{e}^{-\xi(x-x_0)}, & x < x_0, \\ c_3\mathrm{e}^{\xi(x-x_0)} + c_4\mathrm{e}^{-\xi(x-x_0)}, & x_0 \le x \end{cases}$$

where $c_1 = \left(2D\xi(1-\mathrm{e}^{-(\xi+V\xi_0)L_x})\right)^{-1}$, $c_2 = \left(2D\xi(\mathrm{e}^{-(\xi-V\xi_0)L_x}-1)\right)^{-1}$, $c_3 = \left(2D\xi(\mathrm{e}^{(\xi+V\xi_0)L_x}-1)\right)^{-1}$, and $c_4 = \left(2D\xi(1-\mathrm{e}^{-(\xi-V\xi_0)L_x})\right)^{-1}$ with $V = u/(2D\xi_0)$, $\xi_0 = (\gamma/D)^{1/2}$, and $\xi = \xi_0\left(V^2+1\right)^{1/2}$.

The representative time-independent base-state concentration profiles $C_0^A(x)$ and $C_0^B(x)$ of the reactants $A$ and $B$ are shown in **Figure 2** with the red and blue lines, respectively. The production of the reactants $A$ and $B$ appears as spikes in the profiles of $C_0^A$ and $C_0^B$ around $x_1$ and $x_2$, respectively, where the enzyme-coated patches are located. **Figures 2A–C** illustrate the changes in the chemical concentration profiles in the periodic system with $L_x = 3$ mm caused by the fluid velocity that increases from $u = 0$ (**Figure 2A**), to $u = 1$ (**Figure 2B**), and reaches $u = 2\mu\mathrm{ms}^{-1}$ (**Figure 2C**). **Figures 2D–H** demonstrate the changes in the chemical concentrations that occur in the infinite system, $L_x \to \infty$, as the fluid velocity either increases in the positive direction (of the $x$-axis) from $u = 0$ (**Figure 2D**), to $u = 1$ (**Figure 2E**), and to $u =$

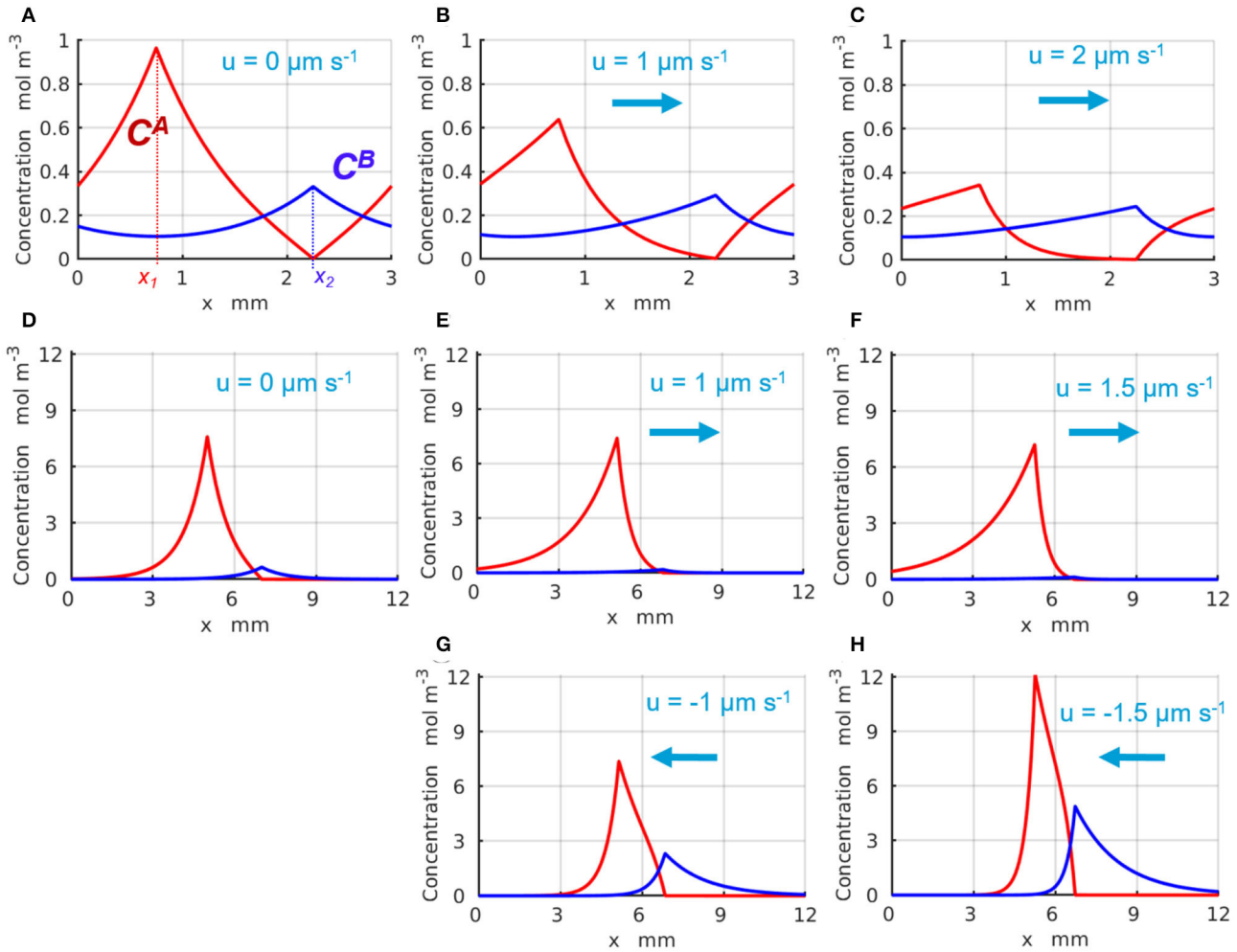


**FIGURE 2 |** Distribution of the base state concentrations $C_0^A(x)$ (red) and $C_0^B(x)$ (blue) along the quasi-1D channel. The peaks in $C_0^A(x)$ and $C_0^B(x)$ occur at the respective locations of the enzymes 1 and 2. For a periodic system **(A–C)** of length $L = 3$mm and the inter-patch distance $\Delta x = 1.5$ mm, the concentration profiles are plotted at the fluid velocities $u =$ **(A)** 0, **(B)** 1, and **(C)** $2\mu\text{m}\cdot\text{s}^{-1}$. For an infinite system ($L_x \to \infty$), the profiles are shown at **(D)** $u = 0\ \mu\text{m}\cdot\text{s}^{-1}$ and $\Delta x = 2$ mm; **(E)** $u = 1\ \mu\text{m}\cdot\text{s}^{-1}$ and $\Delta x = 1.766$ mm; **(F)** $u = 1.5\ \mu\text{m}\cdot\text{s}^{-1}$ and $\Delta x = 1.528$ mm; **(G)** $u = -1\ \mu\text{m}\cdot\text{s}^{-1}$ and $\Delta x = 1.766$ mm; and **(H)** $u = -1.5\ \mu\text{m}\cdot\text{s}^{-1}$ and $\Delta x = 1.528$ mm.

$1.5\mu\text{m}\,\text{s}^{-1}$ (**Figure 2F**), or increases in the negative direction to $u = -1$ (**Figure 2G**) and then to $u = -1.5\mu\text{m}\,\text{s}^{-1}$ (**Figure 2H**). The positive fluid velocities (**Figures 2E,F**) are seen to suppress the spike in the concentration $C_0^B$ at $x_2$, whereas the negative velocities (**Figures 2G,H**) promote the latter. Note that in the infinite system, the concentrations $C_0^A(x)$ and $C_0^B(x)$ exponentially decay to zero away from the corresponding enzyme-coated patches located at $x_1$ and $x_2$ (see **Figures 2D–H**).

## THE LINEAR STABILITY PROBLEM

We study the stability of the base state (Equations 14 and 15), by introducing small perturbations $C^j = c^j(x)e^{\omega t}$ with a complex growth rate $\omega = \omega_r + i\omega_i$, and linearizing Equations (9) and (10) around the base state. The dynamics of the perturbations is described by the following equations:

$$\partial_x^2 c^A - u\partial_x c^A - (\gamma + \omega)c^A = -k_1\sigma_1 F_1' c^B \delta(x - x_1) + k_2\sigma_2 F_2' c^A \delta(x - x_2) \quad (16)$$

$$\partial_x^2 c^B - u\partial_x c^B - (\gamma + \omega)c^B = -k_2\sigma_2 F_2' c^A \delta(x - x_2) \quad (17)$$

with the periodic boundary conditions $c^j(0) = c^j(L_x)$. Here, $i = \sqrt{-1}$ and the primes in $F_\alpha{}'$, $\alpha = 1, 2$, denote the derivatives of $F_\alpha$ with respect to $C^j$. Equations (16) and (17) are solved numerically using the shooting method (Stoer and Burlisch, 1980). The boundary value problem has solutions satisfied by the complex values $\omega(\Delta x, L_x, u, \gamma, k_\alpha\sigma_\alpha, K^j)$. The stability curves, $(k_1\sigma_1)_c(u)$ vs. $\Delta x$, are defined by the condition $\omega_r = 0$, and separate the domain of the time-independent steady bases states with $\omega_r < 0$ from the domain of oscillatory regimes, where $\omega_r > 0$ and $\omega_i \neq 0$.

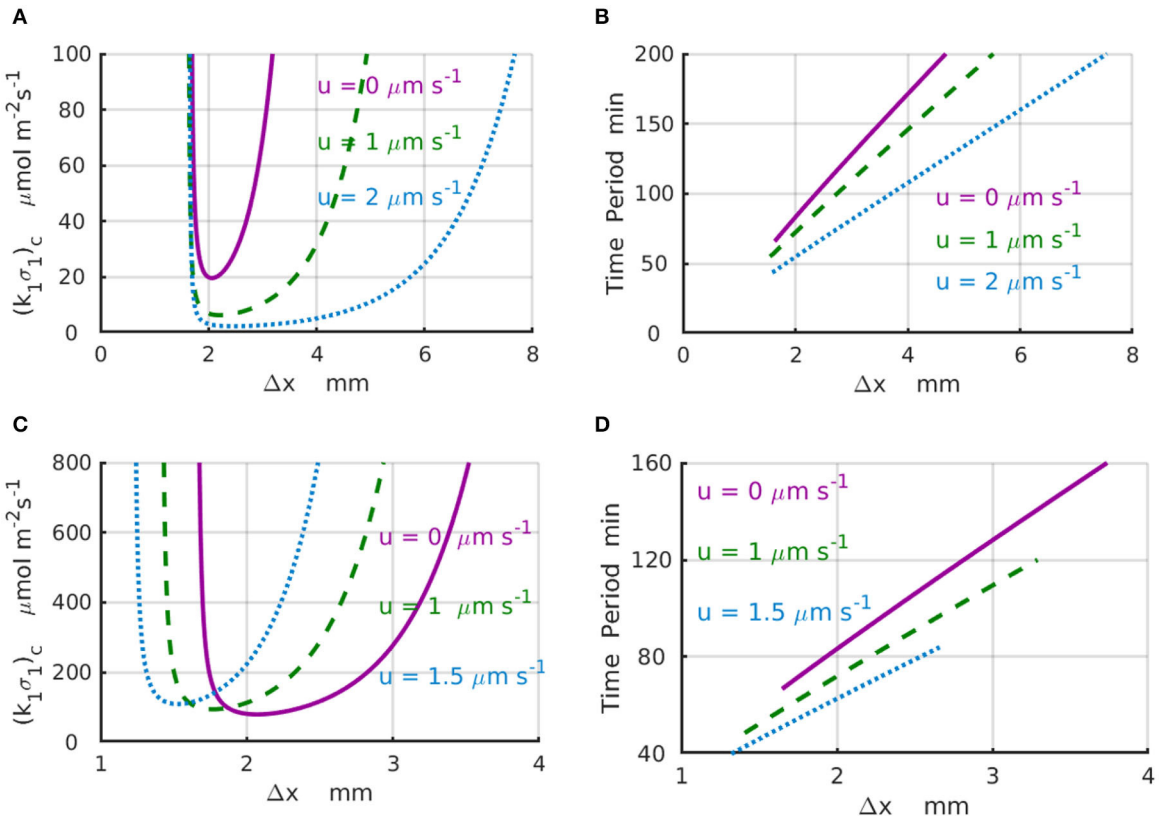


**FIGURE 3 |** Domain of chemical oscillations for different velocities of the imposed flow. **(A)** Stability curves, $(k_1\sigma_1)_c(\Delta x)$, for the fluid velocities of $u = 0$ (solid magenta line), 1 (dashed green line), and $2\mu\text{m}\cdot\text{s}^{-1}$ (dotted azure line) for a periodic system with the length of $L = 4$mm. **(B)** Periods of chemical oscillations as a function of the distance $\Delta x$ between the two enzymes-coated patches obtained along the stability curves in **(A)**. **(C)** Stability curves, $(k_1\sigma_1)_c(\Delta x)$, for the fluid velocities of $u = 0$ (solid magenta line), 1 (dashed green line), and $1.5\mu\text{m}\cdot\text{s}^{-1}$ (dotted azure line) for an infinite system with $L_x \to \infty$. The respective critical distances between the enzyme-coated patches are $\Delta x = 2$, 1.766, and 1.528mm. **(D)** Periods of chemical oscillations as a functions of the distance between the two enzymes obtained along the stability curves in **(C)**.

Results of the linear stability analysis performed for representative values of the imposed fluid velocities are presented in the **Figure 3** for a finite system with $L_x = 4$mm (**Figures 3A,B**) and an infinite system with $L_x \to \infty$ (**Figures 3C,D**). In particular, **Figure 3A** shows the stability curves, $(k_1\sigma_1)_c$ vs. $\Delta x$, calculated for the fluid velocities increasing from $u = 0$ (solid magenta line) to $u = 1$ (dashed green line), and then to $u = 2\mu\text{ms}^{-1}$ (dotted azure line). The shape of the stability curves demonstrates that the spatial separation $\Delta x = x_2 - x_1$ between the enzyme-coated patches is a parameter that controls the existence of the chemical oscillations in the system. The periods of the critical chemical oscillations $T = 2\pi/|\omega_i|$ for the same velocities are shown in **Figure 3B**. To illustrate the effect of the imposed fluid flow, we consider a system with $\Delta x = 2$mm. An increase in the fluid velocity from zero (solid magenta line) to $u = 2\mu\text{ms}^{-1}$ (dotted azure line) results in a 5-fold decrease in the critical reaction rate $(k_1\sigma_1)_c$ required to start the chemical oscillations in the system with $\Delta x = 2$mm (**Figure 3A**). At the same time, the corresponding period of oscillation decreases from $T(u = 0) \approx 86$ min to $T(u = 2\mu\text{m s}^{-1}) \approx 56$ min (**Figure 3B**). Note also that the critical distance between the enzyme-coated patches $\Delta x_c$, at which the chemical oscillations first appear at the lowest value of $(k_1\sigma_1)_c$, is not affected much by the velocity variations.

For the infinite system ($L_x \to \infty$), the stability curves $(k_1\sigma_1)_c(\Delta x)$ and corresponding plots of the period of the chemical oscillations are shown in **Figures 3C,D** for the fluid velocities increasing from $u = 0$ (solid magenta line) to $u = 1$ (dashed green line), and then to $u = 1.5\mu\text{m s}^{-1}$ (dotted azure line). For a fixed distance between the enzyme-coated patches, $\Delta x = 2$mm, the increase of the fluid velocity from $u = 0$ to $1.5\mu\text{m s}^{-1}$ requires more than a 2-fold increase in the reaction rate in order to surpass the critical value $(k_1\sigma_1)_c$ needed to excite the chemical oscillations. In contrast with the case of finite system, an increase in the velocity for the infinite system leads to a slight decrease in the critical distance between the enzyme-coated patches from $\Delta x_c = 2$mm at $u = 0$ to $\Delta x_c = 1.77$mm at $u = 1\mu\text{m s}^{-1}$, and then to $\Delta x_c = 1.56$mm at $u = 1.5\mu\text{m s}^{-1}$. Therefore, in an infinite system, larger reaction rates are required to start the chemical oscillations in the presence of the flow. Simultaneously, the corresponding periods

of the oscillation decrease substantially as shown in **Figure 3D**. In particular, when the fluid velocity increases from $u = 0$ to $u = 1.5\mu$m s$^{-1}$, the period of oscillation decreases more than twice, namely, from $T \approx 86$ min at $\Delta x_c = 2$mm (solid magenta line) to $T \approx 40$ min at $\Delta x_c = 1.56$mm (dotted azure line).

The stability analysis reveals that for a fixed reaction rate $k_1\sigma_1$, the chemical instability can occur only within a limited range of distances between the enzyme-coated patches $\Delta x_{\min} < \Delta x < \Delta x_{\max}$. When $k_1\sigma_1 < (k_1\sigma_1)_c$, the linear stability analysis indicates that the system is in a stable steady state with a time-independent distribution of the concentration profiles $C_0^j(x)$ along the channel (**Figure 2**). At the supercritical reaction rate $k_1\sigma_1 > (k_1\sigma_1)_c$ (**Figure 4**), the linear stability analysis predicts an instability, at which the concentrations of chemicals $A$ and $B$, $C^j(x,t)$, $j = A, B$, exhibit temporal oscillations with a frequency $|\omega_i|$.

The calculations also reveal that depending on the design of the system, the imposed fluid flows can substantially reduce the amount of the enzyme [determined by the critical reaction rate $(k_1\sigma_1)_c$] required to enable the chemical oscillations in the channel. As well, the flows along the channel can substantially increase the frequencies $|\omega_i| = 2\pi/T$ of the chemical oscillation. Moreover, there are conditions, such as at the point $\Delta x = 1.5$ mm and $k_1\sigma_1 = 200\mu$mol m$^{-2}$s$^{-1}$ shown in **Figure 3C**, when the time-independent chemical distributions at zero flow velocity could be turned into the chemical oscillations by simply accelerating the flow to a velocity $u = 2\mu$m s$^{-1}$.

The characteristic values of the physical parameters within the instability regions (see **Figures 3A,C**), where the chemical oscillations exist, determine the relevant time scales $\Delta x/u$, $\Delta x^2/D$, and $\Delta x C_0/k_1\sigma_1$ characterizing the rates of advective and diffusive transport, and the reaction rate, respectively. Ratios between these time scales indicate the relative importance of the different mechanisms contributing to the dynamics of the chemical oscillations. For example, the Peclet number, $\mathrm{Pe} = \frac{u\Delta x}{D}$, is defined as the ratio of the diffusive to advective time scales. For a characteristic length scale of $\Delta x = 2$ mm, reagent diffusivity of $D \sim 10^{-9}$m$^2$s$^{-1}$ and fluid velocity of $u \sim 1\mu$ms$^{-1}$, the resulting value of $\mathrm{Pe} \sim 2$ indicates that the diffusive and advective transport mechanisms are of comparable importance in the system's behavior. On the other hand, the comparison of the stability curves shown in **Figures 3A,C** for velocities $u = 0$, 1, and 2 $\mu$ms$^{-1}$, with the corresponding values $\mathrm{Pe} = 0$, 2, and 4, imply that the imposed fluid flow affects chemical oscillations (i.e., noticeably reduces the reaction rate and time period) when the Peclet number is comparable to one.

The relevant diffusive Damkohler number, $\mathrm{Da}_1^{\mathrm{d}} = \frac{k_1\sigma_1\Delta x}{DC_0}$, is defined as a ratio of the diffusive to reaction time scale, and can be calculated as $(k_1\sigma_1)_c$ (from **Figure 3**) multiplied by the factor $\frac{\Delta x}{DC_0} \sim 2.10^6$mol$^{-1}$m$^2$s (where the scale $C_0 \sim 1$ molm$^{-3}$ is suggested by the base state solutions in **Figure 2**). For the given range, $10 < (k_1\sigma_1)_c < 10^3$ $\mu$mol m$^{-2}$s$^{-1}$, in **Figure 3**, the diffusive Damkohler number varies between the limits $2 \cdot 10 < \mathrm{Da}_1^{\mathrm{d}} < 2 \cdot 10^3$. The similarly defined advective Damkohler number, $\mathrm{Da}_1^{\mathrm{a}} = \frac{k_1\sigma_1}{uC_0}$, varies in the range $10 < \mathrm{Da}_1^{\mathrm{a}} < 10^3$. The diffusive and advective Damkohler numbers, which are substantially >1, indicate that chemical reactions occur faster than the diffusive and advective mechanisms can transport reagents along the channel between the enzyme-coated patches. This transport-limited scenario for the chemical oscillations provides conditions where the advective flux can significantly amplify the diffusive transport.

## 1D REGIMES WITH SUPERCRITICAL REACTION RATES

To investigate the system beyond the stability boundaries, we numerically solve Equations (9) and (10) in a 1D cell $-L_x/2 \le x \le L_x/2$, with the periodic boundary conditions (Equation 11). We discretize the spatial domain of length $L_x$ into $N_x$ nodes, each representing a cube with a side equal to the grid spacing of $\mathrm{d}x = 100\mu$m, and apply a second order finite difference scheme to integrate the reaction-diffusion equations. Each reaction source term ($\propto F_\alpha$) was modeled as an element of size d$x$. As initial conditions, we use the uniform spatial distribution of reactants $C^j(x, t = 0) = r^j$, where $0 \le r^j \le 1$ is a random number. To match the situations analyzed within the linear stability theory, we perform computations in the domains with two different lengths. The simulations in the short domain, $L_x = 4$mm, are designed to match the stability analysis developed for the periodically alternating enzyme-coated patches. In these simulations, the chemical processes within one periodic cell affect through the boundary conditions the dynamics of the reactants in the neighboring cells. The simulations in the long domain of $L_x = 50$ mm ensure the absence of the chemical interactions between the neighboring cells (because the chemical concentrations decay exponentially with the distance away from the enzyme-coated patches) and, therefore, match the prediction of the stability analysis performed for the case of the infinitely long channel with $L_x \to \infty$.

The chemical oscillations, which occur at the supercritical reaction rates $k_1\sigma_1 > (k_1\sigma_1)_c$ in the short domain of $L_x = 4$ mm, are presented in **Figure 4**. **Figure 4A** displays the temporal variations of the concentrations $C^A(x_1, t)$ (red line) and $C^B(x_2, t)$ (blue line) that take place at the locations of the enzyme-coated patches $x_1$ and $x_2$ for the control parameters $u = 1$ $\mu$s$^{-1}$ and $k_1\sigma_1 = 10$ $\mu$mol m$^{-2}$s$^{-1}$. **Figure 4B** shows maximal (dashed lines) and minimal (solid lines) values of the concentrations $C^A(x, t)$ and $C^B(x, t)$ achieved during the period of oscillation. Similarly, **Figure 4C** shows the temporal variations of the reactant concentrations $C^A(x_1, t)$ (red line) and $C^B(x_2, t)$ (blue line), while **Figure 4D** shows the maximal (dashed lines) and minimal (solid lines) values of the concentrations $C^A(x, t)$ and $C^B(x, t)$ calculated at the parameters $u = 1\mu$m s$^{-1}$ and $k_1\sigma_1 = 98$ $\mu$mol m$^{-2}$s$^{-1}$. Comparison of the oscillation dynamics presented in **Figure 4A** for $k_1\sigma_1 = 10$ $\mu$mol m$^{-2}$s$^{-1}$ and **Figure 4C** for $k_1\sigma_1 = 98$ $\mu$mol m$^{-2}$s$^{-1}$ reveals that the chemical oscillations at higher reaction rates deviate from the sinusoidal kinetics observed at sufficiently low reaction rates.

To characterize the supercritical regimes of the chemical oscillations, we define the oscillation amplitude of the reactant $A$

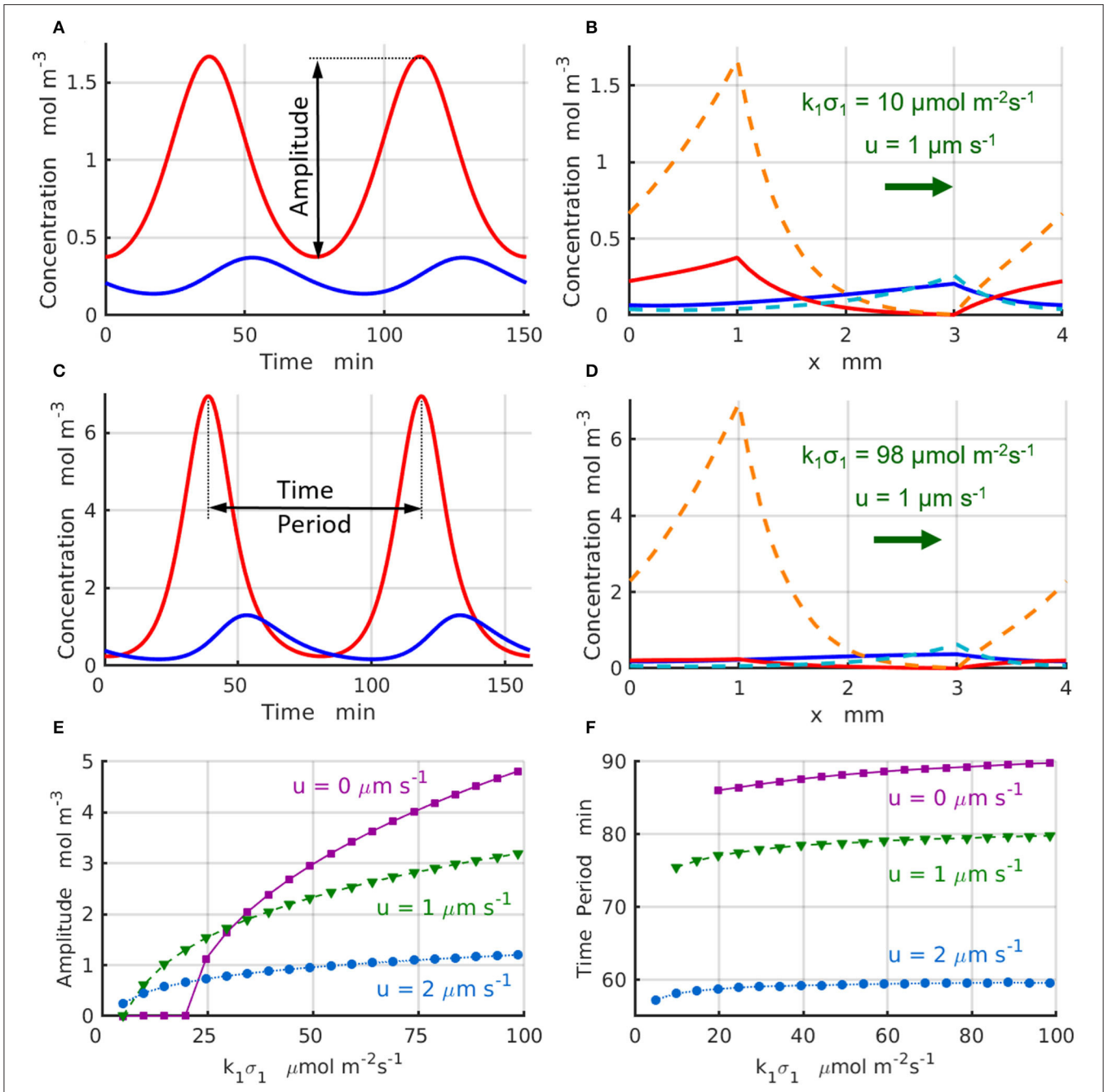


**FIGURE 4 |** Chemical oscillations in a periodic system with $L_x = 4$mm and $\Delta x = 2$ mm at the supercritical reaction rates, $\mu_1 > \mu_c$. The concentrations $C^A(x_1, t)$ (red) and $C^B(x_2, t)$ (blue) as functions of time at $u = 1\mu\text{m}\cdot\text{s}^{-1}$, $k_1\sigma_1 =$ **(A)** 10 and **(C)** 98 $\mu\text{mol}\cdot\text{m}^{-2}\text{s}^{-1}$. Maximal (dashed lines) and minimal (solid lines) values of the concentrations within one period of the oscillation at $u = 1\mu\text{m}\cdot\text{s}^{-1}$, $k_1\sigma_1 =$ **(B)** 10 and **(D)** $98\mu\text{mol}\cdot\text{m}^{-2}\text{s}^{-1}$. **(E)** Amplitude and **(F)** period of the chemical oscillations as functions of the reaction rate $k_1\sigma_1$ for the inter-patch distance $\Delta x = 2$ mm at $u = 0$ (solid magenta lines and squares), 1 (dashed green lines and triangles), and $2\mu\text{m}\cdot\text{s}^{-1}$ (dotted azure lines and circles).

as $A^A = \max_{0\le t\le T}\left(C^A(x_1,t)\right) - \min_{0\le t\le T}\left(C^A(x_1,t)\right)$. The amplitudes as functions of the reaction rate $k_1\sigma_1$ are plotted in **Figure 4E** for the values of fluid velocities increasing from $u = 0$ (solid magenta line and squares) to $u = 1$ (dashed green line and triangles), and then to $u = 2\mu\text{m}\,\text{s}^{-1}$ (dotted azure lines and circles). The regimes are supercritical and the amplitudes grow approximately in proportion to the square root of the distance from the bifurcation point, $A^A \propto \left(k_1\sigma_1 - (k_1\sigma_1)_c\right)^{1/2}$. As seen in **Figure 4E**, the amplitude of oscillations decreases with an increase in the velocity of the imposed flow. Finally,

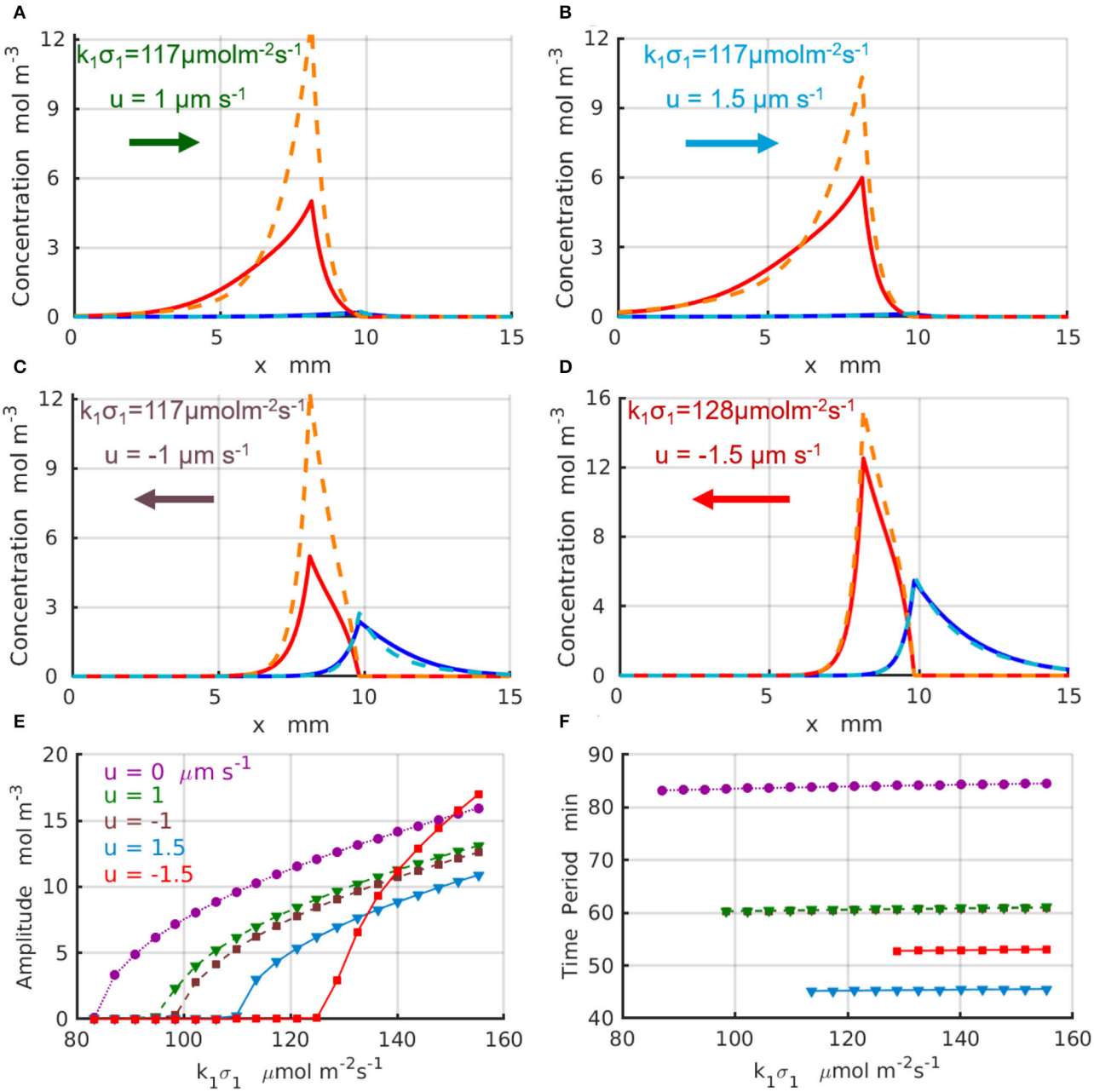


**FIGURE 5 |** Chemical oscillations in an infinite system with $L_x \to \infty$ at the supercritical reaction rates $\mu_1 > \mu_c$. Maximal (dashed lines) and minimal (solid lines) concentration profiles $C^A$ (red) and $C^B$ (blue) within one period of oscillations for the set of parameter $(\Delta x, k_1\sigma_1, u)$ **(A)** $(1.766\text{mm}, 117\mu\text{mol}\cdot\text{m}^{-2}\text{s}^{-1}, 1\mu\text{m}\cdot\text{s}^{-1})$; **(B)** $(1.528\text{mm}, 117\mu\text{mol}\cdot\text{m}^{-2}\text{s}^{-1}, 1.5\mu\text{m}\cdot\text{s}^{-1})$; **(C)** $(1.766\text{mm}, 117\mu\text{mol}\cdot\text{m}^{-2}\text{s}^{-1}, -1\mu\text{m}\cdot\text{s}^{-1})$; **(D)** $(1.528\text{mm}, 128\mu\text{mol}\cdot\text{m}^{-2}\text{s}^{-1}, -1.5\mu\text{m}\cdot\text{s}^{-1})$. **(E)** Amplitudes and **(F)** periods of the chemical oscillations as functions of the reaction rate $k_1\sigma_1$ for parameters $u = 0$ and $\Delta x = 2$ mm (dotted magenta line and circles), $u = 1\mu\text{m}\cdot\text{s}^{-1}$ and $\Delta x = 1.766$ mm (dashed green line and triangles), $u = -1\mu\text{m}\cdot\text{s}^{-1}$ and $\Delta x = 1.766$ mm (dashed brown line and squares), $u = 1.5\mu\text{m}\cdot\text{s}^{-1}$ and $\Delta x = 1.528$ mm (solid azure line and triangles), and $u = -1.5\mu\text{m}\cdot\text{s}^{-1}$ and $\Delta x = 1.528$ mm (solid red line and squares).

**Figure 4F** shows that the period oscillations, $T$, decreases with an increase in both the reaction rate $k_1\sigma_1$ and the fluid velocity. The simulation results projected onto the onset of chemical oscillations are in a good agreement with the critical reaction rates $(k_1\sigma_1)_c$ predicted by the stability analysis (**Figures 3A,B**).

The results for the chemical oscillations catalyzed by two enzyme-coated patches placed in the long simulation domain of $L_x = 50$ mm are presented in **Figure 5**. The periodic temporal variations of the concentrations $C^A(x_1, t)$ and $C^B(x_2, t)$ are qualitatively similar to those presented in **Figures 4A,C**. **Figures 5A–D** show the maximal (dashed lines) and minimal

(solid lines) values of the concentration profiles $C^A$ (red) and $C^B$ (blues) achieved during one period of oscillation; the control parameters are indicated in the figure and specified in the caption. The oscillation amplitudes $A^A$ as functions of the reaction rate $k_1\sigma_1$ are plotted in **Figure 5E** for the fluid velocity increasing in the positive direction (of the $x$-axis) from $u = 0$ (dotted magenta line and circles) to $u = 1\mu$m s$^{-1}$ (dashed green line and triangles), and then to $u = 1.5\mu$m s$^{-1}$ (solid azure line and triangles). **Figure 5E** shows the amplitudes for the fluid velocities increasing in the negative direction to $u = -1\mu$m s$^{-1}$ (dashed brown line and squares) and $u = -1.5\mu$m s$^{-1}$ (solid red line and squares). At most tested parameter sets, the amplitude of the oscillations decreases with an increase in magnitude of the fluid velocity. In the case of negative velocity of the imposed flow $u = -1.5\mu$m s$^{-1}$ (solid red line and squares), however, the amplitude of the chemical oscillations increase with an increase in $k_1\sigma_1$ faster than that for the oscillations without fluid flow (dotted magenta line and circles). Finally, **Figure 5F** shows the period of the oscillations, $T$, which increases with an increase in the reaction rate $k_1\sigma_1$ and decreases with the increasing fluid velocities. In particular, at the fluid flows with velocity $u = 1.5\mu$m s$^{-1}$ (solid azure line and triangles) the oscillation period, $T \approx 46$ min, decreases almost twice relative to the case without flow $u = 0$ (dotted magenta line and circles). The simulations projected onto the onset of the chemical oscillations confirm the values of the critical reaction rates $(k_1\sigma_1)_c$ predicted by the linear stability analysis and presented in **Figures 3C,D**.

The non-linear 1D simulations reveal that an increase in the frequency of the chemical oscillations under increasing velocities of the imposed flow is in most of the cases accompanied by a reduction of the oscillation amplitude. We found however that there are some parameters and system configurations, for which both the amplitude and frequency of chemical oscillation exhibit a simultaneous increase as indicated by the red lines in **Figures 5E,F**. Therefore, the design of the system and careful choice of the control parameters, such as the reaction rates and velocity of the imposed flow, are important for tuning the frequency of chemical oscillations to either suppress or amplify the oscillations.

## 2D CHEMICAL OSCILLATIONS UNDER POISEUILLE FLOW

To test the relevance of the developed 1D model, we compare its predictions with the results of simulations of a more realistic two-dimensional system. We solve Equations (1)–(3) in a periodic 2D unit cell with $0 \le x \le L_x$, $0 \le z \le H$. At the solid walls ($z = 0, H$) that bound the 2D channel, we require the no-slip conditions for the fluid velocities and zero chemical flux across the parts of the walls free of the enzymes, as described by Equation (7). The periodic boundary conditions in the $x$ direction are enforced through the Equation (8). The chemical reactions are catalyzed by the enzymes 1 and 2, which are immobilized at the patches of a finite length $\delta x$ and are introduced through the boundary conditions given by Equations (4) and (5).

The solution to the Navier-Stokes equation (Equation 2), with an imposed pressure gradient $\nabla p = (f, 0, 0)$ along the channel and the no-slip boundary conditions (Equation 7), on the walls yields the Poiseuille flow, $\mathbf{u} = (u_x, 0, 0)$, with a parabolic velocity profile across the channel, $u_x = \frac{f}{2\mu} z\,(H - z)$. We use an average across the channel fluid velocity, $u_a = \frac{H^2 f}{12\mu}$, in order to characterize the effects of the flow on the chemical oscillations, and to compare the obtained results with those of the 1D model controlled by a constant velocity, $u$. For the sake of simplicity, we compare the results obtained for the 1D and 2D models only for the short periodic domain, $L_x = 4$mm.

In the 2D simulations, the results depend on the length of a patch, $\delta x$, in addition to the inter-patch distance $\Delta x$ and the geometry of the channel described by $L_x$ and $H$. These simulations involve a rectangular domain of size $L_x \times H$, which is discretized using a grid $80\mathrm{d}x \times N_z\mathrm{d}x$ with the grid spacing $\mathrm{d}x = 50\mu m$; the number of nodes in the vertical direction $N_z = H/\mathrm{d}x$ is defined by $H$. We use the Lattice Boltzmann method to solve the continuity and Navier-Stokes equations (Equations 1 and 2). A second order finite difference scheme is applied to solve the reaction-diffusion equations (Equation 3). Additionally, we use the patches of equal length $\delta x = 0.2$mm, and set the distance between them to $\Delta x = 2$ mm. The reaction rates are assigned the values $k_1\sigma_1 = 98\mu$mol m$^{-2}$s$^{-1}$ and $k_2\sigma_2 = 3403\mu$mol m$^{-2}$s$^{-1}$.

**Figure 6** demonstrates the effect of the imposed flow on the 2D chemical oscillations for channels of different width $H$. In particular, **Figure 6A** displays the parabolic profile $u_x(z)$ of the imposed flow for the channel with $H = 0.5$mm and the average velocity $u_a = 2\mu$m s$^{-1}$. **Figure 6B** shows the temporal variations in the concentrations $C^A(x_1, z, t)$ (red) and $C^B(x_2, z, t)$ (blue) of the reactants $A$ and $B$, respectively, calculated at $z = 0.1H$ for the velocity $u_a = 2\mu$m s$^{-1}$. **Figures 6C,D** show the 2D distributions of the reactant $C^A$ (yellow) along the channel corresponding to the maximal (**Figure 6C**) and minimal (**Figure 6D**) values achieved within one period of the oscillation (see **Figure 6B**). **Figures 6E,F** present the amplitude $A^A$ and period of the chemical oscillations $T$ as functions of the channel height $H$ plotted for the three values of averaged velocity of the imposed flow $u_a = 1$, 1.5, and $2\mu$m s$^{-1}$ labeled with green triangles, brown squares, and azure circles, respectively. The amplitudes in **Figure 6E** are calculated as $A^A = \max_{0\le t\le T}\left(C^A(x_1, z, t)\right) - \min_{0\le t\le T}\left(C^A(x_1, z, t)\right)$ for $z = 0.1H$.

The results presented in **Figure 6E** indicate that for wider 2D channels, the oscillation amplitudes $A^A$ progressively decrease toward zero. This happens because the geometry of the 2D channels departs from the one-dimensional limit and the discrepancy between 1D and 2D models increases as the channel thickness $H$ increases. Due to the difference in the geometry of the channel and enzyme-coated patches, the amplitudes $A^A$ of the 2D oscillations $C^A(x_1, z, t)$ calculated at the location $x = x_1$ and $z = 0.1H$ (in the 2D-domain) are significantly lower than the amplitudes of the 1D oscillations $C^A(x_1, t)$ calculated (in the 1D-domain) for the same reaction rates and presented in **Figure 4E**. In the agreement with the predictions of the

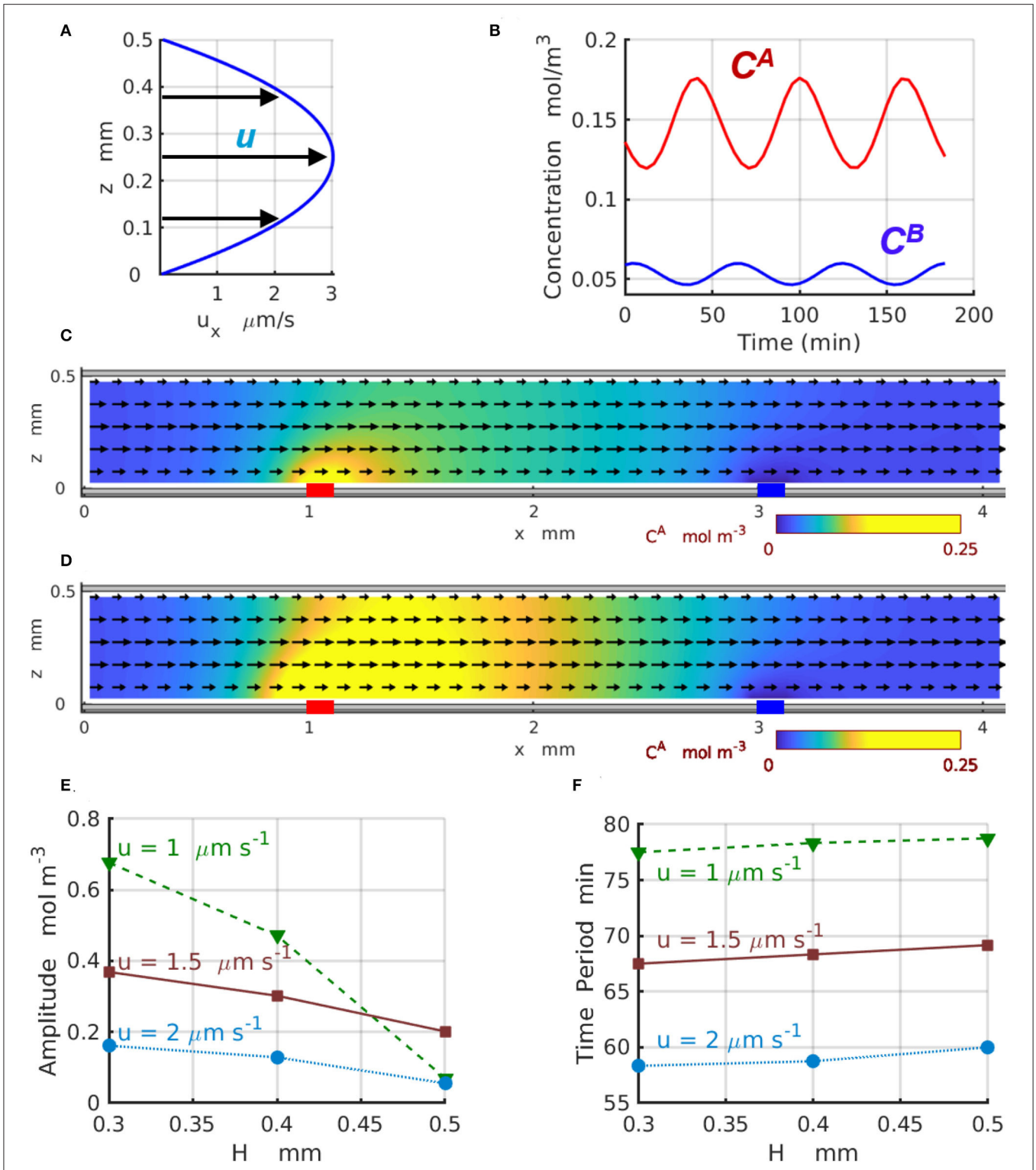


**FIGURE 6 |** Chemical oscillations in a 2D periodic system with $L_x = 4$mm. **(A)** Profile of the imposed flow with the averaged velocity $u_a = 2\mu\text{m} \cdot \text{s}^{-1}$. **(B)** Concentrations $C^A(x_1, z, t)$ (red) and $C^B(x_2, z, t)$ (blue) as functions of time at $z = 0.1H$. The spatial distributions of **(C)** minimal and **(D)** maximal concentration $C^A(x, z, t)$ within one period of oscillation at $u_a = 2\mu\text{m} \cdot \text{s}^{-1}$ and $k_1\sigma_1 = 98\ \mu\text{mol} \cdot \text{m}^{-2}\text{s}^{-1}$. Yellow color indicates regions with high concentrations of reagent *A*. The black arrows show the direction and relative magnitude of the imposed fluid flow. **(E)** Amplitude and **(F)** period of the chemical oscillations as functions of the channel width *H* at the averaged fluid velocity of $u_a = 1$ (dashed green line and triangles), 1.5 (solid brown line and squares), and (dotted azure lines and circles).

one-dimensional model, the two-dimensional model also shows a reduction in the oscillation amplitude that occurs as the flow velocity increases. At the same time, the period of the 2D chemical oscillations $C^A(x_1, z, t)$, shown in the **Figure 6F** for the average velocities $u_a = 1$ (green triangles) and $2\mu$m s$^{-1}$ (azure circles), is comparable with the period of the 1D oscillations $C^A(x_1, t)$ presented in **Figure 4F** for the comparable fluid velocities $u$. The oscillation periods within the two models are slightly different because the distance $\Delta x$ between the enzyme-coated patches in 1D and 2D models are not the same. The period of the 2D-oscillations $T$, shown in **Figure 6F**, increases with an increase in the channel width $H$, but decreases with the increasing flow velocities what is consistent with the predictions of the 1D model presented in **Figure 4F**. The dynamics of the 2D chemical oscillations are also presented in the **Supplementary Video 1**.

## CONCLUSIONS

We developed a model to analyze the chemical oscillations produced by enzyme-coated patches in a long, narrow fluidic channel. In contrast to previous models for non-linear chemical dynamics (Scott, 1994; Epstein and Pojman, 1998), we introduced non-linearity into the system through the boundary conditions on the reaction-diffusion equations. The imposed pressure-driven flow along this fluidic channel affects the transport of reagents throughout the fluid and hence, affects the oscillatory behavior in the system. To analyze the effects of the imposed flow, we first described the behavior of the system through a one-dimensional model. The predictions of the 1D model were compared with the results of simulations for two-dimensional channels with a finite thickness. The agreement between the two approaches validates the applicability of the one-dimensional model in capturing the dynamic behavior within the long, narrow channel.

Through our analytical model and simulations, we found that the distance between the enzyme-coated patches dictates the existence of chemical oscillations within the channel. We also identified parameters that control the amplitude and frequency of the chemical oscillations. In particular, we showed that in millimeter-size channels, imposed flows with velocities on the order of 1$\mu$m s$^{-1}$ can substantially increase the frequency of the oscillations and modify the range of parameters for which the oscillations occur.

The imposed pressure-driven flow can also significantly reduce the reaction rates needed to produce chemical oscillations by the enzymatic reactions. The flow alters the chemical flux $\mathbf{j} = D\nabla C + \mathbf{u}C$, which now includes both diffusive and advective contributions to the chemical transport. Additionally, for a range of parameters considered here, the imposed flow reduces the amplitude of the chemical oscillation. Moreover, sufficiently fast flows cause the reagents in the solution to become well-mixed and thereby suppress the oscillations.

These findings elucidate how an externally applied flow affects the chemical oscillations produced by coupled chemical reactions. These results allow us to establish design rules for regulating the dynamics of coupled reaction-diffusion processes and can facilitate the development of chemical reaction networks that act as chemical clocks. Notably, the period of oscillations in biochemical reaction networks (Novak and Tyson, 2008; Lim et al., 2013) is typically on the order of hours. Significantly shorter periods of chemical oscillations can be obtained by combining the localized enzymatic reactions considered here and imposed fluid flows, thereby providing faster chemical clocks for a range of applications.

Finally, we note that instead of utilizing an externally imposed flow, catalytic reactions that generate density variations as reactants are converted to products in fluid-filled chambers can give rise to solutal buoyancy forces, which propel the motion of the fluid through the chambers. As we showed in recent modeling studies, these inherent, chemically-generated flows are also effective at controlling the chemical oscillations in the system (Shklyaev et al., 2020).

## DATA AVAILABILITY STATEMENT

All datasets presented in this study are included in the article/**Supplementary Material**.

## AUTHOR CONTRIBUTIONS

OS performed the stability analysis and simulations. VY developed the quasi-1D approximation and identified parameters crucial for the effect. AB organized the work and analyzed the data. All authors contributed to the article and approved the submitted version.

## ACKNOWLEDGMENTS

The development of the analytical model was supported by funds from the Center for Bio-Inspired Energy Science, an Energy Frontier Research Center funded by the US Department of Energy, Office of Science, Basic Energy Sciences under Award DE-SC0000989. Authors also gratefully acknowledge funding from NSF grant 1740630 for the development of the computational model.

## SUPPLEMENTARY MATERIAL

The Supplementary Material for this article can be found online at: https://www.frontiersin.org/articles/10.3389/fchem.2020.00618/full#supplementary-material

**Supplementary Video 1 |** Oscillations of the concentration of chemical A. Yellow color indicates regions with high concentrations of reagent A. The black arrows show the direction and relative magnitude of the imposed fluid flow. The averaged velocity of the imposed flow is 2 micrometers per second.

## REFERENCES


Chandrasekhar, S. (1961). *Hydrodynamic and Hydro Magnetic Stability*. Clarendon, TX: Oxford.

Elowitz, M. B., and Leibler, S. (2000). A synthetic oscillatory network of transcriptional regulators *Nature* 403, 335–338. doi: 10.1038/35002125

Epstein, I. R., and Pojman, J. A. (1998). *An Introduction to Nonlinear Chemical Dynamics: Oscillations, Waves, Patterns, and Chaos*. New York, NY: Oxford.

Jez, J. M., and Cahoon, R. E. (2004). Kinetic mechanism of glutathione synthetase from *Arabidopsis thaliana*. *J. Biol. Chem.* 279, 42726–42731. doi: 10.1074/jbc.M407961200

Jez, J. M., Cahoon, R. E., and Chen, S. (2004). Arabidopsis thaliana glutamate-cysteine ligase. *J. Biol. Chem.* 279, 33463–33470. doi: 10.1074/jbc.M405127200

Jin, W., and Chen, H. (2000). A new method of determination of diffusion coefficients using capillary zone electrophoresis (peak-height method). *Chromatographia* 52:17. doi: 10.1007/BF02490786

Lim, W. A., Lee, C. M., and Tang, C. (2013). Design principles of regulatory networks: searching for the molecular algorithms of the cell. *Mol. Cell* 49, 202–212. doi: 10.1016/j.molcel.2012.12.020

Novak, B., and Tyson, J. (2008). Design principles of biochemical oscillators. *Mol. Cell Biol.* 9, 981–991. doi: 10.1038/nrm2530

Prigogine, I., and Lefever, R. (1968). Symmetry breaking instabilities in dissipative systems. II. *J. Chem. Phys.* 48:1695. doi: 10.1063/1.1668896

Scott, S. K. (1994). *Oscillations, Waves, and Chaos in Chemical Kinetics*. New York, NY: Oxford.

Shklyaev, O. E., Yashin, V. V., Stupp, S. I., and Balaz, A. C. (2020). Enhancement of chemical oscillations by self-generated convective flows. *Commun. Phys.* 3:70. doi: 10.1038/s42005-020-0341-3

Shum, H., Yashin, V. V., and Balazs, A. C. (2015). Self-assembly of microcapsules regulated via the repressilator signaling network. *Soft Matter* 11, 3542–3549. doi: 10.1039/C5SM00201J

Stoer, J., and Burlisch, R. (1980). *Introduction to Numerical Analysis*. New York, NY: Springer-Verlag.

Turing, A. M. (1952). The chemical basis of morphogenesis. *Philos. Trans. R. Soc. Lond. B* 237:37. doi: 10.1098/rstb.1952.0012


**Conflict of Interest:** The authors declare that the research was conducted in the absence of any commercial or financial relationships that could be construed as a potential conflict of interest.

*Copyright © 2020 Shklyaev, Yashin and Balazs. This is an open-access article distributed under the terms of the Creative Commons Attribution License (CC BY). The use, distribution or reproduction in other forums is permitted, provided the original author(s) and the copyright owner(s) are credited and that the original publication in this journal is cited, in accordance with accepted academic practice. No use, distribution or reproduction is permitted which does not comply with these terms.*

frontiers in Chemistry

REVIEW
published: 21 August 2020
doi: 10.3389/fchem.2020.00707

# Dynamics of Ultrathin Vanadium Oxide Layers on Rh(111) and Rh(110) Surfaces During Catalytic Reactions

*Bernhard von Boehn and Ronald Imbihl**

*Institut für Physikalische Chemie und Elektrochemie, Leibniz Universität Hannover, Hanover, Germany*

Over the past 35 years rate oscillations and chemical wave patterns have been extensively studied on metal surfaces, while little is known about the dynamics of catalytic oxide surfaces under reaction conditions. Here we report on the behavior of ultrathin V oxide layers epitaxially grown on Rh(111) and Rh(110) single crystal surfaces during catalytic methanol oxidation. We use photoemission electron microscopy and low-energy electron microscopy to study the surface dynamics in the $10^{-6}$ to $10^{-2}$ mbar range. On $VO_x$/Rh(111) we find a ripening mechanism in which $VO_x$ islands of macroscopic size move toward each other and coalesce under reaction conditions. A polymerization/depolymerization mechanism of $VO_x$ that is sensitive to gradients in the oxygen coverage explains this behavior. The existence of a substructure in $VO_x$ islands gives rise to an instability, in which a $VO_x$ island shrinks and expands around a critical radius in an oscillatory manner. At $10^{-2}$ mbar the $VO_x$ islands are no longer stable but they disintegrate, leading to turbulent redistribution dynamics of $VO_x$. On the more open and thermodynamically less stable Rh(110) surface the behavior of $VO_x$ is much more complex than on Rh(111), as V can also populate subsurface sites. At low V coverage, one finds traveling interface pulses in the bistable range. A state-dependent anisotropy of the surface is presumably responsible for intriguing chemical wave patterns: wave fragments traveling along certain crystallographic directions, and coexisting different front geometries in the range of dynamic bistability. Annealing to 1000 K causes the formation of macroscopic $VO_x$ islands. Under more reducing conditions dendritic growth of a $VO_x$ overlayer is observed.

**Keywords: vanadium oxide, chemical waves, methanol oxidation, heterogeneous catalysis, oxide redistribution**

OPEN ACCESS

***Edited by:***
*Marek Orlik,*
*University of Warsaw, Poland*

***Reviewed by:***
*Victor Bychkov,*
*Semenov Institute of Chemical Physics (RAS), Russia*
*Rajkumar Kore,*
*University of Kansas, United States*

****Correspondence:***
*Ronald Imbihl*
*imbihl@pci.uni-hannover.de*

***Specialty section:***
*This article was submitted to Physical Chemistry and Chemical Physics, a section of the journal Frontiers in Chemistry*

***Received:*** *05 May 2020*
***Accepted:*** *09 July 2020*
***Published:*** *21 August 2020*

***Citation:***
*von Boehn B and Imbihl R (2020) Dynamics of Ultrathin Vanadium Oxide Layers on Rh(111) and Rh(110) Surfaces During Catalytic Reactions. Front. Chem. 8:707. doi: 10.3389/fchem.2020.00707*

## INTRODUCTION

Chemical waves and kinetic oscillations on catalytic surfaces have been studied starting from about 1980 with the vast majority focusing on reactions on metal surfaces (Ertl, 1991; Imbihl and Ertl, 1995; Imbihl, 2005). Low pressure ($p < 10^{-3}$ mbar) single crystal studies of catalytic CO oxidation and catalytic NO reduction on Pt, Rh, Pd and Ir catalysts yielded a plethora of different phenomena and they led to experimentally verified mechanisms. Despite the fact that the majority of the catalysts in chemical industry is based on oxidic materials, up to 2010 hardly any study of non-linear phenomena on oxidic catalysts existed. The reasons why metal catalyst were preferred against oxidic catalysts area easy to understand. Oxidic surfaces are structurally more complex, they are more difficult to prepare and surface analytical techniques based on electrons or ions are often of limited value due to beam damaging and electrical charging effects.

A concept to avoid these difficulties is based on the use of model systems in which ultrathin oxide layers are deposited on a metallic support. The main model system chosen here are submonolayer coverages of vanadium oxide deposited on a Rh(111) single crystal surface. Vanadium oxide based catalyst are widely applied in industrial catalysis, e. g., in partial oxidation reactions of hydrocarbons, in the selective catalytic reduction (SCR) in environmental catalysis, and in the production of sulfuric acid (Bond and Tahir, 1991). Important for the high catalytic activity is the ability of V to easily switch its oxidation state between +2 and +5. In most industrial applications, vanadium oxide catalysts are used in form of ultrathin layers, or as isolated clusters supported on an oxidic material of negligible catalytic activity. Of key importance is therefore knowledge about the dispersion of $VO_x$ on a support material and redistribution dynamics under reaction conditions, which change the catalyst dispersion.

Besides the connection to "real catalysis," the choice of the model system of supported submonolayer oxide films offers several advantages: (i) $VO_x$ on Rh(111) exhibits a large number of ordered overlayers which have been exceedingly well characterized by surface analytical methods (Schoiswohl et al., 2004a,b; Surnev et al., 2013); for most of these overlayers structure models are available. (ii) Due to the electrically conducting support, electron-based analytical techniques can be applied. (iii) The system it strictly two-dimensional. Since V-oxides in their catalytically most active form are present either as isolated clusters or at monolayer coverages on a support material, studies of model catalysts with ultrathin layers of V-oxide are relevant to "real catalysis."

The first aim of these studies was to see whether the spatially uniform distribution of the $VO_x$ catalyst present after preparation is lifted under the influence of a catalytic reaction. Mostly the partial oxidation of methanol was chosen as reaction system, but also the $H_2 + O_2$ and other simple oxidation reactions were investigated. In fact, macroscopic stripe patterns and patterns of circular islands of $VO_x$ developed under reaction conditions. The circular $VO_x$ islands that developed exhibited a rather remarkable behavior. Two close-by islands moved toward each other and finally coalesced under reaction conditions (Hesse et al., 2015). Effectively, this leads to larger islands, similar to Ostwald ripening.

In order to see whether this type of behavior can be generalized, different reactions were investigated with $VO_x$ on Rh(111) and, moreover, the Rh(111) substrate was exchanged against Rh(110) (von Boehn and Imbihl, 2018). The growth of $VO_x$ on the more open and thermodynamically less stable surface Rh(110) surface is much more complex than on Rh(111) (von Boehn et al., 2017). In addition, this system had hardly been explored, so that no structure models were available. On the other hand, intriguing chemical wave patterns have been found in catalytic methanol oxidation on $VO_x$/Rh(110), a behavior distinctly different from $VO_x$/Rh(111) where only $VO_x$ redistribution but no chemical wave patterns have been found. The results with both substrates, Rh(111) and Rh(110), are reviewed in this report.

Model catalyst studies and "real catalysis" cannot be connected without addressing the so-called "pressure and materials gap" problem in heterogeneous catalysis (Schlögl, 2015). The main strategy to close the pressure gap is the use of *in situ* or operando techniques, because only then one obtains the structure/composition of the active catalyst that is required for establishing a structure-function relationship. The low-energy electron microscope (LEEM) that found extensive use in this study is a typical UHV instrument designed to be operated close to $10^{-10}$ mbar. In an effort to bridge at least a large part of the pressure gap, this LEEM instrument was modified, so that it could be operated up to $10^{-1}$ mbar (Franz et al., 2019). Applied to catalytic methanol oxidation on Rh(111)/$VO_x$, this modified instrument revealed that at $10^{-2}$ mbar the $VO_x$ islands are no longer stable but disintegrate, displaying turbulent behavior (von Boehn et al., 2020).

One aim of this review is to summarize the progress that has been achieved in the study of non-linear phenomena on catalytic oxide surfaces using the example of ultrathin supported V-oxide layers. A second goal is to demonstrate the significance of non-linear dynamics for catalytic research. Quite impressive wave patterns have been found in catalytic reactions on single crystalline metal surfaces, but asked about the significance for catalysis, many scientists would be very reluctant to concede any significance at all. Several examples presented in this review, like $VO_x$ redistribution patterns connected to an activation of the catalyst or reaction-induced ripening of oxide islands, demonstrate very convincingly that a coherent understanding of the properties of a catalyst is not possible without taking dynamic phenomena into account.

# REACTION DYNAMICS ON $VO_X$/RH(111)

## Choice of Model System and Methods of Investigation

As a model system for studying the redistribution of $VO_x$ catalysts during several catalytic reactions we utilize submonolayer $VO_x$ films on Rh(111). The system $VO_x$/Rh(111) has been extremely well characterized in the monolayer and submonolayer coverage range (Schoiswohl et al., 2004b, 2005, 2006). Numerous ordered overlayers exist and structure models are available for many of them. All these structures can be described as network structures following the same building principle: $VO_n$ ($n = 3$–5) units are connected by sharing oxygen atoms (Schoiswohl et al., 2004b). An example of such a two-dimensional network structure, the so-called $(\sqrt{7} \times \sqrt{7})$R19.1° structure, is shown in **Figure 1A**. The most abundant structural unit is a $VO_5$ pyramid with a V atom being above the center of a square base formed by four O atoms (V atom hidden in **Figure 1A** by an O-atom on top of it).

This system exhibits several advantages: (i) the system is strictly two-dimensional; (ii) $VO_x$ is highly mobile on the flat Rh(111) surface, (iii) submonolayer $VO_x$ films on Rh(111) have a high catalytic activity in many oxidation reactions, and *iv)* charging problems are avoided thus allowing the use of electron-based surface analytical techniques. It should be added that the

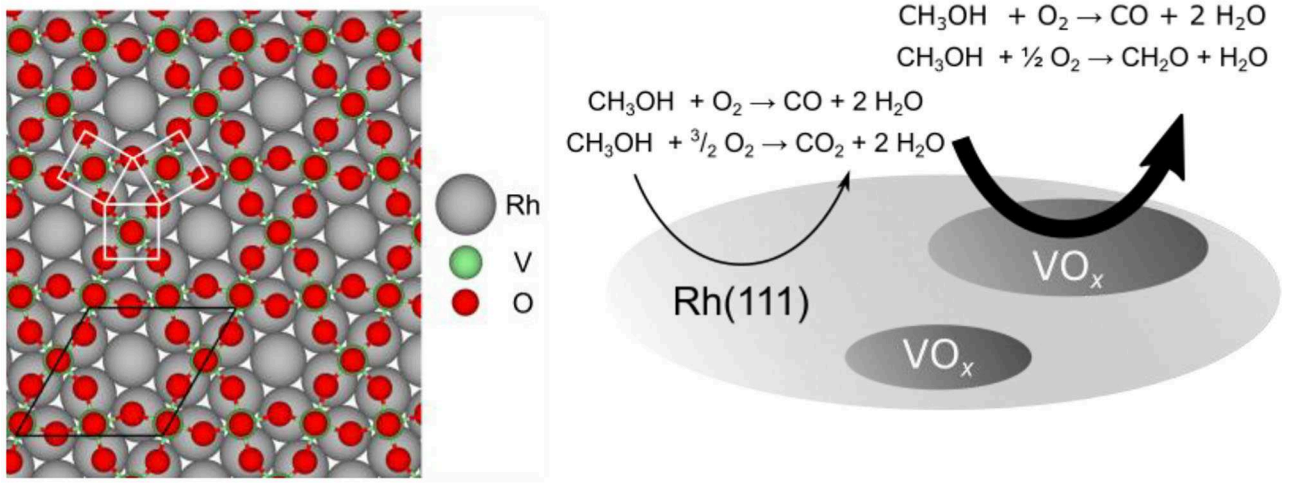


**FIGURE 1 |** Structure and reactivity of $VO_x$/Rh(111) model catalysts. **(A)** Structure model for the ($\sqrt{7} \times \sqrt{7}$)R19.1° vanadium oxide phase on Rh(111) (Schoiswohl et al., 2004b). The unit cell and a $VO_5$ pyramid is indicated in the model. **(B)** Schematic representation of catalytic $VO_x$ "microreactors" on Rh(111) during catalytic methanol oxidation. The main reactions on the bare Rh surface and vanadium oxide covered surface are indicated. Reprinted from von Boehn et al. (2020). Copyright (2020), with permission from Elsevier.

properties of ultrathin V-oxide layers can be markedly different from the properties of V-oxide bulk compounds (Surnev et al., 2013).

In industrial heterogeneous catalysis, typically metallic catalysts are dispersed on an oxidic support, e.g., $SiO_2$, $Al_2O_3$, or $TiO_2$. Here, oxides are deposited on a metallic support instead of a metal supported on an oxidic surface and, accordingly, the concept has been termed "inverse model catalyst" approach (Levin, 1987; Boffa et al., 1994; Surnev et al., 2013; Rodriguez et al., 2016). The concept of inverse model catalysts has several advantages. Charging problems with electron or ion based analysis techniques are avoided and the interface metal/oxide can be nicely studied. Moreover, the concept of inverse model catalysts has also been applied as a method to guide the development of novel catalysts (Zhang and Medlin, 2018).

In order to study the redistribution dynamics of $VO_x$ spatially resolving techniques are required. In photoemission electron microscopy (PEEM) the sample surface is illuminated with UV light and the ejected photoelectrons are imaged (Rotermund, 1993). PEEM images primarily local work function variations with a lateral resolution of typically 0.1–1 μm. However, PEEM provides no or only indirect chemical and structural information. A technique that can provide the missing information is low-energy electron microscopy (LEEM) (Bauer, 2019) in its spectroscopic variant (SPELEEM) (Schmidt et al., 1998; Menteş et al., 2014). In LEEM, elastically backscattered, i.e., diffracted electrons in the energy range 0–200 eV are used to image the surface. Since the main contrast mechanism is diffraction contrast, LEEM is sensitive to structural changes of the surface, with the resolution being for most instruments around 10–15 nm, even though a resolution down to ∼2 nm is possible (Wichtendahl et al., 1998). By putting in an aperture one can obtain diffraction images of an area as small as 1 μm diameter (μLEED). Similarly, at synchrotrons providing the X-ray photons, one can use the instrument to obtain X-ray photoelectron spectroscopy from a 1 μm spot (μXPS). One can thus characterize the local surface structure as well as the local chemical composition. Since this instrument combines the spatial resolution of a microscope with the ability to perform local spectroscopy, this technique has also been termed "spectromicroscopy."

## Catalytic Activity and Dynamics of $VO_x$/Rh(111)

In industrial partial oxidation of methanol, the "formox" process (Franz et al., 2010), formaldehyde is the desired product. In methanol oxidation over $VO_x$/Rh(111) three catalytic reactions have to be considered, as schematically shown in **Figure 1B**. On the bare Rh(111) surface carbon dioxide, $CO_2$, is formed as product of the total oxidation:

$$CH_3OH + 3/2O_2 \rightarrow CO_2 + 2H_2O. \quad (1)$$

Besides total oxidation, also carbon monoxide, CO, and formaldehyde, $CH_2O$, are formed as products of the partial oxidation of methanol according to:

$$CH_3OH + O_2 \rightarrow CO + 2H_2O, \quad (2)$$

$$CH_3OH + 1/2O_2 \rightarrow CH_2O + H_2O. \quad (3)$$

While CO is produced on both surfaces, bare Rh(111) and $VO_x$ covered Rh(111), the formation of formaldehyde is restricted to the $VO_x$ covered parts of the surface (Hesse et al., 2015).

The mechanism of methanol oxidation over oxide-supported V-oxide has been clarified in a number of quantum chemical studies (Döbler et al., 2005; Göbke et al., 2009; Kropp et al., 2014). More specifically, vanadyl groups (V=O) were shown to play an essential role in the reaction mechanism of formaldehyde formation from methanol over $VO_x$ catalysts. Such vanadyl groups were found in some of the two-dimensional network structures of $VO_x$ on Rh(111), for example in the $(\sqrt{7} \times \sqrt{7})R19.1^\circ$ shown in **Figure 1A** (Schoiswohl et al., 2004b). In general, a mechanistic explanation of partial oxidation reactions over oxidic surfaces is often based on a two-step model originally proposed by Mars and van Krevelen (Frank et al., 2009; Carrero et al., 2014). First lattice oxygen from the oxidic catalyst is transferred to the reactant, which is oxidized. In a second step, the reduced oxide catalyst is reoxidized.

We investigate whether the initial homogeneous distribution of V-oxide is maintained during a catalytic reaction. The starting point of every $VO_x$ redistribution experiment is a Rh(111) surface homogeneously, on a μm length scale, covered with a submonolayer quantity of $VO_x$. It should be stressed that if the surface is homogeneous on a macroscopic scale (> 1 μm), on a microscopic scale it might be heterogeneous. Such a surface is exposed to a gas atmosphere consisting of methanol and oxygen in the $10^{-4}$ mbar range and heated to 1030 K (0.2–0.5 K/s), starting from 300 K. At around 770–820 K the initially homogeneous surface state is lifted and a regular stripe pattern develops, as shown in a series of PEEM images (stage I) in the top panel of **Figure 2**. In PEEM a low work function (WF) surface is imaged as bright area, high WF regions as dark area. Adsorbed oxygen, due to the high dipole moment of the adsorbate complex O-Rh, appears dark in PEEM, but so does V-oxide (if V is in a $V^{4+}$ or $V^{5+}$ state). Therefore, with PEEM alone, the interpretation of the images is not clear. Subsequent μXPS measurements (below) showed that the dark islands in **Figure 2** represent V-oxide covered area, whereas the surrounding area is largely V-oxide free (Lovis et al., 2011; Hesse et al., 2015).

Remarkably, the condensation of the highly dispersed $VO_x$ into a stripe pattern is accompanied by a drastic increase of the formaldehyde production (bottom panel of **Figure 2**). As the temperature is further increased the stripe pattern coarsens up to roughly 980 K (stage II), followed by a transformation into a spot pattern of circular, several tens to hundreds μm wide vanadium oxide islands (stage III).

The formation of a $VO_x$ stripe pattern followed by a transition into a spot pattern of $VO_x$ islands is observed in a number of different chemical reactions on $VO_x$/Rh(111), including the oxidation of $H_2$, CO and ammonia (Lovis and Imbihl, 2011; von Boehn et al., 2016). **Figure 3A** shows the coarsening of a $VO_x$ stripe pattern under constant reaction condition on $VO_x$/Rh(111) during the $H_2 + O_2$ reaction at 773 K. The pattern is the result of V and O forming a dense $VO_x$ coadsorbate phase. The surrounding bright surface is bare Rh(111) surface. The initially thin, dark stripes in the first PEEM image of **Figure 3A** increase their width, and after about 1000 s further progress is happening rather slowly. However, the coarsening still continues and we cannot deduce a value to which the curve asymptotically approaches.

This behavior is also reflected in a plot of the wavenumber $k = 1/\lambda$ of the stripe pattern vs. time plot, as demonstrated in **Figure 3B**. The coarsening process obeys a power law $k(t) \propto t^{-\beta}$ with $\beta = 0.23 \pm 0.03$, as shown in **Figure 3C**. For the dependence of the wavenumber $k$ on the pressure, a power law $k(p) \propto p^{\alpha}$ was experimentally determined with $\alpha = 0.33 \pm 0.05$. The wavenumber $k$ increases with increasing pressure in the pressure range between $10^{-6}$ and $10^{-4}$ mbar.

For explaining pattern formation in this system, the concept of reactive phase separation seemed to be applicable. Attractive or repulsive interactions between adsorbed particles on a surface can result in the condensation into a dense phase. Thermodynamically, an island of infinite size should finally result but, coupled to a chemical reaction, a finite size is selected. On a potassium promoted Rh(110) surface reactive phase separation was observed during the $H_2 + O_2$ reaction (De Decker et al., 2004). Later on, reactive phase separation was also demonstrated on Pd and Au alloyed Rh(110) surfaces in the $H_2 + O_2$ reaction (Locatelli et al., 2005, 2006). The prerequisites for reactive phase separation to occur are not very restrictive, since only a sufficient mobility of the components and different chemical affinity between the reacting adsorbates are required. What does not fit into the concept of reactive phase separation in the present case is that the coarsening does not approach a finite value. A control experiment in which V-oxide on Rh(111) was annealed in $O_2$ only, revealed that also in this case $VO_x$ islands of macroscopic size are formed (von Boehn et al., 2016). The condensation of $VO_x$ into stripes and circular islands under reaction conditions therefore appears to be driven by thermodynamics.

Under strongly reducing conditions, the reduction of $VO_x$ can proceed until metallic V is formed, which forms surface and subsurface alloys with Rh(111) at sufficiently high temperature (1023 K) in vacuum (Píš et al., 2012). However, even low oxygen pressures in the $10^{-7}$-$10^{-8}$ mbar range suffice to stabilize V as an oxide on the surface (Schoiswohl et al., 2005). Thus, under the conditions of catalytic reactions V is localized on the Rh(111) surface and no V/Rh surface or subsurface alloy is formed. This simplifies the analysis considerably.

## $VO_x$ Islands Coalescence

### Experimental Observations

In the last stage of the self-organization process, stage III in **Figure 2**, circular tens to hundreds μm wide $VO_x$ islands are distributed on the Rh(111) surface. Remarkably, if two V-oxide islands are within a critical distance of the order of 100 μm, they move toward each other and coalesce under reaction conditions. The series of PEEM images in **Figure 4A** shows the coalescence of two neighboring $VO_x$ islands during catalytic methanol oxidation in the $10^{-4}$ mbar range. As the inter-island distance decreases, the movement of the two islands accelerates until they finally merge, as shown in **Figure 4B**. Interestingly, this coalescence proceeds exclusively under the conditions of an ongoing catalytic reaction. Stopping the supply of one of the two reactants, oxygen and methanol, instantly freezes the island movement.

One also notes that above a critical size the islands in **Figure 4A** exhibit a substructure consisting of an inner bright

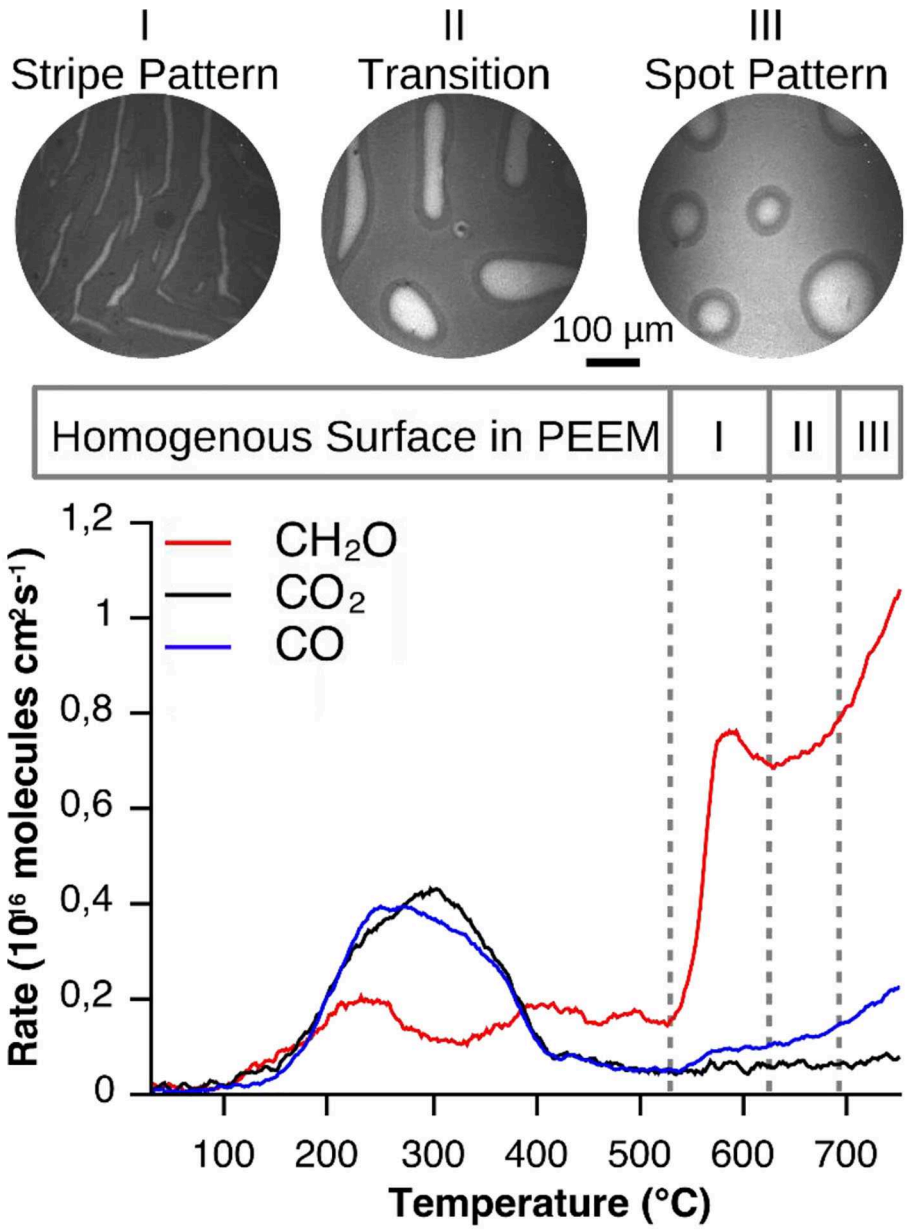


**FIGURE 2 |** Vanadium oxide redistribution and reaction rates recorded during catalytic methanol oxidation over $VO_x$/Rh(111). Experimental conditions: $\theta_V = 0.23$ MLE, $p$(CH3OH) $= 1 \times 10^{-4}$ mbar, $p(O_2) = 1 \times 10^{-4}$ mbar, 0.2°C/s. Reprinted figure with permission from Hesse et al. (2015). Copyright (2015) by the American Physical Society.

core, surrounded by an outer dark ring. This substructure is the result of V in the core being in a more reduced state than in the outer ring. This will be described below in more detail.

The island coalescence leads to an island ripening as in classical Ostwald ripening, where large islands grow at the expense of smaller ones. However, whereas Ostwald ripening occurs close to thermodynamic equilibrium, ripening via island coalescence takes place only under conditions far from equilibrium. The island coalescence mechanism is similar to Smoluchowski ripening, where island coarsening proceeds via collision of larger adatom aggregates, clusters or islands that diffuse randomly on the surface (Thiel et al., 2009). Smoluchowski ripening, however, does not require a chemical reaction, and the diffusing islands and clusters comprise only a small number of atoms. The unusual behavior seen here is the directed movement of large macroscopic islands that would normally require the existence of a macroscopic force.

### The Polymerization/Depolymerisation Mechanism

For understanding the peculiar behavior of $VO_x$ islands under reaction conditions, one has to take a closer look at the surface chemistry of V-oxides on Rh(111). Molecular oxygen has a

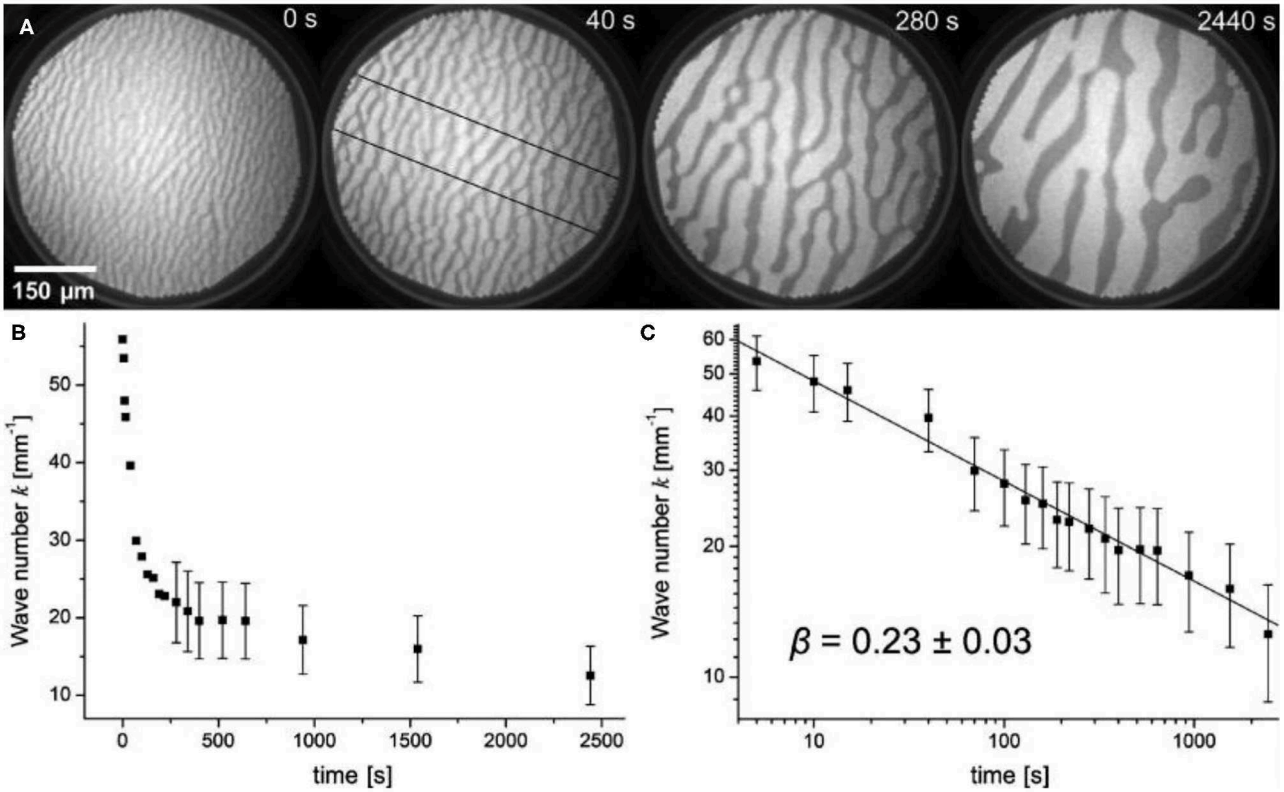


**FIGURE 3 |** $VO_x$ stripe pattern showing coarsening of a stripe pattern under constant reaction conditions in the $O_2 + H_2$ reaction on $VO_x$/Rh(111). **(A)** Series of PEEM images showing the coarsening. **(B)** Plot of the wavenumber $k$ as a function of time, determined along the cross sections indicated in the second image in a. **(C)** Double-logarithmic plot of $k$ as a function of time. Experimental conditions: $\theta_V = 0.2$ MLE, $p(O_2) = 1 \times 10^{-5}$ mbar, $p(H_2) = 4 \times 10^{-6}$ mbar. Reprinted with permission from Lovis and Imbihl (2011). Copyright (2011) American Chemical Society.

low sticking coefficient on the $VO_x$ covered Rh(111) surface, but it can readily adsorb on the metallic Rh(111) surface. As a consequence, $O_{ad}$ is diffusively transported from the surrounding metallic Rh(111) surface toward the $VO_x$ islands, where formaldehyde production almost exclusively takes place and where the oxygen is consumed. Due to the high catalytic activity of $VO_x$, the macroscopic V-oxide islands can therefore be considered as "catalytic microreactors" which consume oxygen for the oxidation reaction, and thus act as sinks for adsorbed oxygen. The diffusive supply of $O_{ad}$ to the $VO_x$ islands generates gradients in the oxygen coverage around the V-oxide islands.

Observations with scanning tunneling microscopy on $VO_x$ islands on Rh(111) demonstrated that at 380 K, isolated $V_6O_{12}$ clusters can detach from a large $VO_x$ island (Schoiswohl et al., 2004a). If the cluster is part of a network structure in a $VO_x$ island, additional oxygen is needed to detach the clusters, because in the network the individual units are connected by sharing corner oxygen atoms. If we take a $V_2O_3$ composition for the large $VO_x$ islands, we can formulate a polymerization/depolymerisation (PD) or association/dissociation equilibrium:

$$(V_2O_3)_n + 3mO_{ad} \rightleftharpoons (V_2O_3)_{n-3m} + m\,(V_6O_{12})\,. \qquad (4)$$

This is a chemical equilibrium that is controlled by the oxygen coverage. A high oxygen coverage favors the dissociation of the large island into small clusters; conversely, a low oxygen coverage shifts the equilibrium toward aggregation of the clusters. The oxygen gradients developing under reaction conditions around $VO_x$ islands and the PD equilibrium suffice to explain the island coalescence as schematically depicted in **Figure 5**. In region I in **Figure 5A**, the oxygen coverage is considerably lower than in region II, since two neighboring $VO_x$ islands compete as sinks for adsorbed oxygen. According to the PD equilibrium of Equation (4), a high oxygen coverage in regions II favors depolymerization of the $VO_x$ islands into small $V_6O_{12}$ clusters. Since the low oxygen coverage in region I shifts the equilibrium to the polymerization side, the small $V_6O_{12}$ clusters become attached again to the $VO_x$ islands, but now on the opposite side from where they became detached. The net result is that the two neighboring islands move toward each other.

An essential requirement of this mechanism is that the $V_6O_{12}$ clusters and adsorbed oxygen exhibit a sufficiently high diffusivity. Both is the case as shown by experimental data (Barth, 2000; Mavrikakis et al., 2002; Schoiswohl et al., 2004a). Experiments in which $VO_x$ islands pinned to defects "evaporated" demonstrated the existence of small mobile $VO_x$ clusters, because desorption of $VO_x$ into the gas phase can be

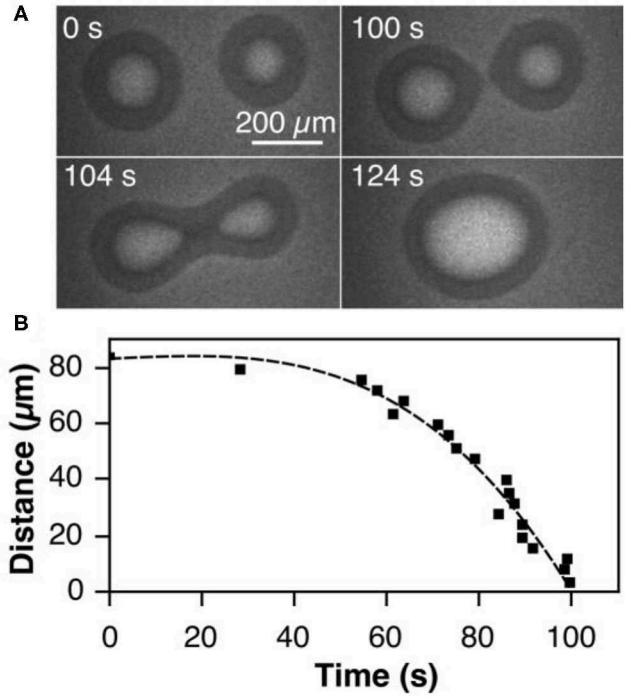


**FIGURE 4 |** Coalescence of neighboring $VO_x$ islands during catalytic methanol oxidation over $VO_x$/Rh(111). **(A)** PEEM images showing different stages of the coalescence process. **(B)** Inter-island distance of the coalescence process shown in a as a function of time. Experimental conditions: $\theta_V = 0.23$ MLE, $p(CH3OH) = 1 \times 10^{-4}$ mbar, $p(O_2) = 1 \times 10^{-4}$ mbar, $T = 750$ °C. Reprinted figure with permission from Hesse et al. (2015). Copyright (2015) by the American Physical Society.

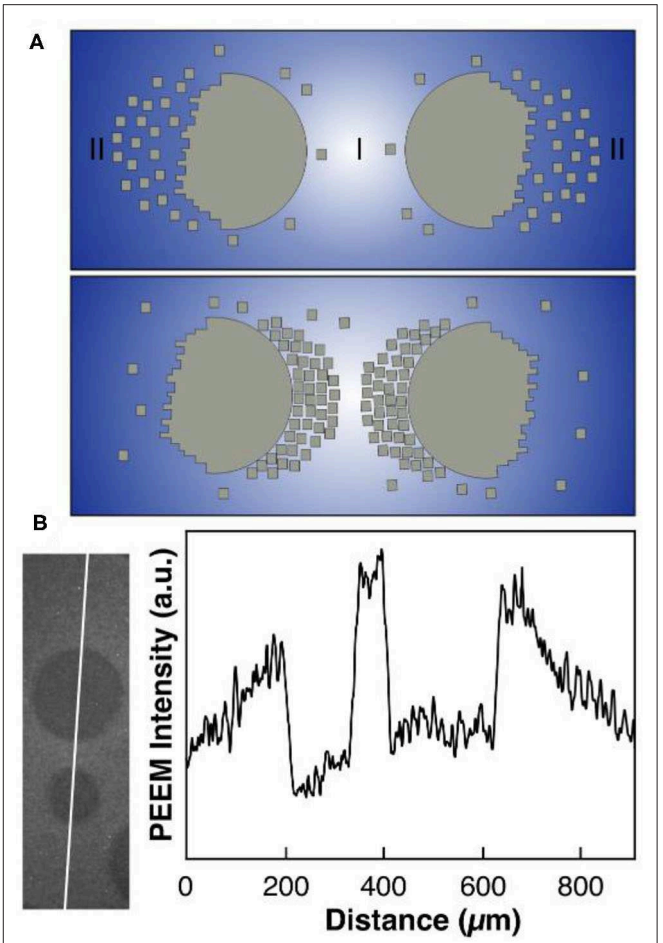


**FIGURE 5 |** Polymerization/depolymerization mechanism explaining the coalescence of $VO_x$ islands. **(A)** Scheme illustrating the movement of two neighboring $VO_x$ islands via mobile $V_nO_m$ clusters (small squares) under reaction conditions. The intensity of the blue background represents the oxygen coverage. **(B)** Gradients in the oxygen coverage around $VO_x$ islands extracted from PEEM. Experimental conditions: $\theta_V = 0.23$ MLE, $p(CH_3OH) = 8 \times 10^{-5}$ mbar, $p(O_2) = 1 \times 10^{-4}$ mbar, $T = 750$ °C. Reprinted figure with permission from Hesse et al. (2015). Copyright (2015) by the American Physical Society.

excluded (Hesse et al., 2015). The diffusivity of atomic oxygen on Rh(111) fixes the length scale of the oxygen gradients, and this value of roughly 100 μm is equal the critical distance below which two neighboring islands start to feel the attraction of the other island. The existence of oxygen gradients around $VO_x$ islands shows up in brightness variations in PEEM (**Figure 5B**) and, more directly, in concentration profiles recorded with μXPS (below). The mechanism sketched above explains why island movement only occurs under reaction conditions since, without reaction, the oxygen gradients immediately vanish. Clearly, no macroscopic force is needed to move the islands because the movement takes place via the transport of small $V_nO_m$ clusters.

## Modeling $VO_x$ Islands Coalescence

The island coalescence in the system $CH_3OH + O_2/VO_x$/Rh(111) has been reproduced with a skeleton reaction-diffusion model (De Decker et al., 2019). This model considers a highly simplified reaction mechanism, but takes into account the PD mechanism including the adsorption of oxygen and the existence of energetic interactions between the adparticles. Strong lateral interactions between the $VO_x$ polymers are evidenced by the nearly circular shape of the $VO_x$ islands, which indicates a strong internal cohesion.

The small $V_nO_m$ clusters through which $VO_x$ mass transport is mediated are represented as "monomers" M in the model, extended V-oxide areas are described as "polymer" P. The polymerization / depolymerization equilibrium in Equation (4) can then be written as:

$$P + M + [^*, O_{ad}] \rightleftharpoons 2P + O_{ad}, \quad (5)$$

with $[^*, O_{ad}]$ representing an unoccupied adsorption site for $O_{ad}$.

Adsorbed oxygen is formed by dissociative adsorption from the gas phase,

$$O_{2(g)} + 2\,[^*, O_{ad}] \rightleftharpoons 2\,O_{ad}, \quad (6)$$

and through the condensation process of monomers described in Equation (5). Oxygen is removed through desorption and

through reaction with a molecule X (e.g., methanol) according to

$$O_{ad} + X_{ad} \rightarrow XO_{(g)} + [^*, O_{ad}]. \quad (7)$$

As outlined above, this reaction proceeds with a considerable higher rate on the vanadium oxide islands (catalytic "microreactors") than on the bare metal surface. The different catalytic activity is taken into account via the rate constant of the catalytic reaction, which is a function of the local polymer coverage $\theta_P$.

The surface diffusion of atomic oxygen ($D_O$), of the monomer M ($D_M$), and of the polymer P ($D_P$) are taken into account with $D_O > D_M >> D_P$. Due to the existence of energetic interactions between adsorbed particles and due to site exclusion, diffusion is non-Fickian.

Numerical integration of the reaction-diffusion-equations shows that a region of bistability exists in which the homogeneous distribution of $VO_x$ decays spontaneously into a P-rich and a P-poor phase in a quasi-spinodal decomposition. The domain size does not approach an asymptotic value in time but continuously increases as experimentally observed in the $H_2 + O_2$ reaction on $VO_x$/Rh(111) (**Figure 3**).

As one increases both, the reaction rate and the $O_2$ adsorption rate, which in experiments corresponds to elevated temperature and pressure, one observes the behavior depicted in **Figure 6**. Close-by islands move toward each other and coalesce. Directly after coalescence the islands are deformed, but the circular shape is restored within a short time. The distance between the two coalescing islands plotted vs. time in **Figure 6E** displays qualitatively the same behavior as the experimental dependence in **Figure 4B**. A close look at the concentration profiles corroborates the mechanistic interpretation given above. It is the sensitivity of the PD equilibrium to gradients in the oxygen coverage that leads to the transport of $VO_x$ and causes the movement of the $VO_x$ islands toward each other.

The reaction-diffusion equations allow even to derive an equation of motion for the islands using Newtonian mechanics. Numerical integration of this Newtonian law reproduces well the trajectories obtained from simulations of the full model, as demonstrated in **Figure 6E** (dashed blue line).

## $VO_x$ Island Substructure

The PEEM images in **Figures 2**, **4A** show that the $VO_x$ islands exhibit a substructure consisting of a bright core and a dark outer ring. The missing chemical information is provided by μXPS, allowing also for quantification of the surface coverages. After preparation of a $VO_x$ island in the $10^{-4}$ mbar range, local XP spectra were taken under reaction conditions in the $10^{-6}$ mbar range across the island (Hesse et al., 2015). One thus obtains a cross section through the island displayed in **Figure 7A**. A shift of the V 2p core level toward higher binding energy (BE) in **Figure 7B** indicates that vanadium in the outer ring is in a more oxidized state than in the core region. A comparison of the V 2p BEs from the spectra with the BEs from V-oxide bulk compounds (neglecting possible effects from the monolayer thickness), shows that in the center of the island $V^{3+}/V^{4+}$ species prevail, whereas in the outer ring V is mainly in the oxidation state +4/+5. This finding agrees with the picture of $VO_x$ islands as "microreactors," because with oxygen being transported diffusively from the island boundary, naturally an oxygen concentration gradient will arise inside the island caused by oxygen consumption in the reaction. Above a critical island size, the supply of oxygen will not be high enough to maintain a high oxidation state of vanadium in the core region of the island, and a reduction through reaction with methanol will occur.

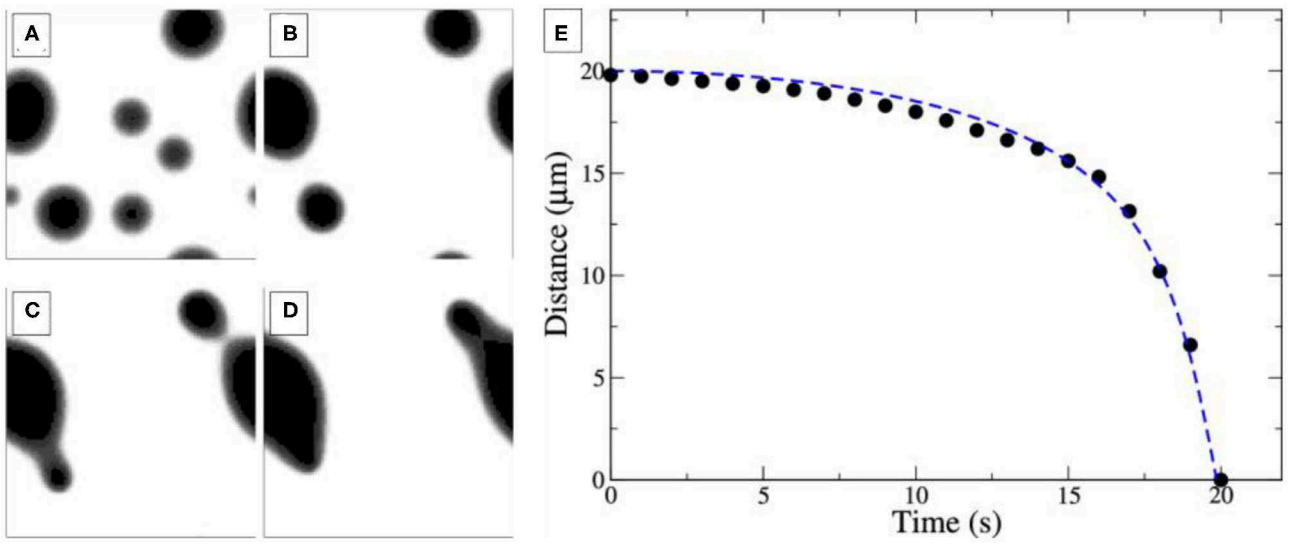


**FIGURE 6 |** Simulations of coalescing $VO_x$ islands on Rh(111). The system size is 50 × 50 μm$^2$. **(A–D)** Four snapshots taken at $t = 0$ s **(A)**, 30 s **(B)**, 80 s **(C)**, and 130 s **(D)**, with $t = 0$s corresponding to the time when reaction conditions are turned on. **(E)** Inter-island distance. For details and simulation parameters please refer to the original publication. Adapted with permission from Makeev and Imbihl (2019). Copyright (2019) American Chemical Society.

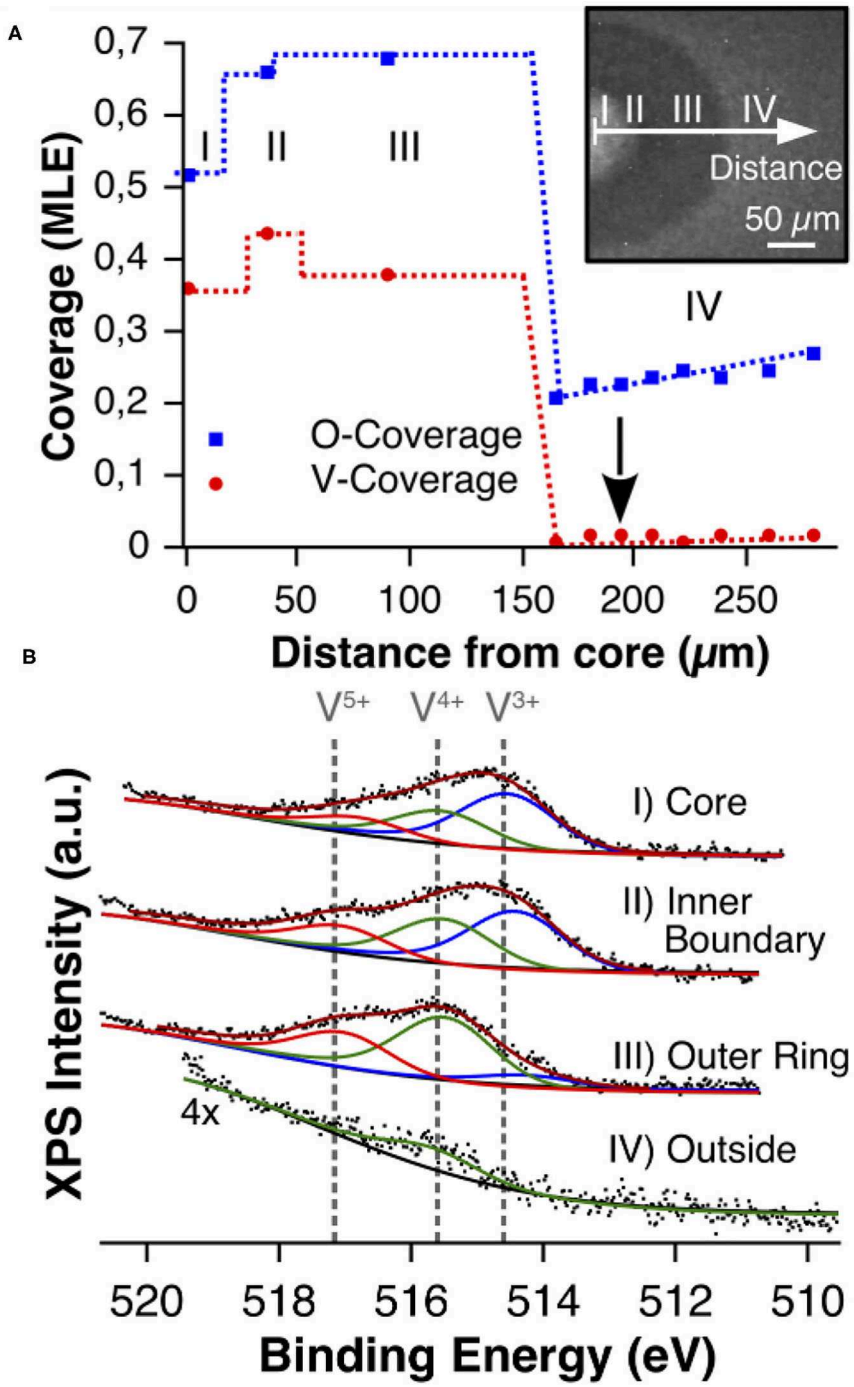


**FIGURE 7 |** Chemical characterization of a $VO_x$ island with XPS during catalytic methanol oxidation over $VO_x$/Rh(111). **(A)** V and O coverage profile recorded under reaction conditions in the $10^{-6}$ mbar range. The position 0 μm refers to the island center. **(B)** V $2p_{3/2}$ core level spectra recorded with μXPS on various positions inside and outside (arrow) the $VO_x$ island. Reprinted figure with permission from Hesse et al. (2015). Copyright (2015) by the American Physical Society.

As expected from the picture of the "microreactor," the oxygen coverage is high outside the $VO_x$ islands and a gradient is clearly visible from a high oxygen coverage far away from the island toward a lower coverage at the boundary. Outside the $VO_x$ islands, only a small amount of vanadium oxide is detected, representing the mobile $V_nO_m$ clusters through which the island coalescence proceeds.

Besides the island radius, the existence of a substructure also depends on the reaction conditions. A high amount of methanol favors the formation of a reduced core. One should add that $VO_x$

islands can be prepared with a substructure involving a number of clearly distinguishable phases (von Boehn, 2020). The effect of the substructure on the dynamics of an island is demonstrated in the following.

## Oscillating $VO_x$ Islands

Two subsequent LEEM images showing two stages in the oscillatory behavior of a circular $VO_x$ island during catalytic methanol oxidation are shown in **Figure 8A**. Reaction conditions are in the $10^{-4}$ mbar range. Different from PEEM, whose main contrast mechanism is based on local work function variations, LEEM is a structure sensitive microscopy technique, which additionally allows for laterally resolved LEED measurements. The brightness levels in LEEM are not related to the brightness levels in PEEM, since the contrast mechanisms are different. In the LEEM images one observes a core region, a dark outer ring and, in addition to the substructure visible in PEEM, a band separating core and outer ring.

Surprisingly, despite constant parameters, the islands exhibits an oscillatory cycle in which the island undergoes a periodic expansion and contraction, simultaneously with periodic brightness variations in the core of the island (von Boehn et al., 2020). The transformations from a bright core to a dark core and vice versa take place via reaction fronts nucleating at the boundary of the core. The periodic LEEM intensity changes of the different $VO_x$ phases as well as the changes in the positions of the three interfaces are displayed in **Figure 8B**. Practically only the outer ring changes its size and the size oscillations display a strict phase relationship with the periodic intensity changes in the core that we can associate with a reduction and oxidation, respectively. A remarkable fact is that in this "breathing" of the island a considerable mass transport of $VO_x$ has to occur to accomplish the variations in island size.

With *in situ* μLEED ordered $VO_x$ overlayers could be identified in the breathing island: a $(\sqrt{7} \times \sqrt{7})R19.1°$ structure for the outer ring and a $(\sqrt{3} \times \sqrt{3})$-Moiré structure for the core region (von Boehn et al., 2020). To understand the occurrence of different phases in the $VO_x$ island is quite straightforward using the picture of the $VO_x$ islands as catalytic micro-reactors. Since inside the oxide islands a gradient in the chemical potential of oxygen exists, a cross section through a $VO_x$ island corresponds to a cross section through a phase diagram of $VO_x$ on Rh(111), with the chemical potentials of oxygen and vanadium as intensive variables.

Such a phase diagram has been calculated with density functional theory (DFT) for the system $VO_x$/Rh(111) and the result is displayed in **Figure 9A**. The $(\sqrt{7} \times \sqrt{7})R19.1°$ structure of the highly oxidized ring is present, but the $(\sqrt{3} \times \sqrt{3})$-Moiré structure of the core does not occur in the phase diagram. This $(\sqrt{3} \times \sqrt{3})$-Moiré structure has not been reported in the literature and no structure model exists. Probably, this structure does not represent an equilibrium structure and therefore does not show up in a phase diagram of $VO_x$/Rh(111). Since V in the reduced core is present as $V^{3+}$, a $(2 \times 2)$ $V_2O_3$ structure with a V coverage of 0.5 MLE is predicted from the phase diagram for the reduced island core.

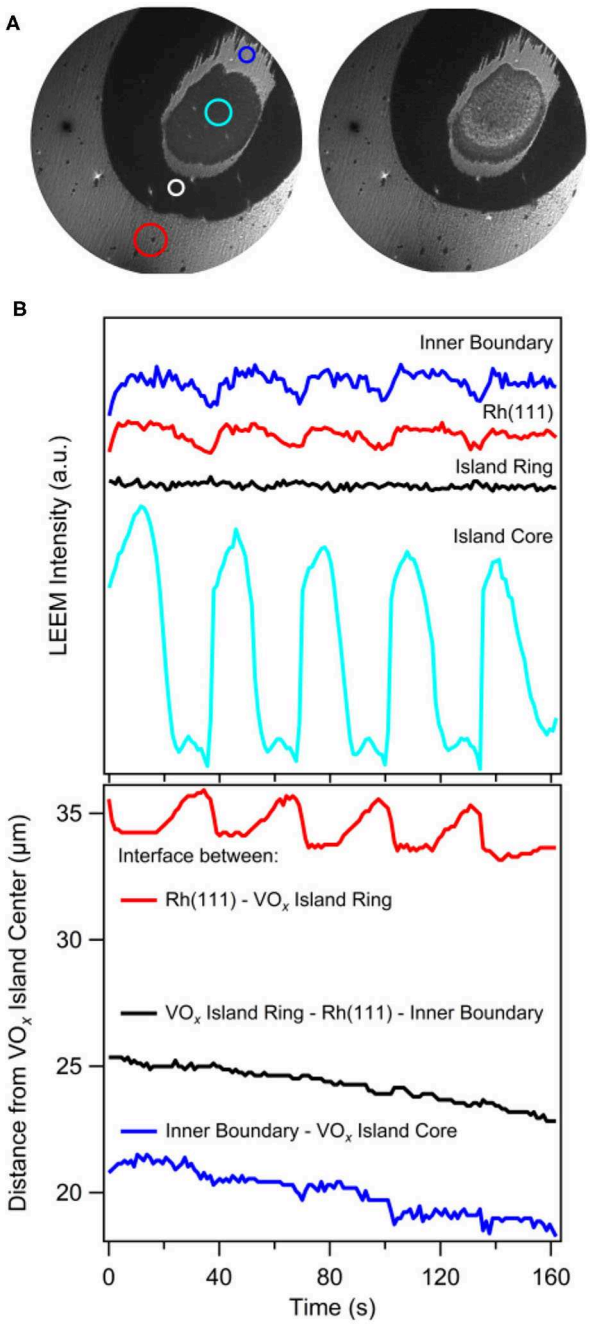


**FIGURE 8 |** Oscillating $VO_x$ islands during methanol oxidation on $VO_x$/Rh(111). **(A)** Two LEEM images showing a circular $VO_x$ island with the substructure consisting of a core and a ring, with the core being in its oxidized (left) and its reduced (right) state. **(B)** Local LEEM intensity (taken from areas indicated by colored circles in a) (top) and the position of the different interfaces (bottom) as a function of time. Experimental conditions: 2 eV electron energy, $1 \times 10^{-4}$ mbar $CH_3OH$ and $1 \times 10^{-4}$ mbar $O_2$, $T = 1030$ K. Reprinted from von Boehn et al. (2020). Copyright (2020), with permission from Elsevier.

The phase diagram reveals that the reduced $VO_x$ phases have a higher V density than oxidized $VO_x$ phases, a relation that also became apparent from the experimentally determined V

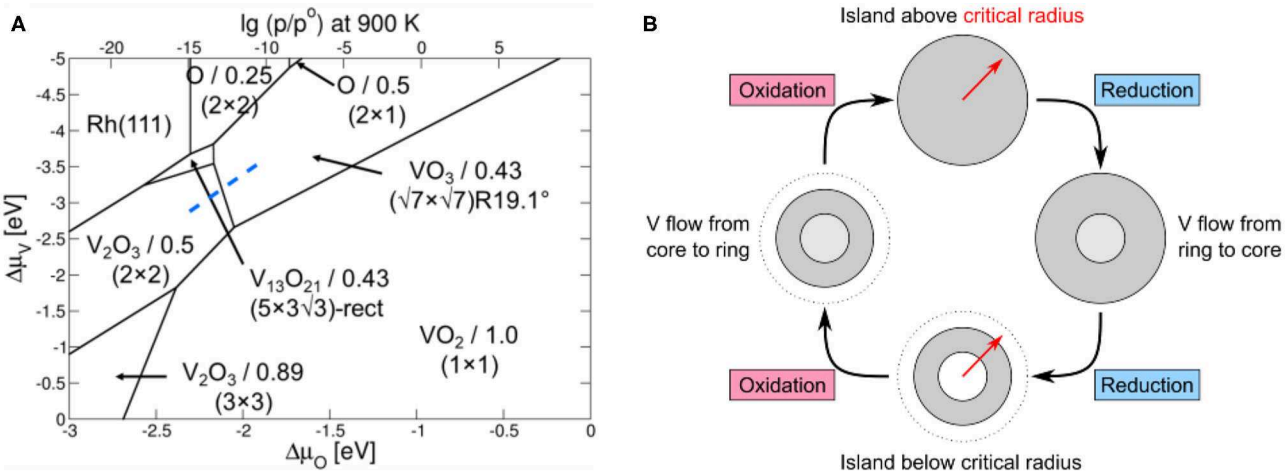


**FIGURE 9 |** Mechanism explaining the $VO_x$ island oscillations shown in **Figure 8**. **(A)** DFT phase diagram of the 2D $VO_x$ phases on Rh(111). The $VO_x$ structures and corresponding coverages are given. The transition between an oxidized phase and a reduced phase is indicated by the dashed blue line. Reprinted from von Boehn et al. (2020). Copyright (2020), with permission from Elsevier. **(B)** Sketch of a tentative mechanism explaining the periodic, "breathing-like" expansion and contraction of a vanadium oxide island. Reprinted with permission from von Boehn (2020).

and O coverages for the different 2D-$VO_x$ phases on Rh(111) (Schoiswohl et al., 2004b, 2005; von Boehn et al., 2020). For explaining the size oscillation, only one other relation is required. Since periodic oxidation/reduction fronts transform the core of the island, the island size has to be in the vicinity of the critical radius for existence of a reduced core. With these two ingredients, *i)* different V densities for reduced and oxidized $VO_x$ phase, and *ii)* the island size being around the critical radius for the formation of a reduced core in $VO_x$, we can set up a mechanism for the size oscillations. We assume that in the oxidation/reduction of the island core, we move along the blue dashed line in the PD of **Figure 9A**.

A Schematic Representation of the Proposed Mechanism is Shown in **Figure 9B**:

i) Initially, the island is above the critical island radius, but the core is still in a completely oxidized state. Due to the long distance over which $O_{ad}$ has to diffuse, not enough oxygen reaches the core, and a reduction of the core sets in. Since the reduced $VO_x$ phase has a higher V density, extra V atoms are needed. They are taken from the outer ring and are transported from there to the island center.
ii) The transport of V atoms to the island core results in a shrinking of the oxidized ring, which eventually falls below the critical radius.
iii) Due to the shorter distance O atoms now have to cover, the O coverage in the island core increases, finally triggering the transformation of the core back into the oxidized state.
iv) Due to the lower V density in the oxidized state, extra V atoms are expelled from the core. They migrate back to the outer ring, which grows thus closing the oscillatory cycle.

The oscillatory change of the $VO_x$ island size requires that a mass transport of vanadium is involved in addition to the transport of oxygen. According to the Onsager relations, a gradient in the chemical potential of oxygen is connected with a corresponding gradient in the chemical potential of vanadium (Mikhailov and Loskutov, 1991; Mikhailov, 1994). Clearly, a thermodynamic driving force for the transport of V therefore exists, but it is not clear in what form V is transported, since no experimental data exist for the diffusion inside $VO_x$ islands. V mass transport within the island may occur via diffusion of isolated V atoms or via V-oxo complexes.

## Bridging the Pressure Gap

The existence of a pressure gap in heterogeneous catalysis means that the results obtained at low pressure cannot, in general, be extrapolated to reaction conditions at higher pressure. In order to bridge the pressure gap, a variety of *in situ* and operando techniques have been developed in order to characterize a catalyst as close as possible to realistic conditions (Topsøe, 2003; Dou et al., 2017). The LEEM is a typical ultrahigh-vacuum (UHV) instrument designed for operating at $10^{-10}$-$10^{-8}$ mbar. The operational range of LEEM has recently been extended up to 0.1 mbar, a range also denoted as near-ambient-pressure (NAP) range (Franz et al., 2019). With NAP-LEEM, the redistribution dynamics of $VO_x$ catalysts on Rh(111) could be followed up to the $10^{-2}$ mbar range (von Boehn et al., 2020).

After deposition of 0.2 MLE V in vacuum, the pressure was raised into the $10^{-2}$ mbar range. The reaction dynamics of methanol oxidation over $VO_x$/Rh(111) was followed with NAP-LEEM during heating up, as shown by the NAP-LEEM images in **Figure 10A**. Circular $VO_x$ islands with the familiar core—ring structure form. As the temperature is raised beyond 650 K, this structure starts to disintegrate beginning at the outer ring. A slight island expansion is followed by the nucleation and growth of bright areas in the outer ring. Simultaneously, additional dark, channel-like structures develop. At slightly higher temperature, a bright phase nucleates also in the island core. After a few

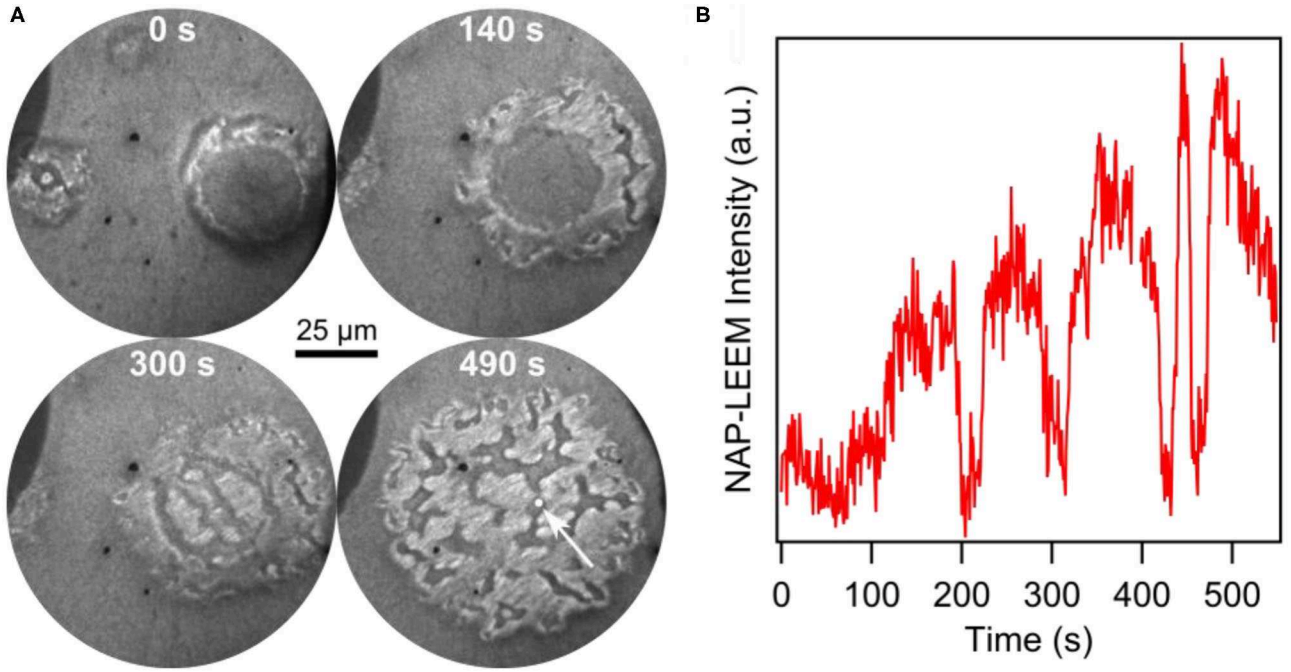


**FIGURE 10 |** Transition of a $VO_x$ island from a core-ring structure to turbulent dynamics during catalytic methanol oxidation over $VO_x$/Rh(111) at $10^{-2}$ mbar. **(A)** Series of NAP-LEEM images (3.1 eV) recorded between 650 and 670 K. The time elapsed since the beginning of the island disintegration is indicated. **(B)** Local LEEM intensity as a function of time taken in the circular white area of 3 µm diameter (white arrow in the last image of **(A)**. Reprinted from von Boehn et al. (2020). Copyright (2020), with permission from Elsevier.

seconds the original core-shell structure of the $VO_x$ island is gone and the area is covered by bright and dark phases that continuously change. The dark, channel-like areas meander on the surface, forming long extensions, which often break and reconnect with other parts of the dark phase. A time series of the local NAP-LEEM intensity displayed in **Figure 10B** demonstrates irregular behavior. The visual impression is that of a turbulent redistribution dynamics.

Due to the lack of surface analytical techniques that can operate *in situ* in the $10^{-2}$ mbar range, no further chemical or structural information is available. Obviously, a stable $VO_x$ distribution on the support surface cannot be maintained in the $10^{-2}$ mbar range, as evidenced by the turbulent redistribution dynamics. At a pressure of $10^{-2}$ mbar, gradients in the oxygen coverage are presumably stronger than at low pressure, which might be a cause for the lack of stability in the island structure. Furthermore, in the NAP regime, the reaction conditions can no longer be considered as strictly isothermal, as it is the case under vacuum conditions up to roughly $10^{-3}$ mbar.

## Oxidation With NO

One of the first questions that were asked after catalytic methanol oxidation exhibited quite remarkable reaction dynamics on $VO_x$/Rh(111), was how general the island coalescence mechanism is. Experiments in which methanol oxidation was replaced by the $H_2 + O_2$ reaction, the $NH_3 + O_2$ reaction, and catalytic CO oxidation on $VO_x$/Rh(111) showed in fact qualitatively the same behavior as in catalytic methanol oxidation (von Boehn et al., 2016). However, all these reactions have in common that $O_2$ is used as oxidizing agent. Replacing $O_2$ by NO as oxygen source leads in fact to a quite different behavior (von Boehn et al., 2018a).

**Figure 11A** shows a PEEM image of the $VO_x$/Rh(111) surface after the sample has been heated up to 1030 K in a gas mixture of $CH_3OH$ and NO. This pattern evolved from a pattern of thin parallel stripes existing around 900 K. As in methanol oxidation with $O_2$, the $VO_x$ covered parts of the surface appear as dark area in PEEM, the bare Rh(111) surface as bright area. In **Figure 11A**, holes in the $VO_x$ layer are surrounded by $VO_x$ covered surface. With NO a pattern forms that is inverse to the island patterns seen in the oxidation of methanol with $O_2$. Such a hole pattern is also observed in ammonia oxidation with NO.

The $VO_x$ hole pattern is rather static, compared to the circular $VO_x$ islands, which move toward each other and coalesce in methanol oxidation with oxygen. Nevertheless, a coarsening of the $VO_x$ depleted holes, similar to Ostwald ripening, is observed at 1030 K. This causes an elongation of the holes. Compared to the reaction with $O_2$, the interface between the $VO_x$ covered area and the bare Rh(111) surface is broad and fuzzy. As shown with LEEM, the elongated holes are aligned to atomic steps on the Rh(111) surface (von Boehn, 2020). Atomic steps are always present on a surface resulting from a slight (unavoidable) deviation of the surface orientation from the ideal cutting angle during preparation. Another striking difference with the $VO_x$ redistribution patterns observed with $O_2$ is the absence of a substructure of reduced

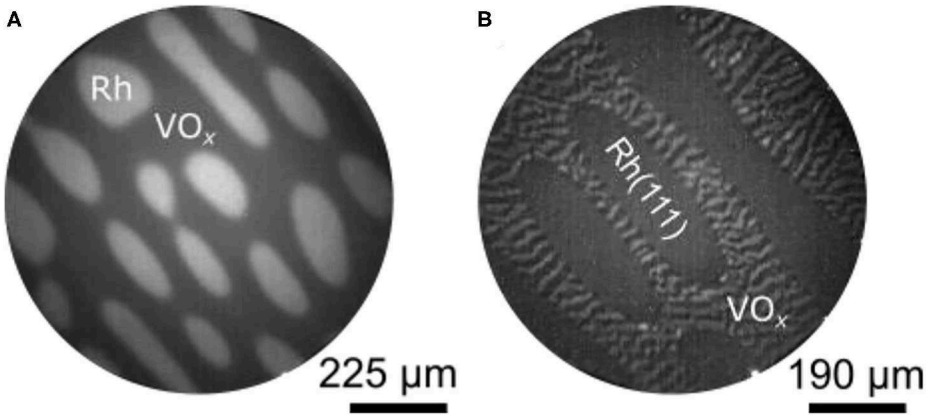


**FIGURE 11 |** V-oxide redistribution in catalytic methanol oxidation with NO and $O_2$ over $VO_x$/Rh(111). **(A)** PEEM image showing a hole pattern during the $CH_3OH$ + NO reaction. (b) Change in the $VO_x$ distribution as NO is exchanged against $O_2$. Experimental conditions: **(A)** $T = 1030$ K, $1 \times 10^{-4}$ mbar NO and $1.5 \times 10^{-4}$ mbar $CH_3OH$; **(B)** $T = 1030$ K, $1 \times 10^{-4}$ mbar NO and $3 \times 10^{-4}$ mbar $CH_3OH$, $\theta_V = 0.3$ MLE. Reprinted from von Boehn et al. (2018a), with the permission of AIP Publishing.

and oxidized phases in the $VO_x$ layer during oxidation with NO.

The different effect that NO and $O_2$ have on the distribution pattern can be demonstrated nicely by exchanging the oxidizing agent NO against $O_2$ after a hole pattern has already been formed. The result displayed **Figure 11B** shows the same surface as **Figure 11A**, but with a gas atmosphere switched to methanol and $O_2$. Upon heating at 800 K a $VO_x$ stripe pattern develops exclusively in the $VO_x$ covered parts of the surface. As the stripes further coarsen, the familiar core—ring structure of a reduced core and an oxidized ring evolves around 900 K, and the stripe pattern is transformed into an island pattern at 1,000 K.

Compared to methanol oxidation with $O_2$, the oxidation of methanol with NO shows a low catalytic activity on $VO_x$/Rh(111). Since the dissociation rate of NO on the Rh(111) surface is rather high, one could have expected the opposite. The low catalytic activity might be the main reason why no detectable oxygen gradients exist in the $VO_x$ layer and in the holes. The absence of a substructure in the $VO_x$-layer is clearly a consequence of the absence of oxygen gradients. O-concentration profiles obtained with *in situ* µXPS during the NO + $NH_3$ reaction showed that the interface $VO_x$ covered surface/bare metal surface is rather broad and exhibits no steep gradient, quite in contrast to the oxidation with $O_2$ where gradients at the interface are steep (von Boehn, 2020). This latter observation of a broad interface can be taken as evidence for a reduced line tension at the interface compared to the oxidation reaction with $O_2$.

The low dynamics in the oxidation reactions with NO suggest that it is thermodynamics that is responsible for why island pattern are formed in reactions with $O_2$ and hole patterns in reactions with NO. More specifically, it should be a question of the interfacial energies and of the line tension. The conclusion that the line tension $VO_x$/metal surface is reduced in the case of NO points in this direction, but quantitative data are required in order to reach definite answers.

## Summary

Ultrathin vanadium oxide layers on Rh(111) exhibit a wealth of redistribution dynamics, ranging from the development of stripe, island and hole patterns, over oscillatory behavior to turbulent redistribution dynamics under the conditions of methanol oxidation in the $10^{-4}$ and $10^{-2}$ mbar range. Reaction-induced oxygen gradients are essential for a peculiar ripening mechanism resulting in the movement and coalescence of neighboring $VO_x$ islands. The island movement was explained with a polymerization/depolymerisation mechanism. These oxygen gradients can also cause a phase separation inside the vanadium oxide islands, resulting in a substructure consisting of a reduced core and an outer oxidized ring. The dependence of the stability of the reduced core on the island size can lead to periodic phase transitions and simultaneous size oscillations of the vanadium oxide islands. As the total pressure is increased into the NAP regime, the core—ring structure of the $VO_x$ islands can no longer be stabilized and turbulent redistribution is observed. Exchanging the oxidizing agent $O_2$ by NO results in the formation of a hole pattern instead of a $VO_x$ island pattern. The different redistribution patterns seen with NO and $O_2$ are probably the consequence of the low catalytic activity of $VO_x$/Rh(111) in the reactions with NO, which prevents the formation of oxygen gradients.

# REACTION DYNAMICS ON $VO_X$/RH(110)

## Structure and Reactivity of $VO_x$/Rh(110)

Characteristic for the Rh(110) surface is its enormous structural variability as evidenced by a large number of adsorbate-induced surface reconstructions studied in detail with adsorbed atomic oxygen and nitrogen (Kiskinova, 1996). Compared to the system $VO_x$/Rh(111) that has been extremely well explored (Schoiswohl et al., 2004b, 2005, 2006), the main difference is that only a handful of studies have been performed for $VO_x$/Rh(110). It was shown that metallic vanadium on Rh(110) has a considerable

tendency to diffuse into subsurface sites forming a subsurface V/Rh alloy (Píš et al., 2013). With LEED it was demonstrated that both, V/Rh(110) and $VO_x$/Rh(110), exhibit a number of ordered overlayer structures upon sequential deposition, but for none of these overlayers a structure model exists (von Boehn et al., 2017). Since no structure models exist, also the V coverage calibration has to be considered as tentative.

In catalytic methanol oxidation $VO_x$ on Rh(110) is far less reactive than on Rh(111), displaying only negligible activity with respect to formaldehyde production (von Boehn and Imbihl, 2018). Apparently, the system $VO_x$/Rh(110) is more complex than $VO_x$/Rh(111) and $VO_x$ on the Rh(110) surface behaves quite differently than on Rh(111). Aside from a much more complex chemistry, the main new aspect that is introduced with respect to pattern formation is the anisotropy of the Rh(110) surface. A structural model of the unreconstructed Rh(110) surface in **Figure 12A** demonstrates this anisotropy.

## Overview

In the following, we investigate the behavior of a submonolayer coverage of V-oxide, i. e. of a V coverage in the range $0.1 \leq \theta_V \leq 0.4$ ML, during catalytic methanol oxidation with $O_2$ in the $10^{-4}$ mbar range. The start is always a surface that after deposition of $VO_x$ appears homogeneous in PEEM. It should be stressed that if the surface is homogeneous on a macroscopic scale ($> 1\,\mu$m), on a microscopic scale it might be heterogeneous.

The sample is then heated up in a $CH_3OH + O_2$ atmosphere but, depending on whether we heat up above 900 K or stay below that temperature, we have a surface with $VO_x$ islands of macroscopic size or a spatially homogeneous surface (the term homogeneous here always refers to a macroscopic length scale). Accordingly, we differentiate in the following between chemical wave patterns on a homogeneous surface and between chemical waves on a pre-patterned surface. Finally, we also consider the $VO_x$ redistribution process itself.

## Chemical Waves on a Homogeneous Surface

### Traveling Interface Pulses

The $CH_3OH + O_2$ reaction on the unpromoted Rh(110) surface displays bistability, i. e. one has reaction fronts separating an oxygen covered surface from a surface with a low O coverage. Close to the equistability point of the two stable surface phases, one observes a phenomenon which for the first time before has been observed in catalytic ammonia oxidation on Rh(110) (Lovis and Imbihl, 2011; Rafti et al., 2015). Distortions of the interface away from its equilibrium position travel pulse-like along the interface. These traveling interface pulses (TIPs), or traveling interface modulations (TIMs) as they were called originally, represent a front instability. A general mathematical model showing their existence has been formulated (Rafti et al., 2012), but no realistic mathematical model existed at the beginning of these studies. On a surface promoted with a low coverage of V-oxide ($\theta_V = 0.1$ ML) these TIPs are much stronger in amplitude and they are much more stable than on a bare Rh(110) surface (von Boehn and Imbihl, 2017). As shown in the PEEM image in **Figure 12B**, waves with roughly triangular shape travel with a velocity of $\sim$17 $\mu$m/s along the interface. Despite the anisotropy of the Rh(110) surface no clear-cut dependence of the excitations on the crystallographic directions has been found. One notes that the area after being passed by the TIPs exhibits an enhanced brightness, which then decays within a few tens of seconds. This brightness variation indicates a temporary modification of the surface either by structural defects or by a chemical modification. Since no indication for a chemical modification was found, the brightness changes were assigned to structural defects.

To explain the formation of defects around the interface, one has to keep in mind that the interface oxygen covered/oxygen free surface also represents the boundary between two different substrate structures, the so-called "missing row" reconstructions on the oxygen covered surface and the non-reconstructed ($1 \times 1$) surface of the oxygen free surface (von Boehn, 2020). Since the two substrate structures differ in their density of surface atoms, any structural variation caused, for example, by fluctuations in the oxygen coverage, will be associated with a mass transport of Rh atoms, thus causing structural defects. A roughening of the surface caused by defects will, in general, lead to an increase in catalytic activity. This means that fluctuations in the adsorbate coverages around the interface will be amplified by a positive feedback.

The mechanism sketched above is the basis of a realistic three-variable model that semi-quantitatively reproduces well the experimentally observed TIPs (Makeev and Imbihl, 2019). As shown in the bifurcation diagram of **Figure 12C**, the TIPs occur in a very narrow parameter window near the equistability point in the region of so-called dynamic bistability (or double metastability) where oxidation and reduction fronts coexist. The simulation in **Figure 12D** shows an enhanced defect concentration in the leading edge of each pulse. TIPs occur on Rh(110) during catalytic ammonia and methanol oxidation, but TIPs have not been found in the $H_2 + O_2$ reaction. From the proposed mechanism, one should expect that TIPs should also occur in the bistable $O_2 + H_2$ reaction on Rh(110). This, however, is not the case. The mathematical model provides the explanation, which is that the region of dynamic bistability becomes vanishingly small due to the fast diffusion of adsorbed hydrogen, thus removing one of the essential requirements for the occurrence of TIPs (Makeev and Imbihl, 2019).

### Varying Front Geometries and Traveling Wave Fragments

In a coverage range $0.2 \leq \theta_V \leq 0.4$, we observe dynamic bistability in a temperature range that extends roughly from 700 to 850 K. As shown in **Figure 13A**, upon a parameter change, initially an elliptical oxygen island develops imaged as dark area in PEEM. After $\approx$ 20 s, a bright front nucleates inside the dark island, but this bright front, as it grows, exhibits a different anisotropy than the elliptical dark island. Apparently the anisotropy of the Rh(110) surface varies depending on the type of front. Such a behavior has before been observed in the $H_2 + NO$ reaction on Rh(110), and was traced back to a state-dependent anisotropy (Gottschalk et al., 1994; Mertens and Imbihl, 1994). In the case of the $H_2 + NO$ reaction, the different substrate reconstructions causing the state-dependent anisotropy

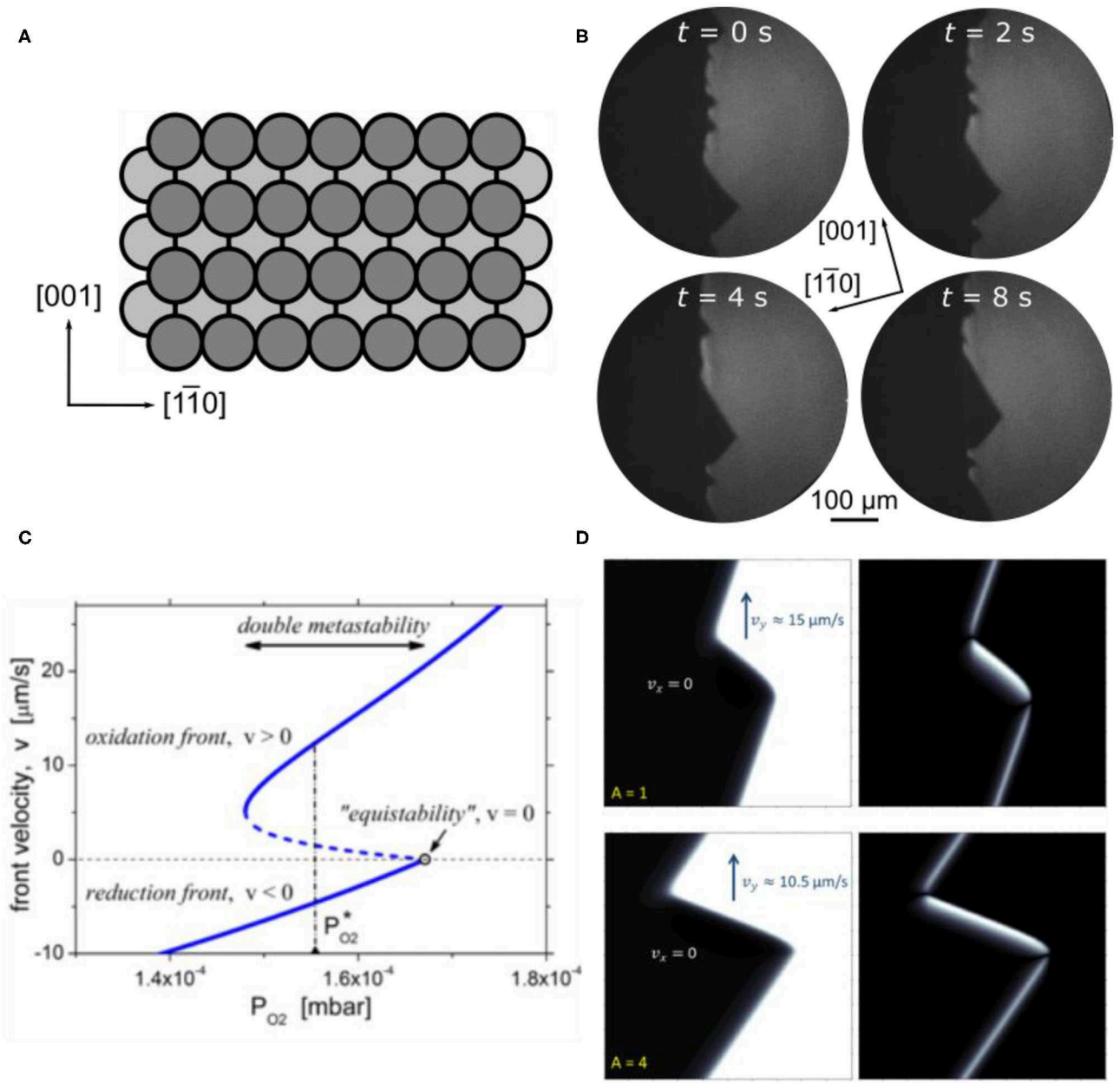


**FIGURE 12 |** Traveling interface pulses on $VO_x$/Rh(110) during methanol oxidation. **(A)** Sketch of the Rh(110) surface. **(B)** PEEM images showing traveling interface pulses on a Rh(110) surface promoted with some V-oxide. Experimental conditions: $\theta_V = 0.1$ MLE, $T = 820$ K, $p(CH_3OH) = 3 \times 10^{-4}$ mbar, $p(O_2) = 0.8 \times 10^{-4}$ mbar. Reproduced from Ref. (von Boehn and Imbihl, 2017) with permission from the PCCP Owner Societies. **(C)** Dependence of the TIP front velocity on the oxygen pressure (1D model). The solid (dashed) lines represent the stable (unstable) solutions. In the double metastable region, oxidation and reduction fronts coexist; the dash-dotted vertical line shows the oxygen pressure at which TIPs of stationary size exist in 2D simulations. **(D)** Solitary TIP. The system size is 100 × 100 $\mu m^2$. The color-coded spatial distributions of the oxygen coverage $\theta_O$ (left) and the defect concentration (right) given by difference between the oxygen coverage and the degree of reconstruction $|\theta_O$-$\theta_{rec}|$ (right) are presented. **(C,D)** Reprinted figures with permission from Makeev and Imbihl (2019). Copyright (2019) by the American Physical Society.

have been identified, but for the present system no structure models exist yet.

Another phenomenon that results from a state-dependent anisotropy is also found here, which are traveling wave fragments (TWFs). **Figure 13B** displays PEEM images showing different stages in the development of TWFs. These TWFs typically nucleate at some defect and then propagate with constant velocity along the [1$\bar{1}$0]-direction, which is the direction along which the troughs of the Rh(110) surface (**Figure 12A**) are oriented. TWFs have been found before in catalytic CO-oxidation on Pt(110) ("soliton-like" behavior) (Rotermund et al., 1991), and in the $H_2$ + NO reaction on Rh(110) (Mertens et al., 1995).

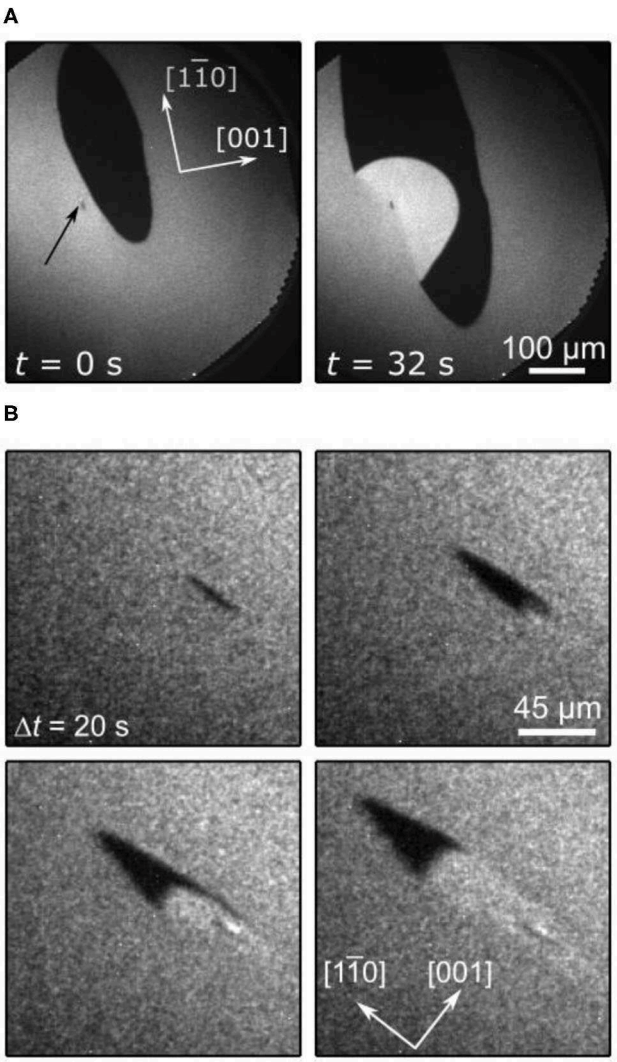


**FIGURE 13 |** Double metastability and traveling wave fragments in methanol oxidation over $VO_x$/Rh(110). Shown are PEEM images. **(A)** A propagating oxidation front (black) collides with a surface defect, resulting in the nucleation of a reduction front (bright). **(B)** Traveling wave fragment propagating along the [1$\bar{1}$0] direction. Field of view:173 × 173 µm$^2$, Experimental conditions: $T$ = 790 K **(A)** and 740 K **(B)**, $p(O_2) = 1\times10^{-4}$ mbar, $p(CH_3OH) = 3 \times 10^{-4}$ mbar, $\theta_V = 0.4$ MLE. Reprinted with permission from von Boehn and Imbihl (2018). Copyright (2018) American Chemical Society.

In **Figure 13A**, and less clearly in **Figure 13B**, we can identify three distinct gray levels—a medium gray, dark and bright—which we can assign to the resting state, the excited state and the refractory state of the surface. *In situ* LEEM is feasible in the $10^{-4}$ mbar range. In such a LEEM/µLEED investigation ordered overlayers could be assigned to the different phases of chemical waves on $VO_x$/Rh(110) (von Boehn, 2020). Even with this information a mechanistic interpretation of the patterns presented above remains very difficult due to (i) a complete lack of structure models and (ii) the missing chemical information. *In situ* µXPS at synchrotrons requires a pressure $< 10^{-5}$ mbar, but since the chemical waves only showed up beyond $1 \times 10^{-4}$ mbar, the former condition excluded any *in situ* XPS study of chemical waves. Nevertheless, the similarity of the patterns observed here with the chemical wave patters seen in the $H_2 + NO$ reaction on Rh(110) suggests a common origin of state-dependent anisotropy, namely the switching of the surface between reconstructions with varying anisotropy.

## $VO_x$ Redistribution Patterns

### Island Formation

Annealing $VO_x$ on Rh(110) in a reacting atmosphere to 1,020 K generates $VO_x$ islands of macroscopic dimensions. Apparently, only at this temperature the mobility of $VO_x$ on Rh(110) becomes high enough to accomplish a mass transport over macroscopic distances. At 1,020 K a $VO_x$ island size of 100 µm is reached within minutes. Similar to Rh(111), the islands exhibit a substructure consisting of a dark outer ring and a bright core region in PEEM. Quite differently from $VO_x$/Rh(111), however, the islands do not move under reaction conditions and they do not coalesce (von Boehn and Imbihl, 2018).

The $VO_x$ islands respond to changes in the gas phase composition. Depending on whether they appear bright in PEEM ($p(CH_3OH)$ high) or dark ($p(CH_3OH)$ low), we speak of reduced or oxidized islands. The terms "oxidized" and "reduced" are used here on a pure phenomenological basis. In fact, the response to changes in the gas atmosphere was the main criterion to distinguish between $VO_x$ covered areas and areas with a low $VO_x$ coverage. Since no chemical analysis has been conducted, these assignments should best be considered as preliminary.

### Chemical Wave Patterns

When, after preparation, such a surface with large reduced $VO_x$ islands is heated up into the temperature window of dynamic bistability chemical wave patterns develop. As demonstrated by the PEEM images in **Figure 14**, TWFs nucleate and propagate across the $VO_x$ islands. These TWFs propagate along the [1$\bar{1}$0]-direction of Rh(110), similarly to TWFs on the homogeneous surface in **Figure 13B**. Initially, dark elliptically shaped islands nucleate outside the $VO_x$ islands. They invade the reduced $VO_x$ islands acting as oxidation fronts. The oxidation fronts are soon followed by reduction fronts transforming the oxidized state into a refractory state appearing bright in PEEM. These bright reduction fronts also nucleate at the boundaries of the $VO_x$ islands. The bright refractory state then relaxes into the resting state characterized by a medium gray level. A comparison with **Figure 13B** shows that the nature of the TWFs seen on the pre-patterned surface does not appear to be different from the TWFs on the homogeneous surface.

### Incomplete Phase Separation

The process of $VO_x$ redistribution could be followed *ex situ* with LEEM/µLEED allowing to establish correlations between the different surface phases and ordered overlayers (von Boehn et al., 2018b). The chemistry evolving in this process could not be followed *in situ* since µXPS is not feasible at $10^{-4}$ mbar. However, by generating an island structure at $10^{-4}$ mbar in a preparation chamber followed by transfer to the LEEM chamber,

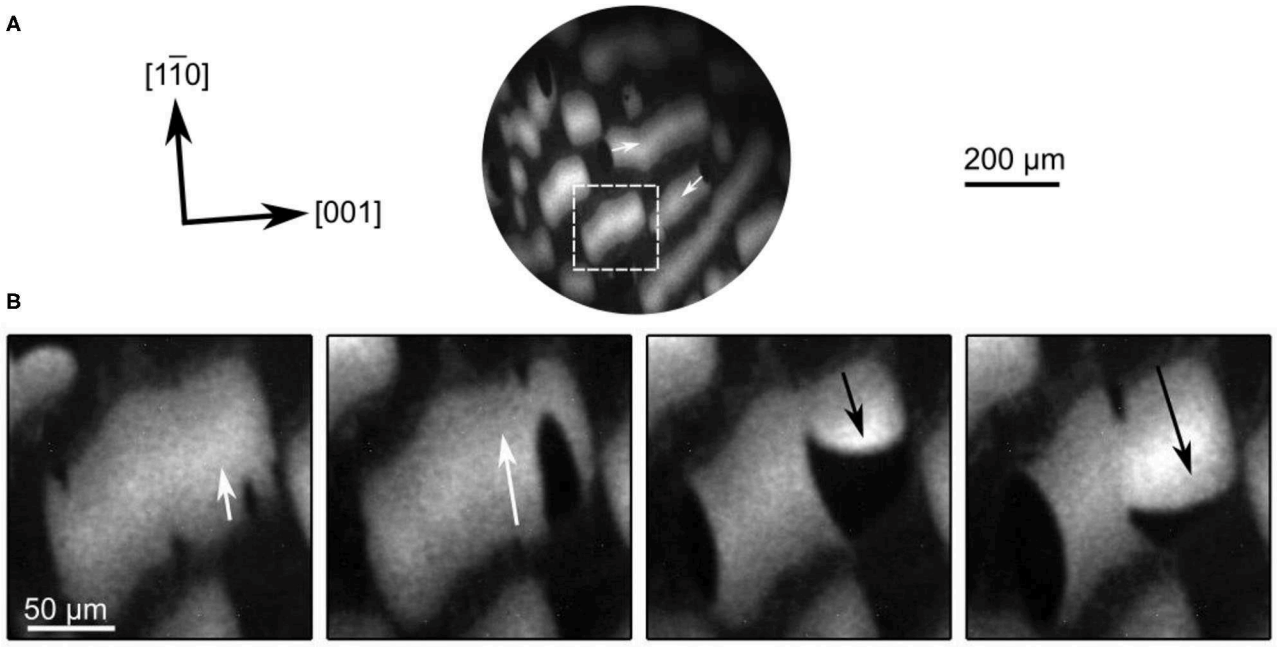


**FIGURE 14 |** PEEM images showing traveling wave fragments propagating on $VO_x$ islands (bright areas) during methanol oxidation on $VO_x$/Rh(110). **(A)** Nucleation of wave fragments at the borders of the $VO_x$ islands. The white arrows mark the propagation direction. (s) Magnified section of the images in a. Experimental conditions: T = 830 K, $p(O_2) = 1 \times 10^{-4}$ mbar, $p(CH_3OH) = 3 \times 10^{-4}$ mbar, $\Delta t = 10$ s between frames 1–2 and 3–4, 20 s between frames 2–3 in **(B)**. Reprinted with permission from von Boehn and Imbihl (2018). Copyright (2018) American Chemical Society.

µXPS could at least be performed *ex situ* under UHV conditions. The data showed that different from the system $VO_x$/Rh(111) no complete phase separation into $VO_x$ islands and into an almost $VO_x$ free metal surface occurred. A substantial part of $VO_x$, roughly 15% of the signal inside the islands, is also present in the area surrounding the islands. Moreover, part of the vanadium has penetrated the Rh bulk residing in subsurface sites. These results indicate that $VO_x$ redistribution on Rh(110) is more complex than on Rh(111).

### Dendritic Growth

One starts with the uniform surface present in PEEM after deposition of 0.4 ML $VO_x$. Upon heating in the $CH_3OH + O_2$ atmosphere, $p(CH_3OH)$ is varied such that the surface is kept in a reduced state, but not far from the transition to an oxidized state. In the temperature range 960–1020 K one observes nucleation and dendritic growth of the $VO_x$ phase (von Boehn and Imbihl, 2018), as demonstrated by the PEEM images in **Figure 15**. Within a few minutes after the heating schedule has been stopped at 1,020 K, the whole imaged area is filled with the dendritic $VO_x$ structure. The main axis of the dendritic structure is oriented along the [1$\bar{1}$0]-direction, which is the direction of the [1$\bar{1}$0] troughs of Rh(110). The dendritic growth of branches always stops short before they get in contact with each other such that they are still about 20 µm apart.

## Summary

The behavior of $VO_x$ on Rh(110) in catalytic methanol oxidation is distinctly different from $VO_x$ on Rh(111). The catalytic activity is much lower than on Rh(111) and we observe no moving and coalescing $VO_x$ islands. Chemically and structurally the $VO_x$/Rh(110) surface is much more complex than $VO_x$ on Rh(111), since a population of subsurface sites by vanadium is involved. Furthermore, the complete lack of structural models for any of the ordered $VO_x$ phases on Rh(110) complicates the interpretation of data. On the other hand, one is rewarded with a rich variety of intricate chemical wave patterns and $VO_x$ redistribution processes.

Dynamic bistability with varying front geometries and traveling wave fragments can be attributed to a state-dependent anisotropy caused by surface reconstructions with different diffusional anisotropy. Despite the identification of numerous surface phases by µLEED/LEEM, an excitation mechanism for the chemical waves could not yet be established due to a lack of chemical information. *In situ* µXPS was not feasible under the conditions where chemical waves occur, a problem well known in catalysis under the name "pressure gap." With further developments of surface analytical *in situ* techniques, capable of operating at elevated pressure, this obstacle should be overcome in the near future.

## CONCLUSION

Studying catalytic reactions on $VO_x$/Rh(111) and $VO_x$/Rh(110), the range of non-linear phenomena in catalysis has been expanded from metal surfaces to oxidic systems. The most significant finding for $VO_x$/Rh(111) is an island ripening

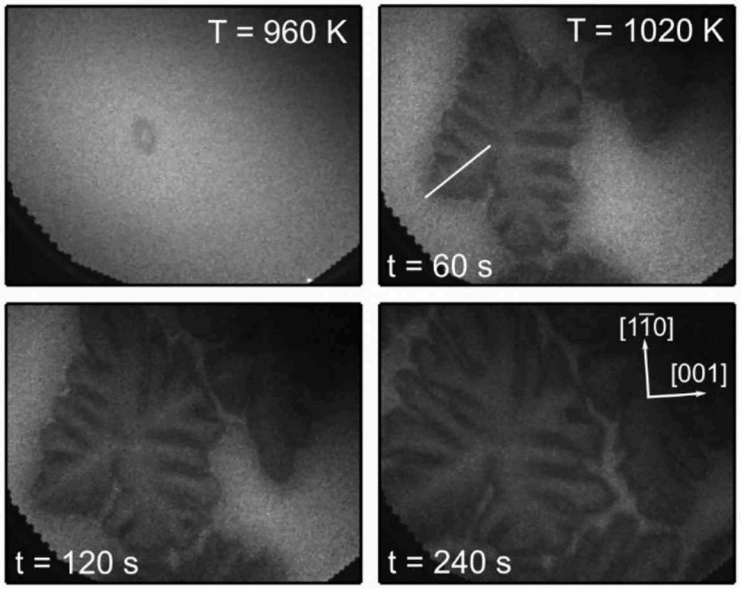


**FIGURE 15 |** Dendritic growth of $VO_x$ islands on Rh(110) during methanol oxidation imaged with PEEM. Experimental conditions: $p(O_2) = 1 \times 10^{-4}$ mbar, $p(CH_3OH) \approx 3 \times 10^{-4}$ mbar, $\theta_V = 0.4$ MLE, 500 × 400 $\mu m^2$ field of view. Reprinted with permission from von Boehn and Imbihl (2018). Copyright (2018) American Chemical Society.

mechanism that operates under non-equilibrium conditions. This mechanism differs from classical Ostwald ripening and also from Smoluchowski ripening. The $VO_x$ island coalescence could be explained with a polymerization/depolymerization mechanism. The system $VO_x$/Rh(110) is more complex than $VO_x$/Rh(111), but one is rewarded with a wealth of chemical wave patterns in addition to $VO_x$ redistribution structures. Overall, one finds that supported V-oxide layers at submonolayer coverages are highly dynamic, giving rise to new phenomena that have not been observed on metal surfaces. The observations made here are closely related to the well-known "pressure and materials gap" in heterogeneous catalysis: structure and composition of the V-oxide layer are strongly pressure dependent. Moreover, comparing $VO_x$ on Rh(111) and Rh(110), one finds that the catalytic properties and the pattern forming properties of the V-oxide layer vary drastically depending on the orientation of the metallic substrate. The results obtained here also demonstrate the relevance of non-linear effects in catalysis.

## AUTHOR CONTRIBUTIONS

BB and RI wrote and edited the manuscript. All authors contributed to the article and approved the submitted version.

## FUNDING

The authors are indebted to the Deutsche Forschungsgemeinschaft (DFG) for financial support through project: 409299786. BB thanks the Department of Inorganic Chemistry of the Fritz Haber Institute of the Max Planck Society for financial support.

## ACKNOWLEDGMENTS

We thank Yannick De Decker for helpful comments on the manuscript, and Andrea Locatelli and Tevfik O. Menteş for the long-lasting collaboration, which enabled to chemically characterize the systems $VO_x$/Rh(111) and $VO_x$/Rh(110).

## SUPPLEMENTARY MATERIAL

The Supplementary Material for this article can be found online at: https://www.frontiersin.org/articles/10.3389/fchem.2020.00707/full#supplementary-material

**Data Sheet 1 |** Short description of the videos in the supplementary material.

**Supplementary Video 1 |** $VO_x$ stripe and island pattern formation during methanol oxidation (PEEM).

**Supplementary Video 2 |** $VO_x$ island oscillation during methanol oxidation (LEEM).

**Supplementary Video 3 |** Turbulent $VO_x$ redistribution (NAP-LEEM).

**Supplementary Video 4 |** Formation of a $VO_x$ hole pattern in the $CH_3OH + NO$ reaction (PEEM).

**Supplementary Video 5 |** Traveling interface modulations on $VO_x$/Rh(110) during methanol oxidation (PEEM).

**Supplementary Video 6 |** Traveling wave fragments on $VO_x$ islands during methanol oxidation (PEEM).

**Supplementary Video 7 |** Dendritic island growth on $VO_x$/Rh(110) during methanol oxidation (PEEM).

## REFERENCES


Barth, J. (2000). Transport of adsorbates at metal surfaces: from thermal migration to hot precursors. *Surf. Sci. Rep.* 40, 75–149. doi: 10.1016/S0167-5729(00)00002-9

Bauer, E. (2019). "LEEM, SPLEEM and SPELEEM," in *Springer Handbook of Microscopy*, eds P. W. Hawkes and J. C. H. Spence (Cham: Springer International Publishing), 2. doi: 10.1007/978-3-030-00069-1_9

Boffa, A. B., Lin, C., Bell, A. T., and Somorjai, G. A. (1994). Lewis acidity as an explanation for oxide promotion of metals: implications of its importance and limits for catalytic reactions. *Catal. Lett.* 27, 243–249. doi: 10.1007/BF00813909

Bond, G. C., and Tahir, S. F. (1991). Vanadium oxide monolayer catalysts Preparation, characterization and catalytic activity. *Appl. Catal.* 71, 1–31. doi: 10.1016/0166-9834(91)85002-D

Carrero, C. A., Schloegl, R., Wachs, I. E., and Schomaecker, R. (2014). Critical literature review of the kinetics for the oxidative dehydrogenation of propane over well-defined supported vanadium oxide catalysts. *ACS Catal.* 4, 3357–3380. doi: 10.1021/cs5003417

De Decker, Y., Marbach, H., Hinz, M., Günther, S., Kiskinova, M., Mikhailov, A. S., et al. (2004). Promoter-induced reactive phase separation in surface reactions. *Phys. Rev. Lett.* 92:198305. doi: 10.1103/PhysRevLett.92.198305

De Decker, Y., Raghamy, A., and Imbihl, R. (2019). Modeling the formation and propagation of $VO_x$ islands on Rh(111) under reactive conditions. *J. Phys. Chem. C* 123, 11602–11610. doi: 10.1021/acs.jpcc.9b00427

Döbler, J., Pritzsche, M., and Sauer, J. (2005). Oxidation of methanol to formaldehyde on supported vanadium oxide catalysts compared to gas phase molecules. *J. Am. Chem. Soc.* 127, 10861–10868. doi: 10.1021/ja051720e

Dou, J., Sun, Z., Opalade, A. A., Wang, N., Fu, W., and Tao, F. F. (2017). Operando chemistry of catalyst surfaces during catalysis. *Chem. Soc. Rev.* 46, 2001–2027. doi: 10.1039/C6CS00931J

Ertl, G. (1991). Oscillatory kinetics and spatio-temporal self-organization in reactions at solid surfaces. *Science* 254, 1750–1755. doi: 10.1126/science.254.5039.1750

Frank, B., Fortrie, R., Hess, C., Schlögl, R., and Schomäcker, R. (2009). Reoxidation dynamics of highly dispersed $VO_x$ species supported on γ-alumina. *Appl. Catal. A Gen.* 353, 288–295. doi: 10.1016/j.apcata.2008.11.002

Franz, A. W., Kronemayer, H., Pfeiffer, D., Pilz, R. D., Reuss, G., Disteldorf, W., et al. (2010). "Formaldehyde," in *Ullmann's Encyclopedia of Industrial Chemistry*, ed B. Elvers (Chichester: Wiley), 1–34. doi: 10.1002/14356007.a11_619.pub2

Franz, T., von Boehn, B., Marchetto, H., Borkenhagen, B., Lilienkamp, G., Daum, W., et al. (2019). Catalytic CO oxidation on Pt under near ambient pressure: a NAP-LEEM study. *Ultramicroscopy* 200, 73–78. doi: 10.1016/j.ultramic.2019.02.024

Göbke, D., Romanyshyn, Y., Guimond, S., Sturm, J. M., Kuhlenbeck, H., Döbler, J., et al. (2009). Formaldehyde formation on vanadium oxide surfaces $V_2O_3$(0001) and $V_2O_5$(001): how does the stable methoxy intermediate form? *Angew. Chem. Int. Ed. Engl.* 48, 3695–3698. doi: 10.1002/anie.200805618

Gottschalk, M., Eiswirth, B., and Imbihl (1994). Chemical waves in media with state-dependent anisotropy. *Phys. Rev. Lett.* 73, 3483–3486. doi: 10.1103/PhysRevLett.73.3483

Hesse, M., von Boehn, B., Locatelli, A., Sala, A., Menteş, T. O., and Imbihl, R. (2015). Island ripening via a polymerization-depolymerization mechanism. *Phys. Rev. Lett.* 115:136102. doi: 10.1103/PhysRevLett.115.136102

Imbihl, R. (2005). Nonlinear dynamics on catalytic surfaces. *Catal. Today* 105, 206–222. doi: 10.1016/j.cattod.2005.02.045

Imbihl, R., and Ertl, G. (1995). Oscillatory kinetics in heterogeneous catalysis. *Chem. Rev.* 95, 697–733. doi: 10.1021/cr00035a012

Kiskinova, M. (1996). Surface structure and reactivity: reactions on face-centered cubic (110) metal surfaces involving adatom-induced reconstructions. *Chem. Rev.* 96, 1431–1448. doi: 10.1021/cr950226y

Kropp, T., Paier, J., and Sauer, J. (2014). Support effect in oxide catalysis: methanol oxidation on vanadia/ceria. *J. Am. Chem. Soc.* 136, 14616–14625. doi: 10.1021/ja508657c

Levin, M. (1987). The enhancement of CO hydrogenation on rhodium by $TiO_x$ overlayers. *J. Catal.* 106, 401–409. doi: 10.1016/0021-9517(87)90252-1

Locatelli, A., Mentes, T. O., Aballe, L., Mikhailov, A., and Kiskinova, M. (2006). Formation of regular surface-supported mesostructures with periodicity controlled by chemical reaction rate. *J. Phys. Chem. B* 110, 19108–19111. doi: 10.1021/jp065090u

Locatelli, A., Sbraccia, C., Heun, S., Baroni, S., and Kiskinova, M. (2005). Energetically driven reorganization of a modified catalytic surface under reaction conditions. *J. Am. Chem. Soc.* 127, 2351–2357. doi: 10.1021/ja045285k

Lovis, F., Hesse, M., Locatelli, A., Menteş, T. O., Niño, M. Á., Lilienkamp, G., et al. (2011). Self-organization of ultrathin vanadium oxide layers on a Rh(111) surface during a catalytic reaction. Part II: A LEEM and spectromicroscopy study. *J. Phys. Chem. C* 115, 19149–19157. doi: 10.1021/jp206600q

Lovis, F., and Imbihl, R. (2011). Self-organization of ultrathin vanadium oxide layers on a Rh(111) surface during a catalytic reaction. Part I: A PEEM study. *J. Phys. Chem. C* 115, 19141–19148. doi: 10.1021/jp2065425

Makeev, A., and Imbihl, R. (2019). Simulation of traveling interface pulses in bistable surface reactions. *Phys. Rev. E* 100:42206. doi: 10.1103/PhysRevE.100.042206

Mavrikakis, M., Rempel, J., Greeley, J., Hansen, L. B., and Nørskov, J. K. (2002). Atomic and molecular adsorption on Rh(111). *J. Chem. Phys.* 117, 6737–6744. doi: 10.1063/1.1507104

Menteş, T. O., Zamborlini, G., Sala, A., and Locatelli, A. (2014). Cathode lens spectromicroscopy: methodology and applications. *Beilstein J. Nanotechnol.* 5, 1873–1886. doi: 10.3762/bjnano.5.198

Mertens, F., and Imbihl, R. (1994). Square chemical waves in the catalytic reaction NO + $H_2$ on a rhodium(110) surface. *Nature* 370, 124–126. doi: 10.1038/370124a0

Mertens, G., Eiswirth, B., and Imbihl, M. (1995). Traveling-wave fragments in anisotropic excitable media. *Phys. Rev. E* 51, R5193–R5196. doi: 10.1103/PhysRevE.51.R5193

Mikhailov, A. S. (1994). *Foundations of Synergetics I: Distributed Active Systems*. Berlin, Heidelberg: Springer. doi: 10.1007/978-3-642-78556-6

Mikhailov, A. S., and Loskutov, A. Y. (1991). *Foundations of Synergetics II: Complex Patterns*. Berlin, Heidelberg: Springer. doi: 10.1007/978-3-642-97294-2

Píš, I., Skála, T., Cabala, M., Šutara, F., Libra, J., Škoda, M., et al. (2012). Structural, electronic and adsorption properties of V–Rh(111) subsurface alloy. *J. Alloys Compd.* 543, 189–196. doi: 10.1016/j.jallcom.2012.07.122

Píš, I., Stetsovych, V., Mysliveček, J., Kettner, M., Vondráček, M., Dvořák, F., et al. (2013). Atomic and electronic structure of V–Rh(110) near-surface alloy. *J. Phys. Chem. C* 117, 12679–12688. doi: 10.1021/jp402985v

Rafti, M., Borkenhagen, B., Lilienkamp, G., Lovis, F., Smolinsky, T., and Imbihl, R. (2015). Traveling interface modulations and anisotropic front propagation in ammonia oxidation over Rh(110). *J. Chem. Phys.* 143, 184701. doi: 10.1063/1.4935274

Rafti, M., Uecker, H., Lovis, F., Krupennikova, V., and Imbihl, R. (2012). Traveling interface modulations in the $NH_3$ + $O_2$ reaction on a Rh(110) surface. *Phys. Chem. Chem. Phys.* 14, 5260–5264. doi: 10.1039/c2cp23970a

Rodriguez, J. A., Liu, P., Graciani, J., Senanayake, S. D., Grinter, D. C., Stacchiola, D., et al. (2016). Inverse oxide/metal catalysts in fundamental studies and practical applications: a perspective of recent developments. *J. Phys. Chem. Lett.* 7, 2627–2639. doi: 10.1021/acs.jpclett.6b00499

Rotermund, H. H. (1993). Investigation of dynamic processes in adsorbed layers by photoemission electron microscopy (PEEM). *Surf. Sci.* 283, 87–100. doi: 10.1016/0039-6028(93)90965-M

Rotermund, J., and Oertzen, A., von, and Ertl (1991). Solitons in a surface reaction. *Phys. Rev. Lett.* 66, 3083–3086. doi: 10.1103/PhysRevLett.66.3083

Schlögl, R. (2015). Heterogeneous catalysis. *Angew. Chem. Int. Ed. Engl.* 54, 3465–3520. doi: 10.1002/anie.201410738

Schmidt, T., Heun, S., Slezak, J., Diaz, J., Prince, K. C., Lilienkamp, G., et al. (1998). SPELEEM: combining LEEM and spectroscopic imaging. *Surf. Rev. Lett.* 05, 1287–1296. doi: 10.1142/S0218625X98001626

Schoiswohl, J., Kresse, G., Surnev, S., Sock, M., Ramsey, M. G., and Netzer, F. P. (2004a). Planar vanadium oxide clusters: two-dimensional evaporation and diffusion on Rh(111). *Phys. Rev. Lett.* 92:206103. doi: 10.1103/PhysRevLett.92.206103

Schoiswohl, J., Sock, M., Eck, S., Surnev, S., Ramsey, M. G., Netzer, F. P., et al. (2004b). Atomic-level growth study of vanadium oxide nanostructures on Rh(111). *Phys. Rev. B*. 69, 155403. doi: 10.1103/PhysRevB.69.155403

Schoiswohl, J., Surnev, S., Netzer, F. P., and Kresse, G. (2006). Vanadium oxide nanostructures: from zero- to three-dimensional. *J. Phys. Condens. Matter* 18, R1–R14. doi: 10.1088/0953-8984/18/4/R01

Schoiswohl, J., Surnev, S., Sock, M., Eck, S., Ramsey, M. G., Netzer, F. P., et al. (2005). Reduction of vanadium-oxide monolayer structures. *Phys. Rev. B*. 71, 165437. doi: 10.1103/PhysRevB.71.165437

Surnev, S., Fortunelli, A., and Netzer, F. P. (2013). Structure-property relationship and chemical aspects of oxide-metal hybrid nanostructures. *Chem. Rev.* 113, 4314–4372. doi: 10.1021/cr300307n

Thiel, P. A., Shen, M., Liu, D.-J., and Evans, J. W. (2009). Coarsening of two-dimensional nanoclusters on metal surfaces. *J. Phys. Chem. C* 113, 5047–5067. doi: 10.1021/jp8063849

Topsøe, H. (2003). Developments in operando studies and *in situ* characterization of heterogeneous catalysts. *J. Catal.* 216, 155–164. doi: 10.1016/S0021-9517(02)00133-1

von Boehn, B. (2020). Redistribution dynamics of ultrathin vanadium oxide layers under catalytic conditions and activation of diffusion by surface acoustic waves. (Doctoral Thesis. Hannover: Leibniz University Hannover). Available online at: doi: 10.15488/9805

von Boehn, B., and Imbihl, R. (2017). Large amplitude excitations traveling along the interface in bistable catalytic methanol oxidation on Rh(110). *Phys. Chem. Chem. Phys.* 19, 18487–18493. doi: 10.1039/C7CP01890H

von Boehn, B., and Imbihl, R. (2018). Chemical wave patterns and oxide redistribution during methanol oxidation on a V-oxide promoted Rh(110) surface. *J. Phys. Chem. C* 122, 12694–12703. doi: 10.1021/acs.jpcc.8b00852

von Boehn, B., Mehrwald, S., and Imbihl, R. (2018a). Hole patterns in ultrathin vanadium oxide layers on a Rh(111) surface during catalytic oxidation reactions with NO. *Chaos* 28, 45117. doi: 10.1063/1.5020360

von Boehn, B., Mente,ş, T. O., Locatelli, A., Sala, A., and Imbihl, R. (2017). Growth of vanadium and vanadium oxide on a Rh(110) surface. *J. Phys. Chem. C* 121, 19774–19785. doi: 10.1021/acs.jpcc.7b04809

von Boehn, B., Mente,ş, T. O., Locatelli, A., Sala, A., and Imbihl, R. (2018b). Reactive phase separation during methanol oxidation on a V-oxide-promoted Rh(110) surface. *J. Phys. Chem. C* 122, 10482–10488. doi: 10.1021/acs.jpcc.8b02544

von Boehn, B., Penschke, C., Li, X., Paier, J., Sauer, J., Krisponeit, J.-O., et al. (2020). Reaction dynamics of metal/oxide catalysts: methanol oxidation at vanadium oxide films on Rh(111) from UHV to $10^{-2}$ mbar. *J. Catal.* 385, 255–264. doi: 10.1016/j.jcat.2020.03.016

von Boehn, B., Preiss, A., and Imbihl, R. (2016). Dynamics of ultrathin V-oxide layers on Rh(111) in catalytic oxidation of ammonia and CO. *Phys. Chem. Chem. Phys.* 18, 19713–19721. doi: 10.1039/C6CP03637F

Wichtendahl, R., Fink, R., Kuhlenbeck, H., Preikszas, D., Rose, H., Spehr, R., et al. (1998). SMART: an aberration-corrected XPEEM/LEEM with energy filter. *Surf. Rev. Lett.* 05, 1249–1256. doi: 10.1142/S0218625X98001584

Zhang, J., and Medlin, J. W. (2018). Catalyst design using an inverse strategy: From mechanistic studies on inverted model catalysts to applications of oxide-coated metal nanoparticles. *Surf. Sci. Rep.* 73, 117–152. doi: 10.1016/j.surfrep.2018.06.002

**Conflict of Interest:** The authors declare that the research was conducted in the absence of any commercial or financial relationships that could be construed as a potential conflict of interest.

*Copyright © 2020 von Boehn and Imbihl. This is an open-access article distributed under the terms of the Creative Commons Attribution License (CC BY). The use, distribution or reproduction in other forums is permitted, provided the original author(s) and the copyright owner(s) are credited and that the original publication in this journal is cited, in accordance with accepted academic practice. No use, distribution or reproduction is permitted which does not comply with these terms.*

frontiers in Chemistry

ORIGINAL RESEARCH
published: 30 September 2020
doi: 10.3389/fchem.2020.561788

# Chemical Oscillations With Sodium Perborate as Oxidant

*Krisztina Kurin-Csörgei, Eszter Poros-Tarcali, István Molnár, Miklós Orbán* and István Szalai**

*Laboratory of Nonlinear Chemical Dynamics, Department of Analytical Chemistry, Institute of Chemistry, L. Eötvös University, Budapest, Hungary*

The peroxo compounds $H_2O_2$ and $K_2S_2O_8$ represent one of the major constituents in many oscillatory chemical systems. In this contribution we demonstrate that beside $H_2O_2$ and $S_2O_8^{2-}$ the sodium perborate ($NaBO_3{\cdot}H_2O$) can act as alternative oxidizing agent in oscillatory reactions. So far the $H_2O_2$ has been successfully substituted with $NaBO_3$ in two oscillators: in the $BO_3^-$–$S_2O_3^{2-}$–Cu(II) flow system potential and pH oscillations, in the strongly alkaline Cu(II)-catalyzed $BO_3^-$–$SCN^-$ batch reaction, which are rather different in their chemistry and dynamics, potential oscillations were observed. In spite of the significant differences in the oxidizing nature of $H_2O_2$ and $NaBO_3$ we assume that the oscillatory cycle in the $BO_3^-$–substrate and in the $H_2O_2$–substrate systems is similar in many aspects, therefore the numbers of this new subgroup of the oscillators may be considered to be borate-mediated $H_2O_2$ oscillators. Mechanisms are suggested and simulations are shown to describe the oscillatory behaviors observed in the perborate chemistry based oscillators by using the assumption that the oxidation reactions of the intermediates $(HO)_3B(OOH)^-$ and $(HO)_2B(OOH)_2^-$ anions, which are dominant species in alkaline and neutral pH solutions of perborate, are much faster than that of $H_2O_2$.

**Keywords: oscillatory reactions, perborate, non-linear dynamics, pH-oscillator, copper(II)-catalysis**

OPEN ACCESS

***Edited by:***
*Annette F. Taylor,*
*The University of Sheffield,*
*United Kingdom*

***Reviewed by:***
*Judit Horváth,*
*The University of Sheffield,*
*United Kingdom*
*Ivan Valent,*
*Comenius University, Slovakia*

****Correspondence:***
*Miklós Orbán*
*orbanm@chem.elte.hu*
*István Szalai*
*szalai.istvan@chem.elte.hu*

***Specialty section:***
*This article was submitted to Physical Chemistry and Chemical Physics, a section of the journal Frontiers in Chemistry*

***Received:*** *13 May 2020*
***Accepted:*** *27 August 2020*
***Published:*** *30 September 2020*

***Citation:***
*Kurin-Csörgei K, Poros-Tarcali E, Molnár I, Orbán M and Szalai I (2020) Chemical Oscillations With Sodium Perborate as Oxidant. Front. Chem. 8:561788. doi: 10.3389/fchem.2020.561788*

## INTRODUCTION

The known oscillatory chemical reactions in which peroxo compounds are involved as oxidant include the classical Bray ($H_2O_2$–$IO_3^-$) and Briggs-Rauscher [$H_2O_2$–$IO_3^-$–MA—Mn(II)] reactions, some one-substrate pH-oscillators [$H_2O_2$–$S^{2-}$; $H_2O_2$–$S_2O_3^{2-}$–Cu(II); $H_2O_2$–$S_2O_4^{2-}$; $H_2O_2$–$Fe(CN)_6^{4-}$], a few two-substrate pH-oscillators [$H_2O_2$–$SO_3^{2-}$–$Fe(CN)_6^{4-}$; $H_2O_2$–$SO_3^{2-}$–$S_2O_3^{2-}$; $H_2O_2$–$HSO_3^-$–$HCO_3^-$], the Cu(II) catalyzed $H_2O_2$–$SCN^-$ and $S_2O_8^{2-}$–$S_2O_3^{2-}$ systems, and the Ag(I)-catalyzed $S_2O_8^{2-}$–$S^{2-}$ reaction. Among the listed systems two representative oscillators, the Cu(II)-catalyzed $H_2O_2$–$S_2O_3^{2-}$ (Orbán and Epstein, 1987) and the $H_2O_2$–$SCN^-$ reactions (Orbán, 1986) were selected to test for observing oscillations when the $H_2O_2$ is replaced with $NaBO_3$. In the $H_2O_2$–$S_2O_3^{2-}$–Cu(II) system addition of acid ($H_2SO_4$), in the $H_2O_2$–$SCN^-$–Cu(II) reaction addition of base (NaOH) as auxiliary reagent was also necessary to tune the systems to the oscillatory domain. Both oscillators are highly reproducible, they show wide variety of dynamical phenomena and the main reaction steps in their chemical mechanism are well-established. The $H_2O_2$–$S_2O_3^{2-}$–Cu(II) system represents a typical pH oscillator. In a CSTR it exhibits large amplitude pH and potential oscillations and bistability between high pH (∼9) and low pH (∼5) steady states in a broad range of chemical compositions. The $H_2O_2$–$SCN^-$–Cu(II) reaction displays even richer dynamics. Under flow conditions it shows three types of bistability

involving low and high potential steady states and an oscillatory state. In the oscillatory regime periodic changes appear in the potential of Pt and copper selective electrodes, in the color between yellow and colorless and in the rate of oxygen gas evolution, the pH is high (≥9) and steady. It is a unique feature of the $H_2O_2$–$SCN^-$–Cu(II) system that it oscillates even at zero flow rate, i.e., at batch as well. During batch oscillations, the pH decreases slowly and smoothly. This oscillator has been used in many applications, for example, it is capable to generate oscillatory luminescence by adding luminol (Iranifam et al., 2010), it constituted the basis of analytical determination of many organic compounds present in a trace amount ($<10^{-8}$ M) by following the changes in its oscillatory characteristics due to the interaction between the components of the oscillator and the target species (Jiménez-Prieto et al., 1997), it is also used for demonstration of chemical oscillations in classroom (Pimieta and Micheau, 1999).

The motivation of our work was to extend further the variety of the oscillatory chemical reactions by introducing such oxidant, sodium perborate, which has not been suggested so far to use as key component in giving rise to periodic changes in chemical systems. Beside seeking after non-linear systems, which are novel in composition, their background chemistry and simulation of their dynamical behavior are also subject to discussion in this study.

## MATERIALS AND METHODS

The sodium perborate ($NaBO_3{\cdot}H_2O$, Acros Organics), sodium thiosulfate ($Na_2S_2O_3{\cdot}5H_2O$, Reanal), potassium thiocyanate (KSCN, VWR Chemicals), copper sulfate and nitrate ($CuSO_4{\cdot}5H_2O$, $Cu(NO_3)_2{\cdot}3H_2O$, VWR Chemicals) were available commercially and used without further purification. The $NaBO_3$ content of the solid reagent was analyzed by permanganometry, its purity was 95.0%. For the reaction mixtures used in the experiments four stock solutions were prepared: 0.1 M $NaBO_3{\cdot}H_2O$, 0.1 M $Na_2S_2O_3{\cdot}5H_2O$, 0.1 M KSCN, $4 \times 10^{-2}$ M $CuSO_4{\cdot}5H_2O$. The perborate stock solution was prepared daily. The aqueous solution of perborate undergoes slow decomposition, but its rate is slow and negligible during the time of an experiment, only 5% loss of the oxidation power of the stock solution was measured after 8 hours of its preparation. This stock solution is highly alkaline (pH > 10) due to the hydrolysis of $NaBO_3$. The experiments have been carried out in a double wall glass reactor of $V = 30$ cm$^3$, thermostated at $T = 25°$C, and operated under flow and batch configuration. The reaction vessel was equipped with combined glass electrode (Radelkis OP-0823P) and a combined Pt-calomel electrode (Mettler Toledo). In CSTR (abbreviation of Continuously-fed Stirred Tank Reactor) mode the reactor was fed with the appropriate reagents by a Gilson Minipuls peristaltic pump through four inlet tubes. The constant volume of the reactor content was ensured by removal of the outflow solution through the hole in the cup by another pump which rotated in the opposite direction. The stirring rate of 500 rpm was applied using a Heidolph MR 3000 stirrer. The electrodes were connected to pH-meters (Hanna pH-209). The responses of the electrodes were collected by personal computer through a pH-meter and a 16 bit A/D converter (NI-6010-PCI) with a sampling rate of 2 Hz. In the batch experiments the same experimental setup was used, here the reagents were mixed directly in the reactor dish.

The simulations were performed with the program XPPAUT [XPPAUT 8.0, 2016], by using cvode stiff solver, which based on a backward differentiation formula method. The step size, the absolute and the relative error tolerance were $10^{-2}$, $10^{-15}$, and $10^{-5}$, respectively. The general form of the differential equations used in the CSTR simulations was the following:

$$d[X_i]/dt = \Sigma_j x_{ij} v_j + k_0([X_i]_0 - [X_i])$$

where $[X_i]$ is the concentration of component X in the reactor, $x_{ij}$ is the stoichiometric number of that species in the jth reaction, $k_0$ is a first order rate constant corresponds to the inflow and outflow in a CSTR, and $[X_i]_0$ is the concentration of a component X in the input flow. The calculations of the equilibrium diagram were made by the program Medusa (Medusa).

## RESULTS

Using the procedures described in the Materials and Methods section we were successful with observing periodic responses in both perborate—reductant—Cu(II) systems but the oscillatory concentrations differed significantly from those when $H_2O_2$ was used as oxidant. At this stage of our research we have not intended to establish the complete oscillatory domain and phase diagrams, our aim was just to find "optimum concentrations" and conditions where (and in the vicinity of them) the perborate oxidation takes place in oscillatory manner.

### $BO_3^-$–$S_2O_3^{2-}$–Cu(II) Flow System

In the $BO_3^-$–$S_2O_3^{2-}$–Cu(II) flow system—like in the $H_2O_2$ version—the bistability and oscillations in the pH and in the potential of the Pt vs. calomel electrode pair readily appeared. However, only much lower concentrations of perborate than that of $H_2O_2$ could be tested, due to the poor solubility of $NaBO_3{\cdot}H_2O$ (15 g/dm$^3$ at $T = 20°$C). Besides, much higher input acid had to be introduced into the reaction mixture to partly neutralize the strong alkalinity originated from the hydrolysis of sodium perborate. The oscillatory potential and pH traces vs. time, measured in the perborate—thiosulfate—copper(II) system at an "optimum input concentration" are shown in **Figure 1**.

### $BO_3^-$–$SCN^-$–Cu(II) Batch System

The $BO_3^-$–$SCN^-$–Cu(II) reaction behaved also in oscillatory fashion but it exhibited poorer dynamics compared to the original $H_2O_2$–$SCN^-$–Cu(II) system. Up to now we failed to produce experimentally measured bistabilities or oscillations in CSTR, which were observed in the $H_2O_2$ version. However, our expectation, to find more examples where perborate plays the role of oxidant in oscillatory reaction was fulfilled: in the $BO_3^-$–$SCN^-$–Cu(II) reaction potential oscillations appeared but only under batch condition, and in a pH ≥ 9.5 solutions. The oscillations in the potential of a Pt electrode and the pH vs.

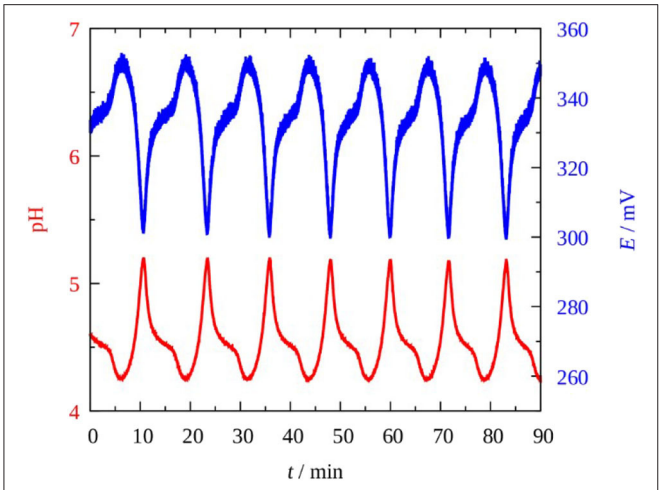


**FIGURE 1 |** pH (red) and potential oscillations in the Pt vs. SCE electrode pair (blue) in the $Cu^{2+}$-catalyzed sodium perborate–sodium thiosulfate CSTR system. $[NaBO_3]_0 = 0.075$ M; $[H_2SO_4]_0 = 0.0375$ M; $[Na_2S_2O_3]_0 = 5 \times 10^{-3}$ M; $[Cu^{2+}]_0 = 5 \times 10^{-5}$ M; $k_0 = 2 \times 10^{-3} s^{-1}$; $T = 25°C$.

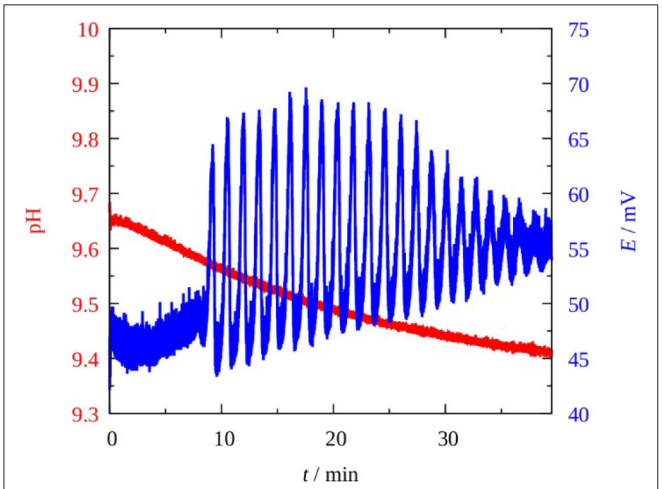


**FIGURE 2 |** Potential oscillations in the Pt vs. SCE electrode pair (blue) and the change in the pH (red) in the $Cu^{2+}$-catalyzed sodium perborate–potassium thiocyanate batch system. $[NaBO_3] = 0.030$ M; $[HCl] = 1.5 \times 10^{-3}$ M; $[KSCN] = 0.025$ M; $[Cu^{2+}] = 10^{-4}$ M; $T = 25°C$.

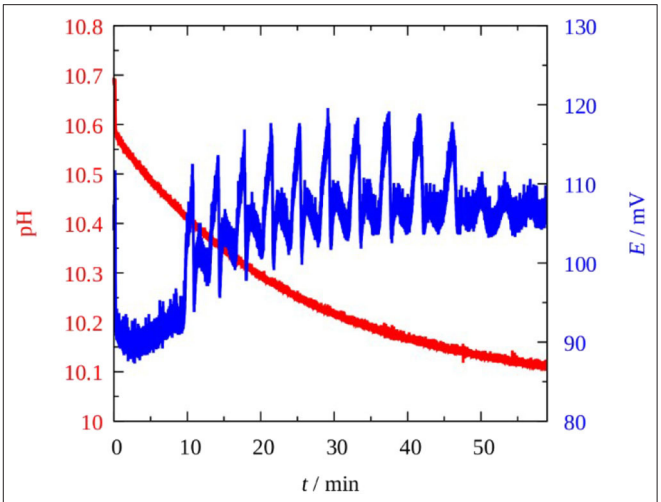


**FIGURE 3 |** Complex potential oscillations in the Pt vs. SCE electrode pair (blue) and the change in the pH (red) in the $Cu^{2+}$-catalyzed sodium perborate–potassium thiocyanate batch system. $[NaBO_3] = 0.010$ M; $[KSCN] = 0.025$ M; $[Cu^{2+}] = 4 \times 10^{-4}$ M; $T = 25°C$.

time traces recorded under batch condition at an "optimum concentration" is shown in **Figures 2**, **3** shows complex type oscillations recorded at lower initial pH and higher [Cu(II)] than used in **Figure 2**. Within a range of concentrations, $[NaBO_3] \sim [KSCN] = 0.005$–$0.05$ M, $[CuSO_4 \cdot 5H_2O] = 5 \times 10^{-5}$–$0.001$ M, generally 10–20 cycles with amplitude of 15–20 mV and period of 5–10 min appear after an induction period of 5–10 min. The pH remains nearly constant ($pH \geq 9.5$), it decreases a few tenth of a unit during a run. The perborate—thiocyanate—Cu(II) mixture is yellow (even without $SCN^-$) due to the formation of copper-peroxo complexes [$HO_2$-Cu(I) and/or $HO_2$-$Cu(OH)_2^-$] between the catalyst and superoxo radicals ($HO_2^{\cdot}$, $OH^{\cdot}$, $O_2^{\cdot -}$) which are involved in the mechanism of the peroxide oxidation reactions. The highly intense yellow color (absorption coefficient $\varepsilon > 1{,}600$ $M^{-1}cm^{-1}$ at $\lambda = 345$ nm) may cover up the color oscillations if there are any. The potential oscillations are accompanied with $O_2$ evolution and with formation of a brown compound which is supposed to be a ring structured dimer of the copper peroxide (Luo et al., 1988). The reaction mixture becomes colorless when the oscillatory state terminates and the precipitate settles. A slow sigmoidal increase in the potential indicates that the reaction between $BO_3^-$ and $SCN^-$ still proceeds and by analogy of the reaction between $H_2O_2$ and $SCN^-$ the following brutto stoichiometry is supposed to prevail (Wilson and Harris, 1961):

$$4\,BO_3^- + SCN^- + 3\,H_2O \rightarrow 4\,BO_2^- + HSO_4^- + HCO_3^- + NH_4^+$$

Among the products (using copper nitrate as catalyst), the presence of $SO_4^{2-}$ (with $Ba^{2+}$) and that of $NH_4^+$ (with Nessler reagent) could be detected.

## NUMERICAL SIMULATIONS

To clarify the role of the perborate species in these oscillatory systems we performed numerical simulations. It is well-established that below pH = 7 perborate species are not stable, therefore in acid solution the active oxidant is hydrogen peroxide. Obviously, the mechanisms of these perborate oscillators must include the corresponding hydrogen peroxide chemistry. The question, what we address here is the following: do the perborate species contribute substantially to the development of the oscillations or the dynamics is mainly governed by the reactions of hydrogen peroxide? According to the literature between pH = 8 and 12 the kinetic effect of the existing different perborate species can be significant (Burgess and Hubbard,

2013). Independent studies indicate that $(HO)_2B(OOH)$ is unreactive while the analogous reactions of $(HO)_3B(OOH)^-$ and $(HO)_2B(OOH)_2^-$ anions are much faster than that of the $H_2O_2$ (Davies et al., 2005; Lobachev et al., 2016). The equilibrium distribution of the different perborate species in a perborate solution, which in acidic medium is a 1:1 mixture of $H_3BO_3$ and $H_2O_2$, as function of pH (**Figure 4**) was calculated by following the paper of Pizer and Tihal (1987). In the calculation all relevant equilibrium processes, R4, R5, R9, R10, R11 reactions (**Tables 1**, **2**), and the formation of $(HO)_2B(OOH)$ in reaction R16 (Pizer and Tihal, 1987), were considered.

$$H_3BO_3 + H_2O_2 \rightleftharpoons (HO)_2B(OOH) + H_2O \; K_{16} = 0.01 \; M^{-1} \; R16$$

The result clearly shows that in the range of pH = 8–12 $(HO)_3B(OOH)^-$ is the dominant form of perborate but $(HO)_2B(OOH)_2^-$ also exists in a relatively high ratio. As the concentration of $(HO)_3B(OOH)^-$ in this pH range is larger than that of the hydrogen peroxide, it is likely that its kinetic role is not negligible.

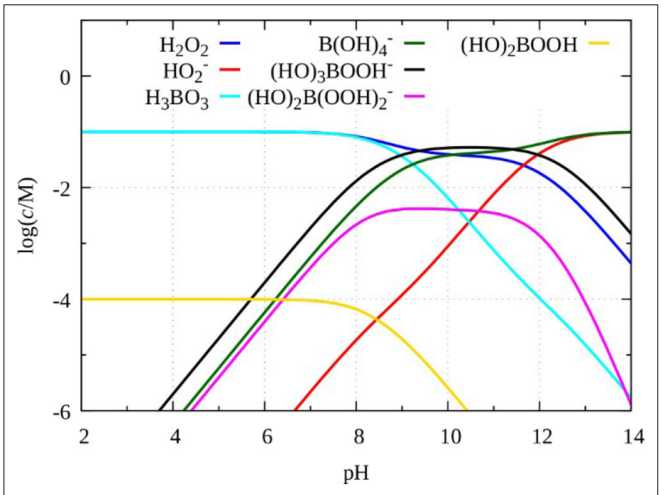


**FIGURE 4 |** Species distribution in a mixture of 0.1 mol/dm$^3$ boric acid and 0.1 mol/dm$^3$ $H_2O_2$ calculated by using reactions R4, R5, R9, R10, R11, and R16.

## $BO_3^-$–$S_2O_3^{2-}$–Cu(II) Flow System

As a starting point we used the model of the $H_2O_2$–$S_2O_3^{2-}$–Cu(II) flow system published by Jedrusiak et al. (2017) recently, which an extended version of the original mechanism proposed by Kurin-Csörgei et al. (1996). This model consists of 8 reactions and 9 variables (**Table 1**) which is capable of simulating not only the pH oscillations but the time evolution of the concentration of the copper(II) and copper(I) species in the form of thiosulfate complexes. We extended this model with the formation and the oxidation reactions of $(HO)_3B(OOH)^-$ and $(HO)_2B(OOH)_2^-$ (**Table 2**). Reactions R12–R15 describe the catalytic effect of the perborate species on reactions R1 and R2, but at the moment we have no direct kinetic information about these reactions. As a first assumption we applied similar rate laws for these catalytic reactions like that of R1 and R2, but the rate constants are multiplied by a dimensionless factor $f_{cat}$. We also assume that the reactivity of $(HO)_3B(OOH)^-$ and $(HO)_2B(OOH)_2^-$ are the same, therefore we apply identical rate constants for reactions R12 and R14.

To clarify the potential role of $(HO)_3B(OOH)^-$ and $(HO)_2B(OOH)_2^-$ in the dynamics of the system, we calculated a bifurcation diagram by varying the value of $f_{cat}$. As it is presented in **Figure 5A** oscillations develop above a critical value of $f_{cat}$, that is about 200, with a finite amplitude through a subcritical bifurcation. It is important to point out that at $f_{cat}$= 0, that means hydrogen peroxide solely governs the system, the model does not show oscillations, at the conditions corresponding to the experiments presented here. This result confirms not only that the catalytic effect of the perborate species has a significant contribution in the development of oscillations, but this effect must be large enough. Typical concentration oscillations of $H^+$ and $(HO)_3B(OOH)^-$ are shown in **Figure 5B**. The amplitude in pH and the period is in good agreement with the experimental observations.

**TABLE 1 |** Model of the $H_2O_2$–$S_2O_3^{2-}$–Cu(II) system.

| Step | Reaction | Reaction rate | Rate constant |
|---|---|---|---|
| R1 | $H_2O_2 + S_2O_3^{2-} \rightarrow HOS_2O_3^- + OH^-$ | $v_1 = k_1[H_2O_2][S_2O_3{}^{2-}] + k_1'[H_2O_2][S_2O_3{}^{2-}][OH^-][Cu^{2+}]_T$ | $k_1 = 0.019 \; M^{-1} \; s^{-1}$<br>$k_1' = 3{\cdot}10^8 \; M^{-3} \; s^{-1}$ |
| R2 | $3H_2O_2 + HOS_2O_3^- \rightarrow 2SO_4^{2-} + 3H^+ + 2H_2O$ | $v_2 = k_2[H_2O_2][HOS_2O_3^-]$ | $k_2 = 0.6 \; M^{-1} \; s^{-1}$ |
| R3 | $S_2O_3^{2-} + HOS_2O_3^- \rightarrow S_4O_6^{2-} + OH^-$ | $v_3 = k_3[S_2O_3{}^{2-}][HOS_2O_3^-]$ | $k_3 = 60 \; M^{-1} \; s^{-1}$ |
| R4 | $H_2O \rightleftharpoons OH^- + H^+$ | $v_4 = k_4[H_2O] - k_{-4}[OH^-][H^+]$ | $k_4[H_2O] = 10^{-3} \; M \; s^{-1}$<br>$k_{-4} = 1.8{\cdot}10^{11} \; M^{-1} \; s^{-1}$ |
| R5 | $H_2O_2 \rightleftharpoons HO_2^- + H^+$ | $v_5 = k_5[H_2O_2] - k_{-5}[HO_2^-][H^+]$ | $k_5 = 2.2{\cdot}10^{-2} \; s^{-1}$<br>$k_{-5} = 1.6{\cdot}10^{10} \; M^{-1} \; s^{-1}$ |
| R6 | $H_2O_2 + 2Cu(S_2O_3)_2^{3-} + 2H^+ \rightarrow 2Cu(S_2O_3)_2^{2-} + 2H_2O$ | $v_6 = k_6[H_2O_2][Cu(S_2O_3)_2^{3-}][H^+]^2$ | $k_6 = 10^{14} \; M^{-1} \; s^{-1}$ |
| R7 | $S_2O_3^{2-} + Cu(S_2O_3)_2^{2-} \rightarrow Cu(S_2O_3)_2^{3-} + S_2O_3^-$ | $v_7 = k_7[S_2O_3{}^{2-}][Cu(S_2O_3)_2^{2-}]$ | $k_7 = 10^{10} \; M^{-1} \; s^{-1}$ |
| R8 | $2S_2O_3^- \rightarrow S_4O_6^{2-}$ | $v_8 = k_8[S_2O_3^-]^2$ | $k_8 = 10^4 \; M^{-1} \; s^{-1}$ |

*Here* $[Cu^{2+}]_T = [Cu(S_2O_3)_2^{3-}] + [Cu(S_2O_3)_2^{2-}]$.

**TABLE 2 |** Reactions of the boron species related to the $H_2O_2$–$S_2O_3^{2-}$–Cu(II) system.

| Step | Reaction | Reaction rate | Rate constant |
|---|---|---|---|
| R9 | $H_3BO_3 + H_2O \rightleftharpoons B(OH)_4^- + H^+$ | $v_9 = k_9[H_3BO_3] - k_{-9}[B(OH)_4^-][H^+]$ | $k_9 = 0.575\ s^{-1}$<br>$k_{-9} = 10^9\ M^{-1}\ s^{-1}$ |
| R10 | $H_3BO_3 + H_2O_2 \rightleftharpoons (HO)_3B(OOH)^- + H^+$ | $v_{10} = k_{10}[H_3BO_3][H_2O_2] - k_{-10}[(HO)_3B(OOH)^-][H^+]$ | $k_{10} = 0.20\ M^{-1}\ s^{-1}$<br>$k_{-10} = 10^9\ M^{-1}\ s^{-1}$ |
| R11 | $(HO)_3B(OOH)^- + H_2O_2 \rightleftharpoons (HO)_2B(OOH)_2^- + H_2O$ | $v_{11} = k_{11}[(HO)_3B(OOH)^-][H_2O_2] - k_{-11}[(HO)_2B(OOH)_2^-]$ | $k_{11} = 2{\cdot}10^9\ M^{-1}\ s^{-1}$<br>$k_{-11} = 10^9\ s^{-1}$ |
| R12 | $(HO)_3B(OOH)^- + S_2O_3^{2-} + H_2O = HOS_2O_3^- + 2OH^- + H_3BO_3$ | $v_{12} = f_{cat}k_1[(HO)_3B(OOH)^-][S_2O_3{}^{2-}] + f_{cat}k_1'[(HO)_3B(OOH)^-][S_2O_3{}^{2-}][OH^-][Cu^{2+}]_T$ | $f_{cat}$ adjustable |
| R13 | $3(HO)_3B(OOH)^- + HOS_2O_3^- = 2SO_4^{2-} + 3H_3BO_3 + 2H_2O$ | $v_{13} = f_{cat}k_2[(HO)_3B(OOH)^-][HOS_2O_3^-]$ | $f_{cat}$ adjustable |
| R14 | $(HO)_2B(OOH)_2^- + S_2O_3^{2-} + H_2O = HOS_2O_3^- + OH^- + (HO)_3B(OOH)^-$ | $v_{14} = f_{cat}k_1[(HO)_2B(OOH)_2^-][S_2O_3{}^{2-}] + f_{cat}k_1'[(HO)_2B(OOH)_2^-][S_2O_3{}^{2-}][OH^-][Cu^{2+}]_T$ | $f_{cat2}$ adjustable |
| R15 | $3(HO)_2B(OOH)_2^- + HOS_2O_3^- + H_2O = 2SO_4^{2-} + 3(HO)_3B(OOH)^- + 3H^+$ | $v_{15} = f_{cat}k_2[(HO)_2B(OOH)_2^-][HOS_2O_3^-]$ | $f_{cat}$ adjustable |

*Here $k_1$, $k_1'$,$k_2$ refer to* ***Table 1****.*

## $BO_3^-$–$SCN^-$–Cu(II) Batch System

A detailed mechanism of the $H_2O_2$–$SCN^-$–Cu(II) oscillatory reaction was published by Luo et al. (1989), which consists of 30 reactions and 26 variables and many estimated rate constants. The extension of this model with the assumed reactions of the perborate species would result in a poorly defined mechanism, since we have no direct kinetic data about these reactions. To obtain information about the effect of the replacement of $H_2O_2$ by perborate, we decided to use a recently published simple five variables core model (**Table 3**), which was deduced from the original one by Wiśniewski et al. (2015). In this model the concentration of the oxidant, that is $H_2O_2$, is a constant parameter. When we apply this model for the perborate oscillator, we assume that there are at least two oxidants, hydrogen peroxide and one of the perborate species.

According to the experiments there are some significant differences between the applied conditions in the $H_2O_2$–$SCN^-$–Cu(II) and in the $HBO_3$–$SCN^-$–Cu(II) systems, which are the followings: (1) while the typical concentration of $H_2O_2$ is in the range of 0.1–0.5 M (Orbán, 1986), that of the perborate is in between 0.005 and 0.06 M; (2) the pH of the reacting medium is in between 10 and 11 in case of $H_2O_2$ but it is rather between 9 and 10 in the perborate system.

In the model the concentration of oxidant affects the rates of reactions RI and RIII. We found that, the dynamics of the model is quite insensitive to the variation of the rate of RI, as oscillations can be found at very low concentration of the oxidant, e.g., at $10^{-6}$ M. Therefore, we focused on reactions R3, where the oxidant in the original model is $HO_2^-$, which has relatively high concentration, e.g., 0.03–0.04 M, at the usual conditions of the original $H_2O_2$–$SCN^-$–Cu(II) oscillatory reaction. However, when perborate is applied at the lower pH as it is in the experiments, the estimated concentration of $HO_2^-$ significantly lowers. Equilibrium calculations with total perborate concentration 0.005–0.06 M by using R4, R5, R9, R10, R11, and R16 show that concentration of $HO_2^-$ drops to $10^{-4}$ M or even below. Consequently, the rate constant of RIII must be also decreased by the same factor, that is about 200, if only $HO_2^-$ is considered as effective oxidant in this process. The value of $k_{III}$ which fits to the actual concentration of $HO_2^-$ is around $5{\cdot}10^3$ $M^{-1}\ s^{-1}$. **Figure 6** represents a bifurcation diagram as the value of $k_{III}$ is varied. The oscillations (**Figure 7**) appear through a supercritical Hopf bifurcations at $k_{III} = 1.84{\cdot}10^4\ M^{-1}\ s^{-1}$, that is 50 times smaller than the value expected for the case when solely $HO_2^-$ is the oxidant. We concluded that in the perborate system $HO_2^-$ itself as an oxidant cannot support the development of oscillations, because process RIII would be too slow. Therefore, we assume that the different perborate species [$(HO)_3B(OOH)^-$ and $(HO)_2B(OOH)_2^-$] are involved as oxidant in this process. The role of the perborate species in this compound reaction is likely to react with $Cu(OH)_2$ to produce $Cu(OH)_3$ and $HO_2Cu(OH)_2^-$.

## DISCUSSION

The question may be raised whether the oscillations that appear in the perborate oxidations represent a new subgroup among the known chemical periodic reactions or if they are simply $H_2O_2$-based oscillators assisted by borate chemistry. To approach this question the species, their reactivity and the equilibria in which they are involved should be considered. Deary et al. (2013) listed more than a dozen of species and equilibria that may exist in a mixture of $H_2O_2$ and boric acid at different pHs. The general chemical formula of sodium perborate is $NaBO_3{\cdot}nH_2O$ ($n = 1, 2, 4$). It is often presumed to be a stabilized form of $H_2O_2$ because it functions like $H_2O_2$ does in many practical applications. However, the sodium perborate is not just an adduct of $H_2O_2$ with tetraborate like e.g., sodium percarbonate ($2\ Na_2CO_3{\cdot}3\ H_2O_2$) or urea peroxide ($CO(NH_2)_2{\cdot}H_2O_2$). In its aqueous solution, which is highly alkaline (pH $\sim$ 11) the perborate is present in a form of dimer anion $B_2O_4(OH)_4^{2-}$ (diperoxoborate) in which the two boron atoms are bound by two peroxide groups. In the perborate oxidation reactions, the diperoxo form releases $H_2O_2$ and $B(OH)_4^-$ or $H_3BO_3$ and depending on the pH different species (shown already in **Figure 4**) play the key

role in the oxidation process. At the high pH range (pH = 8–11) the reactive $(HO)_2B(OOH)_2^-$ and $(HO)_3B(OOH)^-$ anions are the major oxidant. At medium pHs the peroxoborates exist in equilibrium with $H_2O_2$, $B(OH)_4^-$ or $H_3BO_3$,

$$(HO)_3B(OOH)^- + H_2O \leftrightarrow H_2O_2 + B(OH)_4^- \text{ or}$$
$$(HO)_3B(OOH)^- + H_2O \leftrightarrow H_2O_2 + H_3BO_3 + OH^-$$

here the perborates oxidize along with $H_2O_2$. In the acidic pH-range the equilibrium is completely shifted toward the formation of $H_2O_2$ and $H_3BO_3$ and the perborate reacts like $H_2O_2$. One of our plans is to use perborate in acidic environment. Here the perborate would function as reductant, like the $H_2O_2$ acts in the $KMnO_4$–$H_2O_2$–$H_3PO_4$ oscillatory reaction (Nagy and Treindl, 1989).

A chemical background that prevails in the perborate oscillators is assumed to resemble pretty much to the processes which dominate in the analogous $H_2O_2$–$S_2O_3^{2-}$/$SCN^-$–Cu(II) oscillators. The role and effect of the copper (II) catalyst is obviously similar in each system: the Cu(II) oxidizes the sulfur component and it is reduced to copper(I), what is temporarily stabilized by the reductant or its intermediate, then the Cu(I), being unstable in this oxidation state, is reoxidized to Cu(II) by the oxidant. Adding ligand which forms complex with copper ions influences this catalytic cycle. EDTA prevents to bring about oscillations in a mixture of oscillatory composition due to its

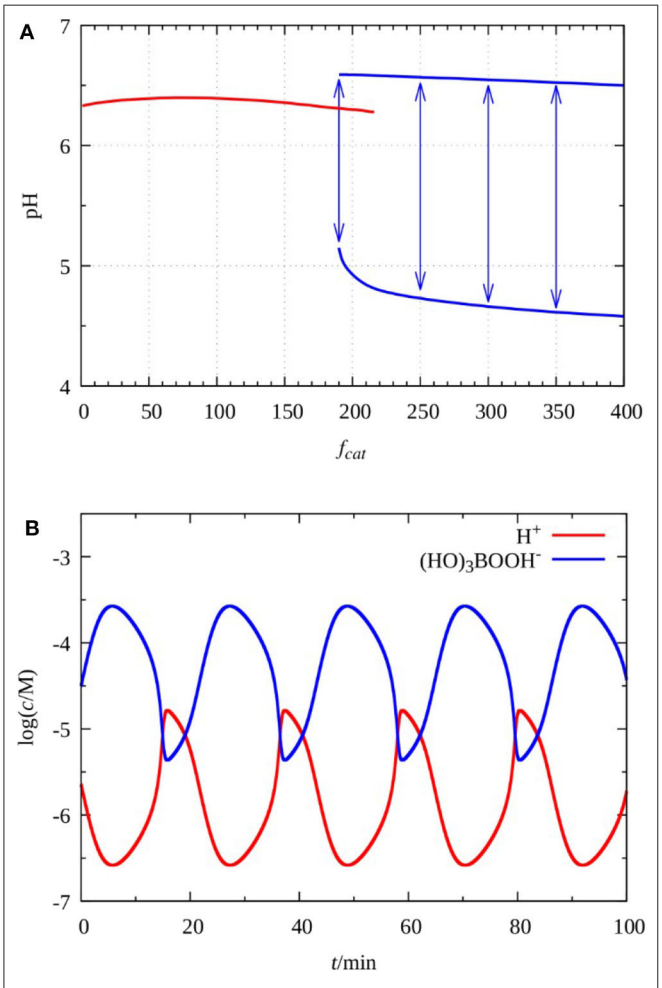


**FIGURE 5 |** Simulated bifurcations diagram as a function of parameter $f_{cat}$. The arrows indicates the amplitude of oscillations **(A)** and oscillations in the concentration of $H^+$ and $(HO)_3B(OOH)^-$ at $f_{cat}$= 220 **(B)**. The parameters of the simulations $k_0 = 0.002\ s^{-1}$, $[S_2O_3^{2-}]_0 = 0.01$ M, $[(HO)_3B(OOH)^-]_0 = 0.062$ M, $[Cu^{2+}]_T = 1.5 \times 10^{-5}$ M, $[H^+]_0 = 0.066$ M.

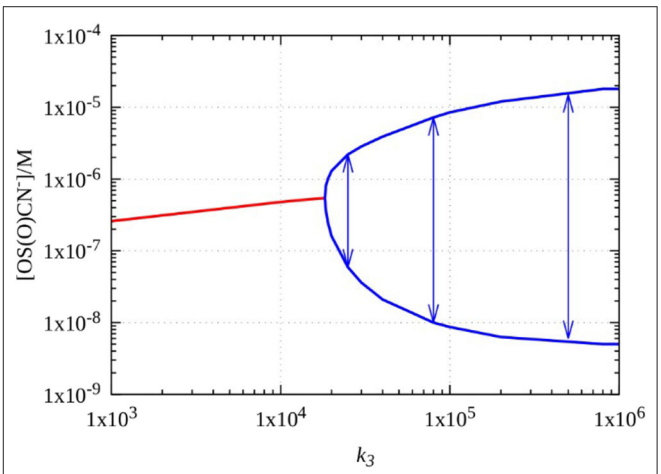


**FIGURE 6 |** Simulated bifurcations diagram of the five variables model of the $H_2O_2$–$SCN^-$–Cu(II) reaction as a function of parameter $k_{III}$, the arrows indicates the amplitude of oscillations.

**TABLE 3 |** The five variables model of the $H_2O_2$–$SCN^-$–Cu(II) system (Wiśniewski et al., 2015).

| Step | Reaction | Reaction rate | Rate constant |
|---|---|---|---|
| RI | $2H_2O_2 + SCN^- \rightarrow$ **OS(O)CN$^-$** $+ 2H_2O$ | $v_I = k_I[H_2O_2][SCN^-]$ | $k_I = 1.33{\cdot}10^{-7}\ M^{-1}\ s^{-1}$ |
| RII | $OOS(O)CN^-$ **+ OS(O)CN$^-$** $+ H_2O \rightleftharpoons$ **2OS(O)CN$^{\cdot}$** $+ 2OH^-$ | $v_{II} = k_{II}$**[OS(O)CN$^-$]** $- k_{-II}$**[OS(O)CN$^{\cdot}$]**$^2$ | $k_{II} = 5{\cdot}10^{-2}\ s^{-1}$<br>$k_{-II} = 4{\cdot}10^6\ M^{-1}\ s^{-1}$ |
| RIII | **$Cu(SCN)_2^-$** $+$ **OS(O)CN$^{\cdot}$** $+ HO_2^{\cdot} + 2OH^{\cdot} \rightarrow$ **OS(O)CN$^-$** $+$ **$HO_2Cu(OH)_2^-$** $+ 2SCN^-$ | $v_{III} = k_{III}$**[$Cu(SCN)_2^-$][OS(O)CN$^{\cdot}$]** | $k_{III} = 1{\cdot}10^6\ M^{-1}\ s^{-1}$ |
| RIV | **$HO_2Cu(OH)_2^-$** $+ 2SCN^- \rightarrow$ **$Cu(SCN)_2^-$** $+$ **$HO_2^{\cdot}$** $+ 2OH^{\cdot}$ | $v_{IV} = k_{IV}$**[$HO_2Cu(OH)_2^-$]** | $k_{IV} = 6{\cdot}10^3\ M^{-1}\ s^{-1}$ |
| RV | **$2HO_2^{\cdot} \rightarrow H_2O_2 + O_2$** | $v_V = k_V$**[$HO_2^{\cdot}$]**$^2$ | $k_V = 2{\cdot}10^2\ M^{-1}\ s^{-1}$ |

*The variables are:* **$OS(O)CN^-$**, **$Cu(SCN)_2^-$**, **$OS(O)CN^{\cdot}$**, **$HO_2Cu(OH)_2^-$**, **$HO_2^{\cdot}$**. *The concentrations of the other reactants ($H_2O_2$, $SCN^-$, $H_2O$, $OOS(O)CN^-$, $OH^-$, $HO_2^-$) are constant. The initial concentrations used in the simulations are: $[H_2O_2][SCN^-] = 0.075$ M, [**$OS(O)CN^-$**] $= 10^{-8}$ M, [**$Cu(SCN)_2^-$**] $= 10^{-4}$ M, [**$OS(O)CN^{\cdot}$**] $= 10^{-8}$ M, [**$HO_2Cu(OH)_2^-$**] $= 10^{-8}$ M, [**$HO_2^{\cdot}$**] $= 10^{-8}$ M.*

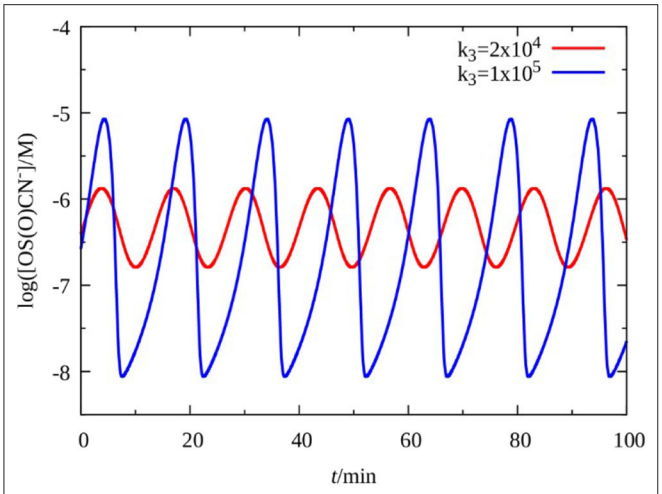


**FIGURE 7 |** Simulated oscillations in the five variables model of the $H_2O_2$–$SCN^-$–Cu(II) reaction as a function of parameter $k_3$.

high affinity to bind Cu(II) in a stable complex. In presence of $NH_4OH$, however, when the rate of reduction of copper (II) is much slower than in its absence (Byerley et al., 1973), the duration of the oscillatory phase and the number of oscillations significantly increased. Exclusive role of $Cu^{2+}$ as catalyst is shown by the fact, that when it was replaced with $Ag^+$, $Ni^{2+}$, $Co^{2+}$, or $Fe^{2+}$ oscillations were not observed.

As far as the mechanistic description is concerned most steps may be identical in the $H_2O_2$ and $BO_3^-$ oscillators. The analogous initial steps in the oxidation of $S_2O_3^{2-}$ or $SCN^-$ by $H_2O_2$ and $BO_3^-$ are expressed in Equations (1)–(4):

$$H_2O_2 + S_2O_3^{2-} \rightarrow HOS_2O_3^- + OH^- \quad (1)$$

$$BO_3^- + S_2O_3^{2-} + H_2O \rightarrow HOS_2O_3^- + BO_2^- + OH^- \quad (2)$$

$$H_2O_2 + SCN^- \rightarrow OSCN^- + H_2O \quad (3)$$

$$BO_3^- + SCN^- \rightarrow OSCN^- + BO_2^- \quad (4)$$

In the formation of $HOS_2O_3^-$ and $OSCN^-$ in Equations (2) and (4) a monocyclic three membered peroxide intermediate, called dioxaborirane $[(HO)_2BOO^-]$ which forms from $(HO)_3B(OOH)^-$ by losing one $H_2O$ was proposed to act as most reactive species (Deary et al., 2013):

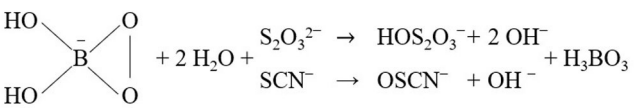


Further steps in the oxidation of $HOS_2O_3^-$ and $OSCN^-$ intermediates are assessed to proceed through the reactions listed in **Table 1**, R1—R8 and in **Table 3**, RI—RV. In the systems where the reductant is $S_2O_3^{2-}$, the intermediate $HOS_2O_3^-$ formed in steps (1) or (2) undergoes two-way reaction (catalyzed by $Cu(II)(S_2O_3)_2^{2-}/Cu(I)(S_2O_3)_2^{3-}$) according to R2 and R3 in **Table 1**. Step R2 produces, while step R3 consumes $H^+$ with a time-lag between them which results in oscillations in pH. When the substrate in the oscillators is $SCN^-$, the oxidation of $OSCN^-$ formed in Equation (3) or (4) takes place through reactions RI—RV in **Table 3**, The positive feedback, which one of the preconditions for oscillations to occur, is involved in RII + RIII.

The reactions of the boron species related to the $H_2O_2$–$S_2O_3^{2-}$–Cu(II) oscillatory systems are shown in **Table 2**, where the participation of the dominant boron intermediate $(HO)_3B(OOH)^-$ and its role in the oscillatory mechanism are clearly demonstrated.

## CONCLUSIONS

It is customary to categorize the known chemical oscillatory reactions into groups or families. The groups are usually named after the major component which is present in each member and which plays key role in bringing about periodic behavior in its reactions with appropriate partners. Up to now we have distinguished $BrO_3^-$, $BrO_2^-$, $ClO_2^-$, $IO_3^-$, $IO_4^-$, $MnO_4^-$, $S_2O_8^{2-}$, and $H_2O_2$-based oscillators with many variants in each class. All listed components function as powerful oxidant and each contains an element that possesses multiple oxidation states.

In this report we have demonstrated that sodium perborate ($NaBO_3 \cdot H_2O$), similarly to some oxyhalogens, permanganate or peroxides, can also be used as major reactant in constructing oscillatory reactions. It was proven by the successful replacement of $H_2O_2$ with $NaBO_3$ which resulted in the extension of the number of chemical oscillators with two members: the $BO_3^-$–$S_2O_3^{2-}$–Cu(II) and the $BO_3^-$–$SCN^-$–Cu(II) systems. Our associated experimental and numerical results show that this is not a simple replacement of the oxidant, but the development of oscillations is supported by the catalytic effect of borate on peroxide chemistry. pH oscillators are often applied as a source of periodic driving force to initiate rhythmic changes, motions or deformations in different physico-chemical systems. A new variant, like the $BO_3^-$–$S_2O_3^{2-}$–Cu(II) system, may open some new possibilities in this direction. To approach this goal we intend to improve the perborate-based oscillators. Attempts will be made to find experimental conditions under which pH-oscillations of higher amplitude than were measured earlier, would appear. However, use of higher initial concentrations to enhance the pH-oscillations is hampered by the low solubility of $NaBO_3 \cdot H_2O$. The solubility problem may be to overcome by adding short polyols (1.2-propylene diol, ethylene glycol, glycerol, sorbitol, etc.) to the oscillatory mixture, which increases significantly the solubility of perborate due to the formation of perborate-polyol complex. We do not expect serious interference between the polyols and the main components $BO_3^-$ and $S_2O_3^{2-}$ but if reduction of the Cu(II) catalyst by the polyol takes place, oscillations may not occur in the combined system. If our efforts are successful, phase diagrams in different parameter spaces will be established.

The non-linearity originates from the peroxo group present in both oxidants, therefore the set of reaction which produces the oscillatory dynamics may be partly similar

or even identical in both $BO_3^-$ and $H_2O_2$ oscillators. In the taxonomy of the liquid phase chemical oscillators the systems based on the Cu(II)-catalyzed perborate oxidation of $S_2O_3^{2-}$ and $SCN^-$ can be referred to as borate-assisted peroxide oscillators.

## DATA AVAILABILITY STATEMENT

The original contributions presented in the study are included in the article/supplementary material, further inquiries can be directed to the corresponding authors.

## AUTHOR CONTRIBUTIONS

KK-C, EP-T, and MO performed the experiments. IM and IS made the numerical simulations. KK-C, MO, and IS wrote the manuscript. MO supervised the whole project. All authors revised and checked the draft. All authors contributed to the article and approved the submitted version.

## FUNDING

The authors thank the support of the National Research Development and Innovation Fund (119360).

## REFERENCES

Burgess, J., and Hubbard, C. D. (2013). "Chapter six - catalysis or convenience? perborate in context," in *Advances in Inorganic Chemistry*, eds R. van Eldik and C. D. Hubbard (Cambridge, MA: Academic Press), 217–310. doi: 10.1016/B978-0-12-404582-8.00006-7

Byerley, J. J., Fouda, S. A., and Rempel, G. L. (1973). Kinetics and mechanism of the oxidation of thiosulphate ions by copper(II) ions in aqueous ammonia solution. *J. Chem. Soc. Dalton Trans.* 8, 889–893. doi: 10.1039/dt9730000889

Davies, D. M., Deary, M. E., Quill, K., and Smith, R. A. (2005). Borate-catalyzed reactions of hydrogen peroxide: kinetics and mechanism of the oxidation of organic sulfides by peroxoborates. *Chem. Eur. J.* 11, 3552–3558. doi: 10.1002/chem.200401209

Deary, M. E., Durrant, M. C., and Davies, D. M. (2013). A kinetic and theoretical study of the borate catalysed reactions of hydrogen peroxide: the role of dioxaborirane as the catalytic intermediate for a wide range of substrates. *Org. Biomol. Chem.* 11, 309–317. doi: 10.1039/C2OB26842F

Iranifam, M., Segundo, M. A., Santos, J. L. M., Lima, J. L. F. C., and Sorouraddin, M. H. (2010). Oscillating chemiluminescence systems: state of the art. *Luminescence* 25, 409–418. doi: 10.1002/bio.1203

Jedrusiak, M., Matyszczak, G., and Orlik, M. (2017). On the phase shifts in the dynamics of the $H_2O_2$ –$Na_2S_2O_3$ – $H_2SO_4$ – $CuSO_4$ oscillator revealed by comparison of potentiometric responses of different indicator electrodes. *Int. J. Chem. Kinet.* 49, 250–258. doi: 10.1002/kin.21071

Jiménez-Prieto, R., Silva, M., and Pérez-Bendito, D. (1997). Application of oscillating reaction-based determinations to the analysis of real samples. *Analyst* 122, 287–292. doi: 10.1039/a606506f

Kurin-Csörgei, K., Orbán, M., Rábai, G., and Epstein, I. R. (1996). Model for the oscillatory reaction between hydrogen peroxide and thiosulfate catalysed by copper(II) ions. *J. Chem. Soc. Faraday Trans.* 92, 2851–2855. doi: 10.1039/FT9969202851

Lobachev, V. L., Dyatlenko, L. M., and Zubritskii, M. Y. (2016). Kinetics and mechanism of diethyl sulfide oxidation by sodium peroxoborate in aqueous solutions. *Kinet. Catal.* 57, 742–749. doi: 10.1134/S0023158416060094

Luo, Y., Kustin, K., and Epstein, I. R. (1988). Systematic design of chemical oscillators. 44. Kinetics and mechanism of hydrogen peroxide decomposition catalyzed by $Cu^{2+}$ in alkaline solution. *Inorg. Chem.* 27, 2489–2496. doi: 10.1021/ic00287a023

Luo, Y., Orbán, M., Kustin, K., and Epstein, I. R. (1989). Mechanistic study of oscillations and bistability in the copper(II)-catalyzed reaction between hydrogen peroxide and potassium thiocyanate. *J. Am. Chem. Soc.* 111, 4541–4548. doi: 10.1021/ja00195a001

Medusa Available online at: https://www.kth.se/che/medusa/downloads-1.386254 (accessed March 22, 2020).

Nagy, A., and Treindl, L. (1989). Design of a permanganate chemical oscillator with hydrogen peroxide. *J. Phys. Chem.* 93, 2807–2810. doi: 10.1021/j100344a022

Orbán, M. (1986). Oscillations and bistability in the copper(II)-catalyzed reaction between hydrogen peroxide and potassium thiocyanate. *J. Am. Chem. Soc.* 108, 6893–6898. doi: 10.1021/ja00282a009

Orbán, M., and Epstein, I. R. (1987). Systematic design of chemical oscillators. 39. Chemical oscillators in group VIA: the copper(II)-catalyzed reaction between hydrogen peroxide and thiosulfate ion. *J. Am. Chem. Soc.* 109, 101–106. doi: 10.1021/ja00235a017

Pimieta, V., and Micheau, J. C. (1999). Pedagogic interest of the $H_2O_2$, $Cu^{2+}$, $SCN^-$, $OH^-$ oscillatory reaction. *Chem. Educ.* 4, 206–210. doi: 10.1007/s00897990336a

Pizer, R., and Tihal, C. (1987). Peroxoborates. Interaction of boric acid and hydrogen peroxide in aqueous solution. *Inorg. Chem.* 26, 3639–3642. doi: 10.1021/ic00268a046

Wilson, I. R., and Harris, G. M. (1961). The oxidation of thiocyanate ion by hydrogen peroxide. II. The acid-catalyzed reaction. *J. Am. Chem. Soc.* 83, 286–289. doi: 10.1021/ja01463a007

Wiśniewski, A., Jedrusiak, M., Mojzych, I., and Orlik, M. (2015). Model calculations and experimental studies as a route toward simplification of the kinetic mechanism of the $H_2O_2$-NaSCN – NaOH – $CuSO_4$ homogeneous oscillator. *Int. J. Chem. Kinet.* 47, 671–683. doi: 10.1002/kin.20940

XPPAUT 8.0 (2016). Available online at: http://www.math.pitt.edu/~bard/xpp/xpp.html (accessed March 22, 2020).

**Conflict of Interest:** The reviewer JH declared a past co-authorship with one of the authors IS to the handling editor.

The remaining authors declare that the research was conducted in the absence of any commercial or financial relationships that could be construed as a potential conflict of interest.

*Copyright © 2020 Kurin-Csörgei, Poros-Tarcali, Molnár, Orbán and Szalai. This is an open-access article distributed under the terms of the Creative Commons Attribution License (CC BY). The use, distribution or reproduction in other forums is permitted, provided the original author(s) and the copyright owner(s) are credited and that the original publication in this journal is cited, in accordance with accepted academic practice. No use, distribution or reproduction is permitted which does not comply with these terms.*

frontiers in Chemistry

ORIGINAL RESEARCH
published: 23 October 2020
doi: 10.3389/fchem.2020.583165

# Chemical Oscillation and Morphological Oscillation in Catalyst-Embedded Lyotropic Liquid Crystalline Gels

*Guanying Li, William Cortes, Qizheng Zhang and Ye Zhang**

*Bioinspired Soft Matter Unit, Okinawa Institute of Science and Technology Graduate University, Okinawa, Japan*

Liquid crystalline gels offer promising means in generating smart materials due to programmable mechanics and reversible shape changes in response to external stimuli. We demonstrate a simple and convenient method of constructing catalyst-embedded lyotropic liquid crystalline (LLC) gels and achieve chemomechanical oscillator by converting chemical waves in Belousov–Zhabotinsky (BZ) reaction. We observe the directed chemical oscillations on LLC sticks accompanied by small-scale oscillatory swellings–shrinkages that are synchronized with the chemical waves of an LLC stick. To amplify the mechanical oscillations, we further fabricate small LLC fibers and achieve macroscopically oscillatory bending–unbending transition of the LLC fiber driven by a BZ reaction.

**Keywords: belousov-zhabotinsky reaction, lyotropic liquid crystalline gels, non-covalent catalyst-embedment, chemical oscillation, morphological oscillation**

OPEN ACCESS

***Edited by:***
*Irving Robert Epstein,*
*Brandeis University, United States*

***Reviewed by:***
*Seth Fraden,*
*Brandeis University, United States*
*Dong Chen,*
*Zhejiang University, China*

****Correspondence:***
*Ye Zhang*
*ye.zhang@oist.jp*

***Specialty section:***
*This article was submitted to Physical Chemistry and Chemical Physics, a section of the journal Frontiers in Chemistry*

***Received:*** *14 July 2020*
***Accepted:*** *16 September 2020*
***Published:*** *23 October 2020*

***Citation:***
*Li G, Cortes W, Zhang Q and Zhang Y (2020) Chemical Oscillation and Morphological Oscillation in Catalyst-Embedded Lyotropic Liquid Crystalline Gels. Front. Chem. 8:583165. doi: 10.3389/fchem.2020.583165*

## INTRODUCTION

Belousov–Zhabotinsky (BZ) reaction performed in low-density media such as in solution gives fascinating rhythmic color oscillations and spatiotemporal patterns. In a soft matter, typically in gels, chemical oscillation can be converted into mechanical motion by periodic gel–sol transition, swelling, and contraction. Since Yoshida et al. first demonstrated a copolymer gel as chemomechanical oscillator (Yoshida et al., 1996), approaches of self-assembly of copolymers (Yoshida and Ueki, 2014; Kim et al., 2017), cross-linking polymers (Zhang et al., 2013a, 2014), branched polyethylene glycols (PEGs) (Ueki et al., 2014), and the use of gelatin (Smith et al., 2013; Buskohl and Vaia, 2016) have been widely adapted to make self-oscillating BZ gels. We have also developed post-self-assembly cross-linking approach to construct mixed peptide–polymer oscillatory gels (Zhang et al., 2012a, 2013b). Autonomous gels that can self-oscillate driven by BZ reaction have demonstrated great potential in the design of smart materials, such as biomimetic actuators, mass transport surface, and oscillatory reactors (Yoshida, 2010; Yoshida and Ueki, 2014; Kim et al., 2017; Hou et al., 2019; Cheng and Perez-Mercader, 2020).

Liquid crystals self-organize at the molecular level while maintaining fluidity. Because of the anisotropic orientation, liquid crystals are sensitive to external fields. Assembly of liquid crystals to form liquid crystalline gels can further sensitize their response to stimuli, giving rise to macroscale mechanical responses, such as bending, twisting, and buckling (Ware et al., 2015; White and Broer, 2015). In this regard, liquid crystalline gels are the ideal soft material to construct BZ reaction driving mechanical oscillators (Bléger, 2018). To our surprise, only a few attempts of incorporating

chemical oscillations into liquid crystal system have been carried out (Balasubramanian and Rodley, 1991; Shintate et al., 2018), and no example has ever been proposed for self-oscillating liquid crystals in BZ reaction.

We hypothesize that the oxidation–reduction cycle of metal catalyst in the BZ system will locally change the hydrophobic/hydrophilic environment, inducing novel orientations of mesogens in liquid crystalline gels and macroscopically self-oscillating by converting the continuous chemical waves. Herein for conceptual proof, we demonstrate a simple and convenient method of constructing catalyst-embedded lyotropic liquid crystalline (LLC) gels and realize macroscopic mechanical oscillations of bending–unbending transition driven by BZ reaction in LLC gels for the first time.

# RESULTS AND DISCUSSION

## Design of Catalyst-Embedded LLC Gels

Poly(*p*-phenylene-sulfoterephthalamide) (S-PPTA) is employed as LLC mesogen in this work (**Figure 1A**) due to (1) its high solubility in water, making it accessible and compatible to perform a BZ reaction in aqueous solution; (2) its lyotropic nematic behavior which is independent of the molar mass of the polymer (Viale et al., 2005); and (3) its negative surface charges, providing the electrical charge attraction for the positively charged metal catalyst, ruthenium(II) tris(bipyridine) chloride in this case. At low concentration, S-PPTA mesogens are in isotropic phase because the surface charges repulsively impede the alignment of mesogens. The introduction of catalyst not only helps overcome the charged repulsion of mesogen molecules, aligning mesogens for liquid crystal phase transition, but more importantly, the catalyst molecules non-covalently crosslink mesogens, driving the assembly of mesogens to form liquid crystalline gels. Compared with covalent immobilization of catalyst into a polymer chain, our approach of non-covalent catalyst embedment is time-saving and minimal in the preparation procedures.

## Preparation of Catalyst-Embedded LLC Gels

S-PPTA is dissolved in water to yield a slightly viscous solution at 0.25 wt.% concentration, which is lower than the reported critical gelation concentration (1.0 wt.%) (Ohsedo et al., 2015). LLC gel forms immediately by injecting catalyst solution into the above S-PPTA solution. The formed LLC gels stand isolated and can be manipulated individually inside the S-PPTA solution (**Figure 1B**). The LLC gels can be aligned and dragged to form strings (**Figure 1C**), showing promising potentials in programmable fabrication of different shapes. The dragged LLC strings as well as LLC gel blocks exhibit strong birefringence inside the gel under a polarized optical microscope (POM) (**Figures 1C,E**), whereas the S-PPTA solution droplet only shows weak birefringence on the edge (**Figure 1D**). Fluorescent images (**Figures 1D,E**) confirm the ruthenium(II)-based catalyst assists in forming LLC gels and reveal the microstructures inside LLC gels (**Figure 1F**).

The mechanical properties of catalyst-embedded LLC gels are evaluated. Rheological analysis indicates the S-PPTA solution is fluidic liquid at a concentration of 0.25 wt.%. In the presence of catalyst, the formed LLC gels show remarkable enhancement in the mechanical properties (**Figure 2A**). The storage modulus shows a higher than 4-order magnitude of enhancement; the loss modulus shows a higher than 3-order magnitude of enhancement.

Microstructures of catalyst-embedded LLC gels are also investigated via scanning electron microscopy (SEM). S-PPTA forms assembled films in solution. Zoomed-in SEM image indicates the films are organized by aligned filaments (**Figure 2B**). In the LLC gels, highly organized micro-disks with hexagonal shape are observed under SEM. High-resolution image from side view shows layer-by-layer assembly forming highly organized micro-disks with different thicknesses, ranging from 145 to 502 nm (**Figure 2C**). Energy-dispersive X-ray spectroscopy (EDX) spectra of selected SEM images (**Figure 2D**) show characteristic peaks of catalyst molecule in the assembled micro-disks of LLC gels. The energy of Ru Lα is observed at 2.578 keV (theoretically at 2.558 keV), and the energies of Cl Kα and Cl Kβ are observed at 2.648 and 2.782 keV (theoretically at 2.621 keV for Cl keV and at 2.812 keV for Cl Kβ, respectively). These results support our design of catalyst-embedded LLC gels through electric charge attraction.

## Chemical Oscillations in Catalyst-Embedded LLC Gels

Due to the easy processing properties of the catalyst-embedded LLC gels, we make LLC sticks by slowly dragging the freshly prepared LLC gel block using a pipette (**Figure 1C** and **Supplementary Figure 1**). The prepared LLC sticks are immersed in water overnight to remove unembedded catalyst. The LLC sticks with a diameter around 50–60 μm are cut into pieces with 1–2 mm length and immersed in BZ solution.

We first attempt to optimize BZ oscillations on the catalyst-embedded LLC gels. High concentration of $NaBrO_3$ (0.5M) leads to the failure of BZ oscillation because of fast oxidation of catalyst; high concentration of malonic acid (0.3 M) generates many bubbles which seriously interfere with the reaction recording. Under low concentration BZ reaction ($[NaBrO_3] = 0.050$ M, [malonic acid] = 0.021 M, $[H_2SO_4] = 0.50$ M), however, the catalyst is exchanged by protons and releases to the solution, resulting in fading and continuous shrinkage of liquid crystalline gels (**Supplementary Figure 2**).

Optimized chemical condition ($[NaBrO_3] = 0.28$ M, [malonic acid] = 0.071 M, $[H_2SO_4] = 0.50$ M) is applied to perform BZ reaction on the catalyst-embedded LLC gels. As shown in **Figure 3**, chemical oscillation occurs at 2 min, as observed in the changing color of the LLC stick switching between dark red [reduced state of the catalyst, Ru(II)] and light yellow [oxidized state of the catalyst, Ru(III)]. The color intensity profile is plotted (**Figure 3A**) and illustrates the co-existence of long-term chemical oscillations (2–5 min) contributed to the BZ patterns on LLC stick, and short-term chemical oscillations (10–15 s) contributed to the BZ patterns in the solution

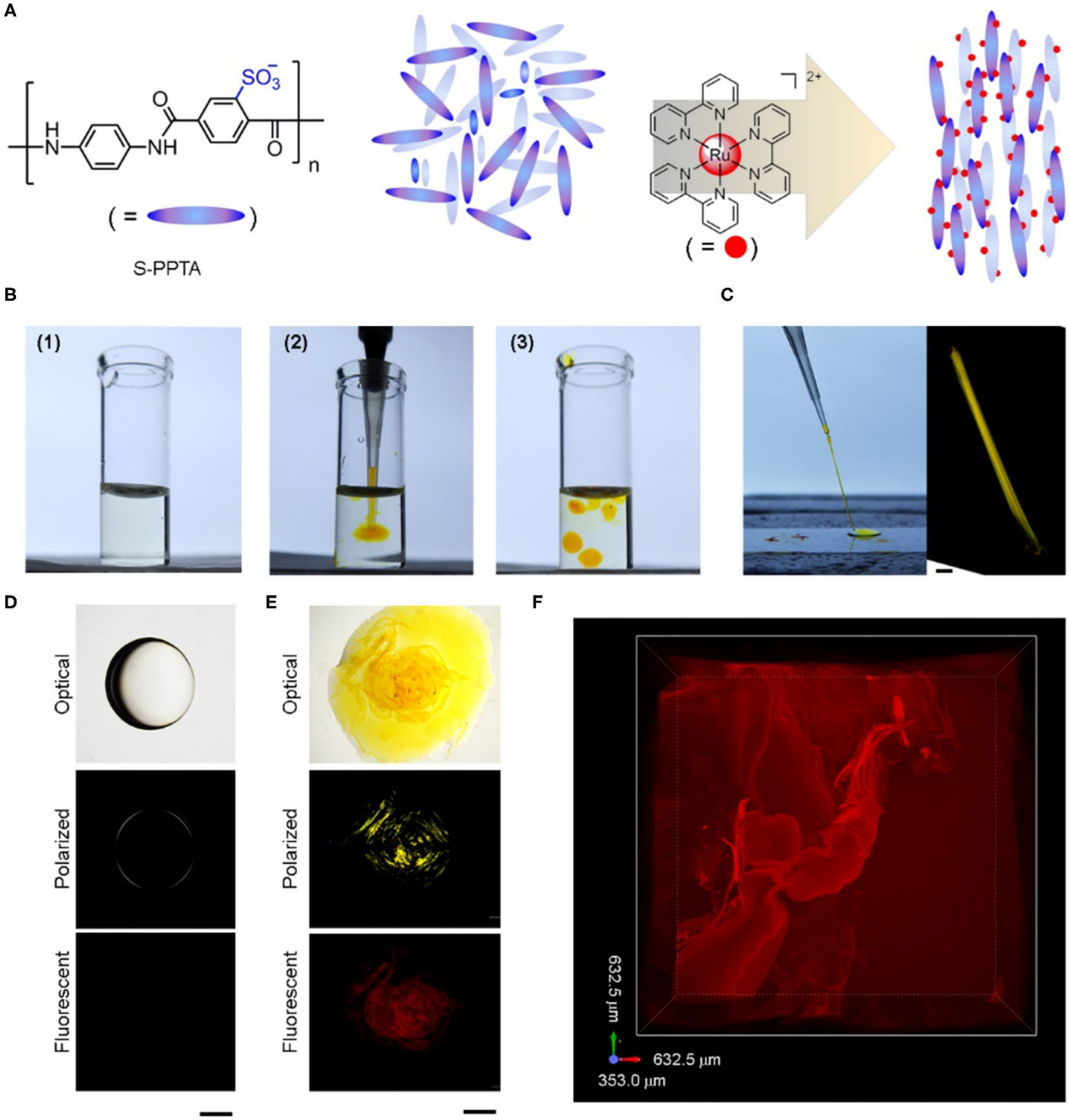


**FIGURE 1 |** Construction of catalyst-embedded LLC gels. **(A)** Schematic illustration of lyotropic liquid crystal organized by electric charge attraction. The chemical structures of mesogen S-PPTA and catalyst ruthenium tris(bipyridine) are also shown. Counter chloride ions in catalyst are omitted for clarity. **(B)** Optical images of (1) S-PPTA solution in water, (2) formation of LLC gel through the injection of catalyst solution into S-PPTA solution, and (3) fabrication of individual LLC gel blocks. **(C)** Dragging of freshly made LLC block on glass cover slice forms aligned LLC string and the birefringence of the aligned string. Scale bar represents 100 μm. **(D,E)** Optical, polarized, and fluorescent images of S-PPTA solution droplet without catalyst **(D)** and LLC gel block containing catalyst **(E)**. Scale bars represent 1 mm. **(F)** Confocal fluorescent image of catalyst-embedded LLC gel. 3D maximum intensity projection view is shown.

(**Supplementary Figure 3**). Within the first 42 min, the chemical waves are oscillating with a long period of 1–5 min; the oxidative waves spread continuously from the stick side that contains more catalyst, as indicated by the deeper red color. Representative series images from the period of 08:01–08:29 (**Figure 3B**) show that the direction of oxidative waves spreading is in accordance with the concentration gradient of Ru(II) catalyst. During the period of 43–60 min, however, the oscillation speeds up with

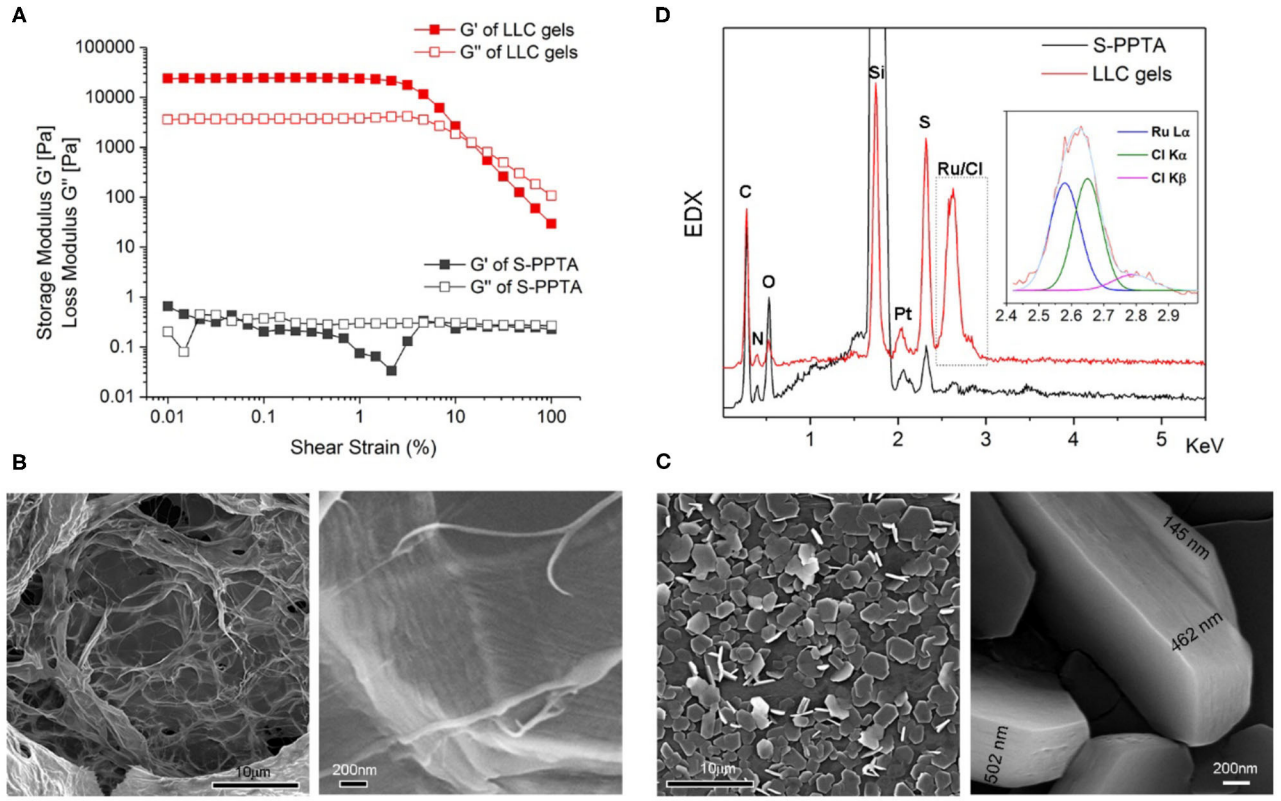


**FIGURE 2 |** Characteristics of LLC gels. **(A)** Strain dependence of dynamic storage moduli (G′) and loss moduli (G″) of S-PPTA solution without catalyst (gray) or catalyst-embedded LLC gels (red). **(B,C)** SEM images of S-PPTA solution without catalyst **(B)** or catalyst-embedded LLC gels **(C)**. **(D)** Energy-dispersive X-ray spectroscopy (EDX) spectra of selected SEM images of S-PPTA (black) or catalyst-embedded LLC gels (red). The peaks at around 2.6 keV are split using multi-peaks fitting for Ru Lα and Cl Kα/Kβ.

a frequency of two oscillations per minute. Meanwhile, the reversed spreading direction of oxidative waves is observed (**Figure 3C**). These phenomena can be reasoned that the pool of Ru(II) catalyst stocked in the LLC stick has ran out.

In addition, the LLC stick shrinks instantly when the BZ solution is added, probably due to the exchange of catalyst by protons under strong acidic condition of BZ reaction. The observation of oscillating pattern in the solution supports the diffusion of catalyst out of the LLC stick. The size of LLC stick during the chemical oscillation is measured and the result shows a general decrease in the diameter of LLC stick (**Supplementary Figure 4**). Despite the general shrinkage of the LLC stick, we observe small-scale diameter oscillation (around 10%) during the long periodic chemical oscillation (0–42 min), which is synchronized with the chemical oscillation profile (**Supplementary Figure 5**). During the sped-up oscillation, no obvious oscillation in the diameter of LLC stick is observed. This finding that LLC stick swells during the oxidized Ru(III) state while it shrinks during the reduced Ru(II) state in a BZ reaction is in accordance with our previous reports (Zhang et al., 2012b, 2014) and other groups' reports (Yoshida and Ueki, 2014; Kim et al., 2017) on polymer gels covalently immobilized with catalyst.

Attempting to reason the acceleration of chemical waves and swelling of LLC sticks, we examine the SEM images of LLC gels after BZ reaction. Even though the mechanical properties of LLC gels after BZ reaction do not display significant differences compared with LLC gels before BZ reaction (**Supplementary Figure 6**), the micro-composites show a remarkably structural difference under SEM. Before the BZ reaction, the hexagonal micro-disks in LLC gels are highly organized and compact that are $<4\,\mu m$ in diameter (**Figure 2C**). After the BZ reaction, however, the micro-disks swell into individual unity with a diameter up to $7.5\,\mu m$, while the fibers are kept aligned in each assembled unity (**Supplementary Figure 7**). The diffusion rate of BZ reactive intermediates within loosely aligned fibers unities is much faster than within compactly packing plates, resulting in speeding up of the chemical wave propagation.

## Morphological Oscillation in Catalyst-Embedded LLC Gels

SEM images of LLC sticks verify at the microscopic level our hypothesis of BZ reaction driving the mechanical response of LLC gels. The macroscopic swelling–shrinkage of LLC stick, however, is covered up by the continuous

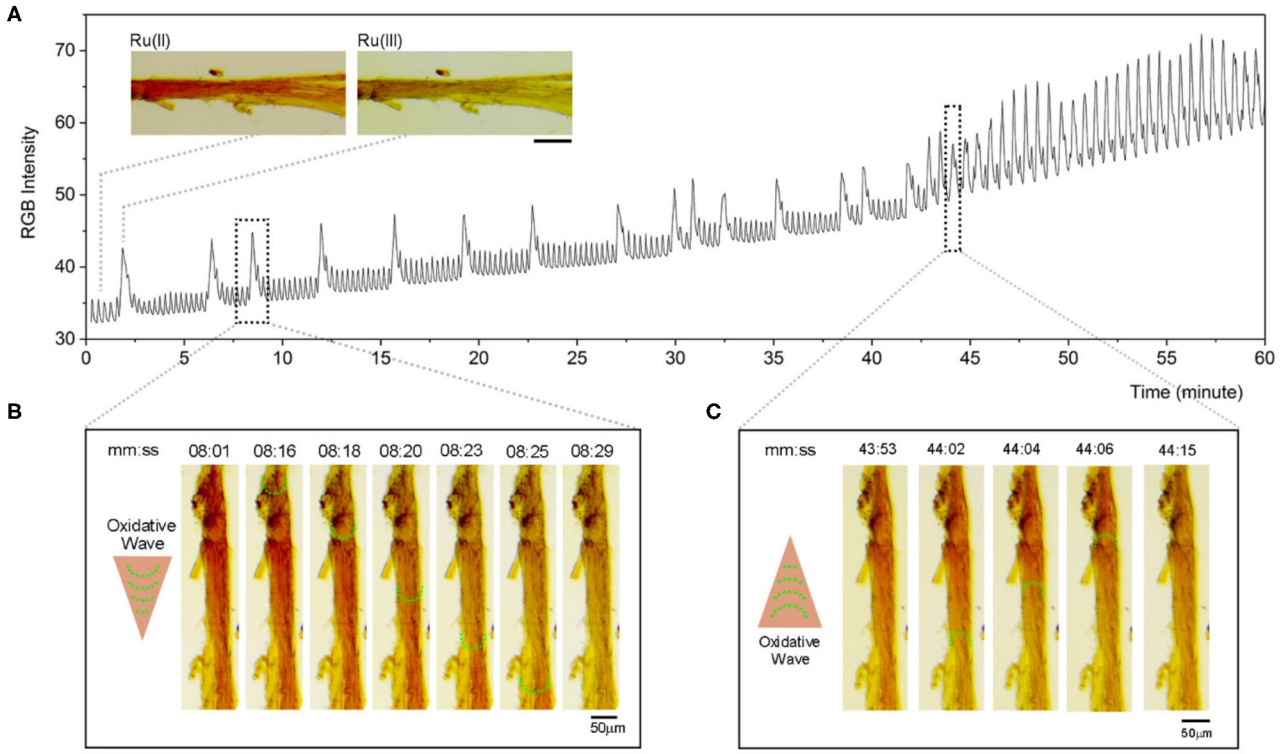


**FIGURE 3 |** Chemical oscillations of catalyst-embedded LLC gels during BZ reaction. **(A)** Color intensity profile of LLC stick immersed in BZ solution ($[H_2SO_4]$ = 0.5 M, $[NaBrO_3]$ = 0.28 M, [malonic acid] = 0.071 M). Inserted images show representative appearances of LLC stick in reduced state (Ru(II), red) or in oxidized state (Ru(III), light yellow). Scale bar represents 100 μm. **(B)** Selected optical images from the time period of 08:01–08:29 (mm:ss) show chemical waves along the LLC gel stick. Arrow and green dotted half-circles indicate the direction of oxidative waves along the stick. **(C)** Selected optical images from a time period of 43:53–44:15 (mm:ss) show chemical waves along the LLC gel stick. Arrow and green dotted half-circles indicate a reversed direction of oxidative waves along the stick. The images were rotated and cropped, and their brightness and contrast were adjusted by applying the same adjustment parameters to each image for clear illustration.

shrinkage of LLC gels during BZ reaction. To amplify the chemomechanical oscillations, we make catalyst-embedded LLC fibers with a smaller diameter (around 30 μm) by stretching the freshly prepared catalyst-embedded LLC strings. SEM images show the highly aligned fibers on the stretched LLC fibers (**Supplementary Figure 8**). POM images of LLC fibers (**Figure 4**) show stronger birefringence than LLC string (**Figure 1C**), indicating a more tightly assembled liquid crystal phase in the stretched LLC fibers.

When the small LLC fiber is immersed into BZ solution, it rapidly responds to the chemical waves and begins to bend at as early as 45 s. The bending rate slows down and stops at 10:24 (**Figure 4A**). The internal bending angle changes from 135 to 50°. The unbending process is observed from the time period of 10:37–12:48 accompanied with the fading birefringence (**Figure 4B**), suggesting a transition from compact liquid crystal phase to a loose packing phase in the LLC fiber. The internal bending angle expands to 72°. In the period of 13:21–14:48, the unbending process continues. LLC fiber straightens to 189° with an increasing birefringence in the LLC fiber (**Figure 4C**). Then a rapid bending process occurs again and completes within 1 min in the period of 14:54–15:42 (**Figure 4D**). At the final stage, the birefringent intensity decreases, and the LLC fiber turns green, suggesting the catalyst has been completely oxidized into Ru(III) and the BZ reaction stops. The plot of angles versus time (**Figure 4E**) clearly shows the LLC fiber bends three times within 16 min driving by a BZ reaction, and stops bending after 16 min. Similar results are observed (**Supplementary Figure 9**), suggesting that macroscopic mechanical oscillator of LLC gels is successfully realized in response to the chemical waves in BZ reaction. The bending duration time of LLC fibers with an average bending cycle of 1.5 (bend–unbend–bend) ranges from 1.6 to 10 min (**Figure 4F**).

The design of liquid crystalline network as stimuli-responsive actuators takes full advantages of the phase transition of molecular assembly (White and Broer, 2015; Kumar et al., 2016). We propose that the mechanical oscillations in LLC gels are due to the transition of molecular assembly between liquid crystal phase and isotropic phase (**Figure 4G**). Initial catalyst-embedded LLC gels before BZ reaction show bright birefringence under a POM. Also, SEM images show crystalline mesogen packing, suggesting the liquid crystal phase assembly of reduced Ru(II) catalyst with S-PPTA mesogen. During BZ reaction, catalyst is oxidized to form Ru(III). The charge change alters local balance and reorganizes the assembly of surrounding mesogens, which turns into isotropic phase. POM

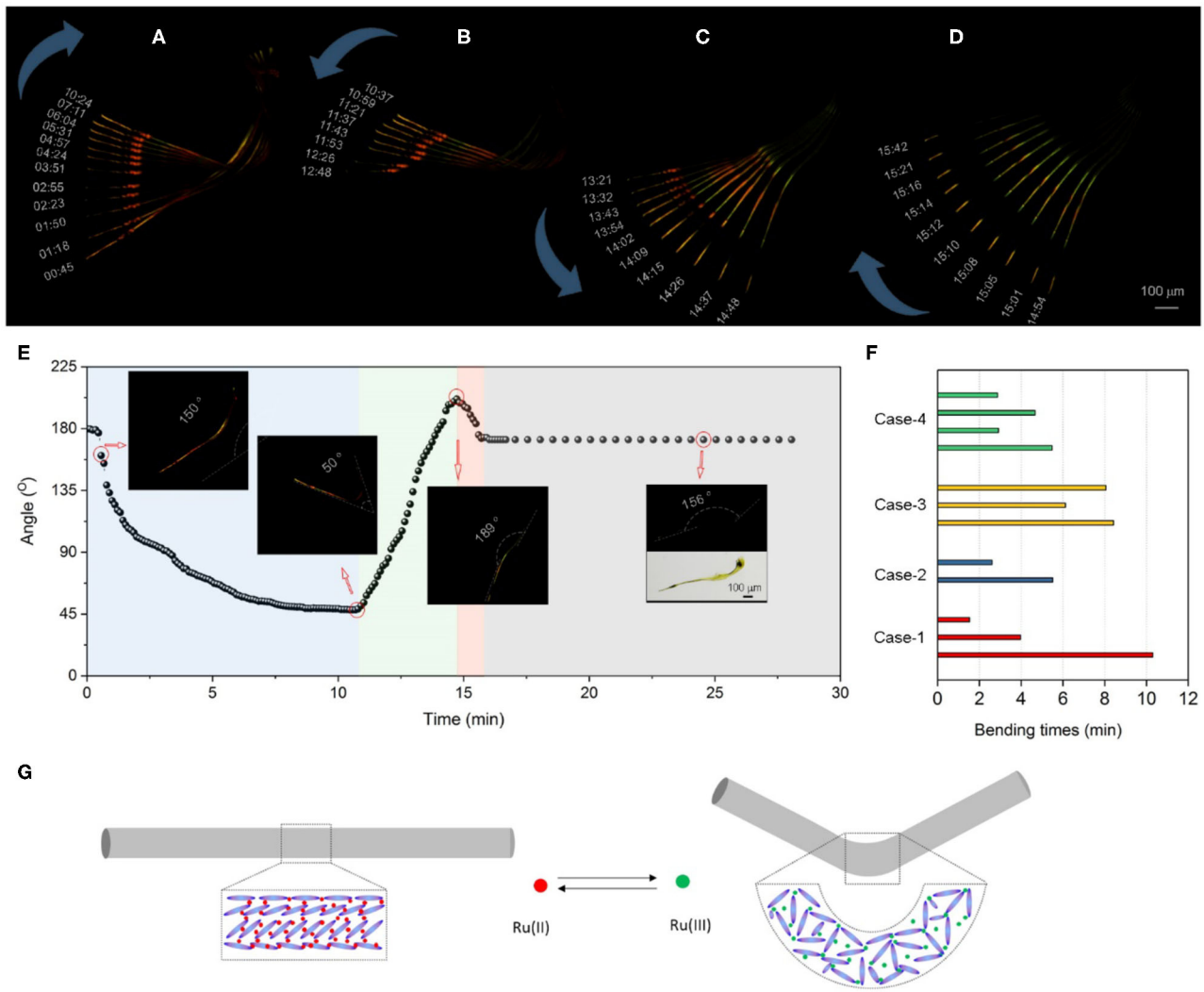


**FIGURE 4 |** Mechanical oscillations of catalyst-embedded LLC gel during BZ reaction. **(A)** POM images at a certain time point show the morphological changes of LLC fiber immersed in BZ solution. **(A–D)** Superimposed POM images from the time period of **(A)** 00:45–10:24, **(B)** 10:37–12:48, **(C)** 13:21–14:48, and **(D)** 14:54–15:42 (mm:ss) of LLC fiber in BZ solution. The blue arrows indicate the morphological oscillation of bending **(A)**, unbending **(B)**, straightening **(C)**, and re-bending **(D)** in BZ solution. **(E)** The plot of fiber angles versus time. Inserted images show representative POM images of fiber at a certain time point. **(F)** Histogram of fiber bending duration time in four cases**. (G)** Schematic drawing of assembly transition from liquid crystal phase to isotropic phase that bends a LLC fiber.

images show that the birefringence of LLC fibers vanishes at the bending site, confirming the isotropic phase transition during mechanical oscillations.

## CONCLUSION

Liquid crystalline gels integrating actuating molecules responsive to external fields (light, heat, magnetic fields, electric fields) have achieved great successes in stimuli-responsive materials (White and Broer, 2015; Kumar et al., 2016; Gelebart et al., 2017). As proof of concept, we demonstrate a simple and convenient method of constructing catalyst-embedded LLC gels and achieve self-oscillating LLC gels by converting chemical waves in a BZ reaction. Our approach of non-covalent crosslinking embedment of catalyst into LLC gels minimizes the preparation procedures, allowing quick conceptual tests with the lowest cost of time. The catalyst-embedded LLC gels are easily processable, capable of different shapes of fabrication. We have successfully achieved both chemical oscillation and mechanical oscillation on LLC gels. Our results suggest the applications of self-oscillating liquid crystalline gels driven by BZ reaction, and also increase the diversity of autonomous soft matter. More efforts are being put into this work to gain insight into more molecular clues on how the mesogen orientation and liquid crystal phase transition change as a consequence of oxidation–reduction oscillation of metal catalyst in BZ reaction. It should be noted that the stability of this non-covalent embedment of catalyst shows limitations in deep development of BZ-reaction-driving autonomous liquid

crystal actuators. An improved version of continuous self-oscillating LLC gels is under development.

# METHODS

## Materials and Instruments

$^{1}$H NMR and $^{13}$C NMR spectra are acquired on an AVANCE 400 (400 MHz; Bruker) spectrometer. The $^{1}$H NMR and $^{13}$C NMR chemical shifts (δ) are given in parts per million referring to internal standard tetramethylsilane (TMS). Rheological measurements of the moduli under varying strain are performed using an MCR 302 rheometer (Anton-Paar) at 25 °C with a cone plate (24.977 mm diameter) at a gap of 0.105 mm and ω of 10 1/s. SEM images are captured using Quanta250 FEG scanning electron microscope (FEI) at 10 kV; EDX spectra are recorded at 20 kV. The SEM samples are placed on silicon wafer and coated with a thin layer of Pt after freeze-drying. The freshly prepared LLC gel block is placed on a glass cover-slide and imaged by a confocal laser scanning microscope (A1; Nikon). Filters are set as ex/em 488/600 ± 20 nm. BZ reaction on the LLC gels is performed at 25 °C under an SMZ18 stereomicroscope (Nikon). Time-lapse optical images or POM images are captured every 2 s to record the chemical oscillations.

## Synthesis of S-PPTA

S-PPTA is synthesized according to literature method (Viale et al., 2005). $^{1}$H NMR (400 MHz, DMSO-d6) δ 10.96 (1H, s), 10.55 (s, 1H), 8.72 (d, J = 4.84 Hz, 1H), 8.41 (s, 1H), 8.04 (s, 1H), 7.89–7.55 (m, 4H). $^{13}$C NMR (101 MHz, DMSO-d6) δ 157.47, 156.97, 144.95, 144.24, 143.34, 130.98, 129.92, 128.98, 126.87, 126.58, 121.44, 120.71, 119.50, 115.66.

## Preparation of LLC Gels

Twenty-five milligrams of S-PPTA is dissolved in 10 ml water at 70°C, then allowed cool to r.t. to yield a 0.25 wt.% solution. A stock solution of 5 mM Ru(II) tris(bipyridine) chloride is prepared in water. To a solution of 500 μl S-PPTA in a glass vial, 20 μl of catalyst stock solution is slowly injected. Orange LLC gel block forms immediately. To make LLC sticks, a freshly prepared LLC gel block is dragged slowly out of S-PPTA solution using a pipette to yield a LLC string, which is allowed to hang in the air for a few minutes until the dragged string is stiff enough to keep its shape when moving the pipette. The LLC sticks are immersed in water overnight to remove unembedded catalyst. To make small LLC fibers, a freshly dragged LLC string is stretched using a pipette on a glass slice. The stretched strings are allowed dry in the air to yield small stiff fibers, which are immersed in water overnight to remove unembedded catalyst.

## Performance of BZ Reaction on LLC Gels

The LLC sticks or LLC fibers are cut into pieces with 1–2 mm length and placed on a glass-bottom dish under a stereo microscope. BZ solution is used as $[H_2SO_4] = 0.5$ M, $[NaBrO_3] = 0.050$ M, [malonic acid] = 0.021 M for low concentration condition; $[H_2SO_4] = 0.5$ M, $[NaBrO_3] = 0.50$ M, [malonic acid] = 0.10 M or $[H_2SO_4] = 0.5$ M, $[NaBrO_3] = 0.20$ M, [malonic acid] = 0.30 M for high concentration condition; $[H_2SO_4] = 0.5$ M, $[NaBrO_3] = 0.28$ M, [malonic acid] = 0.071 M for optimized condition, respectively. Optical images or POM images are captured every 2 s. To analyze chemical oscillations, RGB color intensities of selected ROIs on the LLC stick vs. time are recorded and plotted. For morphological analysis, time-lapsed images are loaded into ImageJ and the "Analyze Particles" analytic package is used to quantify the area of LLC sticks which is divided by length to yield the average diameter of LLC sticks. The calculated average diameters vs. time are plotted. The angles of bending fibers are measured in ImageJ.

# DATA AVAILABILITY STATEMENT

All datasets generated for this study are included in the article/**Supplementary Material**.

# AUTHOR CONTRIBUTIONS

GL and YZ contributed to conception, design of the study, and wrote the article. GL, WC, and QZ performed the experiments and analyzed data. All authors contributed to article revision, and read and approved the submitted version.

# FUNDING

This work was supported by Okinawa Institute of Science and Technology Graduate University, Proof-of-Concept program of OIST, and Takeda Science Foundation for medical science.

# SUPPLEMENTARY MATERIAL

The Supplementary Material for this article can be found online at: https://www.frontiersin.org/articles/10.3389/fchem.2020.583165/full#supplementary-material

# REFERENCES

Balasubramanian, D., and Rodley, G. A. (1991). Incorporation of a chemical oscillator into a liquid-crystal system. *J. Phys. Chem.* 95, 5147–5149. doi: 10.1021/j100166a043

Bléger, D. (2018). Continuously revolving patterns. *Nat. Nanotechnol.* 13, 274–275. doi: 10.1038/s41565-018-0076-4

Buskohl, P. R., and Vaia, R. A. (2016). Belousov-Zhabotinsky autonomic hydrogel composites: regulating waves via asymmetry. *Sci. Adv.* 2:e1600813. doi: 10.1126/sciadv.1600813

Cheng, G., and Perez-Mercader, J. (2020). Dissipative self-assembly of dynamic multicompartmentalized microsystems with light-responsive behaviors. *Chem* 6, 1160–1171. doi: 10.1016/j.chempr.2020.02.009

Gelebart, A. H., Vantomme, G., Meijer, E. W., and Broer, D. J. (2017). Mastering the photothermal effect in liquid crystal networks: a general approach for self-sustained mechanical oscillators. *Adv. Mater.* 29:1606712. doi: 10.1002/adma.201606712

Hou, L., Dueñas-Díez, M., Srivastava, R., and Pérez-Mercader, J. (2019). Flow chemistry controls self-assembly and cargo in Belousov-Zhabotinsky

driven polymerization-induced self-assembly. *Commun. Chem.* 2:139. doi: 10.1038/s42004-019-0241-1

Kim, Y. S., Tamate, R., Akimoto, A. M., and Yoshida, R. (2017). Recent developments in self-oscillating polymeric systems as smart materials: from polymers to bulk hydrogels. *Mater. Horizons* 4, 38–54. doi: 10.1039/C6MH00435K

Kumar, K., Knie, C., Bléger, D., Peletier, M. A., Friedrich, H., Hecht, S., et al. (2016). A chaotic self-oscillating sunlight-driven polymer actuator. *Nat. Commun.* 7:11975. doi: 10.1038/ncomms11975

Ohsedo, Y., Oono, M., Saruhashi, K., and Watanabe, H. (2015). A new water-soluble aromatic polyamide hydrogelator with thixotropic properties. *RSC Adv.* 5, 82772–82776. doi: 10.1039/C5RA16824D

Shintate, M., Inadomi, T., Yamamoto, S., Kuboyama, Y., Ohsedo, Y., Arimura, T., et al. (2018). Anisotropic self-oscillating reaction in liquid crystalline nanosheet hydrogels. *J. Phys. Chem. B* 122, 2957–2961. doi: 10.1021/acs.jpcb.7b11631

Smith, M. L., Slone, C., Heitfeld, K., and Vaia, R. A. (2013). Designed autonomic motion in heterogeneous belousov–zhabotinsky (BZ)-gelatin composites by synchronicity. *Adv. Funct. Mater.* 23, 2835–2842. doi: 10.1002/adfm.201202769

Ueki, T., Takasaki, Y., Bundo, K., Ueno, T., Sakai, T., Akagi, Y., et al. (2014). Autonomous viscosity oscillation via metallo-supramolecular terpyridine chemistry of branched poly(ethylene glycol) driven by the Belousov–Zhabotinsky reaction. *Soft Matter* 10, 1349–1355. doi: 10.1039/C3SM51537K

Viale, S., Li, N., Schotman, A. H. M., Best, A. S., and Picken, S. J. (2005). Synthesis and formation of a supramolecular nematic liquid crystal in poly(p-phenylene–sulfoterephthalamide)–$H_2O$. *Macromolecules* 38, 3647–3652. doi: 10.1021/ma0475636

Ware, T. H., McConney, M. E., Wie, J. J., Tondiglia, V. P., and White, T. J. (2015). Voxelated liquid crystal elastomers. *Science* 347, 982–984. doi: 10.1126/science.1261019

White, T. J., and Broer, D. J. (2015). Programmable and adaptive mechanics with liquid crystal polymer networks and elastomers. *Nat. Mater.* 14, 1087–1098. doi: 10.1038/nmat4433

Yoshida, R. (2010). Self-oscillating gels driven by the belousov–zhabotinsky reaction as novel smart materials. *Adv. Mater.* 22, 3463–3483. doi: 10.1002/adma.200904075

Yoshida, R., Takahashi, T., Yamaguchi, T., and Ichijo, H. (1996). Self-oscillating gel. *J. Am. Chem. Soc.* 118, 5134–5135. doi: 10.1021/ja9602511

Yoshida, R., and Ueki, T. (2014). Evolution of self-oscillating polymer gels as autonomous polymer systems. *NPG Asia Mater.* 6:e107. doi: 10.1038/am.2014.32

Zhang, Y., Li, N., Delgado, J., Gao, Y., Kuang, Y., Fraden, S., et al. (2012a). Post-self-assembly cross-linking of molecular nanofibers for oscillatory hydrogels. *Langmuir* 28, 3063–3066. doi: 10.1021/la203923d

Zhang, Y., Li, N., Delgado, J., Zhou, N., Yoshida, R., Fraden, S., et al. (2012b). Structural modulation of self-oscillating gels: changing the proximity of the catalyst to the polymer backbone to tailor chemomechanical oscillation. *Soft Matter* 8, 7056–7061. doi: 10.1039/c2sm25797a

Zhang, Y., Zhou, N., Akella, S., Kuang, Y., Kim, D., Schwartz, A., et al. (2013a). Active cross-linkers that lead to active gels. *Angew. Chem. Int. Ed.* 52, 11494–11498. doi: 10.1002/anie.201304437

Zhang, Y., Zhou, N., Li, N., Sun, M., Kim, D., Fraden, S., et al. (2014). Giant volume change of active gels under continuous flow. *J. Am. Chem. Soc.* 136, 7341–7347. doi: 10.1021/ja503665t

Zhang, Y., Zhou, R., Shi, J., Zhou, N., Epstein, I. R., and Xu, B. (2013b). Post-self-assembly cross-linking to integrate molecular nanofibers with copolymers in oscillatory hydrogels. *J. Phys. Chem. B* 117, 6566–6573. doi: 10.1021/jp401353e

**Conflict of Interest:** The authors declare that the research was conducted in the absence of any commercial or financial relationships that could be construed as a potential conflict of interest.

*Copyright © 2020 Li, Cortes, Zhang and Zhang. This is an open-access article distributed under the terms of the Creative Commons Attribution License (CC BY). The use, distribution or reproduction in other forums is permitted, provided the original author(s) and the copyright owner(s) are credited and that the original publication in this journal is cited, in accordance with accepted academic practice. No use, distribution or reproduction is permitted which does not comply with these terms.*

frontiers in Chemistry

ORIGINAL RESEARCH
published: 23 October 2020
doi: 10.3389/fchem.2020.560274

# Intermittent Chaos in the CSTR Bray–Liebhafsky Oscillator-Specific Flow Rate Dependence

*Itana Nuša Bubanja*[1], *Ana Ivanović-Šašić*[2], *Željko Čupić*[2]*, *Slobodan Anić*[1,2] and *Ljiljana Kolar-Anić*[1,2]

[1] Faculty of Physical Chemistry, University of Belgrade, Belgrade, Serbia, [2] Institute of Chemistry, Technology and Metallurgy, University of Belgrade, Belgrade, Serbia

Dynamic states with intermittent oscillations consist of a chaotic mixture of large amplitude relaxation oscillations grouped in bursts, and between them, small-amplitude sinusoidal oscillations, or even the quiescent parts, known as gaps. In this study, intermittent dynamic states were generated in Bray–Liebhafsky (BL) oscillatory reaction in an isothermal continuously-fed, well-stirred tank reactor (CSTR) controled by changes of specific flow rate. The intermittent states were found between two regular periodic states and obtained for specific flow rate values from 0.020 to 0.082 $min^{-1}$. Phenomenological analysis based on the quantitative characteristics of intermittent oscillations, as well as, the largest Lyapunov exponents calculated from experimentally obtained time series, both indicated the same type of behavior. Namely, fully developed chaos arises when approaching to the vertical asymptote which is somewhere between two bifurcations. Hence, this study proposes described route to fully developed chaos in the Bray-Liebhafsky oscillatory reaction as an explanation for experimentally observed intermittent dynamics. This is in correlation with our previously obtained results where the most chaotic intermittent chaos was achieved between the periodic oscillatory dynamic state and stable steady state, generated in BL under CSTR conditions by varying temperature and inflow potassium iodate concentration. Moreover, it was shown that, besides the largest Lyapunov exponent, analysis of chaos in experimentally obtained intermittent states can be achieved by a simpler approach which involves using the quantitative characteristics of the BL reaction evolution, that is, the number and length of gaps and bursts obtained for the various values of specific flow rates.

**Keywords: intermittent chaos, Bray–Liebhafsky oscillatory reaction, Lyapunov exponents, continuously-fed well-stirred tank reactor (CSTR), non-linear dynamics**

OPEN ACCESS

***Edited by:***
*Sugata Chowdhury, National Institute of Standards and Technology (NIST), United States*

***Reviewed by:***
*Sirshendu Mondal, National Institute of Technology, Durgapur, India*
*Lars Gundlach, University of Delaware, United States*

***Correspondence:**
*Željko Čupić*
*zcupic@ihtm.bg.ac.rs*

***Specialty section:***
*This article was submitted to Physical Chemistry and Chemical Physics, a section of the journal Frontiers in Chemistry*

***Received:*** *08 May 2020*
***Accepted:*** *17 August 2020*
***Published:*** *23 October 2020*

***Citation:***
*Bubanja IN, Ivanović-Šašić A, Čupić Ž, Anić S and Kolar-Anić L (2020) Intermittent Chaos in the CSTR Bray–Liebhafsky Oscillator-Specific Flow Rate Dependence. Front. Chem. 8:560274. doi: 10.3389/fchem.2020.560274*

## INTRODUCTION

The intermittent dynamic state is a chaotic state where two types of dynamic emerge in time, replacing each other stochastically. (Hilborn, 2004) The extent to which one type dominates the other can vary depending on the control parameter values. (Hilborn, 2004) In here considered case, intermittent dynamic state (also known as intermittent oscillations, intermittent chaos, or simply intermittency) (Pomeau and Manneville, 1980; Hilborn, 2004; Schuster and Just, 2005) represents a chaotic mixture of large amplitude relaxation oscillations grouped in bursts, and between them, there are small-amplitude sinusoidal

oscillations or quiescent parts, known as gaps. This type of deterministic dynamic phenomenon may also be found in some complex chemical (Chopin-Dumas, 1978; Pomeau et al., 1981; Roux et al., 1981; Baier et al., 1989; Kreisberg et al., 1991; Strizhak and Menzinger, 1996; Vukojević et al., 2000; Kolar-Anić et al., 2004; Cadena et al., 2013; Čupić et al., 2014; Bubanja et al., 2016, 2017) and biochemical (Izhikevich, 2000a,b) reaction systems under conditions that do not have an equilibrium.

This study examined the appearance of intermittent chaos in the Bray–Liebhafsky (BL) reaction, which has been systematically investigated for decades by the Belgrade research group (Kolar-Anić et al., 2017). In this catalytic oscillatory reaction hydrogen peroxide is decomposed into water and oxygen in the presence of hydrogen and iodate ions (Bray, 1921; Bray and Liebhafsky, 1931).

$$2H_2O_2 \rightarrow 2H_2O + O_2 \qquad (D)$$

Hydrogen peroxide decomposition is the result of two complex pathways in which hydrogen peroxide acts either as a reducing (R) or as an oxidizing (O) agent:

$$2IO_3^- + 2H^+ + 5H_2O_2 \rightarrow I_2 + 6H_2O + 5O_2 \qquad (R)$$
$$I_2 + 5H_2O_2 \rightarrow 2IO_3^- + 2H^+ + 4\,H_2O \qquad (O)$$

Mentioned reactions (R) and (O) are complex and their mechanisms involve several intermediate species (Bray, 1921; Liebhafsky, 1931; Woodson and Liebhafsky, 1969; Furrow, 1985, 1987; Stanisavljev et al., 2013; Holló et al., 2014). In general, alternating increases and decreases of the intermediate species concentrations in time appear as a consequence of alternating dominations of reactions (R) and (O).

Taking into account that oscillatory dynamic states, the BL reaction can be realized either at relatively higher temperatures, where the potentiometric measurements are very complex or at lower temperatures where such experiments, lasting several days are difficult to control. Due to the fact that the intermittent chaos can be obtained only within a very narrow range of the control parameter values, it is not surprising that only a small number of scientific papers are dedicated to intermittent chaos in BL systems. To the best of our knowledge, only four papers considering intermittent phenomena in the BL system were found. Among them, two papers were published over 40 (Chopin-Dumas, 1978) and 20 years ago (Vukojević et al., 2000) while the remaining two (Bubanja et al., 2016, 2017) were published more recently.

In the most recent papers (Bubanja et al., 2016, 2017), intermittent dynamic states were experimentally generated in the BL reaction system realized in a continuously-fed well-stirred tank reactor (CSTR) under variations of temperature and inflow concentration of potassium iodate. These two last papers, clearly show that experimentally generated intermittent chaos can be analyzed, not only by calculations of the largest Lyapunov exponents ($\lambda$) from experimentally obtained oscillograms but also by the simple quantitative characteristics of the evolution of BL reaction, lengths of bursts, (packages of relaxing oscillations) and lengths of gaps between them (the periods of the sinusoid oscillations of relatively small amplitude when compared to relaxing oscillations). In this instance, a general problem that appears during the calculation of the largest Lyapunov exponents occurs from experimental noise in the signal, which cannot be avoided. Because of noise, even obviously regular oscillations give false-positive values of the largest Lyapunov exponents appearing as false chaotic states.

This study, building upon previous research (Bubanja et al., 2016, 2017), aimed to examine if there is a causality between the structure of intermittent chaos and the specific flow rate as the control parameter and whether this causality is consistent with these previous findings. For appropriate application in the characterization of relations among the different dynamic states, this study adapted previously established methods and techniques, which are described in the Results and Discussion of this paper.

## EXPERIMENT

The BL reaction represents a decomposition of hydrogen peroxide into water and oxygen in the presence of iodate ions and acidic medium. In all our papers and here as well, as the source of iodate ions potassium iodate was used, and for setting up a desired acidity sulfuric acid was taken. Experiments were carried out at a constant temperature of $(63.0 \pm 0.1)^{o}$C, in a 50 mL (Metrohm reaction vessel, product number: EA876-20) glass CSTR vessel wrapped in a water recirculation jacket connected to a thermostat. For homogenization of the reaction mixture, a magnetic stirrer with a stirring speed of $\sigma = 900$ rpm and magnetic stirring bar (uniform triangular prism-shaped magnetic bar, length size 12 mm, and triangle side size 6 mm) covered with polytetrafluorethylen (PTFE) were used. The amounts of reactant species in the reactor were controlled by peristaltic pumps. Three channels were used to deliver solutions of the reactants $KIO_3$, $H_2SO_4$, and $H_2O_2$ prepared in deionized water (18 M$\Omega$·cm), and one channel of the other pump was used to remove the surplus volume of the reaction mixture through a U-shaped glass tube, to keep the constant volume of the reaction mixture $(22.2 \pm 0.2)$ mL. A potentiometric method was used to record the dynamic states of the BL reaction system, and a three-electrode system was applied. A double-junction Ag/AgCl was used as a reference electrode while working an iodide ion sensitive electrode ($I^-$SE) and Pt electrode. Potential changes of Pt vs. Ag/AgCl and $I^-$SE vs. Ag/AgCl during the time (well known in the literature as time series or oscillograms) were traced and recorded at the same time with an electrochemical instrument (PC-Multilab EH4 16-bit ADC) coupled with a personal computer. A schematic view of the experimental setup is given in **Figure 1**.

The experiment was performed first, by filling the reactor with reactants at the total flow rate of 15.0 mL/min, protecting the thermostat reaction vessel from light. Concentrations of stock solutions were chosen so that their inflow concentrations in the reactor were: $[KIO_3]_0 = 0.035$ M, $[H_2SO_4]_0 = 0.077$ M, and $[H_2O_2]_0 = 0.240$ M (M stands for mol·dm$^{-3}$). After 1 min magnetic stirrer was turned on and set to stirring speed of 900 rpm. Then, after 2.95 min the total flow rate was set to 0.84

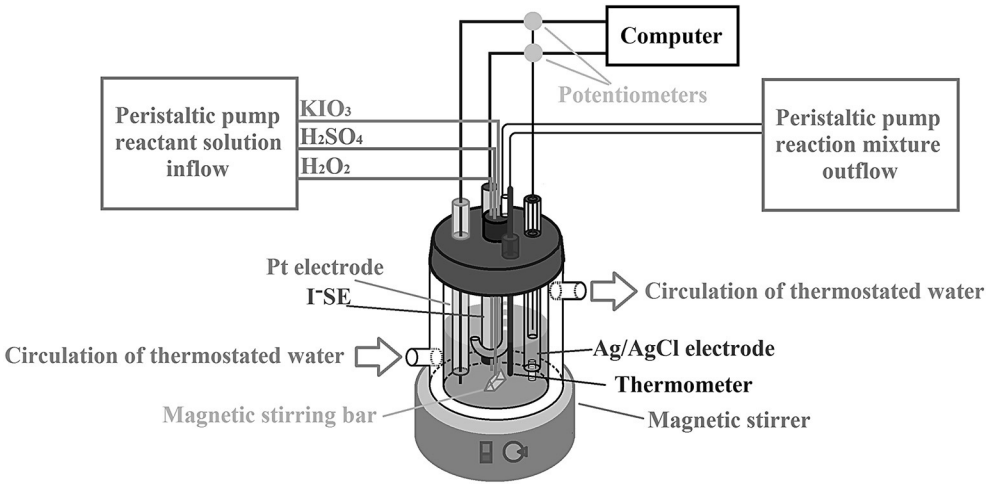


**FIGURE 1 |** A schematic view of the experimental setup used for generating intermittent chaos in the BL system under CSTR conditions by varying the specific flow rate as a control parameter.

mL/min, and we switched on another pump for removing the surplus volume of the reaction mixture. The total flow rate of 0.84 mL/min corresponds to a specific flow rate of 0.038 $min^{-1}$. This value was obtained by dividing the total flow rate ($\upsilon$) with the total volume of the reaction mixture (V):

$$j_0 = \frac{\upsilon_{KIO_3} + \upsilon_{H_2SO_4} + \upsilon_{H_2O_2}}{V} = \frac{\upsilon}{V} = \frac{0.84\ mL/min}{22.2\ mL} = 0.038\ \text{min}^{-1}$$

Every following experiment was performed as an extension of the previous one with a decreased or increased total flow rate of reactants and, therefore, with decreased or increased specific flow rate. Between each experiment, the recording was paused for a period of three retention times (retention time represents the reciprocal value of the specific flow rate). This allowed the system to stabilize in a new dynamic state with a changed control parameter.

## RESULTS AND DISCUSSION

Under CSTR conditions in the considered range of specific flow rate, we found the chaotic mixture of the regular sustained large-amplitude relaxation oscillations grouped in bursts and small-amplitude irregular sinusoidal ones grouped in gaps. Chaotic intermittent nature of recorded time series is reflected in irregular and unpredictable lasting of both, bursts and gaps. **Figure 2**, shows the dynamic states of the BL system in CSTR under variation of specific flow rate ($j_0$), which were monitored by potential changes of iodide ion sensitive ($I^-$SE) vs. Ag/AgCl electrode over time. The first chaotic emergence of low-amplitude oscillations, which occurred when the specific flow rate decreased, shifting the system from a periodic oscillatory dynamic state (**Figure 2A**, gray oscillogram), denotes the emerging of an initial intermittent state (**Figure 2B**). This phenomenon appears when the defined value of the specific flow rate is slightly lower than the value where the periodic dynamic state was found. With further decreasing of specific flow rate the low-amplitude oscillations transform to the short gaps. Their number and duration increase at first and then decrease. Finally, the gaps disappear at a very low specific flow rate, when a periodic oscillatory dynamic state was again obtained (**Figure 2F**). As the specific flow rate increases, starting from the state given in **Figure 2F**, the whole scenario repeats, and the system reaches the periodic oscillatory dynamic state once more.

Thus, in here considered case where the specific flow rate is used as a control parameter, the intermittent chaos was observed between two periodic oscillatory states. When variations of temperature (Bubanja et al., 2016) and inflow concentration of potassium iodate (Bubanja et al., 2017) were used to generate intermittent oscillations in the BL system, intermittencies emerged between the periodic oscillatory state and stable steady state.

In our previous experiments only potential changes of Pt versus Ag/AgCl electrode were used to record dynamics of BL system (Bubanja et al., 2016, 2017). In the present study potential changes of I-SE versus Ag/AgCl electrode were monitored simultaneously with potential changes of Pt versus Ag/AgCl electrode. Our previous experiments identified potential changes of Pt vs. the Ag/AgCl electrode, which were used to record the dynamics of the BL system, in the present study the potential changes of $I^-$SE vs. Ag/AgCl electrode were monitored simultaneously with potential changes of Pt vs. Ag/AgCl electrode. **Figure 3** shows that the same segment of oscillograms obtained by Pt *vs.* Ag/AgCl and $I^-$SE *vs.* Ag/AgCl electrodes for a specific flow rate of $j_0 = 0.068\ \text{min}^{-1}$.

In this system, where the iodide ion sensitive electrode ($I^-$SE) and Pt electrode were used both together within the same reaction mixture, both potentiometric records of the bursts and gaps appear at the same time and have the same number of large amplitude oscillations per burst (**Figure 3**). However, it is noticeable that the potential signal traced with $I^-$SE was less

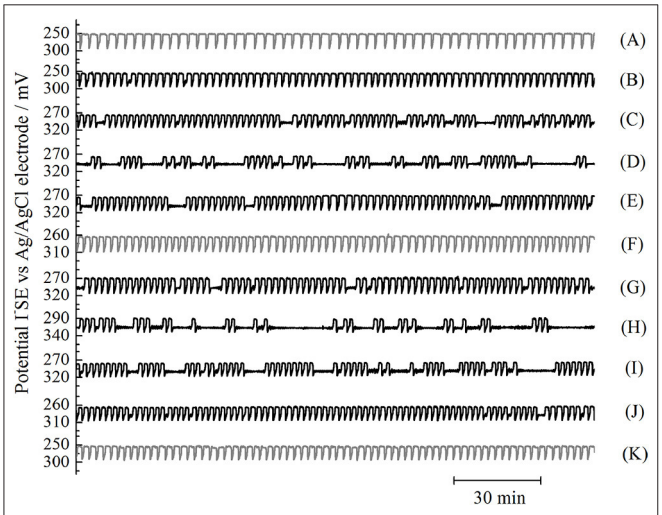


**FIGURE 2 |** Transitions between periodic oscillatory dynamic states [**(A)** $j_0$ = 0.095 $min^{-1}$ **(F)**, $j_0$ = 0.020 $min^{-1}$, and **(K)** $j_0$ = 0.101 $min^{-1}$] via different intermittent states, obtained either by decreasing [**(B)** $j_0$ = 0.077 $min^{-1}$, λ = 34.8; **(C)** $j_0$ = 0.064 $min^{-1}$, λ = 81.6; **(D)** $j_0$ = 0.061 $min^{-1}$, λ = 95.1; **(E)** $j_0$ = 0.038 $min^{-1}$, λ = 68.4] or increasing [**(G)**, $j_0$ = 0.038 $min^{-1}$, λ = 63.4; **(H)** $j_0$ = 0.064 $min^{-1}$, λ = 92.7; **(I)** $j_0$ = 0.072 $min^{-1}$; **(J)** $j_0$ = 0.077 $min^{-1}$, λ = 67.6] specific flow rate. Data from 3 h of the time series (I⁻SE vs. Ag/AgCl potential over time) are shown (note: oscillograms were recorded over a longer period). Oscillograms were obtained for the following experimental conditions: $[KIO_3]_0$ = 0.035 M, $[H_2SO_4]_0$ = 0.077 M, $[H_2O_2]_0$ = 0.240 M, T = 63.0 °C, σ = 900 rpm, while the specific flow rate was varied. For noise removal in Origin 8 application, Savitzky–Golay filtering was applied. Oscillograms in gray correspond to periodic oscillatory states, and those that are black represent intermittent dynamic states. Besides specific flow rates, values of largest Lyapunov exponent, λ are stated where applicable.

noisy than the one obtained when Pt was used as a working electrode. This is in accordance with our previous investigations of the regular periodic oscillations in BL reaction (Anić and Kolar-Anić, 1986; Anić et al., 1987). Since noise level is of crucial importance to any method of chaos quantification, the largest Lyapunov exponents were calculated from time-series obtained by the I⁻SE electrode. For the largest Lyapunov exponent calculations we applied the Wolf algorithm (Wolf et al., 1985). The Wolf algorithm was successfully used to quantify chaos when different chaotic dynamic states were obtained numerically (Ivanović-Šašić et al., 2011). Besides, even when applied to experimentally obtained intermittent chaos the Wolf algorithm showed a good correlation (Bubanja et al., 2016, 2017), considering the noise presence. Therefore, only the time series in which intermittencies were detected were used to calculate the largest Lyapunov exponents by the Wolf algorithm as a function of the control parameter (**Figure 4A**). Moreover, not all recorded intermittent states were appropriate for calculations of the largest Lyapunov exponent since in some long experiments technical problems emerged such as the drift in electrode potential after some time (probably due to unavoidable, slow reference electrode leakage).

As explained above, (**Figure 2**) by varying the control parameters, gaps gradually emerge from periodic oscillatory states due to the development of a new intermittent dynamic state. We noticed that variation of gap lengths (as well as burst lengths) over time is chaotic (irregular/unpredictable) and that somewhere in the middle of the region, for which the control parameter was varied, gaps become more dominant in the considered time frame than the bursts. In our previously published papers, the number of bursts per unit of time ($N_B/\tau$, where $\tau$ is the duration of the experiment) was used as a measure of chaos in intermittent dynamic states. Even though, the number

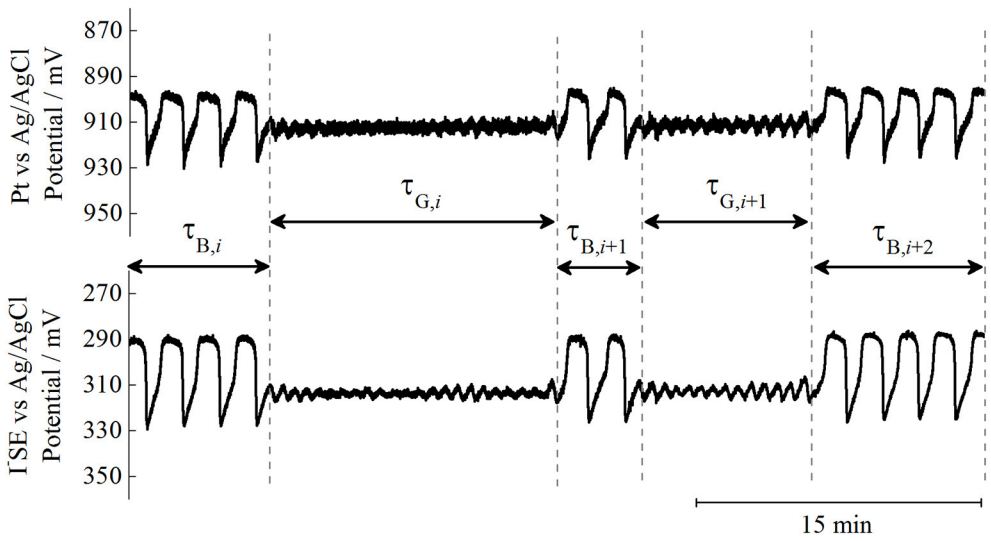


**FIGURE 3 |** Potentiometric traces, recorded by Pt (upper) and I⁻SE (lower) electrodes vs. referent Ag/AgCl, over identical time intervals in order to illustrate different noise levels. Displayed oscillograms were obtained for the following experimental conditions: $[KIO_3]_0$ = 0.035 M, $[H_2SO_4]_0$ = 0.077 M, $[H_2O_2]_0$ = 0.240 M, T = 63.0°C, σ = 900 rpm and $j_0$ = 0.068 $min^{-1}$.

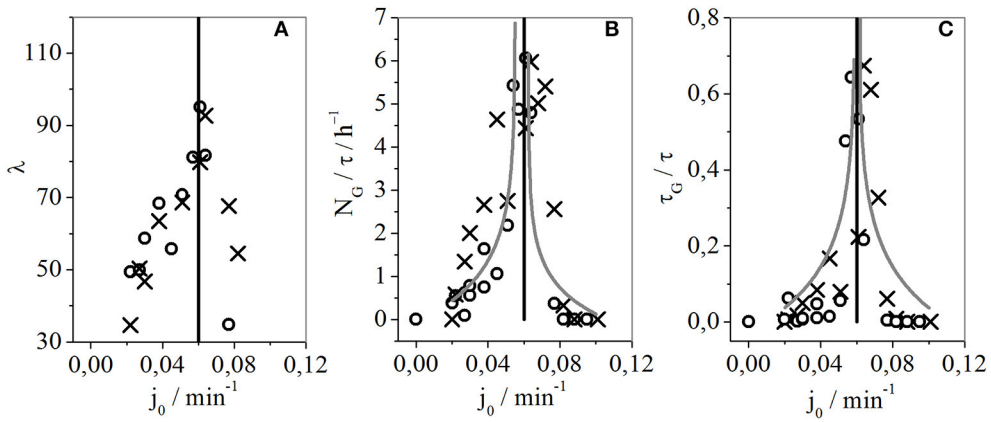


**FIGURE 4 | (A)** Largest Lyapunov exponents, calculated from time series obtained by $I^-$SE vs. Ag/AgCl electrode; **(B)** Number of gaps per unit of time ($N_G/\tau$, where $\tau$ is the duration of the experiment); **(C)** Fraction of time occupied by gaps ($\tau_G/\tau$, where $\tau_G$ is the sum of gaps duration during one experimental recording). In all three cases, the control parameter is the specific flow rate. Cross-shaped symbols (×) and empty circles (○) correspond to the specific flow rate obtained during the increase and decrease directions, respectively.

of bursts and gaps per each time series are almost identical, in presented case it is more correct to use number of gaps per unit of time since chaotic states are generated by inserting the increasing number of gaps between burst packages made of regular periodic oscillations. Taking this into consideration, besides the largest Lyapunov exponents (λ), the measure of chaos in considered intermittent state is obviously the number of gaps per unit of time ($N_G/\tau$). Therefore, the calculated largest Lyapunov exponents, as a function of specific flow rate (**Figure 4A**), were compared with the number of gaps per unit of time as a function of the same control parameter (**Figure 4B**). The functional dependence of the largest Lyapunov exponents *vs.* the specific flow rate follows the functional dependence of the number of gaps per time *vs.* the specific flow rate. Moreover, a significant level of linear correlation among the largest Lyapunov exponent and the number of gaps per unit of time was confirmed (see **Supplementary Material**).

As seen in **Figure 4B**, by further analyzing the results of the experiment we can see that somewhere in the middle of the region for which the control parameter was varied (roughly around 0.06 $min^{-1}$), the dynamic states of the considered reaction system tend to achieve "fully developed chaos." However, as we are closer to the mentioned fully developed chaotic state, the system is more sensitive to control parameters and the realization of these states is more difficult. Consequently, in the vicinity of the vertical asymptote, which is presented in **Figures 4A–C**, the dispersion of experimental points is the most evident. In this region, some experimental results could not be analyzed by the Wolf method using the largest Lyapunov exponents. To capture and record the selected dynamic state the experiment should be very long, which is serious experimental problem. It is difficult to keep the reaction system in so sensitive dynamic state for several days. Nevertheless, the shape of the functional dependence between the largest Lyapunov exponents and specific flow rate matches the general observation of the obtained chaotic dynamics within a narrow range of the flow rates with the intermittent dynamic states.

Moreover, we wanted to define the boundaries of the region of specific flow rates with intermittent dynamic states. However, the task of determining the bifurcation points between the periodic and intermittent oscillations is difficult. In the vicinity of bifurcation, only one short gap might appear just once after several days. Therefore, we decided to look for bifurcation points in analogy with other reaction systems where transitions between qualitative different dynamic states under the changes of control parameter have not caused sudden or unexpected transitions between them, similarly to the appearance of the limit cycle from the stable steady state through supercritical Andronov-Hopf bifurcation. In this study, the packages of small amplitude oscillations grouped in gaps emerge gradually from the regular oscillations described by the large amplitudes. Therefore, the fraction of time occupied by gaps ($\tau_G/\tau$) slowly increases from zero in the vicinity of the bifurcation point. This reflects the slow emerging limit cycle in Andronov-Hopf bifurcation as a function of the control parameter. Hence, we presented $(\tau_G/\tau)^2$ as a function of the control parameter of the specific flow rate (**Figure 5**) and analyzed the linear relationship around critical values.

From **Figure 5** it is very difficult to evaluate the exact critical values of specific flow rates that correspond to bifurcation points. We can only estimate that those bifurcation points occur around 0.020 and 0.082 $min^{-1}$. This roughly estimated region, in which the appearance of the bifurcation point could be expected, is indicated by the shaded area in **Figure 5**. The bifurcation point close to 0.020 $min^{-1}$ corresponds to the bifurcation representing the occurrence of gaps from regular periodic oscillations, obtained for lower specific flow rate values. Bifurcation close to 0.082 $min^{-1}$ corresponds to the occurrence of gaps from regular periodic oscillations, obtained for higher specific flow rate values. Moreover, no hysteresis was obtained when experiments were performed with decreasing/increasing specific flow rates.

As observed from **Figure 2**, in all the intermittent states the lengths of individual gaps and bursts are both chaotically

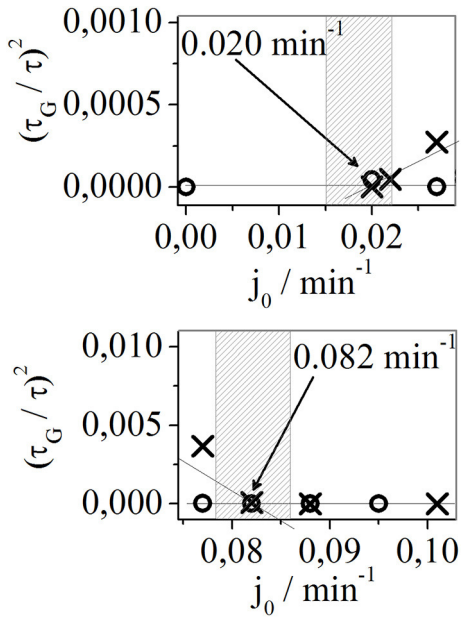


**FIGURE 5 |** The $(\tau_G/\tau)^2$ as a function of the specific flow rate. The bifurcation points are roughly estimated from the linear relationship between $(\tau_G/\tau)^2$ and the specific flow rate in the vicinity of the bifurcation point, marked with arrows. The estimated/expected bifurcation points are shown in the shaded area. As in **Figure 4**, cross-shaped symbols (×) and empty circles (○) correspond to the specific flow rate obtained during the increase and decrease directions, respectively. Only results around critical values are shown.

distributed. However, in accordance with our previous studies in the quantitative analysis of intermittent chaos, we can see that by indicating the number of burst and gap packages whose duration is longer than some time, denoted as $T_0$, the regularity in the distribution of the duration of burst and gap packages, per one experiment, can be observed (**Figure 6**). It should be stressed that relative values of the number of bursts/gaps longer than some $T_0$ in the unit of time $(N(l > T_0)/\tau)$ or, simply $(n/\tau)$ where $n = N(l > T_0)$ was used, and since the graphs for time series of very different overall lengths ought to be compared. Relative values $(n/\tau)$ were obtained by dividing the number of bursts/gaps by the total time of the experimental recording $(\tau)$.

The central graph of **Figure 6** shows the fraction of time occupied by gaps as a function of the specific flow rate. The arrows indicate the results that were used to calculate the relative number of bursts and gaps longer than $T_0$ (**Figures 6A–E**). The central graph in **Figure 6** uses the same symbols as **Figure 4C** to describe the results during an increase or decrease of the specific flow rate. Replicating the trends obtained in a previous study by Dubois et al. (1983), where exponential dependence between some time $T_0$ and the number of laminar phase intervals (gaps or bursts) longer than $T_0$ was used as an indicator of type III intermittency, we applied less complex exponential dependence, to our results. To fit the results shown in **Figures 6A–E**, mathematical form $y = p{\cdot}\exp(q{\cdot}x)$ was used, where y and x stand for $n/\tau$, and $T_0$ respectively, while $p$ and $q$ are parameters used for optimization and their optimal values are given in **Table 1**, which includes the values of the adjusted R-squares. The letters B and G are given in the subscript of the p, q parameters, and adjusted R-squares ($R^2$) to indicate from the data from which each fitting was performed. Namely, values with B in subscript were obtained using the number of burst packages whose duration is longer than $T_0$. The values with G in subscript correspond to the number of gap packages with a duration longer than $T_0$. As can be seen from **Table 1**, the mentioned mathematical form was convenient for all shown cases in **Figure 6**, as well as for both bursts and gaps per case, but with different values for the fitted parameters. Based on the high values of the adjusted coefficient of determination or adjusted R-square (the lowest was 0.946 and the highest was 0.994) we can conclude that the exponential equation fitted data well. That said, in case (**Figure 6D**) the adjusted $R$-square for $q_B$ was slightly lower (at 0.897), as a consequence of the very short duration of this experimental recording and the relatively small number of bursts.

The ratio between fit parameters q for bursts ($q_B$) and gaps ($q_G$) in the same experiment, should reveal whether the black curve is "above" or "below" the gray (**Table 1**). However, regardless of the relative position of the black and gray curves, this was an instance of intermittent chaos. Moreover, even when $q_B$ and $q_G$ are nearly equal intermittent chaos also occurs. However, a higher ratio of $q_B/q_G$ indicates a higher level of complexity. This quantity could be a candidate for identifying the position of vertical asymptote with respect to the control parameter (**Figure 4**), which was expected to have low absolute values for $q_G$ and high for $q_B$, meaning that the ratio would tend to infinity, which would correspond to fully developed chaos. The relative positions of exponential curves can be used to describe the dominant state in the experimentally observed intermittent states. Namely, in intermittent states where lengths of gaps are short, and bursts dominate (**Figures 6A,E**), the exponential curve of bursts is above the corresponding curve for gaps, so the $q_B/q_G$ ratio is $<1$ [$q_B/q_G = 0.0514$ (A), and $q_B/q_G = 0.0363$ (E)], meaning it is opposite when the gaps start to dominate over bursts [**Figure 6** $q_B/q_G = 1.777$ (C), $q_B/q_G = 2.124$ (D)]. From the results seen in **Figure 6B**, it could be concluded that both bursts and gaps are equally dominant in the intermittent state since $q_B/q_G$ is almost 1 ($q_B/q_G = 1.044$). Thus, the method proposed by Dubois et al. (1983) is one way of quantifying the regularity seen in **Figure 4C**. That is, in both bifurcation points, when gaps emerge their fraction gradually increases while approaching a vertical asymptote, where they start to dominate. There, the dynamic states approach fully developed chaos, which is quantified by the largest Lyapunov exponents **Figure 4A**. The number of gaps (**Figure 4B**), the fraction of time occupied by gaps (**Figure 4C**), follow these overall dynamics. These results, which provide insights into the evolution of dynamic states, are in accordance with the known fact that the route to chaos can be realized through intermittent oscillations. Even though any intermittent state is a chaotic one, this study has shown that this tendency and increasing complexity occurs somewhere in the middle, among these two periodic oscillatory states (Nicolis and Prigogine, 1989; Ivanović-Šašić et al., 2011).

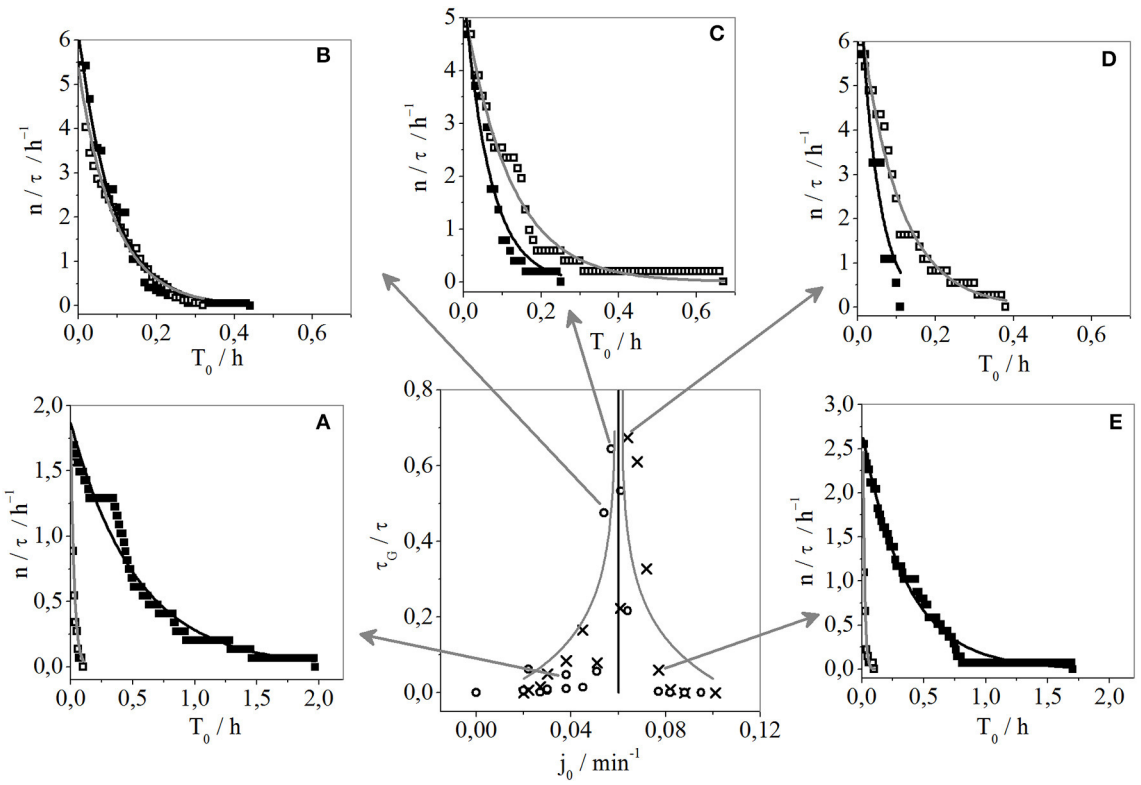


**FIGURE 6 |** Relative number of burst or gap packages per time $\tau$ (n/$\tau$) with duration $l > T_0$ (N($l > T_0$)/$\tau$) or, simply (n/$\tau$) where $n = N(l > T_0)$ obtained for selected specific flow rate experiments (see figure in the middle where fraction of time occupied by gaps ($\tau_G/\tau$) as a function of specific flow rate is presented) denoted by arrows: **(A)** 0.038 $min^{-1}$, **(B)** 0.054 $min^{-1}$, **(C)** 0.057 $min^{-1}$, **(D)** 0.064 $min^{-1}$, and **(E)** 0.077 $min^{-1}$. The number of burst packages longer than $T_0$ are marked with black squares and fitted with a black curve, while the number of gaps for $l > T_0$ are marked with empty squares and fitted with gray curves.

**TABLE 1 |** Values of fit parameters (q, p) and adjusted *R*-square ($R^2$), obtained for results given in **Figure 6** from (A–E).

| Case | $j_0/min^{-1}$ | $q_B$ | $q_G$ | $q_B/q_G$ | $p_B$ | $p_G$ | $R^2_B$ | $R^2_G$ |
|---|---|---|---|---|---|---|---|---|
| (A) | 0.038 | −1.889 | −36.79 | 0.0514 | 1.186 | 1.806 | 0.971 | 0.954 |
| (B) | 0.054 | −11.348 | −10.868 | 1.044 | 6.153 | 5.354 | 0.978 | 0.983 |
| (C) | 0.057 | −14.961 | −8.419 | 1.777 | 5.561 | 5.279 | 0.946 | 0.975 |
| (D) | 0.064 | −21.182 | −9.975 | 2.124 | 8.018 | 6.908 | 0.897 | 0.979 |
| (E) | 0.077 | −2.682 | −73.823 | 0.0363 | 2.693 | 5.147 | 0.986 | 0.994 |

*Letter B in subscript corresponds to results obtained by fitting the number of burst packages whose duration was longer than $T_0$, while letter G is related to the number of gap packages with duration longer $T_0$.*

## CONCLUSIONS

This study examined a mixture of two types of dynamic state (bursts and gaps), which were chaotically combined to create a new intermittent dynamic state. This new intermittent state was experimentally generated in the Bray-Liebhafsky (BL) oscillatory chemical reaction in CSTR under variations of the specific flow rate, using the following experimental conditions: $[KIO_3]_0 = 0.035\,M$, $[H_2SO_4]_0 = 0.077\,M$, $[H_2O_2]_0 = 0.240\,M$, $\sigma = 900$ rpm, $T = 63.0^oC$. We observed intermittent dynamic states between these two regular periodic oscillatory states. By analyzing the bifurcation points, we found that they emerge in the following range of specific flow rates, between around 0.020 and 0.082 $min^{-1}$.

In the intermittent region, chaotic complexity arises from both bifurcations, approaching a vertical asymptote that is somewhere between these flow rates, indicating a potential route to generating fully developed chaos. Hence, this study proposes that described route to fully developed chaos in the Bray-Liebhafsky oscillatory reaction is an explanation for experimentally observed intermittent dynamics.

This experiment obtained similar results to other previous studies, in which temperature and the inflow concentration of potassium iodate were taken as the control parameters

(Bubanja et al., 2016, 2017). If there is a basin where the experimentally intermittent chaos is obtained, changes of any control parameter will govern the system to the closest periodic state or stable steady state. Consequently, future studies could adopt similar methods for the examination and quantification of the intermittent dynamic states.

This study showed that experimentally generated intermittent chaos can be analyzed, not only by calculations of the largest Lyapunov exponents (λ) from experimentally obtained oscillograms but also by simple quantitative analysis of the characteristics of the evolution of BL reaction, including the length of bursts (packages of relaxing oscillations), and the lengths of gaps (between the periods of the sinusoid oscillations of relatively small amplitude, when compared to relaxing oscillations).

## DATA AVAILABILITY STATEMENT

The raw data supporting the conclusions of this article will be made available by the authors, without undue reservation.

## AUTHOR CONTRIBUTIONS

INB performed the Bray-Liebhafsky experiments in CSTR. AI-Š calculated the Lyapunov exponents from the oscillograms obtained by the experiment. All authors created and developed this experiment, including the phenomenological analysis of the recorded intermittencies, and contributed to its conclusions.

## FUNDING

This work was partially supported by the Ministry of Education, Science and Technological Development of the Republic of Serbia (Grant No. OI 172015 and III 45001. Contract numbers: 451-03-68/2020/14/200026 and 451-03-68/2020-14/200146).

## ACKNOWLEDGMENTS

The authors thank Profs. Stanley Furrow and Rinaldo Cervellati, whose joint experimental investigations of the intermittent phenomenon in the Briggs-Rausher reaction inspired us to further broaden investigations of this type of chaos.

## SUPPLEMENTARY MATERIAL

The Supplementary Material for this article can be found online at: https://www.frontiersin.org/articles/10.3389/fchem.2020.560274/full#supplementary-material

## REFERENCES

Anić, S., and Kolar-Anić, Lj. (1986). The oscillatory decomposition of $H_2O_2$ monitored by the potentiometric method with Pt and $Ag^+/S^{2-}$ indicator electrode. *Ber. Bunsenges. Phys. Chem.* 90, 1084–1086. doi: 10.1002/bbpc.19860901131

Anić, S., Mitić, D., Ćurčija, M. (1987). The Bray-Liebhafsky reaction. III. Oscillatory decomposition of $H_2O_2$ in the presence of comparatively high acidity. *J. Serb. Chem. Soc.* 52, 575–579.

Baier, G., Wegmann, K., and Hudson, J. L. (1989). An intermittent type of chaos in the Belousov-Zhabotinsky reaction. *Phys. Lett. A* 141, 340–345. doi: 10.1016/0375-9601(89)90061-3

Bray, W. C. (1921). A periodic reaction in homogeneous solution and its relation to catalysis. *J. Am. Chem. Soc.* 43, 1262–1267. doi: 10.1021/ja01439a007

Bray, W. C., and Liebhafsky, H. A. (1931). Reactions involving hydrogen peroxide, iodine and iodate ion. I. Introduction. *J. Am. Chem. Soc.* 53, 38–44. doi: 10.1021/ja01352a006

Bubanja, I. N., Ivanović-Šašić, A., Čupić, Ž., Anić, S., and Kolar-Anić, Lj. (2017). Intermittent chaos in the Bray-Liebhafsky oscillator. Dependence of dynamic states on the iodate concentration. *Russ. J. Phys. Chem. A* 91, 2525–2529. doi: 10.1134/S0036024417130076

Bubanja, I. N., Maćešić, S., Ivanović-Šašić, A., Čupić, Ž., Anić, S., and Kolar-Anić, Lj. (2016). Intermittent chaos in the Bray-Liebhafsky oscillator. Temperature dependence. *Phys. Chem. Chem. Phys.* 18, 9770–9778. doi: 10.1039/C6CP00759G

Cadena, A., Barragan, D., and Agreda, J. (2013). Bursting in the Belousov-Zhabotinsky reaction added with phenol in a batch reactor. *J. Braz. Chem. Soc.* 24, 2028–2032. doi: 10.5935/0103-5053.20130254

Chopin-Dumas, J. (1978). Diagramme d'etat de la reaction de Bray. *C. R. Acad. Sci.* 287C, 553–555.

Čupić, Ž., Kolar-Anić, Lj., Anić, S., Maćešić, S., Maksimović, J., Pavlović, M., et al. (2014). Regularity of intermittent bursts in Briggs-Rauscher oscillating systems with phenol. *Helv. Chim. Acta* 97, 321–333. doi: 10.1002/hlca.201300178

Dubois, M., Rubio, M. A., and Berge, P. (1983). Experimental evidence of intermittencies associated with a subharmonic bifurcation. *Phys. Rev. Lett.* 51, 1446–1449. doi: 10.1103/PhysRevLett.51.1446

Furrow, S. (1987). Reactions of iodine intermediates in iodate-hydrogen peroxide oscillators. *J. Phys. Chem.* 91, 2129–2135. doi: 10.1021/j100292a031

Furrow, S. D. (1985). "Chemical oscillators based on iodate ion and hydrogen peroxide," in *Oscillations and Traveling Waves in Chemical Systems*, eds. R. J. Field, M. Burger (New York, NY: Wiley), 171–192.

Hilborn, R. C. (2004). *Chaos and Nonlinear Dynamics: An Introduction for Scientists and Engineers, 2nd Edn.* Oxford: Oxford University Press.

Holló, G., Kály-Kullai, K., Lawson, T. B., Noszticzius, Z., Wittmann, M., Muntean, N., et al. (2014). HOI versus HOIO selectivity of a molten-type AgI electrode. *J. Phys. Chem. A* 118, 4670–4679. doi: 10.1021/jp504052w

Ivanović-Šašić, A., Marković, V. M., Anić, S. R., Kolar-Anić, Lj. Z., and Čupić, Ž. D. (2011). Structures of chaos in open reaction systems, Phys. *Chem. Chem. Phys.* 13, 20162–20171. doi: 10.1039/c1cp22496d

Izhikevich, E. M. (2000a). Neural excitability, spiking and bursting. *Int. J. Bifurcat. Chaos* 10, 1171–1266. doi: 10.1142/S0218127400000840

Izhikevich, E. M. (2000b). Subcritical elliptic bursting of Bautm type. *SIAM J. Appl. Math.* 60, 503–535. doi: 10.1137/S003613999833263X

Kolar-Anić, Lj., Anić, S., Čupić, Ž., Ivanović-Šašić, A., Pejić, N., Blagojević, S. I., et al. (2017). "Oscillating reactions," in *Encyclopedia of Physical Organic Chemistry, Volume 2, Part 2 Organic Reactions and Mechanisms*, ed. Z. Wang Z, U. Wille U, E. Juaristi (New York, NY: Wiley), 1127–1222.

Kolar-Anić, Lj., Vukojević, V., Pejić, N., Grozdić, T., and Anić, S. (2004). "Deterministic chaos in open well-stirred Bray-Liebhafsky reaction system" in: *Expermimental Chaos*, ed S. Boccaletti (Melville, NY: American Institute of Physics, AIP conference proceedings), 742, 3–8.

Kreisberg, K., McCormick, W. D., and Swinney, H. L. (1991). Experimental demonstration of subtleties in subharmonic intermittency. *Phys. D* 50, 463–477. doi: 10.1016/0167-2789(91)90010-7

Liebhafsky, H. A. (1931). Reactions involving hydrogen peroxide, iodine and iodate ion. IV. The oxidation of iodine to iodate ion by hydrogen

peroxide. *J. Am. Chem. Soc.* 53, 2074–2090. doi: 10.1021/ja01357a006

Nicolis, G., and Prigogine, I. (1989). *Exploring Complexity*. New York, NY: Freeman.

Pomeau, Y., and Manneville, P. (1980). Intermittent transition to turbulence in dissipative dynamical systems. *Commun. Math. Phys*. 74, 189–197. doi: 10.1007/BF01197757

Pomeau, Y., Roux, J. C., Rossi, A., Bachelart, S., and Vidal, C. (1981). Intermittent behavior in the Belousov-Zhabotinsky reaction. *J. Phys. Lett.* 42, 271–273. doi: 10.1051/jphyslet:019810042013027100

Roux, J. C., Rossi, A., Bachelart, S., and Vidal, C. (1981). Experimental observations of complex dynamical behavior during a chemical reaction. *Phys. D* 2, 395–403. doi: 10.1016/0167-2789(81)90018-X

Schuster, H. G., and Just, W. (2005). *Deterministic Chaos - An Introduction, 4th Edn*. Weinheim: Wiley-VCH.

Stanisavljev, D. R., Milenković, M. C., Popović -Bijelić, A. D., and Mojović, M. D. (2013). Radicals in the Bray-Liebhafsky oscillatory reaction. *J. Phys. Chem. A* 117, 3292–3295. doi: 10.1021/jp402381b

Strizhak, P., and Menzinger, M. (1996). Nonlinear dynamics of the BZ reaction: a simple experiment that illustrates limit cycles, chaos, bifurcations, and noise. *J. Chem. Educ*. 73, 868–873. doi: 10.1021/ed073p868

Vukojević, V., Anić, S., and Kolar-Anić, Lj. (2000). Investigation of dynamic behavior of the Bray–Liebhafsky reaction in the cstr. Determination of Bifurcation Points. *J. Phys. Chem. A* 104, 10731–10739. doi: 10.1021/jp001165x

Wolf, A., Swift, J. B., Swinney, H. L., and Vastno, J. A. (1985). Determining Lyapunov exponents from a time series. *Phys. D*. 16, 285–317. doi: 10.1016/0167-2789(85)90011-9

Woodson H. J., and Liebhafsky H. A. (1969). Pulses in iodide concentrations during the peroxide decomposition of hydrogen peroxide. *Nature* 224:690. doi: 10.1038/224690a0

**Conflict of Interest:** The authors declare that the research was conducted in the absence of any commercial or financial relationships that could be construed as a potential conflict of interest.

*Copyright © 2020 Bubanja, Ivanović-Šašić, Čupić, Anić and Kolar-Anić. This is an open-access article distributed under the terms of the Creative Commons Attribution License (CC BY). The use, distribution or reproduction in other forums is permitted, provided the original author(s) and the copyright owner(s) are credited and that the original publication in this journal is cited, in accordance with accepted academic practice. No use, distribution or reproduction is permitted which does not comply with these terms.*

frontiers in Chemistry

ORIGINAL RESEARCH
published: 28 October 2020
doi: 10.3389/fchem.2020.526679

# *In silico* Determination of Some Conditions Leading to Glycolytic Oscillations and Their Interference With Some Other Processes in *E. coli* Cells

*Gheorghe Maria* [1,2]*

[1] Department of Chemical and Biochemical Engineering, University POLITEHNICA of Bucharest, Bucharest, Romania,
[2] Chemical Sciences Section, Romanian Academy, Bucharest, Romania

Autonomous oscillations of species levels in the glycolysis express the self-control of this essential cellular pathway belonging to the central carbon metabolism (CCM), and this phenomenon takes place in a large number of bacteria. Oscillations of glycolytic intermediates in living cells occur according to the environmental conditions and to the cell characteristics, especially the adenosine triphosphate (ATP) recovery system. Determining the conditions that lead to the occurrence and maintenance of the glycolytic oscillations can present immediate practical applications. Such a model-based analysis allows *in silico* (model-based) design of genetically modified microorganisms (GMO) with certain characteristics of interest for the biosynthesis industry, medicine, etc. Based on our kinetic model validated in previous works, this paper aims to *in silico* identify operating parameters and cell factors leading to the occurrence of stable glycolytic oscillations in the *Escherichia coli* cells. As long as most of the glycolytic intermediates are involved in various cellular metabolic pathways belonging to the CCM, evaluation of the dynamics and average level of its intermediates is of high importance for further applicative analyses. As an example, by using a lumped kinetic model for tryptophan (TRP) synthesis from literature, and its own kinetic model for the oscillatory glycolysis, this paper highlights the influence of glycolytic oscillations on the oscillatory TRP synthesis through the PEP (phosphoenolpyruvate) glycolytic node shared by the two oscillatory processes. The numerical analysis allows further TRP production maximization in a fed-batch bioreactor (FBR).

**Keywords: glycolysis, tryptophan synthesis, *Escherichia coli*, oscillation occurrence, kinetic models, tryptophan synthesis oscillations, bioreactor sensitivity**

OPEN ACCESS

***Edited by:***
*Irving Robert Epstein, Brandeis University, United States*

***Reviewed by:***
*Valentina Venuti, University of Messina, Italy*
*Arthur Sherman, National Institutes of Health (NIH), United States*

***Correspondence:**
*Gheorghe Maria*
*gmaria99m@hotmail.com*

***Specialty section:***
*This article was submitted to Physical Chemistry and Chemical Physics, a section of the journal Frontiers in Chemistry*

***Received:*** *14 January 2020*
***Accepted:*** *23 September 2020*
***Published:*** *28 October 2020*

***Citation:***
*Maria G (2020) In silico Determination of Some Conditions Leading to Glycolytic Oscillations and Their Interference With Some Other Processes in E. coli Cells. Front. Chem. 8:526679. doi: 10.3389/fchem.2020.526679*

## INTRODUCTION

"Autonomous oscillations of species levels in the glycolysis express the self-control of this essential cellular pathway belonging to the CCM, and this phenomenon takes place in a large number of bacteria.

The study of glycolytic oscillations might, therefore, prove crucial for the general understanding of the cell metabolism regulation and the connections among different parts of metabolism. The

key question in this context is the mechanism of the oscillations but, despite much work over the last 40 years, it remains unsettled (Wierschem and Bertram, 2004; Madsen et al., 2005).

A model able to simulate the dynamics of the cell CCM must include linked modules relating to (i) the glycolysis (**Figures 1**, **2**); (ii) the phosphotransferase (PTS) system for GLC import into the cell (**Figure 1**); (iii) the pentose-phosphate pathway (PPP) to generate NADPH and pentoses (5-carbonsugars), as well as ribose 5-phosphate (R5P, a precursor for the synthesis of nucleotides); (iv) the tricarboxylic acid cycle (TCA); (v) the ATP recovery system, and several other pathways" (Palsson, 2005; Kadir et al., 2010; KEGG, 2011; Maria, 2018).

"Modeling bacteria CCM, or parts of CCM, is a subject of very high interest, because the CCM is the essential part of any systematic and structured (model-based) analysis of the cell metabolism with immediate applications, such as biosynthesis optimization, metabolic fluxes evaluation (Stephanopoulos et al., 1998), model-based design of GMO with target characteristics of various applications in the industry, medicine, etc. (Hatzimanikatis et al., 1996; Visser et al., 2004; Styczynski and Stephanopoulos, 2005; Hempel, 2006; Maria and Luta, 2013; Maria, 2018)." Modeling of the CCM kinetics in close connection to the bioreactor environment dynamics falls at the border of several research areas, that is: (bio)chemical physics, computational biochemistry, biochemical engineering, and physical (bio)chemistry.

"To cope with the very high complexity of cell metabolic processes, involving ca. $10^4$ species concentrations, $10^3$ gene expression transcription factors, and ca. $10^5$ enzymatic reactions, adaptable reduced dynamic models, of 'building-blocks' like modular construction, have been developed over the last decades (reviews of Maria, 2017a,b), with including individual/lumped species and/or reactions.

Modeling the glycolysis dynamics is of particular interest, because most of its intermediates are starting points for the cell production of various metabolites of industrial/medical use (e.g., amino acids, succinate, citrate, etc.; Maria, 2018).

By using two adequate dynamic models validated in previous studies (**Tables 2**, **3**), this paper exemplifies how the model-based analysis can be used (i) to predict some of the internal/environmental conditions inducing glycolytic oscillations in the *Escherichia coli* culture grown in a fed-batch bioreactor (FBR), and (ii) to simulate the influence of the glycolytic oscillations on the TRP oscillatory synthesis by means of the key-species PEP shared by the two oscillatory processes. Industrial applications are immediate seeking for the TRP production optimization. The glycolytic oscillations occurrence will be analyzed vs. external ([GLC]ex in the bulk-phase), and internal factors (that is the ATP recovery rate, dependent on the cell phenotype) (Mathews et al., 1999; Maria, 2014)." The main elements of novelty of this paper consists in the following: (i) Testing and highlighting the influence of the connection of the two metabolic pathways (glycolysis and TRP synthesis), of the external factors ([GLC]ex in the bulk phase, cell dilution rate ($\mu$) adjusted to be equal to the bioreactor dilution rate $D$), and of the cell internal factors (activity of some enzymes in the ATP recovery system) on the two approached oscillatory processes in *E. coli* cells. Several operating policies have been checked in this respect (ii) to eventually suggest how to modulate these most influential factors ([GLC]ex, k6, $D = \mu$, and others) before deriving a future optimal operating policy of the FBR (by obtaining, for instance, a timestep-wise GLC feeding policy, not approached here) leading to maximization of the TRP synthesis; (iii) accomplishment of the sensitivity analysis of the studied FBR, which is the preliminary step for any future TRP bioreactor production maximization.

## THE TESTED FBR BIOREACTOR

"The *in silico* study of the glycolytic oscillations connected to the TRP synthesis dynamics is performed by considering a FBR with a suspended *E. coli* cell culture, operated with the initial/nominal conditions given in **Table 1**. It is worth mentioning that the bioreactor includes an excess of sparged air and necessary nutrients for a balanced growth of the cell culture. This FBR was used by Chassagnole et al. (2002) to develop experimental kinetic studies to validate their CCM model (denoted here by CHASSM). The same experiments have also been used by Maria (2014) to validate his reduced kinetic model of glycolysis (denoted here by MGM)."

The adopted FBR model of **Table 2** "is a classical one (Moser, 1988), developed with the following main hypotheses: (i) the operation is isothermal, iso-pH, and iso-DO (dissolved oxygen); (ii) nutrients are added to the FBR, in recommended quantities, together with an aeration in excess for ensuring an optimal biomass maintenance; (iii) a perfectly mixed liquid phase (with no concentration gradients). The mass balance equations account for the main species in the FBR bulk and of the cellular ones referring to the glycolysis and TRP synthesis dynamics. The resulting ODE model of the FBR (**Table 2**) also includes the process kinetics (species dynamics). To obtain the species time trajectories with a satisfactory accuracy, by using **Table 1** (or other) initial conditions, a low-order stiff integrator (ODE23S) of the Matlab™ software was used" (Maria et al., 2018b,c).

## DYNAMIC MODELS FOR THE OSCILLATORY GLYCOLYSIS AND FOR THE OSCILLATORY TRP SYNTHESIS IN THE *E. COLI* CELLS

### Glycolysis Model

"Glycolysis is a sequence of enzymatic reactions (**Figures 1**, **2**) that converts glucose (GLC) into pyruvate (PYR). The free energy released by the subsequent TCA originating from PYR is used to form the high-energy molecules ATP, and NADH that support the glycolysis and the other enzymatic reactions into the cell (Mathews et al., 1999). Consequently, an adequate modeling/simulation of the glycolysis kinetics is of high importance because its intermediates are entry/exit points to/from glycolysis. For instance, most of the monosaccharides, such as fructose or galactose, can be converted to one of these intermediates. In turn, glycolytic intermediates are directly used in subsequent metabolic pathways. For example, DHAP (an

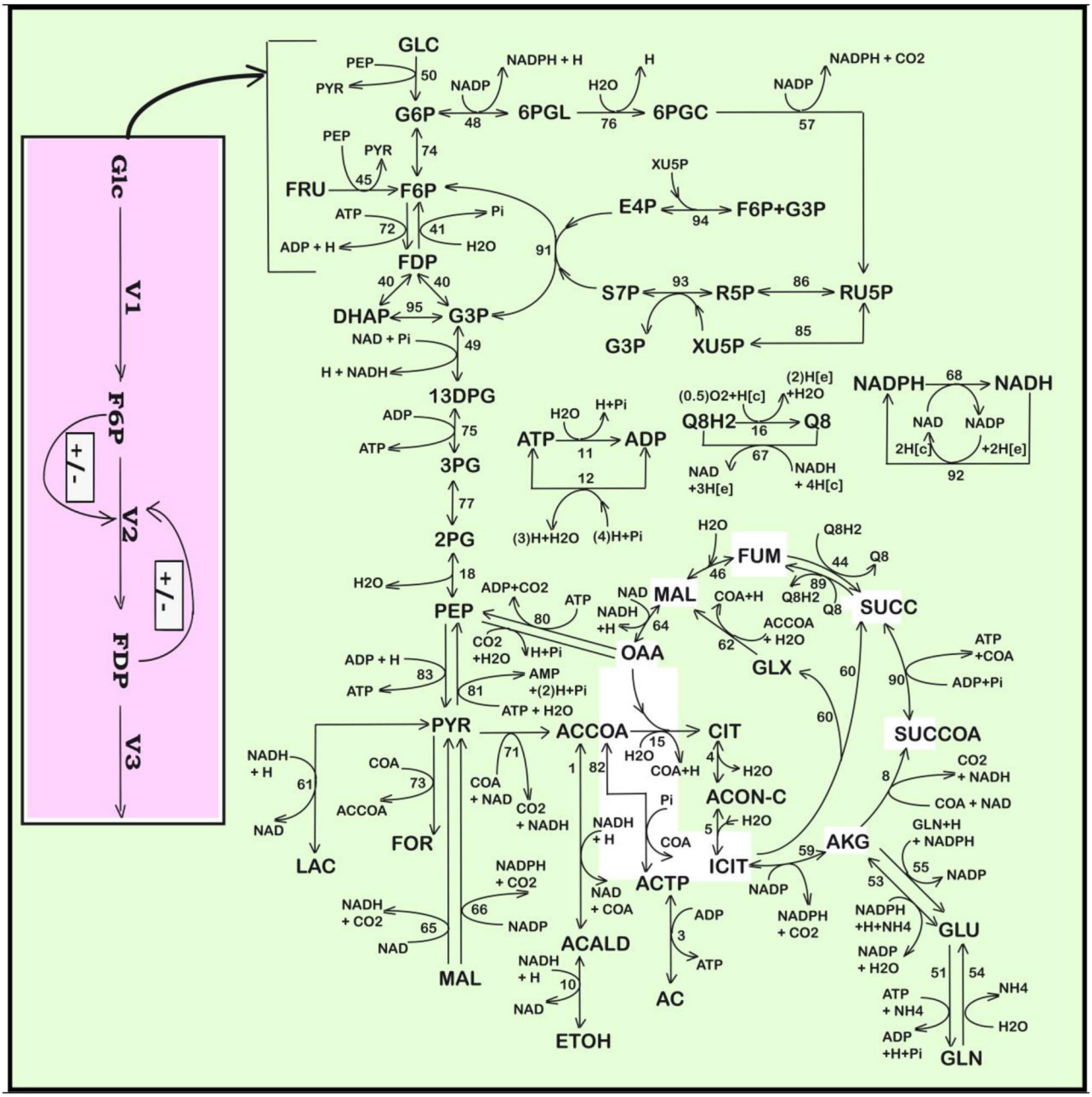


**FIGURE 1 |** Simplified representation of the CCM pathway in *E. coli* of Edwards and Palsson (2000). Fluxes characterizing the membranar transport [*Metabolite*(e) ↔ *Metabolite*(c)] and the exchange with environment have been omitted from the plot (see Maria et al., 2011 for details, and for explanations regarding the numbered reactions). [e], environment; [c], cytosol. Adapted from Maria et al. (2011, 2018c) courtesy of CABEQ JI. The considered 72 metabolites, the stoichiometry of the 95 numbered reactions, and the net fluxes for specified conditions are given by Maria et al. (2011). The pink rectangle indicates the chemical node inducing glycolytic oscillations (after Termonia and Ross, 1981a,b; see also Maria et al., 2018c). Notations + and − denote the feedback positive or negative regulatory loops, respectively. Glc, glucose; F6P, fructose-6-phosphate; FDP, fructose-1,6-biphosphate; V1–V3, reaction rates indicated in **Figure 2**.

intermediate in the F6P conversion to G3P in **Figure 1**) is a source of the glycerol that combines with fatty acids to form fat. In addition, NADPH is also formed by the PPP, which converts GLC into R5P, which is used in the synthesis of nucleotides and nucleic acids. PEP is, as well, the starting point for the synthesis of essential amino acids (AA) such as TRP, cysteine, arginine, serine, etc. (Calhoun and Swartz, 2006; Maria et al., 2018a)."

"Due to the huge importance of the glycolysis in simulating the CCM dynamics, intense efforts have been invested both in the experimental study and in modeling of its dynamics in various

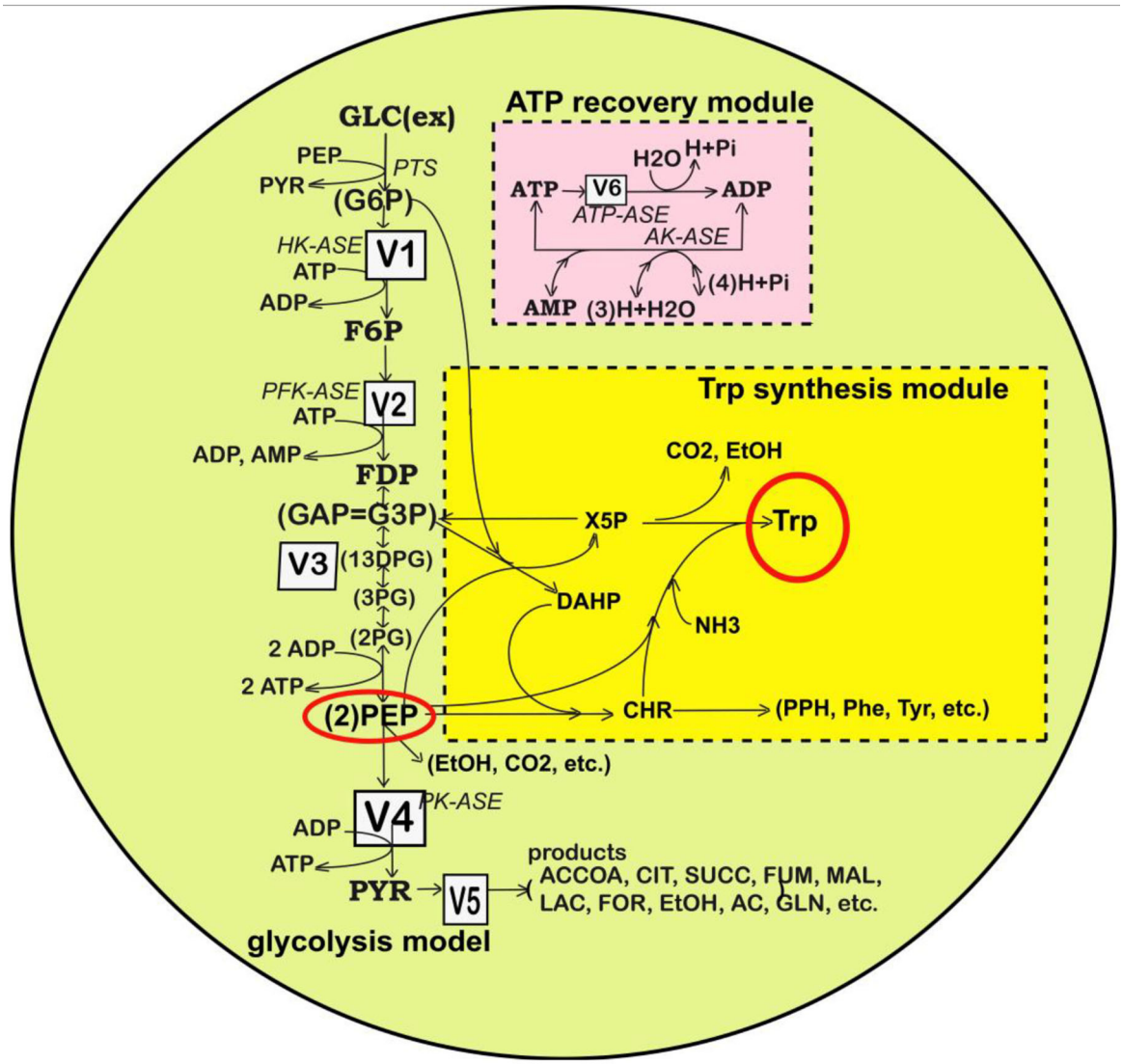


**FIGURE 2 |** Simplified representation of the structured reaction pathway of glycolysis (Maria, 2014), and of the TRP synthesis (in the yellow area) (Maria et al., 2018a) in *E. coli* used by Maria et al. (2018a,b,c) to derive the process kinetic model and the operating conditions of the fed-batch bioreactor that maximize the TRP synthesis. Connection of the TRP synthesis to glycolysis is realized through the PEP node (Maria et al., 2018c; Mihalachi and Maria, 2019). The modular model structure also includes the adenosine co-metabolites ATP, ADP, and AMP synthesis as part of the ATP recovery system (the pink rectangle). Notations: Species in parenthesis are not explicitly included in the glycolysis model. Italic letters denote the enzymes. Squares include notations of enzymatic reactions V1–V5 included in the glycolysis model. Adapted from Maria (2014; 2018b) courtesy of CABEQ JI. GLC(ex), glucose in the cell environment; G6P, glucose-6-phosphate; F6P, fructose-6-phosphate; *HK-ASE*, hexokinase; *PFK-ASE*, phosphofructokinase; *ATP-ASE*, ATP monophosphatase; ADP, adenosine diphosphate; ATP, adenosine triphosphate; AMP, adenosine monophosphate; *AK-ASE*, adenylate kinase; Pi, phosphoric acid; FDP, fructose-1,6-biphosphate; G3P,GAP, glyceraldehyde-3-phosphate; 13DPG=PGP, 1,3-diphosphoglycerate; 3PG, 3-phosphoglycerate; 2PG, 2-phosphoglycerate; PEP, phosphoenolpyruvate; PYR, pyruvate; SUCC, succinate; NAD(P)H, nicotinamide adenine dinucleotide (phosphate) reduced; CIT, citrate; ACCOA, acetyl-coenzyme A; LAC, lactate; ETOH, ethanol; AC, acetate.

bacteria (Reeves and Sols, 1973; Bennett et al., 2009; Flamholz et al., 2013; Alberton et al., 2015)."

"However, modeling in detail the glycolysis kinetics and its regulation is a difficult task due to its high complexity. Despite these difficulties, a large number of extended/lumped kinetic models have been proposed (some of them being mentioned in **Outline 1**) of a complexity varying in the range of 18–30 key species and 48–52 key reactions, with a total of 24–300 or more rate constants. Most of these models are however too complex to be easy to use and identified. Besides, their adequacy is not always satisfactory. Thus, with few exceptions, most of the mentioned models cannot satisfactorily simulate the glycolytic oscillations on a deterministic basis" (Maria, 2014; Mihalachi and Maria, 2019).

Starting from the reaction pathway of **Figure 1**, from the CHASSM and other kinetic models (**Outline 1**), and by

**TABLE 1 |** The nominal operating conditions of Chassagnole et al. (2002) and Maria et al. (2018a) for the FBR with suspended *E. coli* cell culture used to simulate the glycolytic and TRP synthesis processes.

| The fed-batch (FBR) bioreactor initial conditions | | |
|---|---|---|
| **Parameter** | **Nominal value** | **Obs.** |
| Biomass concentration ($C_x$) | 8.7 gDW $L^{-1}$ culture volume | (Chassagnole et al., 2002) assumed to be quasi-constant |
| Batch time | 100 min | |
| Cell content dilution rate ($\mu$) | $10^{-4}$-$10^{-2}$ $min^{-1}$ | To be optimized and adjusted to be identical to $D$ |
| Bioreactor dilution, $D = F_L/V_L$ | $10^{-4}$-$10^{-2}$ $min^{-1}$ (identical to $\mu$) | To be optimized (nominal $1.667 \cdot 10^{-3}$ $min^{-1}$) |
| Glucose feeding solution concentration $C_{GLC}^{feed}$ | 100–200, mM | 200 mM (this paper) To be optimized |
| Initial glucose concentration in the bioreactor $C_{GLC}^{ext}(t=0)$ | 0.0557–1, mM (Chassagnole et al., 2002) | 0.05–1.5 mM (this paper) to be optimized |
| Biomass density ($\rho_x$) | 565.5 gDW (L cytosol)$^{-1}$ | |
| Initial concentrations for the glycolysis species (in mM) | $c_{GLC}^{ext}(t=0) = 0.0557$<br>$c_{F6P}(t=0) = 0.600325977$<br>$c_{FDP}(t=0) = 0.272961814$<br>$c_{PEP}(t=0) = 2.67294507$<br>$c_{PYR}(t=0) = 2.67061526$<br>$c_{ATP}(t=0) = 4.27$<br>[AMDTP] total = 5.82 | Measured by Chassagnole et al. (2002) |
| Initial concentrations for the TRP synthesis (in $\mu$M) | $c_{OR}(t=0) = 0.01$<br>$c_{MRNA}(t=0) = 0.01$<br>$c_E\ (t=0) = k_3 c_{MRNA,o}/\mu$<br>$c_T\ (t=0) = 0.01$ | Measured by Bhartiya et al. (2006) |

applying advanced lumping algorithms belonging to the physical chemistry (based on species lumping rules with preserving the chemical reaction invariants) (see details of Maria, 2004, 2005), Maria (2014) obtained a reduced kinetic model (that is the MGM) of the glycolysis. The MGM (adopted here) "is accounting for 9 key species, 7 lumped reactions, and includes 17 rate constants (**Table 2**). Its parameters have been estimated by using the experimental kinetic data of Chassagnole et al. (2002) and Visser et al. (2004)."

The MGM model proved that "it can satisfactorily simulate the dynamics of the glycolytic species concentrations (steady-state QSS, oscillatory, or transient) according to various internal/external regimes, related to (i) the GLC concentration level/dynamics in the bioreactor, (ii) the cell total energy resources in A(MDT)P, and (iii) the cell phenotype responsible for activity of the enzymes involved in the ATP utilization/recovery system. The MGM has been inserted in the bioreactor model template (**Table 2**) when simulating the dynamics of the [GLC] in the liquid phase simultaneously with that of the cell metabolites. A direct connection between the macro-scale (bioreactor bulk-phase) and the nano-scale (cellular) process variables is thus realized."

According to Franck (1980), "oscillations in chemical systems represent periodic transitions in time of species concentrations. Thus, spontaneous occurrence of self-sustained oscillations in chemical systems is due the coupled actions of at least two simultaneous processes. Oscillations sourced in a so-called *oscillation node* (that is, a chemical species or a reaction), on which concomitant rapid positive (perturbing) and slow negative (recovering) regulatory loops act (see the discussion of Maria et al., 2018c on the glycolytic oscillation occurrence). Because the coupling action between the simultaneous processes is mutual, the total coupling effect actually forms closed feedback loops for each kinetic variable involved. There exists a well-established set of essential thermodynamic and kinetics prerequisites for the occurrence of spontaneous oscillations, as well as their consequences, extensively discussed by Franck (1980) and Maria et al. (2018c)."

"In the glycolysis case, oscillations is due to the antagonistic action of two processes on regulating the V2 reaction rate (i.e., the oscillation node; Termonia and Ross, 1981a,b, 1982; Maria et al., 2018c). The V2 reaction converts F6P in FDP (see the pink rectangle of **Figure 1**, including a lumped representation of the glycolytic oscillations node). Glycolytic oscillations properties (period, amplitude) are determined by both external and internal (phenotype) factors. According to Maria (2014) and Maria et al. (2018a,b,c), the glycolysis dynamics [quasi-steady state (QSS) or oscillatory] depends on several factors:"

i) The glucose level in the liquid-phase {denoted by [GLC]ex}, which varies according to the FBR operating conditions;
ii) "The efficiency and the dynamics of the whole ATP recovery system. Among the involved parameters, an essential one is the k6 rate constant (related to the *ATP-ase* characteristics in **Figure 2**). The involved enzyme characteristics are determined by the cell phenotype (genom) controlling the total energy resources. To not complicate our simulations, the [AMDTP] level was kept unchanged in the present analysis at the value given in **Table 1**" (Maria, 2004).
iii) "As an important remark, the glycolysis is a systemic process, with a complex regulatory structure. Consequently, oscillations are also related to the rate constants of all the

**TABLE 2 |** Species mass balance in the FBR model describing the dynamics of the cellular glycolysis species according to the MGM kinetic model of Maria (2014).

**Mass balance of the main glycolytic species in the living cells of the FBR**

$GLC + PEP \rightarrow F6P + PYR$
$PYR + ATP \rightarrow PEP + ADP + H$
$GLC + ATP \rightarrow F6P + ADP + H$

$$\frac{dc_{GLC}^{ext}}{dt} = D\left(c_{GLC}^{feed} - c_{GLC}^{ext}\right) - \frac{C_x}{\rho_x} V_1$$

$$V_1 = r_{PTS} = \frac{\rho_x}{C_x} \cdot \frac{r_{PTS}^{max} c_{GLC}^{ext} c_{PEP}/c_{PYR}}{\left(K_{PTS,a1} + K_{PTS,a2}\frac{c_{PEP}}{c_{PYR}} + K_{PTS,a3} c_{GLC}^{ext} + c_{GLC}^{ext}\frac{c_{PEP}}{c_{PYR}}\right)\left(1 + \frac{c_{G6P}^{n_{PTS,G6P}}}{K_{PTS,G6P}}\right)}$$

$F6P + ATP \rightarrow FDP + ADP + H$

$$\frac{dc_{F6P}}{dt} = V_1 - V_2 - Dc_{F6P}$$

$$V_2 = r_{PFK} = \frac{(V_1/V_{2m})\, c_{F6P}^{\delta}}{\left(K_{2m}^{\delta} + K_{2m}^{\delta}\left[\frac{K_R^{AMP}}{K_T^{ATP}}\right]^n \left(\frac{c_{ATP}}{c_{AMP}}\right)^n + c_{F6P}^{\delta}\right)}$$

$FDP + 2ADP(+2NAD + 2P) \Leftrightarrow$
$2PEP + 2ATP(+2NADH + 2H + 2H2O)$

$$\frac{dc_{FDP}}{dt} = V_2 - V_3 - Dc_{FDP}$$

$$V_3 = k_3 c_{FDP}^{\alpha} - k_{3p} c_{PEP}^{\beta}$$

$PEP + ADP + H \rightarrow PYR + ATP$

$$\frac{dc_{PYR}}{dt} = V_4 - V_5 - Dc_{PYR}$$

$$V_4 = r_{PK} = \frac{(V_1/V_{4m}) c_{PEP}^{\gamma}}{\left(K_{4m}^{\gamma} + K_{4m}^{\gamma}\left[\frac{K_R^{FDP}}{K_{T,PK}^{ATP}}\right]^m \left(\frac{c_{ATP}}{c_{FDP}}\right)^m + c_{PEP}^{\gamma}\right)}$$

$PYR \rightarrow products(ACCOA, CIT, SUCC, LAC, ETOH, AC, \ldots)$

$$V_5 = \frac{k_5 c_{PYR}^{n_{consum,PYR}}}{K_{consum,PYR} + c_{PYR}}$$

$ATP \rightarrow ADP + H$

$$\frac{dc_{ATP}}{dt} = -V_1 - V_2 + 2\,V_3 + V_4 - V_6 - Dc_{ATP}$$

$$V_6 = k_6 c_{ATP}$$

*Obs.:* k6 takes values according to the micro-organism phenotype (characteristics of the gene encoding the enzyme *ATPase* that catalyze this reaction).

$2ADP \Leftrightarrow ATP + AMP$

$$c_{ATP} c_{AMP} = K c_{ADP}^2$$

*Obs.:* (i) Termonia and Ross (1981a,b, 1982) indicated experimental evidence of a very fast reversible reaction catalyzed by *AKase*, the equilibrium being quickly reached.

(ii) $c_{AMP} + c_{ADP} + c_{ATP} = c_{AMDTP}$ = constant (Termonia and Ross, 1981a,b, 1982).

(iii) $c_{ADP}$ results from solving the thermodynamic equilibrium relationship $c_{ATP} c_{AMP} = K c_{ADP}^2$, that is: $c_{ADP}^2 \frac{K}{c_{ATP}} + c_{ADP} - c_{AMDTP} + c_{ATP} = 0$

(iv) Product formation from PYR has been neglected in the model.

$$\frac{dc_{PEP}}{dt} = 2\,V_3 - V_4 - Dc_{PEP} - y_{trp}(2\,V_3)$$

Completion with terms accounting for the PEP consumption in the TRP synthesis:
$y_{trp} = {}^{r_{syn,trp}}\!/_{r_{syn,pep}} = 1/43.63$ (at QSS), from Stephanopoulos and Simpson (1997)

*The glycolysis kinetic model also includes the modification of Maria et al. (2018a) when coupling with the TRP synthesis model. The model parameters are given by Maria (2014; 2018a). Notations are given in the* ***Figure 2*** *caption.*

involved reactions, and their appropriate ratios (depending on the enzymes' activity of each microorganism)" (Maria et al., 2018c).

## TRP Synthesis Model

"TRP is an aromatic non-polar α-amino-acid essential in humans that is used in the cell biosynthesis of proteins, being also a precursor to the neuro-transmitter serotonin, of the melatonin hormone, and of vitamin PP. Therefore, maximizing its production via model-based analyses is of particular industrial interest" (Slominski et al., 2002).

"The TRP operon of *E. coli* is one of the most extensively studied molecular regulatory systems (Hernandez-Valdez et al., 2010). The TRP synthesis is known as being an oscillatory process. However, due to the process high complexity, only reduced dynamic models involving lumped reactions/species are used, the regulatory performance being included in adjustable model terms and rate constants. For this reason, in the present analysis, the *in silico* simulation of the TRP synthesis was performed by using the lumped kinetic model of Maria et al. (2018a,b).

This kinetic model is based on the simplified TRP synthesis scheme displayed in **Figure 2**, derived from various studies reviewed by Maria et al. (2018a). The adopted model for the TRP synthesis, presented in **Table 3**, is a modification of the Bhartiya et al. (2006) model in order to better fit the experimental kinetic curves of the key species {OR, mRNA, T, E}. Besides, the model was explicitly connected to the glycolysis (as displayed in **Figure 2**), by including in the TRP mass-balance [i.e., ($dc_T/dt$) term in **Table 3**] a term accounting for the PEP precursor, while the PEP consumption term is included in the PEP balance of the MGM model (**Table 2**). Other dynamic models for the TRP synthesis module are reviewed by Maria et al. (2018a,b)."

**TABLE 3 |** The TRP synthesis kinetic model of Maria et al. (2018a) modified to be coupled with the glycolysis model.

**Mass balance of the main species involved in the TRP synthesis in the living cells of FBR**

$$\frac{dc_{OR}}{dt} = k_1 c_{OT} C_1(T) - k_{d1}\, c_{OR} - D c_{OR}$$
$$\frac{dc_{MRNA}}{dt} = k_2 c_{OR} C_2(T) - k_{d2}\, c_{MRNA} - D c_{MRNA}$$
$$\frac{dc_E}{dt} = k_3\, c_{MRNA} - D c_E$$
$$\frac{dc_T}{dt} = k_4 c_{PEP} C_3(T)\, c_E - \frac{g_* T}{T + K_g} - D c_T$$

$$C_1(T) = \frac{K_{i,1}^{\eta_H}}{K_{i,1}^{\eta_H} + T^{\eta_H}}$$
$$C_2(T) = \frac{K_{i,2}^{1.72}}{K_{i,2}^{1.72} + T^{1.72}}$$
$$C_3(T) = \frac{K_{i,3}^{1.2}}{K_{i,3}^{1.2} + T^{1.2}}$$

Obs. The nitrogen source in the TRP synthesis is considered in excess and included in the $k_4$ constant. To be connected to the glycolysis kinetic model, the PEP concentration kinetic trajectory generated by the glycolysis model was explicitly included in the TRP synthesis rate.

*Model parameters are given by Maria et al. (2018a). Notations: TRP, tryptophan; OR, the complex between O and R (aporepressor of the TRP gene); OT, total TRP operon; MRNA, tryptophan mRNA during its encoding gene dynamic transcription and translation; E, enzyme anthranilate synthase; T, TRP; QSS, quasi-steady state.*

**TABLE Outline 1 |** Some dynamic models of glycolysis from the literature.

| References | Oscill.? | Species no. | Reaction no. | Param. no. |
|---|---|---|---|---|
| Sel'kov (1968) | | 5 | 5 | ? |
| Termonia and Ross (1981a,b); Termonia and Ross (1982) | | 9 | 7 | 19 |
| Maria (2014) (MGM) | | 9 | 6 | 19 |
| Hatzimanikatis and Bailey (1997) | N | 6 | 9 | ? |
| Bier et al. (1996) | | 7 | 11 | 17 |
| Buchholz et al. (2002) | N | 3 | 5 | 24 |
| Chassagnole et al. (2002) (CHASSM) | N | 18 | 48 | 127 |
| Westermark and Lansner (2003) | | 6 | 6 | >30 |
| Degenring et al. (2004) | N | 10 | 22 | 123 |
| Costa et al. (2008) | N | 25 | 30 | 116 |
| Costa et al. (2010) | N | 18 | 30 | 110–116 |
| Kadir et al. (2010) | | 24 | 30 | >>300 |
| Peskov et al. (2012) | N | 48 | 75+8 | >200 (?) |

*Some of them include additional modules from the CCM. (N) Indicates the kinetic models not being able to simulate the glycolysis oscillation occurrence (Maria et al., 2011).*

# RESULTS AND DISCUSSION

## Glycolytic Oscillations

Repeated simulations of the bioreactor dynamics using the FBR/MGM kinetic models, with the initial conditions of **Table 1** and the parametric ranges of [GLC]ex ∈ [0.01–1.5] mM (at $t = 0$), and k6 ∈ [$10^{-5}$-20] $min^{-1}$ lead to the following results (Maria et al., 2018a,b,c):

i) "Several glycolytic stationary oscillations domains exist in the *E. coli* cells, as indicated by the thick lines of **Figure 3F** plotted in the {[GLC]ex vs. k6} coordinates.

ii) As displayed in **Figure 3F**, glycolytic stationary oscillations occur for a slow GLC import not only due to a low [GLC]ex level in the environment but also due to small k6 constant values (that correspond to a low recovery rate of the ATP). Conversely, higher concentrations of GLC in the bioreactor will trigger higher GLC import rates. In this case, glycolytic oscillations are also possible if the k6 constant reported large values (for a certain K constant controlling the AMDTP pathway/equilibrium given in the **Table 2**). However, the ATP recovery rate is limited by the AMDTP resources and by the interconversion balance of the AMDTP system (**Figures 1**, **2** and **Table 2**). As reported by Maria et al. (2018a,b,c), in the cells with too small, or too large k6 values, the glycolysis often reaches its (non-oscillatory) steady state."

iii) The "glycolytic oscillation domains plotted in **Figure 3F** are very narrow. Such a result reflects their high sensitivity vs. lots of external and internal factors. Besides, oscillations present a poor stability vs. internal/external factors, as proved by the plotted limit cycles (omitted here; see Maria et al., 2018a,b,c). Experiments in the literature have found that this stability is dependent on the metabolism characteristics of every microorganism. For instance, by contrast, the glycolytic oscillations in yeast have been proved to be very robust even in the presence of environmental noise, with oscillations being a side effect of the trade-offs between robustness and regulatory efficiency of the feedback control of the autocatalytic reaction network (Chandra et al., 2011; Gehrmann et al., 2011)."

iv) The numerical analysis results also indicated that "larger values of k6 lead to a slight decrease in the oscillation period and, eventually, the oscillation disappearance. This is due to the quick consumption of GLC by the cells following a more rapid ATP recovery system (Maria et al., 2018c)."

v) FBR dynamic simulations "have identified glycolytic oscillations with a period of 0.4–1 min, depending on the k6 value and on the [Glc]ex level. For comparison, various experiments in the literature have reported periods in a large range, that is: 0.2 min (Madsen et al., 2005), 2–100 s (Westermark and Lansner, 2003), 15 s (Silva and Yunes, 2006), 1–20 min (Bier et al., 1996), up to 3 h (Rapp, 1979), or 0.2 min to h (Diaz Ricci, 2000)."

vi) The simulated glycolytic oscillations of **Figure 3** (FDP and F6P species) are similar to the experimentally recorded dynamics by Schaefer et al. (1999) and Chiarugi et al. (2006) and also similar to the dynamic simulations of Sel'kov (1968), Bier et al. (1996), Elias (2010), and de la Fuente (2010). In fact, **Figures 3A–E** display an incipient phase of the oscillation occurrence, when the species oscillation amplitude grows. However, over a longer time domain (not shown here), the oscillations stabilize and become stationary.

vii) "The simulated [GLC]ex dynamics in the FBR proved that, for a relatively high [GLC] = 200 mM in the feed, and for all the abovementioned ranges of internal/external operating conditions, the bioreactor evolution is always toward a steady state (QSS), with a faster or slower rate depending on the initial [GLC] in the bioreactor, irrespectively to the cell metabolism (stationary/homeostatic, or unbalanced) (Maria et al., 2018a,b,c).

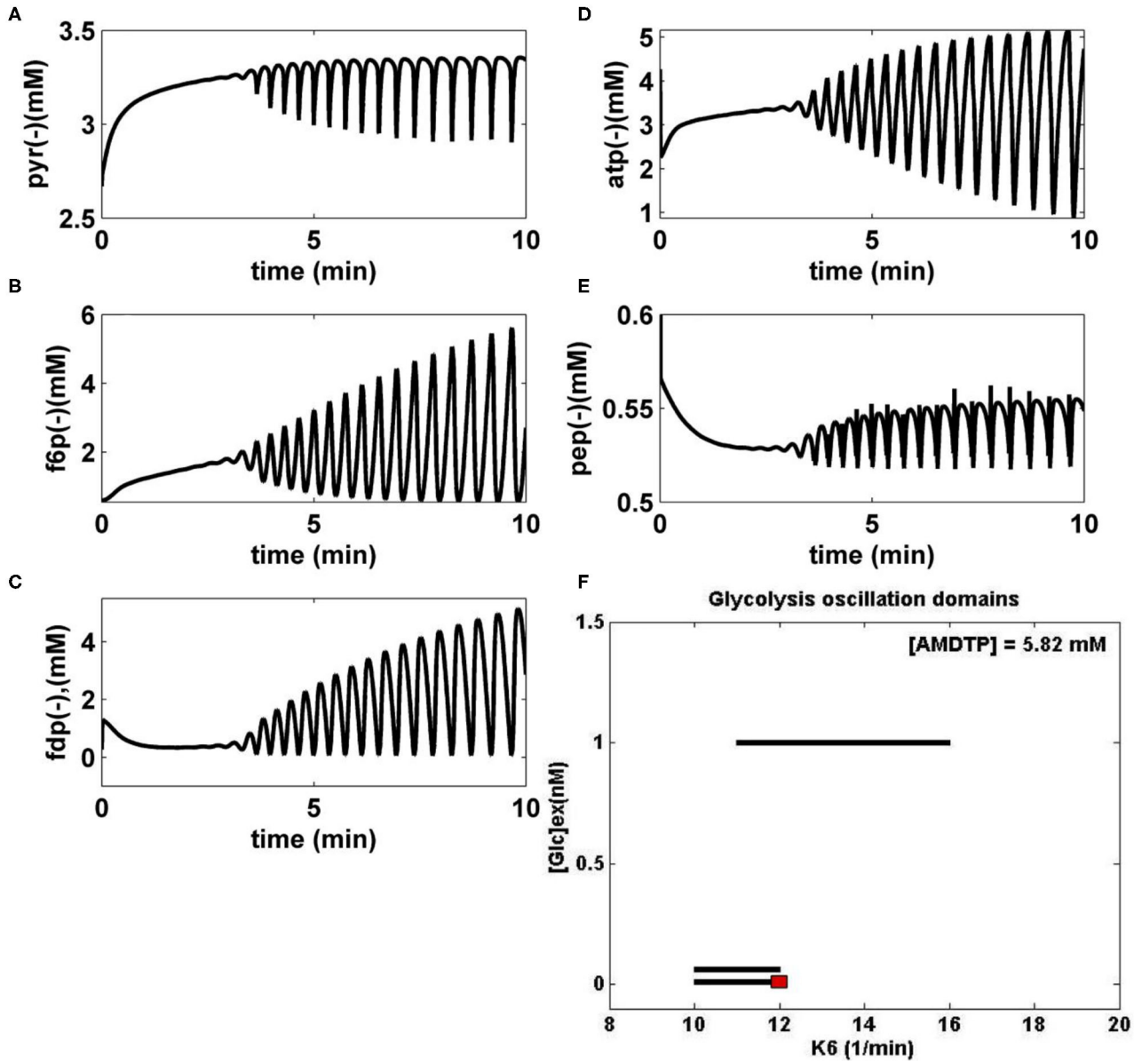


**FIGURE 3 | (A–E)** Simulated glycolytic stationary oscillations of the main glycolytic metabolites (PYR, F6P, FDP, ATP, and PEP) in *E. coli* for the bioreactor nominal operating conditions of **Table 1** ([AMDTP] = 5.82 mmol/L, D = 0.001667·1/min), [GLC]ex = 0.0557 mM (at $t = 0$), and k6 = 12 1/min. The simulated FBR running time is 10 min. **(F)** Glycolytic stationary oscillation domains (thick lines) in *E. coli* plotted in the plane [Glc]ext (at $t = 0$), and k6, for the bioreactor nominal operating conditions of **Table 1**. The red point corresponds to the cell species dynamics plotted in **(A–E)**. [Glc]ex, glucose concentration in the cell environment (bulk phase). Panel **(F)** was adapted from Maria et al. (2018c) courtesy of CABEQ JI.

viii) The factors influencing the glycolysis dynamics mentioned at the end of section Glycolysis Model are confirmed to have a major influence on the glycolysis dynamics as proved by the present analysis."

## TRP Synthesis Oscillations

"Under certain conditions, the TRP synthesis presents oscillations (Bhartiya et al., 2006). Being strongly connected with the glycolysis (via PEP species), it is important to also study the influence of the glycolytic oscillations on the TRP synthesis dynamics. Such an analysis turns out to be of high practical interest in order to adapt the bioreactor operation to maximize the TRP production and, eventually, for the *in silico* design GMO with such an objective (by the modification of the cell metabolic fluxes) (Maria et al., 2018a,b).

In particular, the glycolysis intermediate PEP is the starting point for the synthesis of essential amino acids, including TRP

(Stephanopoulos and Simpson, 1997; Lodish et al., 2000; Calhoun and Swartz, 2006)."

Having PEP as one of the precursors, maximization of TRP synthesis clearly depends on the glycolysis intensity (average levels of glycolytic species) and dynamics (QSS or oscillatory). "On the other hand, as previously discussed, glycolysis is controlled by cell internal and external factors, which indirectly will also influence the TRP synthesis and oscillations, as follows:

(A) The GLC import rate (flux 50 in **Figure 1**) triggered by the external [GLC]ex and by the PEP and PYR levels into the cell;
(B) The limited ATP energy resources and a slow recovery system can slow down the GLC import, the glycolysis and, implicitly, the all-metabolic syntheses, including the TRP production;
(C) The bacteria genome (cell phenotype) plays an essential role, because it determines the characteristics of the *ATP-ase* and *AK-ase* enzymes responsible for the ATP-to-ADP conversion and for the ATP recovery rate during the glycolytic reactions (accounted by means of the K and k6 rate constants in the MGM kinetic model of **Table 2**). In fact, the A(MDT)P interconversion system affects most of the metabolic reactions."
(D) "Being a systemic process, inherently the glycolytic oscillations are also related to the rate constants of all the glycolysis reactions. As an example, Silva and Yunes (2006) found that oscillations are only possible if the [GLC]ex and the maximum reaction rates controlled by the *PFKase* and *GKase* are within specific intervals. The *GKase* is one of the enzymes controlling the V1 lumped reaction related to the PTS import system (GLC to G6P and then to F6P in **Figure 2** and **Table 2**). The *PFKase* controls the V2 reaction (of **Figure 2**) responsible for the FDP synthesis."
(E) The results of section Glycolytic Oscillations demonstrated that both external (like [GLC]ex level) and internal/metabolic parameters (like K, k6 constants) governing the glycolytic oscillations will influence the TRP synthesis dynamics and level.

"As has been proven experimentally by Bhartiya et al. (2006), the TRP synthesis is an oscillatory process with a complex engine. Model-based numerical analyses of Maria et al. (2018a,b) highlighted some of the essential factors on which the TRP process dynamics depends."

As mentioned by Santillan and Mackey (2001), Mackey et al. (2004), and Hernandez-Valdez et al. (2010), "oscillations in the TRP synthesis are produced due to the concomitant activation and high-order repression of the TRP-operon expression, together with a non-linear demand for the end product, making its expression cyclic. Maria et al. (2018a,b) pointed out through model-based simulations that the cell dilution rate (related to the cell cycle), adjusted to be consistent with the liquid residence time in the bioreactor, also exerts a strong influence on the TRP system dynamics."

The numerical analysis of the present paper has been performed by using the FBR reactor model, which includes the *coupled* glycolysis MGM model (section Glycolysis Model; **Table 2**) and the TRP synthesis kinetic model (section TRP Synthesis Model; **Table 3**). "The sensitivity analysis of the TRP production was performed by considering some of the most influential parameters checked in the range of [GLC]ex $\in$ [0.01–1.5] mM (at $t = 0$); k6 $\in$ [$10^{-5}$-20] $min^{-1}$; $D \in [10^{-4}\text{-}10^{-2}]$ $min^{-1}$; and initial [GLC]ex $\in$ [0.005–5] mM (at $t = 0$). The simulation results for only two relevant operating conditions have been plotted in **Figures 4A,B**. This analysis leads to several results and conclusions:

i) The [GLC]ex, the constant k6, and the bioreactor dilution $D$ (considered equal to the cell dilution) exert the highest influence not only on the glycolysis dynamics but also on the TRP synthesis dynamics and production (due to its close link to the glycolysis via PEP). Thus, under the initial FBR conditions of **Table 1**, for a low FBR dilution rate ($D$), and for conditions leading to a QSS glycolysis, the TRP synthesis also displays a stationary evolution (**Figure 4A**). By contrast, at higher dilutions, and when glycolysis meets the conditions necessary for an oscillatory process (of **Figure 3F**), the TRP synthesis also presents an oscillatory dynamics (**Figure 4B**). Consequently, the bioreactor dilution presents a strong influence on the QSS or oscillatory regime of the linked glycolysis and TRP synthesis. The TRP production (see its definition in the caption from **Figures 4A,B**) is influenced accordingly. A value of k6 = 12 $min^{-1}$ was considered in all the tested cases here.
ii) While glycolysis exerts a strong influence on the TRP synthesis dynamics, as proved by **Figures 4A,B**, the reverse influence is minor, as proved by disconnected glycolysis simulations (not reproduced here).
iii) For the high feeding rates (**Table 1**), the initial [GLC] in the FBR bioreactor does not quantitatively influence the TRP bioreactor performances (Maria et al., 2018b).
iv) Simulations of the only TRP synthesis, disconnected from the glycolytic process, but with employing various [PEP] average levels (Mihalachi and Maria, 2019), indicated that PEP average level has a huge influence on the dynamics and concentrations of the TRP synthesis species. In turn, [PEP] is controlled by the glycolysis dynamics, which, in turn, is controlled by the abovementioned external and internal factors.
v) It clearly appears that, beside cell phenotype (governing the TRP operon expression), glycolysis is one of the major factors influencing the TRP production. Thus, by ranging the FBR operating parameters, the TRP production can be maximized (Maria et al., 2018b).
vi) In all the FBR operating cases checked by Maria et al. (2018b) with the initial conditions of **Table 1**, but in the range of $D \in [10^{-4}\text{-}0.01]$ $min^{-1}$, simulations demonstrated that [GLC]ex in the liquid bulk always evolves toward its steady state irrespectively of the stationary or oscillatory dynamics of the cell metabolic processes."

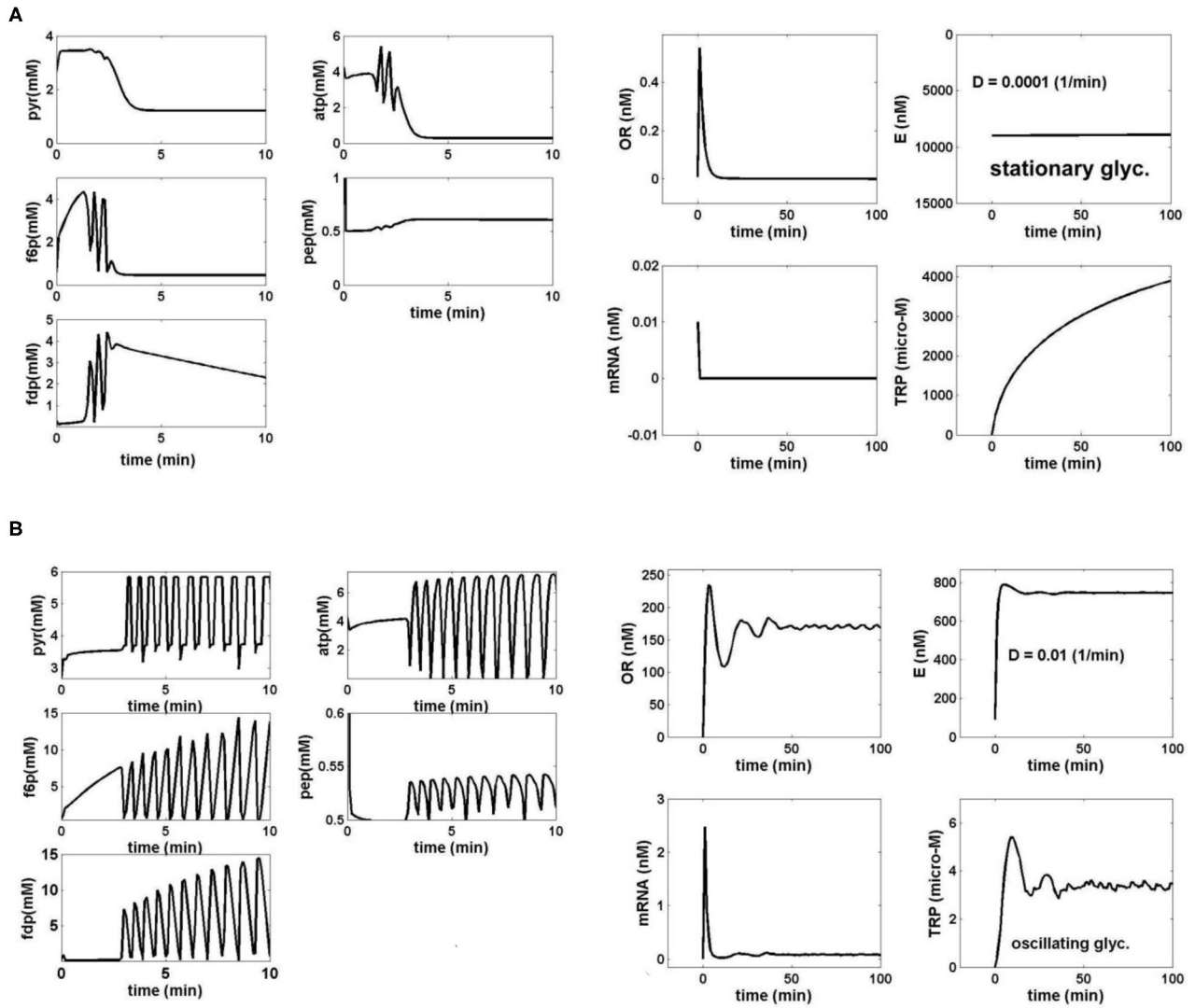


**FIGURE 4 | (A)** Simulated dynamics of the coupled glycolysis and TRP synthesis main species in *E. coli* cells under the bioreactor nominal conditions of **Table 1**, for a cell phenotype with k6 = 12 1/min. The following operating conditions have been checked:
$D = 0.0001$ (1/min) (cell/bioreactor dilutions); [GLC]ex = 1 mM (at $t = 0$), when both glycolysis [left] and TRP synthesis [right] display a stationary behavior (quasi-steady-state, QSS). The realized TRP production over the batch time is 0.39 μM/min.
TRP production (μM/min) = {Dilution rate ($F_L/V_L$)} × {max [TRP] ($t$)}
Species dynamics was generated by using the coupled bioreactor/glycolysis/TRP models of **Tables 2**, **3**. **(B)** Simulated dynamics of the coupled glycolysis and TRP synthesis main species in *E. coli* cells under the bioreactor nominal conditions of **Table 1**, for a cell phenotype with k6 = 12 1/min. The following operating conditions have been checked:
$D = 0.01$ (1/min) (cell/bioreactor dilutions); [GLC]ex = 0.0557 mM (at $t = 0$), when both glycolysis [left] and TRP synthesis [right] display stationary oscillations. The realized TRP production over the batch time is 0.1085 μM/min.
TRP production (μM/min) = {Dilution rate ($F_L/V_L$)} × {max [TRP] ($t$)}
The species dynamics were generated by using the coupled bioreactor/glycolysis/TRP models of **Tables 2**, **3**.

## Engineering Implications—Sensitivity Analysis

From an engineering point of view, the study suggests how to modulate the most influential factors, that is: [GLC]ex {via [GLC](feed), and [GLC](initial)}, $D = \mu$, k6, and others (via cell phenotype), before deriving an optimal FBR operating policy (for instance, a timestep-wise GLC feeding policy) leading to maximization of the TRP synthesis.

An exhaustive or an adaptive model-based search can identify the FBR optimal operating policy that corresponds to a maximum of TRP production (an analysis not developed in this work). In the present study, a brief sensitivity analysis based on the

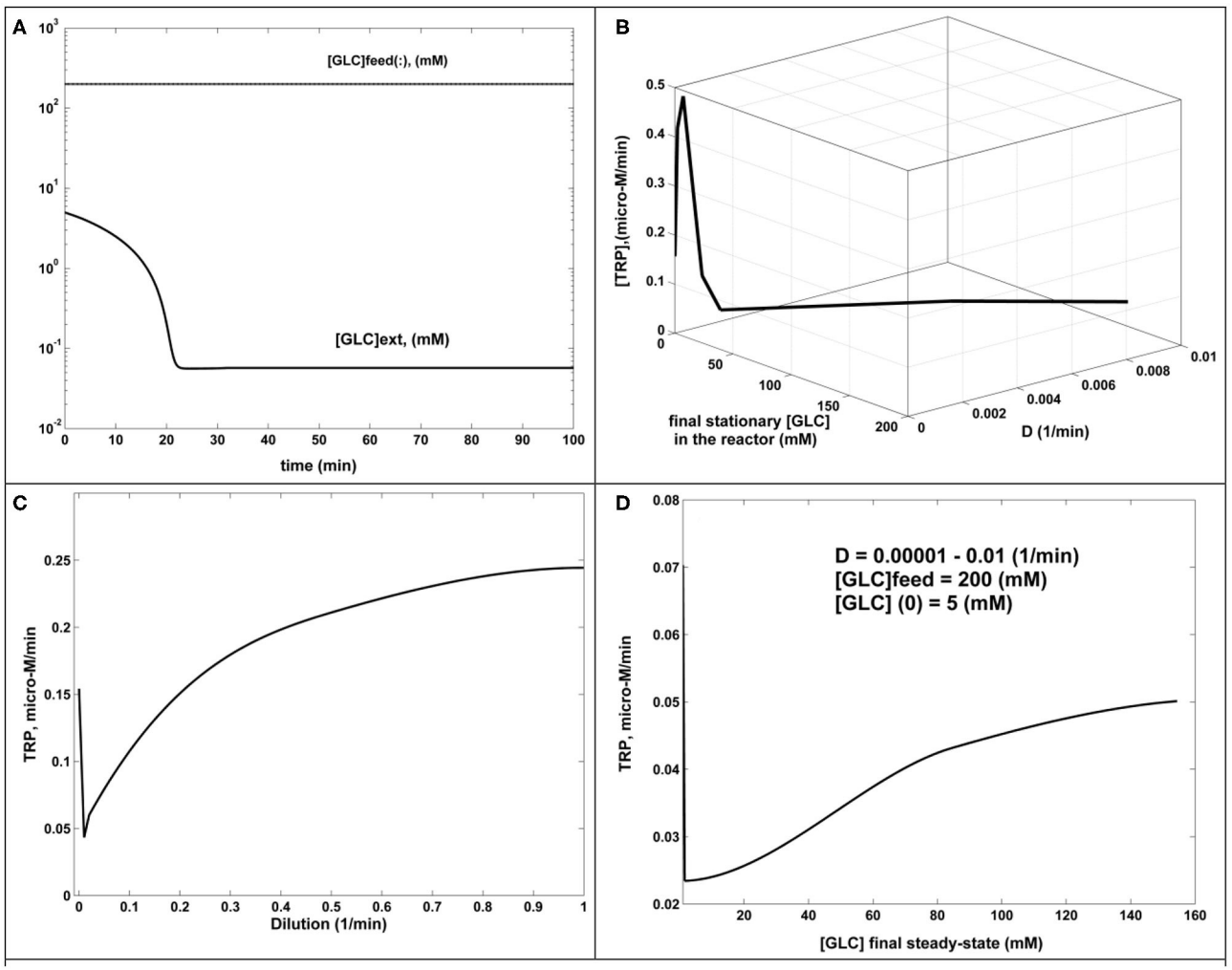


**FIGURE 5 |** The dynamics and sensitivity analysis of the FBR (simulated results). **(A)** [GLC] dynamics in the FBR for [GLC](feed) = 200 mM; [GLC](initial) = 5 mM; $D$ = 0.001 (1/min). The same behavior for $D$ = 0.00001–0.001 (1/min). **(B)** TRP production (μM/min) function of dilution and the [GLC](stationary) at the steady state. Fixed parameters of [GLC](feed) = 200 mM; [GLC](initial) = 5 mM. **(C)** TRP production (μM/min) function of reactor dilution. Fixed parameters: of [GLC](feed) = 200 mM; [GLC](initial) = 5 mM. **(D)** TRP production (μM/min) function of [GLC](stationary) at the steady state, generated for dilutions in the range of 0.00001–0.01 (1/min). Fixed parameters of [GLC](feed) = 200 mM; [GLC](initial) = 5 mM.

above model has been performed, thus preceding the FBR future optimization. Numerical simulations revealed several interesting conclusions:

a.- FBR simulations using various operating parameters proved that FBR efficiency (TRP production) is not influenced by [GLC](initial) <100 mM in the bioreactor, once [GLC](feed) >100 mM.

b.- In all tested cases covering the ranges [GLC](feed) of 100–200 mM, [GLC](initial) of 1–50 mM, and $D$ = 0.00001–0.01 (1/min), the FBR rapidly evolves toward its steady state, corresponding to a usually small [GLC](stationary) (below 1 mM), which proves the FBR efficiency. An example of GLC dynamics in the bioreactor is displayed in **Figure 5A**.

c.- The TRP productivity increases with $D$, as plotted in **Figure 5C**.

d.- The TRP productivity also increases with the [GLC]ex, as plotted in **Figure 5D**, where the external (bulk) concentration is given by the steady-state level of [GLC](stationary). The combined dependency of TRP productivity on the reactor dilution and the [GLC](stationary) is given in **Figure 5B**, confirming conclusions (c) and (d) for a wide range of the reactor dilutions.

As proved in this work, the TRP productivity is also strongly dependent on the oscillatory characteristics of the glycolysis, determined by the abovementioned operating parameters, and on the activity of enzymes involved in the ATP recovery system (that is, the rate constants k6, K, and [AMDTP] of **Table 2**). Thus, from a biological point of view, as mentioned by Silva and Yunes (2006), "glycolytic oscillations are focused on the

maintenance of energy levels in the cell (negative regulation of *PFKase* by ATP) and thus the ability to limit the conversion into energy in situations where it is not needed. Therefore, it would be more advantageous to store it or deviate the flux toward other cell cycle activities such as cell division. Consequently, GMO with modified enzyme activity (especially those related to the ATP use/recovery system of **Figure 2**) will lead to noticeable modifications in the metabolic species dynamics and concentrations."

## CONCLUSIONS

The *in silico* analysis of this paper demonstrates in a meaningful and relevant way the importance of using a detailed enough and adequate structured dynamic model linking the metabolic cellular processes and the bioreactor state variables for engineering purposes. Such a modular hybrid model can link the macro-scale (bioreactor liquid phase) process variables to the nano-scale (cellular) ones.

The structured model not only can be used for future FBR optimization, "but can also be a valuable tool to evaluate the cellular metabolic fluxes (i.e., the homeostatic metabolic reaction rates, not evaluated here), thus opening the possibility to *in silico* re-design the cell metabolism to obtain GMOs with industrial or medical applications (Hatzimanikatis et al., 1996; Stephanopoulos et al., 1998; Visser et al., 2004; Styczynski and Stephanopoulos, 2005; Maria, 2017a,b, 2018).

Thus, the large experimental and computational effort to validate such structured cell models is eventually fully justified through the practical advantages offered by such an engineering analysis.

It is also to be emphasized that such a modular and structured approach of the dynamic cellular models offers the possibility to study the interference of the CCM sub-process (e.g., glycolysis and AA synthesis here), together with the influence of the external conditions. Such a modular simulation platform presents the advantage to be easy to extend by the inclusion of new CCM modules."

## DATA AVAILABILITY STATEMENT

All datasets generated for this study are included in the article/supplementary material.

## AUTHOR CONTRIBUTIONS

The author confirms being the sole contributor of this work and has approved it for publication.

## REFERENCES


Alberton, K. P. F., Alberton, A. L., Di Maggio, J. A., Estrada, V. G., Díaz, M. S., and Secchi, A. R. (2015). Simultaneous parameters identifiability and estimation of an *E. coli* metabolic network model. *BioMed. Res. Int*. 2015:454765. doi: 10.1155/2015/454765

Bennett, B. D., Kimball, E. H., Gao, M., Osterhout, R., Van Dien, S. J., and Rabinowitz, J. D. (2009). Absolute metabolite concentrations and implied enzyme active site occupancy in *Escherichia coli*. *Nat. Chem. Biol.* 5, 593–599. doi: 10.1038/nchembio.186

Bhartiya, S., Chaudhary, N., Venkatesh, K. V., and Doyle, F. J. (2006). Multiple feedback loop design in the tryptophan regulatory network of *E. coli* suggests a paradigm for robust regulation of processes in series. *J. R. Soc. Interface* 3, 383–391. doi: 10.1098/rsif.2005.0103

Bier, M., Teusink, B., Kholodenko, B. N., and Westerhoff, H. V. (1996). Control analysis of glycolytic oscillations. *Biophys. Chem*. 62, 15–24. doi: 10.1016/S0301-4622(96)02195-3

Buchholz, A., Hurlebaus, J., Wandrey, C., and Takors, R. (2002). Metabolomics: quantification of intracellular metabolite dynamics. *Biomol. Eng.* 19, 5–15. doi: 10.1016/S1389-0344(02)00003-5

Calhoun, K. A., and Swartz, J. R. (2006). Total amino acid stabilization during cell-free protein synthesis reactions. *J. Biotechnol*. 123, 193–203. doi: 10.1016/j.jbiotec.2005.11.011

Chandra, F. A., Buzi, G., and Doyle, J. C. (2011). Glycolytic oscillations and limits on robust efficiency. *Science*. 333, 187–192. doi: 10.1126/science.1200705

Chassagnole, C., Noisommit-Rizzi, N., Schmid, J. W., Mauch, K., and Reuss, M. (2002). Dynamic modeling of the central carbon metabolism of *Escherichia coli*. *Biotechnol. Bioeng.* 79, 53–73. doi: 10.1002/bit.10288

Chiarugi, D., Chinellato, M., Degano, P., Lo Brutto, G., Marangoni, R. (2006). "Feedbacks and oscillations in the virtual cell VICE," in *Proceedings of International Conference on Computational Methods in Systems Biology (Trento: CMSB)*, 93–107. doi: 10.1007/11885191_7

Costa, R. S., Machado, D., Rocha, I., and Ferreira, E. C. (2010). Hybrid dynamic modeling of *Escherichia coli* central metabolic network combining Michaelis–Menten and approximate kinetic equations. *BioSystems* 100, 150–157. doi: 10.1016/j.biosystems.2010.03.001

Costa, R. S., Rocha, I., and Ferreira, E. C. (2008). *Model reduction based on dynamic sensitivity analysis: A systems biology case of study* (Ph. D. grant report). University of Minho, Braga, Portugal.

de la Fuente, I. M. (2010). Quantitative analysis of cellular metabolic dissipative, self-organized structures. *Int. J. Mol. Sci.* 11, 3540–3599. doi: 10.3390/ijms11093540

Degenring, D., Froemel, C., Dikta, G., and Takors, R. J. (2004). Sensitivity analysis for the reduction of complex metabolism models. *J. Proc. Control* 14, 729–745. doi: 10.1016/j.jprocont.2003.12.008

Diaz Ricci, J. C. (2000). ADP modulates the dynamic behavior of the glycolytic pathway of *Escherichia coli*. *Biochem. Biophys. Res. Commun*. 271, 244–249. doi: 10.1006/bbrc.2000.2603

Edwards, J. S., and Palsson, B. O. (2000). The *Escherichia coli* MG1655 *in silico* metabolic genotype: its definition, characteristics, and capabilities. *Proc. Natl. Acad. Sci. U.S.A*. 97, 5528–5533. doi: 10.1073/pnas.97.10.5528

Elias, A. C. (2010). *Escherichia coli: Dynamic Analysis of the Glycolytic Pathway* (Ph.D. thesis). Facultad de Bioquímica y Farmacia, Universidad Nacional de Tucumán, San Miguel de Tucumán, Argentina.

Flamholz, A., Noor, E., Bar-Even, A., Liebermeister, W., and Milo, R. (2013). Glycolytic strategy as a tradeoff between energy yield and protein cost. *Proc. Natl. Acad. Sci. U.S.A*. 110, 10039–10044. doi: 10.1073/pnas.1215283110

Franck, U. F. (1980). Feedback kinetics in physicochemical oscillators. *Ber. Bunsenges. Phys. Chem*. 84, 334–341. doi: 10.1002/bbpc.19800840407

Gehrmann, E., Glässer, C., Jin, Y., Sendhoff, B., Drossel, B., and Hamacher, K. (2011). Robustness of glycolysis in yeast to internal and external noise. *Phys. Rev. E* 84:021913. doi: 10.1103/PhysRevE.84.021913

Hatzimanikatis, V., and Bailey, J. E. (1997). Studies on glycolysis- I. Multiple *steady states in bacterial. Chem. Eng. Sci.* 52, 2579–2588. doi: 10.1016/S0009-2509(97)00074-2

Hatzimanikatis, V., Floudas, C. A., and Bailey, J. E. (1996). Analysis and design of metabolic reaction networks via mixed-integer linear optimization. *AIChE J.* 42, 1277–1292. doi: 10.1002/aic.690420509

Hempel, D. C. (2006). Development of biotechnological processes by integrating genetic and engineering methods. *Eng. Life Sci.* 6, 443–447. doi: 10.1002/elsc.200620149

Hernandez-Valdez, A., Santillan, M., and Zeron, E. S. (2010). Cycling expression and cooperative operator interaction in the trp operon of *Escherichia coli*. *J. Theor. Biol.* 263, 340–352. doi: 10.1016/j.jtbi.2009.12.005

Kadir, T. A., Mannan, A. A., Kierzek, A. M., McFadden, J., and Shimizu, K. (2010). Modeling and simulation of the main metabolism in *Escherichia coli* and its several single-gene knockout mutants with experimental verification. *Microb. Cell Fact.* 9:88. doi: 10.1186/1475-2859-9-88

KEGG (2011). *Kyoto Encyclopedia of Genes and Genomes, Kanehisa Laboratories, Bioinformatics Center of Kyoto University*. Available online at: http://www.genome.jp/kegg/pathway.html (accessed September 10, 2020).

Lodish, H., Berk, A., Zipursky, S. L., Matsudaira, P., Baltimore, D., and Darnell, J. E. (2000). *Molecular Cell Biology*. New York, NY: W. H. Freeman & Co. Available online at: http://2009.igem.org/wiki/images/a/a7/The_tryptophan_biosynthetic_pathway.pdf (accessed May 30, 2009).

Mackey, M. C., Santillán, M., Yildirim, N., (2004). Modeling operon dynamics: thetryptophan and lactose operons as paradigms. *C. R. Biologies*. 327, 211–224. doi: 10.1016/j.crvi.2003.11.009

Madsen, M. F., Danø, S., and Sørensen, P. G. (2005). On the mechanisms of glycolytic oscillations in yeast. *FEBS J.* 272, 2648–2660. doi: 10.1111/j.1742-4658.2005.04639.x

Maria, G. (2004). A review of algorithms and trends in kinetic model identification for chemical and biochemical systems. *Chem. Biochem. Eng. Q.* 18, 195–222.

Maria, G. (2005). Relations between apparent and intrinsic kinetics of programmable drug release in human plasma. *Chem. Eng. Sci.* 60, 1709–1723. doi: 10.1016/j.ces.2004.11.009

Maria, G. (2014). *In silico* derivation of a reduced kinetic model for stationary or oscillating glycolysis in *Escherichia coli* bacterium. *Chem. Biochem. Eng. Q.* 28, 509–529. doi: 10.15255/CABEQ.2014.2002

Maria, G. (2017a). *Deterministic Modelling Approach of Metabolic Processes in Living Cells - A Still Powerful Tool for Representing the Metabolic Process Dynamics*. Newbury Park, CA: Juniper Publishers. Available online at: https://juniperpublishers.com/ebook-info.php (accessed June 15, 2017).

Maria, G. (2017b). *A Review of Some Novel Concepts Applied to Modular Modelling of Genetic Regulatory Circuits*. Newbury Park, CA: Juniper Publishers. Available online at: https://juniperpublishers.com/ebook-info.php (accessed March 15, 2017).

Maria, G. (2018). *In-silico Design of Genetic Modified Micro-Organisms (GMO) of Industrial Use, by Using Systems Biology and (Bio)Chemical Engineering Tools*. Simi Valley, CA: Juniper Publishers. Available online at: https://juniperpublishers.com/ebook-info.php (accessed March 21, 2018).

Maria, G., Gijiu, C. L., Maria, C., and Tociu, C. (2018a). Interference of the oscillating glycolysis with the oscillating tryptophan synthesis in the *E. coli cells. Comp. Chem. Eng.* 108, 395–407. doi: 10.1016/j.compchemeng.2017.10.003

Maria, G., and Luta, I. (2013). Structured cell simulator coupled with a fluidized bed bioreactor model to predict the adaptive mercury uptake by *E. coli cells. Comp. Chem. Eng.* 58, 98–115. doi: 10.1016/j.compchemeng.2013.06.004

Maria, G., Mihalachi, M., and Gijiu, C. L. (2018b). *In silico* optimization of a bioreactor with an E. coli culture for tryptophan production by using a structured model coupling the oscillating glycolysis and tryptophan synthesis. *Chem. Eng. Res. Design*. 135, 207–221. doi: 10.1016/j.cherd.2018.05.011

Maria, G., Mihalachi, M., and Gijiu, C. L. (2018c). Model-based identification of some conditions leading to glycolytic oscillations in *E. coli cells. Chem. Biochem. Eng. Q.* 32, 523–533. doi: 10.15255/CABEQ.2017.1241

Maria, G., Xu, Z., and Sun, J. (2011). Multi-objectiveMINLP optimization used to identify theoretical gene knockout strategies for *E. coli cell. Chem. Biochem. Eng. Q.* 25, 403–424. .

Mathews, C. K., van Holde, K. E., and Ahem, K. G. (1999). *Biochemistry*. New Jersey, Prentice Hall.

Mihalachi, M., and Maria, G. (2019). Influence of pep glycolytic precursor on tryptophan synthesis dynamics in *E. coli cells. UPB. Sci. Bull. Series B* 81, 29–36.

Moser, A. (1988). *Bioprocess Technology - Kinetics and Reactors*. Berlin: *Springer* Verlag. doi: 10.1007/978-1-4613-8748-0

Palsson, B. O. (2005). *Systems Biology – Properties of Reconstructed Networks*. Cambridge: *Cambridge* University Press.

Peskov, K., Mogilevskaya, E., and Demin, O. (2012). Kinetic modelling of central carbon metabolism in *Escherichia coli*. *FEBS J.* 279, 3374–3385. doi: 10.1111/j.1742-4658.2012.08719.x

Rapp, P. E. (1979). An atlas of cellular oscillators. *J. Exp. Biol.* 81, 281–306.

Reeves, R. E., and Sols, A. (1973). Regulation of *Escherichia coli* phosphofructokinase *in situ*. *Biochem. Biophys. Res. Commun.* 50, 459–466. doi: 10.1016/0006-291X(73)90862-0

Santillan, M., and Mackey, M. C. (2001). Dynamic behavior in mathematical models of the tryptophan operon. *Chaos* 11, 261–268. doi: 10.1063/1.1336806

Schaefer, U., Boos, W., Takors, R., and Weuster-Botz, D. (1999). Automated sampling device for monitoring intracellular metabolite dynamics. *Analy. Biochem.* 270, 88–96. doi: 10.1006/abio.1999.4048

Sel'kov, E. E. (1968). Self-oscillations in glycolysis. 1. a simple kinetic model. *Eur J. Biochem.* 4, 79–86. doi: 10.1111/j.1432-1033.1968.tb00175.x

Silva, A. S., and Yunes, J. A. (2006). Conservation of glycolytic oscillations in *Saccharomyces cerevisiae*. *Genet. Mol. Res.* 5, 525–535.

Slominski, A., Semak, I., Pisarchik, A., Sweatman, T., Szczesniewski, A., and Wortsman, J. (2002). Conversion of L-tryptophan to serotonin and melatonin in human melanoma cells. *FEBS Lett.* 511, 102–106. doi: 10.1016/S0014-5793(01)03319-1

Stephanopoulos, G., and Simpson, T. W. (1997). Flux amplification in complex metabolic networks. *Chem. Eng. Sci.* 52, 2607–2627. doi: 10.1016/S0009-2509(97)00077-8

Stephanopoulos, G. N., Aristidou, A. A., and Nielsen, J. (1998). *Metabolic Engineering. Principles and Methodologies*. San Diego, CA: Academic Press.

Styczynski, M. P., and Stephanopoulos, G. (2005). Overview of computational methods for the inference of gene regulatory networks. *Comput. Chem. Eng.* 29, 519–534. doi: 10.1016/j.compchemeng.2004.08.029

Termonia, Y., and Ross, J. (1981a). Oscillations and control features in glycolysis: numerical analysis of a comprehensive model. *Proc. Natl. Acad. Sci. U.S.A.* 78, 2952–2956. doi: 10.1073/pnas.78.5.2952

Termonia, Y., and Ross, J. (1981b). Oscillations and control features in glycolysis: analysis of resonance effects. *Proc. Natl. Acad. Sci. U.S.A.* 78, 3563–3566. doi: 10.1073/pnas.78.6.3563

Termonia, Y., and Ross, J. (1982). Entrainment and resonance in glycolysis. *Proc. Natl. Acad. Sci. U.S.A.* 79, 2878–2881. doi: 10.1073/pnas.79.9.2878

Visser, D., Schmid, J. W., Mauch, K., Reuss, M., and Heijnen, J. J. (2004). Optimal re-design of primarymetabolism in *Escherichia coli* using linlog kinetics. *Metab. Eng.* 6, 378–390. doi: 10.1016/j.ymben.2004.07.001

Westermark, P. O., and Lansner, A. (2003). A model of phosphofructokinase and glycolytic oscillations in the pancreatic b-cell. *Biophys. J.* 85, 126–139. doi: 10.1016/S0006-3495(03)74460-9

Wierschem, K., and Bertram, R. (2004). Complex bursting in pancreatic islets: a potential glycolytic mechanism. *J. Theor. Biol.* 228, 513–521. doi: 10.1016/j.jtbi.2004.02.022

**Conflict of Interest:** The author declares that the research was conducted in the absence of any commercial or financial relationships that could be construed as a potential conflict of interest.

*Copyright © 2020 Maria. This is an open-access article distributed under the terms of the Creative Commons Attribution License (CC BY). The use, distribution or reproduction in other forums is permitted, provided the original author(s) and the copyright owner(s) are credited and that the original publication in this journal is cited, in accordance with accepted academic practice. No use, distribution or reproduction is permitted which does not comply with these terms.*

**Notations**

| | | | |
|---|---|---|---|
| $c_j, C_J$, **[J]** | species "**j, J"** concentration | **Indices** | o = initial; syn = synthesis; x = biomass; ≪s≫= stationary (quasi-steady state, QSS) |
| $D$ | bioreactor dilution, $D = F_L/V_L$ | $\rho_x$ | Biomass density |
| $F_L$ | liquid feed flow rate in the bioreactor | $\mu$ | Cell content dilution rate |
| $k_j, K_j$ | rate constants | **Indices** | O = initial; ex, ext = external; syn = synthesis; x = biomass; s = stationary (quasi-steady state, QSS) |
| $t, t_c$ | time, cell cycle | | |
| $V_L$ | liquid volume in the bioreactor | **Super-scripts** | |
| $y_{trp}$ | stoichiometric coefficient | $n$ | reaction order" |

**Abbreviations**

| | |
|---|---|
| 13DPG, PGP | 1,3-diphosphoglycerate |
| 3PG | 3-phosphoglycerate |
| 2PG | 2-phosphoglycerate |
| AA | Amino-acids |
| ACCOA | Acetyl-coenzyme A |
| AC | Acetate |
| ADP | Adenosine diphosphate |
| AK-ASE | Adenylate kinase |
| AMP | Adenosine monophosphate |
| ATP | Adenosine triphosphate |
| ATP-ASE | ATP monophosphatase |
| CCM | Central carbon metabolism |
| CHASSM | The kinetic model of Chassagnole et al. (2002) |
| CIT | Citrate |
| DHAP | Dihydroxyacetone |
| DO | Dissolved oxygen |
| DW | Dry mass |
| E | Enzyme anthranilate synthase in the TRP model |
| ETOH | Ethanol |
| FBR | Fed batch |
| FDP | Fructose-1,6-biphosphate |
| F6P | Fructose-6-phosphate |
| G3P,GAP,3PG | Glyceraldehyde-3-phosphate |
| G6P | Glucose-6-phosphate |
| GLC | Glucose |
| GLC(EX) | Glucose in the external environment |
| GMO | Genetically modified microorganisms |
| HK-ASE | Hexokinase |
| LAC | Lactate |
| MGM | The glycolysis model of Maria (2014) |
| MRNA | Tryptophan messenger ribonucleic acid during its encoding gene dynamic transcription, and translation |
| NAD(P)H | Nicotinamide adenine dinucleotide (phosphate) reduced |
| ODE | Ordinary differential equations |
| OME | Order of magnitude estimate |
| OR | The complex between O and R (aporepressor of the TRP gene) |
| OT | The total TRP operon |
| P, Pi | Phosphoric acid |
| PEP | Phosphoenolpyruvate |
| 13DPG=PGP | 1,3-diphosphoglycerate; |
| PFK-ASE | Phosphofructokinase |
| PK-ASE | Pyruvate kinase |
| PPP | Pentose-phosphate pathway |
| PTS | Phosphotransferase, or phosphoenolpyruvate:glucose, or phosphotransferase system |
| PYR | Pyruvate |
| QSS | Quasi-steady state |
| R5P | Ribose 5-phosphate |
| SBR | Semi-continuous (semi-batch) reactor |
| SUC, SUCC | Succinate |
| TCA | Tricarboxylic acid cycle |
| TF | Gene expression transcription factors |
| TRP | Tryptophan |
| Wt. | Weight |

frontiers in Chemistry

ORIGINAL RESEARCH
published: 29 October 2020
doi: 10.3389/fchem.2020.559650

# Advanced Chemical Computing Using Discrete Turing Patterns in Arrays of Coupled Cells

*František Muzika, Lenka Schreiberová and Igor Schreiber**

*Department of Chemical Engineering, University of Chemistry and Technology, Prague, Czechia*

We examine dynamical switching among discrete Turing patterns that enable chemical computing performed by mass-coupled reaction cells arranged as arrays with various topological configurations: three coupled cells in a cyclic array, four coupled cells in a linear array, four coupled cells in a cyclic array, and four coupled cells in a branched array. Each cell is operating as a continuous stirred tank reactor, within which the glycolytic reaction takes place, represented by a skeleton inhibitor-activator model where ADP plays the role of activator and ATP is the inhibitor. The mass coupling between cells is assumed to be operating in three possible transport regimes: (i) equal transport coefficients of the inhibitor and activator (ii) slightly faster transport of the activator, and (iii) strongly faster transport of the inhibitor. Each cellular array is characterized by two pairs of tunable parameters, the rate coefficients of the autocatalytic and inhibitory steps, and the transport coefficients of the coupling. Using stability and bifurcation analysis we identified conditions for occurrence of discrete Turing patterns associated with non-uniform stationary states. We found stable symmetric and/or asymmetric discrete Turing patterns coexisting with stable uniform periodic oscillations. To switch from one of the coexisting stable regimes to another we use carefully targeted perturbations, which allows us to build systems of logic gates specific to each topological type of the array, which in turn enables to perform advanced modes of chemical computing. By combining chemical computing techniques in the arrays with glycolytic excitable channels, we propose a cellular assemblage design for advanced chemical computing.

**Keywords: chemical computing, discrete Turing patterns, coupled cells, bifurcation analysis, glycolytic oscillations**

OPEN ACCESS

***Edited by:***
*Zeljko Dimitrije Cupic,*
*University of Belgrade, Serbia*

***Reviewed by:***
*Leroy Cronin,*
*University of Glasgow,*
*United Kingdom*
*Stevan Macesic,*
*University of Belgrade, Serbia*

****Correspondence:***
*Igor Schreiber*
*igor.schreiber@vscht.cz*

***Specialty section:***
*This article was submitted to Physical Chemistry and Chemical Physics, a section of the journal Frontiers in Chemistry*

***Received:*** *06 May 2020*
***Accepted:*** *30 September 2020*
***Published:*** *29 October 2020*

***Citation:***
*Muzika F, Schreiberová L and Schreiber I (2020) Advanced Chemical Computing Using Discrete Turing Patterns in Arrays of Coupled Cells. Front. Chem. 8:559650. doi: 10.3389/fchem.2020.559650*

## INTRODUCTION

Living cells can be considered as autonomous systems, which developed through evolution into energetically efficient forms capable of analysis of the environment to find sources of energy and material for maintenance, metabolism, and replication. Their subsystem for environmental analysis requires an intracellular signaling network, such as sensor/receptor-repressor system of *Saccharomyces cerevisiae* for glucose detection based on kinases (Snowdon and Johnston, 2016), or signaling network based on MAPkinases (Sauro and Kholodenko, 2004; Hadač et al., 2017). In multicellular organisms, due to cell differentiation, a signaling network system developed into specialized signaling cells, the neurons, which form a network of cells creating the signaling system of multicellular organisms. To show the energy efficiency of such cells we highlight a human

neuron. It consumes in average $8 \times 10^{-17} \frac{mol}{cell \cdot s}$ to $4 \times 10^{-16} \frac{mol}{cell \cdot s}$ of glucose and $1 \times 10^{-17} \frac{mol}{cell \cdot s}$ to $1 \times 10^{-15} \frac{mol}{cell \cdot s}$ of oxygen (McMurtrey, 2016). Neurons display high arithmetic and pattern recognition performance, when integrated into network (Majaj et al., 2015). Around 40 percent of consumed energy is used for basal energetic consumption and the rest is used to form and send currents among individual neurons, therefore 60 percent of consumed energy is used for data processing (Engl and Attwell, 2015).

Since the network of signaling neurons is energetically efficient, it is a source of ideas and techniques for building artificial signaling systems called neural networks. Examples of physically constructed neural networks include programmable resistive elements (memristors) (Howard et al., 2014); complementary metal–oxide–semiconductors (CMOS), which Shen et al. used to construct a Darwin neural processing unit with 2,048 neurons and power consumption ∼60 mW (Shen et al., 2016); magnetic spin switches in 3D/2D architecture (Roy et al., 2014); a pattern recognition technique, based on network of bistable rectors (Hjelmfelt and Ross, 1993; Hjelmfelt et al., 1993); network of gel droplets containing BZ reaction system (Holley et al., 2011; Górecki et al., 2014) and neuron-like units constructed using excitable channels (Górecka and Górecki, 2006).

Neural network processors can be constructed also from biological materials, for example: substitution of neuron units with DNA cascades (Qian et al., 2011); techniques combining DNA assays and transistors based on natural fluorescence (Lue and Fang, 2008); substitution of neuron units by three types of oscillators under batch conditions (Kim and Winfree, 2011). The neural network can be substituted by a lattice of excitable cells capable of signal addition, subtraction and conduction (Adamatzky, 1998). It can be constructed as a model of linear 3D neural network, using N layers of lattices, where (X-1)-th layer is connected to X-th layer and the X-th layer is connected to (X+1)-th layer, where X = 1, …,N. This theoretical work was followed by an experimental 2D lattice of liquid crystals to perform logic calculations (Adamatzky et al., 2011).

In this work, we explore a simple substitute for a neural network that performs chemical computing by utilizing discrete Turing patterns occurring in a network of mass coupled chemical cells with an autocatalytic reaction. From a theoretical point of view, the origin of biological morphogenesis was proposed by A. Turing (Turing, 1952) as manifestation of spatiotemporal patterns arising due to reaction-diffusion in cyclic arrays of coupled cells or in continuous tissue. Although his theory was shown not to be valid in general (Wolpert, 1969; Kerszberg and Wolpert, 1998), it does seem to apply in special cases, such as functional development of a brain tissue (Garzón-Alvarado et al., 2011), development of digits of mice (Bagudu et al., 2012) or during Saccharomyces cerevisiae cell polarization (Kozubowski et al., 2008; Giese et al., 2017). The key condition for occurrence of Turing patterns is a synergy of input, output, autocatalysis, inhibition, and diffusion. For spontaneous occurrence, diffusion parameters of specific components have to be set to exhibit short range activation and long range inhibition (Meinhardt and Gierer, 1974, 2000; Kondo and Miura, 2010), in other words, diffusion coefficient of an inhibitor has to be higher than diffusion coefficient of an activator. In an array of cells, the Turing instability gives rise to a non-uniform discrete stationary concentration profile throughout the array. A non-uniform concentration profile can thus be viewed as a discrete Turing pattern. In contrast, within a continuous tissue, the Turing instability leads to smooth spatiotemporal structures such as labyrinth (Rudovics et al., 1999; Asakura et al., 2011), dots (Ouyang et al., 1995; Rudovics et al., 1999; Vanag and Epstein, 2001), stripes (Ouyang et al., 1995), hexagons (Horvath et al., 2009; Asakura et al., 2011), or helical patterns in cylindrical layers (Bánsági and Taylor, 2015).

In a system of coupled oscillators, discrete Turing patterns often coexist with oscillations, In particular, they were shown to coexist by Bar-Eli (1984) and Vastano et al. (1987) for equal transport rate coefficient of activator and inhibitor. Such a system can be carefully perturbed to induce transition from oscillations to a discrete Turing pattern. Early experimental research was performed using the BZ oscillatory system, where a membrane between cells was substituted by valves (Crowley and Epstein, 1989) or peristaltic pumps (Bar-Eli and Reuveni, 1985; Dolník and Marek, 1988; Yoshimoto et al., 1993). Following these findings, in our previous work we examined the case of equal transport rate coefficients of activator and inhibitor using a core model of (Goldbeter and Moran, 1984) glycolysis as an oscillatory reaction. We identified coexisting discrete Turing patterns in linear arrays of two and three coupled cells (Muzika and Schreiber, 2013; Muzika et al., 2014) and applied targeted perturbations to perform basic logical functions. In our experimental research, we substituted membrane by a reciprocal peristaltic pumping to form a cyclic array of four coupled subsystems where the reaction of yeast extract and D-glucose took place (Muzika et al., 2016). In agreement with our theoretical predictions we found coexistence of discrete Turing patterns with uniform oscillations and were able to apply specific perturbations, inducing transition between discrete Turing patterns and uniform oscillations.

The paper is organized as follows. In section Model we provide details of the glycolytic model and formulate equations describing arrays of coupled cells with an arbitrary topology. In section Stability And Bifurcation Analysis the analysis of stability and bifurcations of stationary states is used to construct bifurcation diagrams for arrays of three and four coupled cells at various fixed ratios of transport rate coefficients of ATP and ADP and identify various types of discrete Turing patterns, their occurrence, coexistence, and stability within a 2D parameter space. By choosing specific regions with occurrence of multiple discrete Turing patterns in arrays of three and four coupled cells with various topology (linear, cyclic, T-shaped) and for various ratios of transport rate coefficients, one-parameter diagrams are chosen to provide a more detailed insight. Finally, section Chemical Computing Devices is focused on studying various aspects of chemical computing. By creating a system of precisely targeted and precisely timed perturbations to induce transitions between discrete Turing patterns and oscillations, we discuss a

tautology/contradiction gate, advanced logic functions gates, and advanced cellular assemblage design.

## MODEL

Glycolysis is one of the oldest and most common biochemical oscillatory reaction. Its purpose is to release energy from carbohydrates, which a cell synthesizes during photosynthesis or which a cell consumes from an external supply. A mathematical model of the yeast glycolytic reaction chain proposed by Hynne et al. (2001) consists of 24 reactions. It incorporates an autocatalytic enzymatic reaction mediated by phosphofructokinase and it also contains negative feedback enzymatic reactions from the lower part of the glycolytic chain catalyzed by pyruvate kinase and phosphoglycerate kinase. To analyze dynamic behavior in the arrays of mass-coupled cells, it is convenient to reduce the model involving entire glycolytic reaction chain into a core model retaining only the three aforementioned positive and negative feedback reactions. Therefore, for our analysis of bifurcations and stability of stationary states, the core model proposed by Goldbeter and Moran (1984) is used.

From an experimentalist viewpoint both feedback reactions can be regulated through temperature adjustments and also through the level of pH, where synergic effect with fructose 2,6 bisphosphate occurs between pH = 9 and pH = 5. In this range, the activity of phosphofructokinase is increased due to a decreased energy consumption to create bonds (Deville-Bonne et al., 1991; Tlapak-Simmons and Reinhart, 1998). Phosphofructokinase can be stimulated by addition of glycolytic metabolites or by addition of other components. In particular, hydrocarbonate can increase the activity of phosphofructokinase three times. *In vivo* experiments have shown that the addition of hydrocarbonate increased motility of sperm cells (Hereng et al., 2014) due to increased ATP-pool levels. We observed and used the same effect to increase activity of phosphofructokinase in our experimental research of discrete Turing patterns (Muzika et al., 2016). Phosphofructokinase can be inhibited by addition of: (1) ATP by up to 95%, (2) citrate by up to 60%, (3) PEP by up to 50%, (4) fructose 6-phosphate by up to 70%, and (5) phosphoglycerate by up to 60% (Mediavilla et al., 2007). These positive and negative effects provide rationale for modifying corresponding rate coefficients in the core model of glycolysis to a considerable extent. Coupling of cells in multicellular organisms is realized via gap junctions or in the case of artificial cellular assemblages via artificial membranes or artificial ports/junctions. Correspondingly, we add linear diffusion terms to the core model, creating the following model of N coupled cells with various topologies:

$$\begin{aligned}\frac{dx_i}{dt} &= f_x\left(x_i, y_i\right) + qk_{ADP}\sum_{j=1}^{N}\delta_{ij}\left(x_j - x_i\right) + p_i\left(t\right),\\ \frac{dy_i}{dt} &= f_y\left(x_i, y_i\right) + k_{ADP}\sum\nolimits_{j=1}^{N}\delta_{ij}\left(y_j - y_i\right),\end{aligned} \tag{1}$$

$$\begin{aligned}f_x &= \nu + \sigma_{inh}\frac{y_i^n}{M^n + y_i^n} - \sigma_M\frac{x_i\left(1+x_i\right)\left(1+y_i\right)^2}{L + \left(1+x_i\right)^2\left(1+y_i\right)^2},\\ f_y &= \phi\sigma_M\frac{x_i\left(1+x_i\right)\left(1+y_i\right)^2}{L + \left(1+x_i\right)^2\left(1+y_i\right)^2} - k_S y_i - \phi\sigma_{inh}\frac{y_i^n}{M^n + y_i^n},\\ & i = 1, \ldots, N,\end{aligned} \tag{2}$$

where $\{\delta_{ij}\}$ is a non-negative structural matrix specifying the topology of the array. In the special case of 1D (non-cyclic) chain:
$\delta_{ij} = \delta_{ji} = 1$ *for* $j = i - 1;\ i = 2, \ldots, N$,
$\delta_{ij} = 0$ otherwise,
and for a cyclic chain:
$\delta_{ij} = \delta_{ji} = 1$ *for* $j = i - 1;\ i = 2, \ldots, N$,
$\delta_{1N} = \delta_{N1} = 1$,
$\delta_{ij} = 0$ otherwise.
By properly choosing $\{\delta_{ij}\}$, more complex topologies, such as T-shaped array can be defined.

The symbols $x_i$ and $y_i$ represent dimensionless concentrations of ATP and ADP in the i-th cell, respectively. The function $p_i(t)$ represents perturbation of i-th cell by ATP, see section Chemical Computing Devices for more detail. The parameters are as follows: $M$ is Michaelis constant; $\nu$ represents ATP uptake rate; $n$ represents Hill coefficient; $\phi$ is the ratio of dissociation constants of ATP and ADP; $L$ represents allosteric constant specifying affinity of the PFK conformation to the reactive state rather than non-reactive conformation (Monod et al., 1965); $k_s$ represents removal rate coefficient of ADP; $\sigma_M$ represents rate coefficient of autocatalysis; $\sigma_{inh}$ represents rate coefficient of inhibition; $q$ represents ratio of the transport coefficient of ATP relative to ADP; $k_{ADP}$ represents transport coefficient of ADP between each pair of coupled cells. The following parameters are set according to Goldbeter and Moran (1984): $\phi = 1$, $\nu = 1.84$ $s^{-1}$, $L = 5 \times 10^6$, $n = 4$, $M = 10$, $k_s = 0.06$ $s^{-1}$. There is a unique stationary state in one cell that, depending on the two remaining kinetic parameters $\sigma_M$ and $\sigma_{inh}$, is either stable or undergoes an oscillatory instability via a Hopf bifurcation. Below, we treat $\sigma_M$ and $\sigma_{inh}$ as adjustable, as well as the coupling parameters $k_{ADP}$ and $q$. We use these four free parameters to construct various bifurcation diagrams and thus demonstrate their effect on occurrence of discrete Turing patterns and their overlap with homogeneous periodic oscillations.

## STABILITY AND BIFURCATION ANALYSIS

### Bifurcation Scenarios

For the analysis of stationary and dynamic behavior of the glycolytic oscillatory reaction in arrays with various topology we use the program CONT (Kubíček and Marek, 1983; Kohout et al., 2002). We chose such a parameter setup that the system exhibits either a unique stable stationary state or unique stable limit cycle in one cell avoiding thus the region of birhythmicity (Goldbeter and Moran, 1984). These two basic regimes translate in the context of arrays into a uniform stationary state and uniform oscillations. However, their stability generally depends

on the coupling strength. Under parameter settings used in this work, the stable uniform stationary state may lose stability either via a Hopf bifurcation leading to stable uniform oscillations or via a symmetry breaking bifurcation leading to stable discrete Turing patterns (i.e., stable non-uniform stationary states). In addition, symmetry breaking bifurcation may occur also from unstable uniform stationary states. On the other hand, symmetry breaking bifurcation from the uniform oscillations was never observed. These so-called *primary* bifurcations from the uniform stationary states are complemented by *secondary* bifurcations from the non-uniform stationary states, which include limit point bifurcations (folds), secondary Hopf bifurcations as well as secondary symmetry breaking bifurcations. Any Hopf bifurcation curve in a two-parameter plane is either a closed curve or it terminates when touching a curve of limit point bifurcation at the Bogdanov-Takens codimension one point. Also, two Hopf bifurcation curves may intersect at the point of double Hopf bifurcation; additionally, there are other types of singularity points, which we do not mention here. Details of all these transitions depend on the particular array topology and may be quite involved as described below.

In our previous work, an array of two coupled cells (Muzika et al., 2014) and a linear array of three coupled cells (Muzika and Schreiber, 2013) were described through bifurcation diagrams in the parameter plane of $\sigma_M$ and $\sigma_{inh}$ and in the parameter plane of $\sigma_{inh}$ and $k_{ADP}$ at fixed $q$. In the following we use the same parameter planes. The region of stable uniform stationary state (SUSS) in **Figures 1A,B** is a region that all arrays with $q \leq 1$ share throughout all the topologies, because it does not depend on $k_{ADP}$. The region of unstable uniform stationary state (UUSS) and simultaneously stable uniform oscillations (SUO) contains subregions of coexisting stable or unstable non-uniform stationary states (discrete Turing patterns) for all arrays with $q \leq 1$. The regions of Turing patterns are described with numbers in the format a-b, where the first number defines the number of stationary states and the second number defines the number of stable stationary states. **Figure 1A** shows that with increasing positive feedback rate coefficient $\sigma_M$, two triplets of unstable symmetric non-uniform patterns occur through a primary symmetry breaking bifurcation from an unstable uniform stationary state and the limit point curve delimits the region of their occurrence (region 7-0). Three of these unstable non-uniform patterns become stabilized (region 7-3) at $\approx \sigma_M = 70\ s^{-1}$ by a Hopf bifurcation (full red curve), which is called *secondary* stabilization. At higher inhibition rate coefficient $\sigma_{inh}$, four new non-uniform stationary states occur from two non-uniform branches via secondary symmetry breaking bifurcation (from non-uniform symmetric to non-uniform asymmetric) creating the region 11-0. With increasing autocatalytic rate coefficient, two of the unstable non-uniform stationary states are stabilized by a secondary Hopf bifurcation curve (region 11-2). Further simultaneous increase of both $\sigma_M$ and $\sigma_{inh}$ leads to another Hopf bifurcation curve, which destabilizes the stable non-uniform patterns (region 9-0) again, creating a U-shaped region of stable Turing patterns (region 11-2). These two regions of stable non-uniform stationary states (region 11-2 and region 7-3) intersect each other above $\approx \sigma_M = 125\ s^{-1}$ creating a parameter region with five stable non-uniform stationary states (region 11-5). **Figure 1B** represents the parameter plane of $\sigma_{inh}$ and $k_{ADP}$ at $\sigma_M = 100\ s^{-1}$. This bifurcation diagram does not possess the intersection of both regions of stable non-uniform stationary states (region 7-3 and region 11-2 merging to region 11-5 in **Figure 1A**), instead it shows a disc (region 7-3) and two other embedded disks (region 11-2 and region 9-0) delimited by Hopf bifurcations with the region in-between them representing stable Turing patterns (region 11-2).

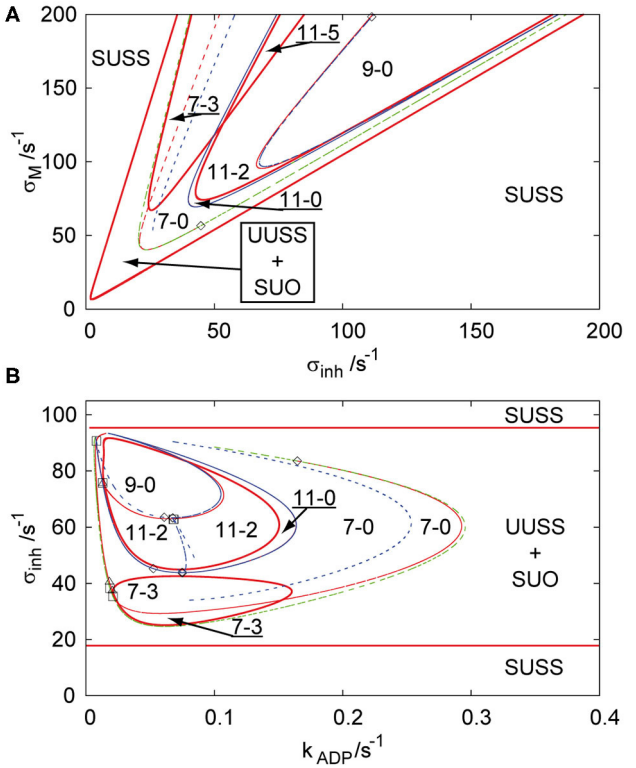


**FIGURE 1 |** Bifurcation diagram for three coupled cells in cyclic array, $q = 1$, in planes: **(A)** $\sigma_{inh}$ and $\sigma_M$, $k_{ADP} = 0.1\ s^{-1}$; **(B)** $\sigma_{inh}$ and $k_{ADP}$, $\sigma_M = 100\ s^{-1}$. Red curve—Hopf bifurcation curve; blue curve—symmetry breaking bifurcation curve; green curve—limit point curve; full line—change of stability across the line, dashed curve—no change of stability across the line; empty square—intersection point of Hopf bifurcation/symmetry breaking bifurcation/limit point curves; empty diamond—Bogdanov-Takens bifurcation point; empty triangle—double Hopf bifurcation point; SUSS, stable uniform stationary state; UUSS, unstable uniform stationary state; SUO, stable uniform oscillations. Each parameter region is marked by a pair of numbers m,n, where m is total number of stationary states and n is the number of stable stationary states.

For more complex topologies of arrays, bifurcation diagrams abound with curves of Hopf bifurcation, symmetry breaking bifurcation, and limit points, therefore we choose to show only the bifurcation diagrams for three additional types of arrays in the parameter plane $\sigma_M$ and $k_{ADP}$. **Figure 2** shows three bifurcation diagrams for an array of four coupled cells with $q = 1$ with the following topologies: linear, T-shaped and cyclic. As in the previous case, at a first glance, the salient features

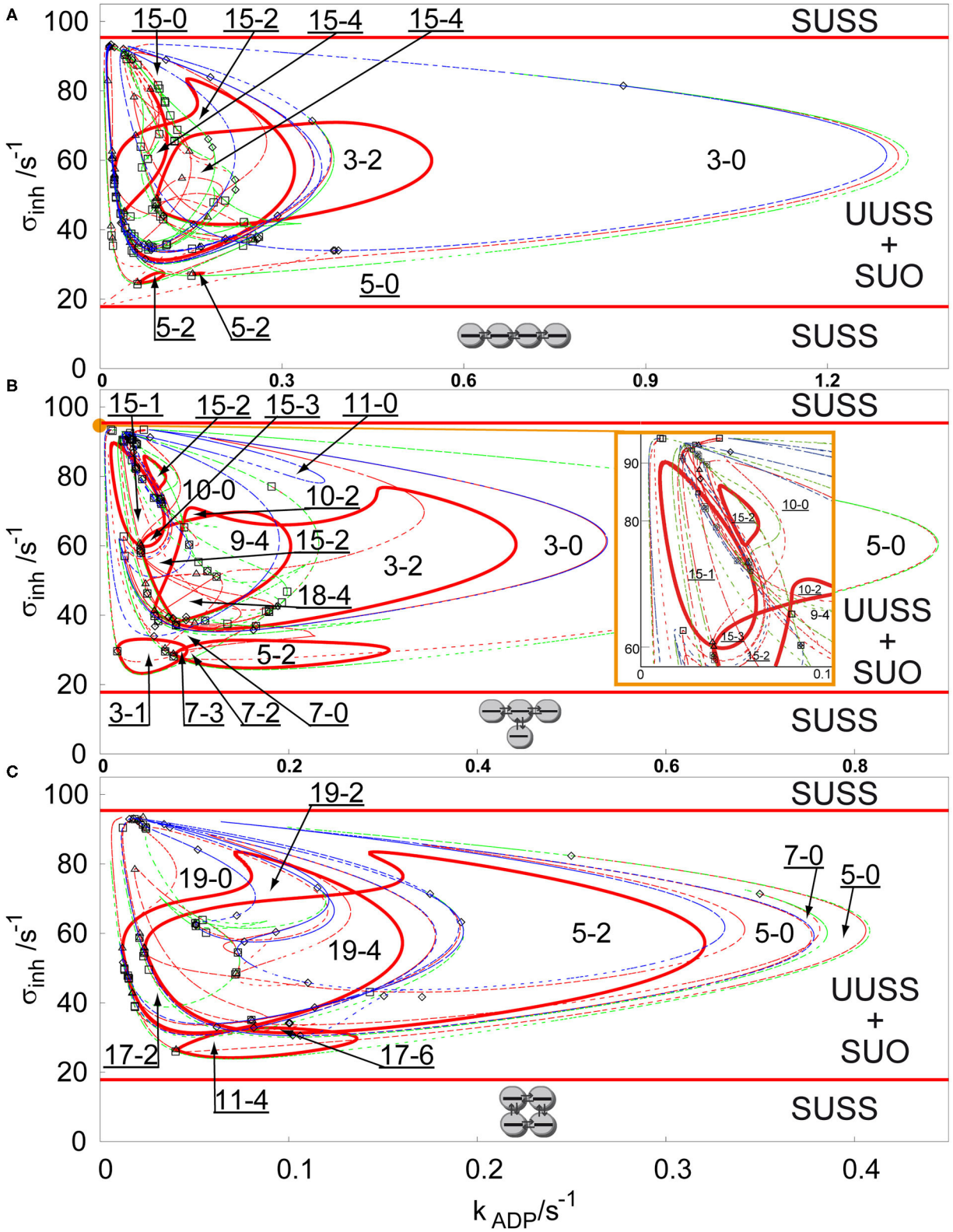


**FIGURE 2 |** Comparison of bifurcation diagram four coupled cells in a parameter plane $\sigma_{inh}$ and $k_{ADP}$, $q = 1$, $\sigma_M = 100\ s^{-1}$ in: **(A)** linear array, **(B)** T-shaped array, **(C)** cyclic array. Red curve—Hopf bifurcation curve; blue curve—symmetry breaking bifurcation curve; green curve—limit point curve; full line—change of stability across

*(Continued)*

**FIGURE 2 |** the line, dashed curve—no change of stability across the line; empty square—intersection point of Hopf bifurcation/symmetry breaking bifurcation/limit point curves; empty diamond—Bogdanov-Takens bifurcation point; empty triangle—double Hopf bifurcation point; SUSS, stable uniform stationary state; UUSS, unstable uniform stationary state; SUO, stable uniform oscillations. Each parameter region is marked by a pair of numbers m,n, where m is total number of stationary states and n is the number of stable stationary states. For clarity, the upper-left corner region with many overlapping curves is magnified and displayed in the inset on the right.

of the diagrams are the disc-like regions of stable non-uniform stationary states (discrete Turing patterns) delimited by red curves of secondary Hopf bifurcation, which are coexisting with the stable uniform oscillations in the region delimited by two parallel lines of primary Hopf bifurcation. The region of non-uniform stationary states in **Figure 2A** (linear array) is the widest region of **Figure 2** and contains up to 15 coexisting stationary states. Two non-uniform stationary states occur from a primary symmetry breaking bifurcation creating region 3-0, which is partly delimited by a limit point curve, where the number of non-uniform stationary states is doubled creating the region 5-0. Secondary Hopf bifurcation curves (full red curves) stabilize the unstable non-uniform stationary states delimiting the region 3-2 and the very small region 5-2. With decreasing $k_{ADP}$ four new pairs of non-uniform stationary states occur and two of them are doubled by a limit point curve, therefore creating 15 stationary states. Two of them are secondarily stabilized creating the region 15-2 and where the region 3-2 intersects with 15-2, they create the region 15-4. Another region delimited by secondary symmetry breaking curve and limit point curve overlaps with this dense region and a small inner part of it is again secondarily stabilized by a Hopf bifurcation curve to form region 5-2.

The bifurcation diagram for a T-shaped array is shown in **Figure 2B**. The region 5-0 is much wider than in the case of the linear array, while the region 3-0 is narrower. The Hopf bifurcation curve (full red curve) secondarily stabilizes a subregion of 3-0 into the region 3-2. Another secondary Hopf bifurcation curve delimits the closed region 5-2 embedded in the region 5-0. Both cases can be observed in the case of the linear array, but the region 5-2 is much wider now. It is also intersected by another limit point curve, adding two unstable non-uniform stationary states creating the small region 7-2 and one stable and one unstable non-uniform stationary state creating the small region 7-3. The primary region 3-0 is further intersected with branch point and limit point curves, where the most interesting are two regions 15-2, which also occur in the case of the linear array, and the region, where stabilizing Hopf bifurcation curves intersect, creating the regions 18-4 and 9-4. The bifurcation diagram for the cyclic 4-array is shown in **Figure 2C**. The region 3-0 is missing, however due to intersections of regions narrowed by a limit point curves, there is a wide region 5-0 with small overlap 7-0. Unstable non-uniform stationary states are again stabilized by a secondary Hopf bifurcation curve creating a region 5-2. Then the whole region 5-0 is intersected by several symmetry breaking bifurcation curves creating up to 19 stationary states (region 19-0), which are stabilized by a Hopf bifurcation curve to form the region 19-2 and then the region intersects with 5-2 to form the region 19-4. This region intersects also with another region 11-4, creating the region 17-6 with the largest number of stable Turing patterns.

For $q > 1$, a stable non-uniform stationary state may emerge directly via a primary symmetry breaking bifurcation from the stable uniform stationary state, which leads to spontaneous occurrence of Turing patterns as well-known from many experiments in spatially extended reactors (Castets et al., 1990; Ouyang et al., 1995; Rudovics et al., 1999; Dolník et al., 2001; Sanz-Anchelergues et al., 2001; Asakura et al., 2011). To ensure sufficient conditions for spontaneous occurrence of Turing patterns, we set $q = 100$ and $\sigma_M = 10\ \mathrm{s}^{-1}$, while the other parameters remain, as they were proposed by Goldbeter and Moran (1984). We are comparing the previously discussed three types of arrays in **Figure 3**. It is clearly seen that the regions of Turing patterns now extend below the lower primary Hopf bifurcation line for each topology occurring via supercritical or transcritical branch point curves for sufficiently low inhibiton rate coefficients $\sigma_{inh}$ and disappearing via subcritical or superscritical symmetry breaking bifurcation curves at $\sigma_{inh} \approx 7\ \mathrm{s}^{-1}$.Notice that $\sigma_M = 10\ \mathrm{s}^{-1}$ (ten times lower than for case of $q = 1$), which causes the non-uniform patterns to occur in the region within the $k_{ADP}$—$\sigma_{inh}$ plane, having ∼10 times lower ranges in both directions.

The linear array, see **Figure 3A**, has again the widest region of non-uniform stationary states. The largest region of stable non-uniform stationary states is the region 3-2, which contains a subregion 3-0 with no stable stationary state delimited by a closed Hopf bifurcation curve, this is an opposite effect to the secondary stabilization by a Hopf bifurcation curve observed earlier. The region 3-2 is further intersected by new pairs of non-uniform solutions arising via symmetry breaking bifurcation curves to form up to 15 stationary states (region 15-4). The regions with three stable non-uniform stationary states represent patterns, where one of them occurs via a secondary symmetry breaking bifurcation. Since the region 9-4 and the region 15-4 intersect the region 9-3 and the region 7-3, two of the stable non-uniform patterns arose from a secondary symmetry breaking bifurcation and therefore they do not have a mirror image as in case of the non-uniform patterns emerging via a primary symmetry breaking bifurcation to form the region 3-2. The T-shaped array is shown in **Figure 3B**. The widest region 5-2 combines the non-uniform stationary states arising from secondary symmetry breaking bifurcation. The Hopf bifurcation curves (full red curves) destabilize stable non-uniform stationary states, creating closed curves of regions 11-2, 13-2, and 7-0, but also, combined with symmetry breaking curves, they give rise to the region 11-5, where there is the highest number of stable non-uniform stationary states. At $k_{ADP} = 0.02\ \mathrm{s}^{-1}$, regions 5-2 and 11-4 further intersects with a symmetry breaking curve

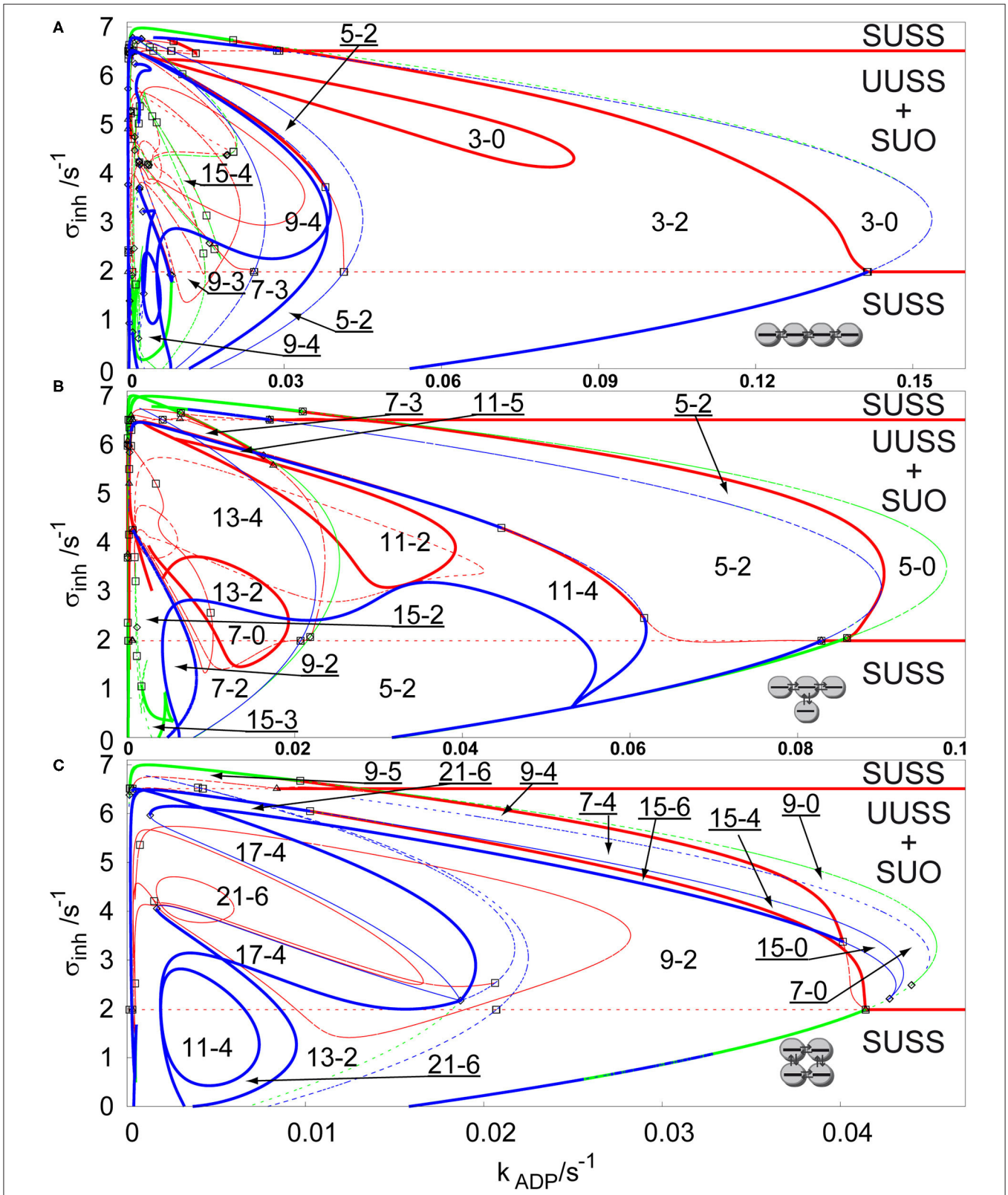


**FIGURE 3 |** Comparison of bifurcation diagrams of four coupled cells in a parameter plane $\sigma_{inh}$ and $k_{ADP}$, $q = 100$, $\sigma_M = 10\ s^{-1}$ in: **(A)** linear array, **(B)** T-shaped array, **(C)** cyclic array. Red curve—Hopf bifurcation curve; blue curve—symmetry breaking bifurcation curve; green curve—limit point curve; full line—change of stability across the line, dashed curve—no change of stability across the line; empty square—intersection point of Hopf bifurcation/symmetry breaking bifurcation/limit point curves; empty diamond—Bogdanov-Takens bifurcation point; empty triangle—double Hopf bifurcation point. Each parameter region is marked by a pair of numbers m,n, where m is total number of stationary states and n is the number of stable stationary states.

adding two new unstable non-uniform stationary states creating the regions 13-4 and 7-2, and further below $k_{ADP} = 0.01\ s^{-1}$, even 15 non-uniform stationary states occur. The cyclic array, shown in **Figure 3C**, has the narrowest region of non-uniform stationary states, but also contains up to 21 non-uniform stationary states. The largest region 9-2 has 9 stationary states, eight of them arose from a secondary symmetry breaking curve. The Hopf bifurcation curve partly delimits the region 9-2 together with the symmetry breaking and limit point bifurcation curves. The regions 15-4, 15-6, 7-4, 9-4, and 9-5 have such mixed boundaries as well. At $k_{ADP} = 0.02\ s^{-1}$ the region 9-2 and smaller regions are intersected with several symmetry breaking bifurcation curves creating three separate regions 21-6 and other regions with 4 stable non-uniform stationary states.

## Coexistence of Discrete Turing Patterns

After two-parameter analysis of arrays of coupled cells with glycolytic oscillatory reaction, we now focus on one-parameter analysis by creating solution diagrams (also called one-parameter bifurcation diagrams), which are a more suitable tool to distinguish the concentration profiles of all stable non-uniform stationary states (discrete Turing patterns). It is possible to construct any number of solution diagrams associated with the bifurcation diagrams presented in **Figures 2**, **3** by fixing one of the two parameters in the bifurcation diagram and plotting stationary value of a selected component (ADP in our case) in a selected cell (first cell) against the other parameter. However, we choose to show only representatives for each case by fixing $k_{ADP}$ at certain value and varying $\sigma_{inh}$ to compare the arrangement of concentration profiles for various arrays. At first, we compare linear, T-shaped and cyclic arrays for $q = 1$, $k_{ADP} = 0.1\ s^{-1}$, $\sigma_M = 100\ s^{-1}$, see **Figure 4**. As described in section Bifurcation Scenarios SUSS regions are present in every cell in every topology of an array for $q \leq 1$, which is apparent when comparing all three topologies in **Figure 4**. The SUSS regions are marked by blue line [the plotted stationary value of ADP is independent of $\sigma_{inh}$ due to specific form of Equation (2)]. The other shared feature are uniform oscillations represented by curves for minima and maxima (black curve) merging at two primary Hopf bifurcation points. The Hopf bifurcation at the right is supercritical, therefore there is a transfer of stability from the SUSS to the SUO. The left Hopf bifurcation point is subcritical and thus the emerging uniform oscillations are unstable (dashed black curve) and only upon a rapid increase of amplitude they become stable via fold bifurcation (full black curve) marking the left boundary of SUO (the corresponding value of $\sigma_{inh}$ is virtually indistinguishable from that corresponding to the Hopf bifurcation).

All stable non-uniform patterns are assigned a symbolic pictographic representation. By increasing $\sigma_{inh}$ in the linear array, **Figure 4A**, after the Hopf bifurcation point giving rise to uniform oscillations, when following the line of unstable uniform stationary states, there is a primary symmetry breaking bifurcation point, which gives rise to two unstable symmetric non-uniform stationary states (green curve), breaking thus the uniform symmetry. These two unstable symmetric non-uniform stationary states become stable via secondary Hopf bifurcations, which delimit a broad window of two stable Turing patterns (full green lines). When we follow the bifurcated upper unstable symmetric non-uniform branch, a secondary symmetry breaking bifurcation point occurs creating two new non-uniform stationary states, which are asymmetric (red curve), therefore breaking the non-uniform symmetry. When $\sigma_{inh}$ is decreased the unstable asymmetric non-uniform stationary state becomes secondarily stabilized by a Hopf bifurcation point and again destabilized by another Hopf bifurcation point, forming the left narrow window of two stable asymmetric Turing patterns (full red curve). A similar scenario occurs on the right when $\sigma_{inh}$ is decreasing past the upper primary Hopf bifurcation point ultimately forming a second wider window of stable asymmetric Turing patterns overlapping with the window of stable symmetric Turing patterns.

The T shaped array is shown in **Figure 4B**. The primary symmetry breaking bifurcation on the line of unstable uniform stationary states also creates a symmetric non-uniform stationary state (green curve) which, unlike in the previous case does not become stabilized.On the other hand, it bifurcates further via a secondary symmetry breaking bifurcation to form unstable asymmetric non-uniform stationary states, which are further stabilized to form three separate windows of stable distinct Turing patterns delimited by pairs of secondary Hopf bifurcation points. While the leftmost window is narrow, the two others are broad and overlapping. The cyclic array in **Figure 4C** displays a symmetry breaking bifurcation from the unstable uniform stationary states from both left and right side of the diagram. Due to the symmetry of the array, this bifurcation gives rise to both symmetric and asymmetric branches simultaneously. The six emerging non-uniform stationary states are unstable but become stabilized by secondary Hopf bifurcations ultimately forming a window of four coexisting stable asymmetric Turing patterns and a much broader window of two coexisting stable symmetric patterns. These windows partly overlap. When further increasing $\sigma_{inh}$ there is another primary symmetry breaking bifurcation point creating a pair of unstable symmetric states with a higher degree of symmetry (see the pictograms), which again become stabilized and form the rightmost broad window delimited by secondary Hopf bifurcation points. The two windows of stable Turing patterns with different symmetry strongly overlap.

The cyclic array of four coupled cell shows the largest variety of stable non-uniform patterns. It is a promising example of evolution of Turing patterns in a cyclic array system with varying ratio of transport rate coefficients $q$, see **Figure 5**. The cyclic array with $q = 1$ is shown in **Figure 4C**. For $q = 1.2$, **Figure 5A**, the windows of stable symmetric non-uniform stationary states are only slightly altered. When comparing stable asymmetric non-uniform stationary states curve in **Figure 5A** with **Figure 4C**, the left window is significantly broader. However, on the right a broad window of stable asymmetric non-uniform stationary states occurs, which is not present for $q = 1$. For $q = 100$, **Figure 5B**, the curves in the diagram are altered significantly including their stability. The left window of stable asymmetric patterns disappeared entirely and at the same time the other window of stable asymmetric patterns that newly occurred for $q = 1.2$ vastly expanded to the left and covers now almost entire range of non-uniform stationary states. In contrast, the

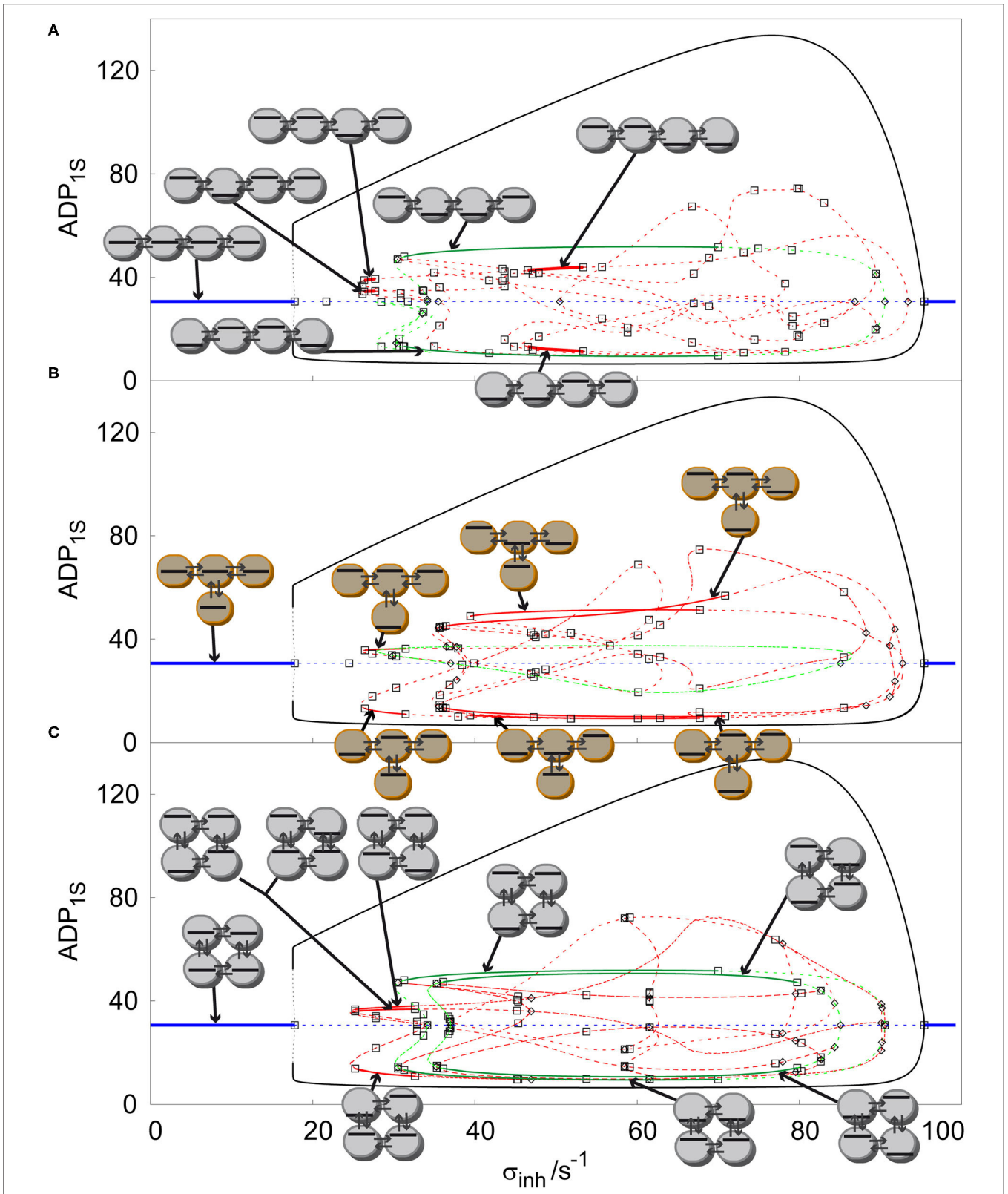


**FIGURE 4 |** Comparison of solution diagrams of four coupled cells $q = 100$, $\sigma_M = 100\ s^{-1}$, $k_{ADP} = 0.10\ s^{-1}$ in: **(A)** linear array, **(B)** T-shaped array, **(C)** cyclic array. Red curve—asymmetric non-uniform stationary state; blue curve—homogeneous stationary state; green curve—symmetric non-uniform stationary state; full line –stable stationary solution, dashed curve- unstable stationary solution; empty square—Hopf bifurcation point; empty diamond—symmetry breaking bifurcation point. Each stable stationary state has assigned a symbolic representation of its pattern.

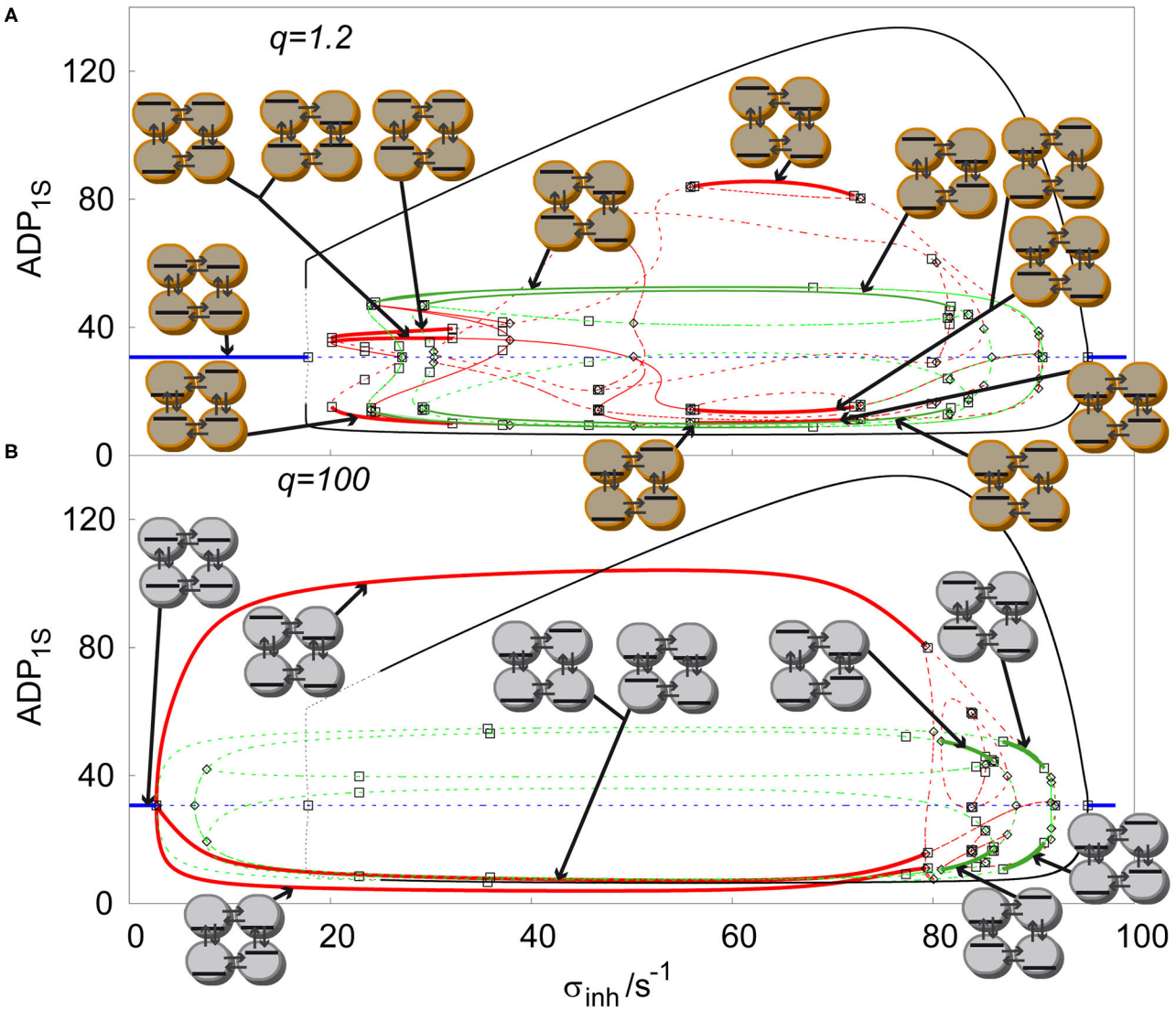


**FIGURE 5 |** Comparison of solution diagrams of four coupled cells in cyclic array, $\sigma_M = 100s^{-1}$, $k_{ADP}$= 0.10 $s^{-1}$, with varied ratio of $q$: **(A)** $q$=1.2, **(B)** $q$ = 100. Red curve—asymmetric non-uniform stationary state; blue curve—homogeneous stationary state; green curve—symmetric non-uniform stationary state; full line—stable stationary solution, dashed curve—unstable stationary solution; empty square—Hopf bifurcation point; empty diamond—symmetry breaking bifurcation point. Each stable stationary state has assigned a symbolic representation of its pattern.

two windows of stable symmetric patterns shifted to the right, became much narrower and do not overlap, neither mutually, not with the window of stable asymmetric patterns. Thus, the effect of varying $q$ is profound as already indicated in **Figure 3**.

## CHEMICAL COMPUTING DEVICES

The bifurcation analysis in Sections Bifurcation Scenarios and Coexistence of Discrete Turing Patterns shows regions of stable Turing patterns in each system of arrays of cells. To perform chemical computing tasks, the system needs to be parametrically set to the specific regions of coexistence of multiple Turing patterns. To model dynamics of switching between Turing patterns, we incorporated perturbation elements in the Equations (1, 2), specifically:

$$p_i(t) = \begin{cases} A_i & t_k \le t < t_k + \Delta T \\ 0 & t_k + \Delta T \le t < t_{k+1} \end{cases} \quad k = 0, 1, 2, \ldots, m; \quad i = 1, \ldots, N. \tag{3}$$

The function $p_i(t)$ represents a sequence of perturbations in reactor $i$ applied by imposing a constant inflow/outflow rate $A_i$, within a time length $\Delta T$. $A_i$ represents the amplitude (positive or negative) of perturbation by the species $x$ (ATP), applied at times given by $t_k$. A sequence $\{t_k\}$ of $m$ perturbations is carefully chosen to avoid effect of previous perturbations to toggle between discrete Turing patterns and oscillations, and also to fit into a clock time given by the *central knockout* system, see section Logic

Gates. Specific perturbation amplitudes $A_i$ and time length $\Delta T$ will be chosen for each type of the chemical computing system. Furthermore, we assume that the level of $y$ (ADP) is monitored in each cell to evaluate the state of the system, because stationary state of y does not depend on $\sigma_{inh}$. The concentration $y$ of uniform stationary state in one cell is used as a concentration *threshold level* assigning to a non-uniform concentration profile in each cell either logic 1, when the concentration is above threshold level or logic 0, when the concentration is below threshold level.

## Tautology and Contradiction

In our previous chemical computing system (Muzika and Schreiber, 2013; Muzika et al., 2014), simultaneous perturbations with $\Delta T = 100$ s are used, which seems to be the minimum perturbation length to achieve transitions under given model parameters (the system shows large amplitude oscillations with the shortest period $T = 50.29$ s). There are also small amplitude oscillations, which are visible through superposition with large amplitude oscillations, having period $T \approx 400$ s. When the system is carefully perturbed by a positive perturbation for a proper time length $\Delta T$, it is possible to induce discrete Turing patterns by perturbation of only one cell in the case of a non-cyclic array. There are numerous possibilities to induce discrete Turing patterns in two coupled cells. An example of such a perturbation using $\Delta T = 600$ s applied at time $t_k = 1{,}400$ s with $A_i = 1.2$, is shown in **Figure 6**. We have found that $\Delta T$ and $t_k$ are mutually dependent when $\Delta T = (2000 - var)$ s, $t_k = (100 + var)$ s, for $A_i = 1.2$, where *var* is a time length to be chosen by the user. It is also possible to induce a discrete Turing pattern by certain combination of multiple short perturbations of only one cell, because when only one cell is perturbed, oscillations in all cells start again after the perturbation ends. In this case the system is able to remember previous perturbation for a certain time. Due to this system "memory" discussed in (Goldbeter and Moran, 1984) the induction of discrete Turing patterns is possible using two positive perturbations with the time delay between both perturbations $\leq 500$ s. In a linear array of three coupled cells, discrete Turing patterns can be induced by a combination of negative ($A_i = -1.0$) and positive ($A_i = 2.0$) perturbations.

Prior to a scheme for advanced cellular assemblages for chemical computing, it is necessary to have a device always defining truth and false statements. In Boolean terminology, we are talking about tautology, which gives always the output true/1 and contradiction, which gives always the output false/0. We propose this device using two coupled cells, where we induce discrete Turing pattern by a perturbation of one cell as shown in **Figure 6**. The induced Turing pattern is resistant to positive perturbation $A_i \leq 1.2$ and negative perturbation $A_i \geq -0.5$ therefore such a device can be used as a tautology function in the first cell and a contradiction function in the second cell. In a system composed of advanced cellular assemblages, it can be used as the basic true/false device necessary for knockout perturbations (Muzika and Schreiber, 2013; Muzika et al., 2014), see sections Logic Gates, Advanced Cellular Assemblages Design.

## Logic Gates

Arrays of coupled cells with glycolytic oscillatory reaction show coexistence of non-uniform stationary states and oscillations, see Sections Bifurcation Scenarios, Coexistence of Discrete Turing

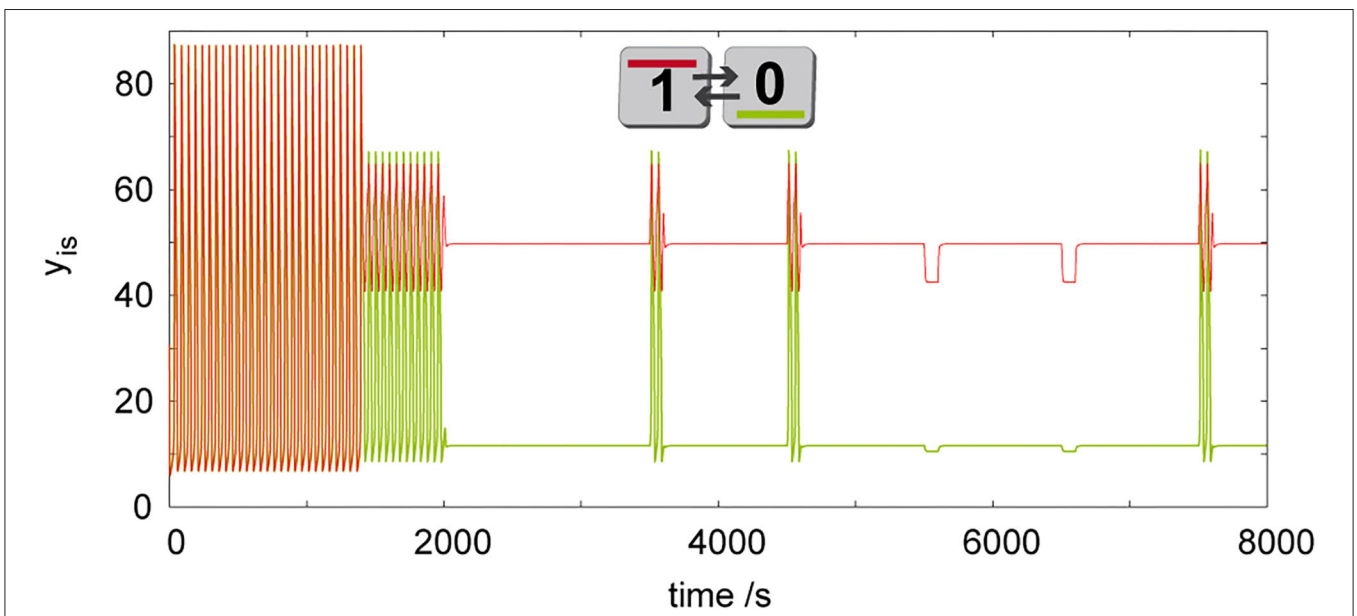


**FIGURE 6 |** Simulation of dynamic behavior of two cells ($q = 1$, $\sigma_M = 100$ s$^{-1}$, $\sigma_{inh} = 35$ s$^{-1}$, $k_{ADP} = 0.1$ s$^{-1}$) working as a tautology/contradiction gate, where discrete Turing pattern is forced by a long time perturbation ($\Delta T = 600$s, $A_i = 1.2$) of only a single cell. To show robustness of the discrete Turing pattern, system is further perturbed in the first cell by perturbations $A_i = 1.2$ at $t_k = \{3{,}500, 4{,}500, 7{,}500\}$ s and by $A_i = -0.5$ at $t_k = \{5{,}500, 6{,}500\}$ s using $\Delta T = 100$ s. The only pattern in this figure is shown by its symbolic representation followed by digital 0/1 output assignment.

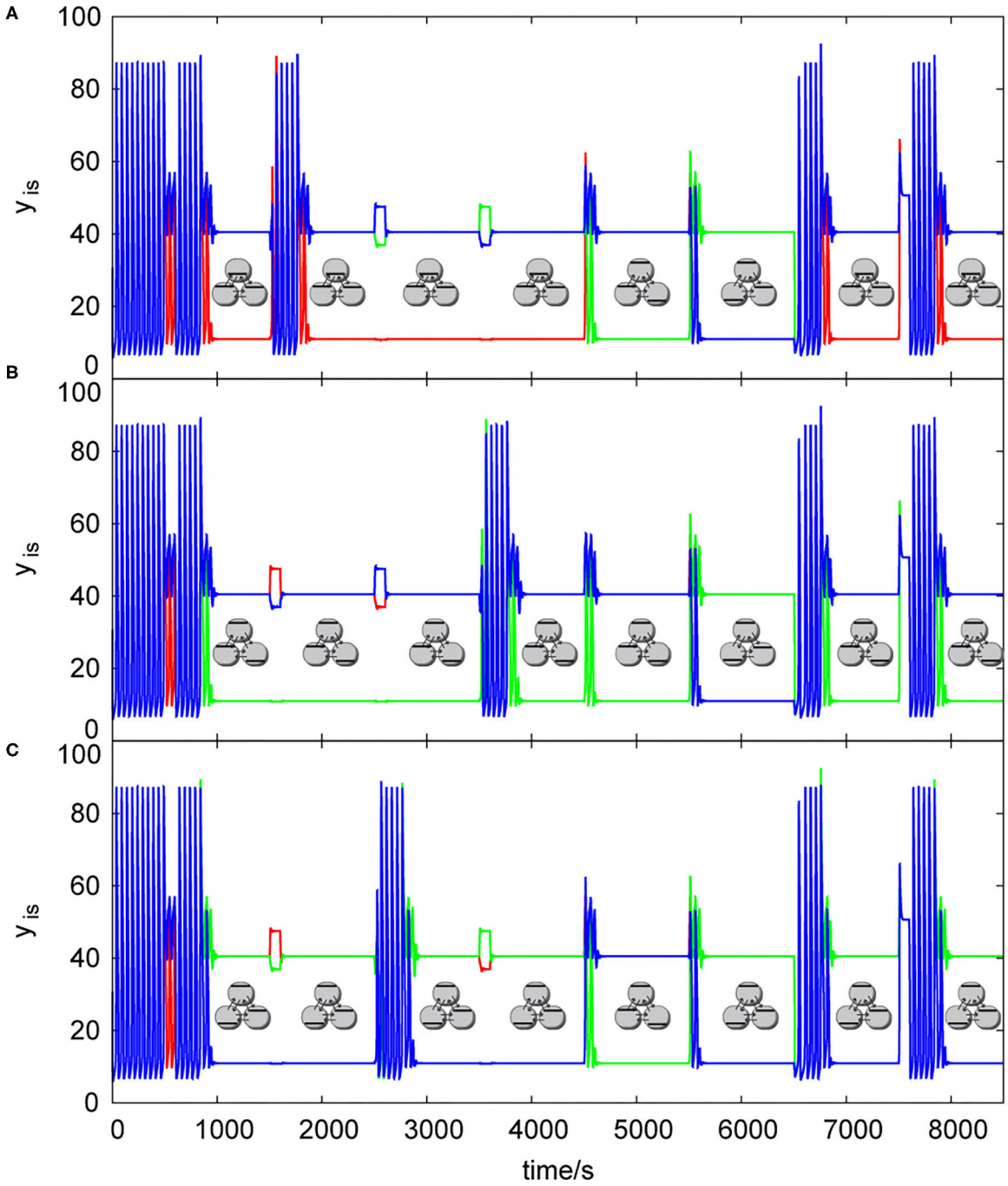


**FIGURE 7 |** List of dynamic simulations of three coupled cells in cyclic array using central knockout perturbations system, $k_{ADP}$= 0.1 $s^{-1}$, $\sigma_{inh}$= 35 $s^{-1}$, $q$ = 1: **(A)** knockout perturbation {0 1 1}—resulting truth table **Table 2B**, **(B)** knockout perturbation {1 0 1}– resulting truth table **Table 3A**, **(C)** knockout perturbation {1 1 0}– resulting truth table **Table 3B**. Each pattern in this figure is shown by its symbolic representation.

Patterns. When parameters are set to the region of coexistence of multiple discrete Turing patterns, an array of coupled cells operating under such conditions can be used for chemical computing, provided it is combined with a microfluidic system with carefully targeted perturbations.

Our chemical computing technique, employing digital ones and zeros, is based on transitions among discrete Turing patterns, therefore we need to avoid oscillatory behavior, which does not correspond to digital 1 or digital 0 in this technique. In previous work we proposed a *local knockout* perturbation system

(Muzika and Schreiber, 2013; Muzika et al., 2014) to induce a transition from stable uniform oscillations to a user predefined discrete Turing pattern. The local knockout perturbation in those systems was applied 200 s after indication of oscillations using $\Delta T = 100$ s.

As a technique more suitable to control larger number of cells in the arrays, we propose a modification of the local knockout perturbation system to a system called the central knockout perturbation system. The difference is that the central knockout perturbation system is designed to control only timings of the knockout perturbation and is triggered at exact times in a row $t_k = \{1{,}000\,k + 600\}$ s, $k = 0, 1, 2, \ldots, max$, where $max$ represents the finite number of perturbation sequences. For three coupled cells using all variations of input perturbations $max = 8$, for four coupled cells using all variations of input perturbations max = 16. Therefore, the central knockout perturbations define a clock rate for chemical computing cells, the current setup has one calculation per one cell per 1000 s.

When the central knockout system is activated it sends a signal to the array of cells, see **Figure 7**, to apply user defined knockout perturbation. The exact knockout perturbation in each array of cells is unique for the array type with specific values of the perturbation amplitudes $A_i$, the perturbation length $\Delta T$ and also the time delay. The central knockout perturbation system allows each array to calculate a logical function by its own internal parameters, it opens valves for input signals in a form of 1/0 and output valves in form of 1/0 using time delays, $t_{input-delay} = -100$ s and $t_{output-delay} = +900$ s. Each cell has a receptor similar to the one in local knockout perturbation system. It responds when $y_{is} > 80$ by giving a signal to the knockout valve. When the signal from the receptor and the signal from the central knockout system occur simultaneously, channels are opened according to user settings and the knockout perturbation is applied. Therefore, each knockout valve can be considered as a simple internal AND gate working on a different principle than our knockout logic gate technique.

The knockout perturbation sequence can be set at any time, each array of cells have its unique sequences, which are able to induce a discrete Turing pattern. The user can choose the sequence by creating temporary barriers in the excitable channels (using any excitable channel technique e.g., that used by Górecka and Górecki, 2006) blocking 0 or 1 signal to each cell from tautology/contradiction array, which are not desired for knockout, therefore only proper knockout sequence will be sent into the array. The influence of knockout perturbations on the behavior of the patterns in a cyclic array of three coupled cells is shown in **Figure 7**. Knockout sequences for three coupled cells in cyclic array are {0 1 1}, {1 0 1}, and {1 1 0}. Each sequence directly influence the type of function calculated in each cell, because it sets the 0 or 1 as the output value instead of oscillations. In **Figure 7A**, cells are oscillating from time = 0 s until the input perturbation |0 1 1|, at time = 500 s with the time length $\Delta T =$ 100 s. Then the transition to a discrete Turing pattern occurs until it is perturbed at time = 1,500 s by the input perturbation |1 0 0|, which leads to uniform oscillations. Oscillations were detected and knockout perturbation {0 1 1} was applied approximately at time 1,720 s with the time length $\Delta T = 100$ s leading to a discrete Turing pattern at time ∼1,840 s. The same sequence of tasks happened with input perturbations |0 0 1| and |0 1 0| until the time 4,500 s, where the input perturbation |1 0 1| with the time length $\Delta T = 100$ s leads to a second discrete Turing pattern. At the time 5,500 s, the input perturbation |1 1 0| is applied with the time length $\Delta T = 100$ s, which leads to a third discrete Turing pattern. At the time 6,500 s, the input perturbation |0 0 0| is applied which leads to uniform oscillations. They are again knocked out to the user predefined discrete Turing pattern using the knockout sequence {0 1 1}. The same knockout sequence is repeated with the last input perturbation |1 1 1|. **Figure 7B** shows the same process using input perturbation sequences in **Table 2A**, but for the knockout sequence {1 0 1}. **Figure 7C** shows again the same process as in **Figure 7A** using input perturbation sequences in **Table 2A**, with the knockout sequence {1 1 0}.

Output functions for each cell in the array assigned to a certain knockout perturbation sequence are described below.

**TABLE 1 |** Two-input logic gates and one-input inverter NOT.

| Logic gate | Algebraic Boolean expression |
|---|---|
| AND | $A_1 \bullet A_2$ |
| OR | $A_1 + A_2$ |
| NOT | $\overline{A_1}$ |
| NAND | $\overline{A_1 \bullet A_2}$ |
| NOR | $\overline{A_1 + A_2}$ |
| XOR | $A_1 \oplus A_2 = A_1 \bullet \overline{A_2} + \overline{A_1} \bullet A_2$ |
| XNOR | $\overline{A_1 \oplus A_2} = \overline{A_1} \bullet \overline{A_2} + A_1 \bullet A_2$ |

## Truth Tables

To determine the output dynamics to specific input perturbation sequences we added the knockout subroutine to the dynamic simulation program (Kubíček and Marek, 1983; Kohout et al., 2002) and thus we were able to determine response dynamics of arrays of cells and based on these results we were able to determine the output function of each cell and summarize the results in the form of truth tables. To properly describe functions in our truth tables, we express logical functions through their Boolean expressions (Boole, 1854) shown in **Table 1**. The output functions differ when using the local and central knockout perturbation system with the same kinetic parameter settings. Here we show only the results for the central knockout perturbation system, because it allows us to propose larger computing constructs.

In three coupled cells in a cyclic array, the highest number of coexisting discrete Turing patterns is found in the parameter range $\sigma_{inh} \approx (25;40)$ s$^{-1}$ and $k_{ADP} \approx (0.04;0.15)$ s$^{-1}$, therefore specific parameters $\sigma_{inh} = 35$ s$^{-1}$, $k_{ADP} = 0.1$ s$^{-1}$ used also in refs. (Muzika and Schreiber, 2013; Muzika et al., 2014) fit into this parameter region. We assume the kinetic parameters to be held constant throughout the assemblage of arrays by maintaining the temperature, concentrations of positive and negative effectors, and the pH level. The table of input perturbation sequences for the array of three coupled cells is shown in **Table 2A**. Dynamical response to these input perturbation sequences in the cyclic array

**TABLE 2 | (A)** Table of input signals valid for three coupled cells in cyclic array. **(B)** Truth table for the logic gate with knockout perturbation {0 1 1} (three coupled cells in cyclic array) $\sigma_{inh}$ =35 $s^{-1}$, $k_{ADP}$ = 0.1 $s^{-1}$.

| (A) | | | (B) | | |
|---|---|---|---|---|---|
| **Input signals** | | | **Output signals** | | |
| **1st cell ($A_1$)** | **2nd cell ($A_2$)** | **3rd cell ($A_3$)** | **1st cell ($y_1$)** | **2nd cell ($y_2$)** | **3rd cell ($y_3$)** |
| 0 | 1 | 1 | 0 | 1 | 1 |
| 1 | 0 | 0 | 0 | 1 | 1 |
| 0 | 0 | 1 | 0 | 1 | 1 |
| 0 | 1 | 0 | 0 | 1 | 1 |
| 1 | 0 | 1 | 1 | 0 | 1 |
| 1 | 1 | 0 | 1 | 1 | 0 |
| 0 | 0 | 0 | 0 | 1 | 1 |
| 1 | 1 | 1 | 0 | 1 | 1 |
| | | | $A_1 \bullet (A_2 \oplus A_3)$ | $\overline{A_1 \bullet A_3} + A_2$ | $\overline{A_1 \bullet A_2} + A_3$ |

**TABLE 3 | (A)** Truth table for the logic gate with knockout perturbation {1 0 1} (three coupled cells in cyclic array) $\sigma_{inh}$ = 35 $s^{-1}$, $k_{ADP}$= 0.1 $s^{-1}$. **(B)** Truth table for the logic gate with knockout perturbation {1 1 0} (three coupled cells in cyclic array) $\sigma_{inh}$=35 $s^{-1}$, $k_{ADP}$=0.1 $s^{-1}$.

| (A) | | | (B) | | |
|---|---|---|---|---|---|
| **Output signals** | | | **Output signals** | | |
| **1st cell ($y_1$)** | **2nd cell ($y_2$)** | **3rd cell ($y_3$)** | **1st cell ($y_1$)** | **2nd cell ($y_2$)** | **3rd cell ($y_3$)** |
| 0 | 1 | 1 | 0 | 1 | 1 |
| 1 | 0 | 1 | 1 | 1 | 0 |
| 1 | 0 | 1 | 1 | 1 | 0 |
| 1 | 0 | 1 | 1 | 1 | 0 |
| 1 | 0 | 1 | 1 | 0 | 1 |
| 1 | 1 | 0 | 1 | 1 | 0 |
| 1 | 0 | 1 | 1 | 1 | 0 |
| 1 | 0 | 1 | 1 | 1 | 0 |
| $A_1 + \overline{A_2 \bullet A_3}$ | $(A_1 \oplus A_3) A_2$ | $\overline{A_1 \bullet A_2} + A_3$ | $A_1 + \overline{A_2 \bullet A_3}$ | $\overline{A_1 \bullet A_3} + A_2$ | $(A_1 \oplus A_2) \bullet A_3$ |

of three coupled cells when using a given knockout perturbation can be viewed as behavior of logic gates responding with output functions to input perturbation sequences. The truth tables for each cell in the cyclic array of three coupled cells responding to the knockout perturbation sequence {0 1 1} is shown in **Table 2B**. The truth tables for the same array when using the knockout perturbation sequence {1 0 1} is shown in **Table 3A**, and tables for the knockout perturbation sequence {1 1 0} is shown in **Table 3B**. By comparing all three truth tables, we can see that the functions $\overline{A_1 \bullet A_2} + A_3$ and $A_1 + \overline{A_2 \bullet A_3}$ are present simultaneously for two different knockout perturbation sequences.

The truth tables for four coupled cells with different topology of arrays, different $q$ and $\sigma_{inh}$, and for different knockout perturbations are shown in **Table 4**. As the functions in four coupled cells in the cyclic array repeat, for a given preset knockout perturbation, the resulting functions are shown for each cell based on the value of knockout perturbation applied to each cell. For example, when the knockout perturbation is set to {1 1 0 0} for $q = 1$ and $\sigma_{inh}$= 50 $s^{-1}$, then the resulting logic gate yields $\overline{\left[\overline{(A_1 \oplus A_3)} \oplus A_4\right]} + A_1 + \overline{A_3 + A_4}$ in the first cell, $\overline{\left[\overline{(A_1 \oplus A_3)} \oplus A_4\right]} + A_2 + \overline{A_3 + A_4}$ in the second cell, $(A_1 \oplus A_2 \oplus A_4) \bullet A_3 \bullet \overline{A_1 \bullet A_2}$ in the third cell and $(A_1 \oplus A_2 \oplus A_4) \bullet A_4 \bullet \overline{A_1 \bullet A_2}$ in the fourth cell.

## Advanced Cellular Assemblages Design

Simple arrays of cells can be used to calculate basic logic functions or to perform regulatory and analysis tasks. A group of arrays of coupled cells can be arranged to form a cellular assemblage capable of advanced chemical computing using its parallel thread potential.

By assembling several arrays of cells to form an advanced design, connecting outputs of each cell to an adjacent cell of another array as an input perturbation via excitable channel technique and connecting each array to the central knockout perturbation system using again excitable channel technique, we would like to describe, how such an assemblage would work using the tautology/contradiction device, see **Figure 8**. The excitable channels system can be formed using gel media with immobilized enzymes or immobilized cells performing glycolysis, set to a parameter region of excitation or hard excitation (Goldbeter and Moran, 1984; Bagyan et al., 2005; Bolyó et al., 2010) in a similar way proposed by Górecka and Górecki (2006). The assemblage is divided into three parts: (1) the central knockout system; (2) chemical computing block; (3) memory block. The central knockout system is formed using one cell oscillating naturally with T $\approx$ 50.3 s; the counter device (similar to Górecki et al., 2003), which stacks up to 20 counts, and then sends a pulse to the tautology/contradiction device while resets itself; and lastly the tautology/contradiction array, see section Tautology and Contradiction, which sends 0 and 1 pulses as a response to the counter device pulses. The whole central knockout perturbation system sends both 1 and 0 signals every ~1,000 s into the system through red and blue channels. The signals carried through channels split at nodes marked by full circles (other crossings of red or blue lines do not correspond to splitting or other interaction). The chemical computing block is proposed as an example and can be formed from completely different types and sizes of arrays of coupled cells. In **Figure 8**, it is formed using NAND based block (Muzika et al., 2014) without switchable knockout perturbation sequences and block of arrays of four coupled cells in a cyclic array with switchable (user defined) knockout perturbation sequences. The perturbation can be set using a knockout valve. In place of the cyclic 4-array there can be any other array of cells depending on the desired data output. The layout of the NAND based block resembles a subgroup of the layout of CMOS NAND in the 8-bit ALU processor unit. This specific choice does not account for the fact that the 0 signal (blue channel) to every left cell in the mass-coupled pairs () needs to be inverted, neither does it optimize the layout or use the parallel computing power. It is a simple example, the optimization of NAND cells layout is not the goal of this work. The third part is a memory block, which can be built using

**TABLE 4 |** Table of output functions in each cell.

| Array type | Output signals | | | |
|---|---|---|---|---|
| | **1st cell** ($y_1$) | **2nd cell** ($y_2$) | **3rd cell** ($y_3$) | **4th cell** ($y_4$) |
| **T-shaped**, $q = 1$ {0 0 1 0}, $\sigma_{inh} = 35\ s^{-1}$ | $A_1 \bullet \overline{A_2} \bullet \overline{A_3 + A_4}$ | Tautology | $A_2 + A_3 + \overline{A_1 \oplus A_4}$ | $\overline{A_1} \bullet A_4 \bullet \overline{A_2 + A_3}$ |
| T-shaped, $q = 1$ {1 0 0 0}, $\sigma_{inh} = 35\ s^{-1}$ | $A_1 + A_4 + \overline{A_2 \oplus A_3}$ | Tautology | $\overline{A_1 + A_4} \bullet \overline{A_2} \bullet A_3$ | $\overline{A_1} \bullet A_2 \bullet \overline{A_3 + A_4}$ |
| **T-shaped**, $q = 1$ {0 0 0 1}, $\sigma_{inh}$=35 $s^{-1}$ | $A_1 \bullet \overline{A_2} \bullet \overline{A_3 + A_4}$ | Tautology | $\overline{A_1 + A_4} \bullet \overline{A_2} \bullet A_3$ | $A_2 + A_4 + \overline{A_1 \oplus A_3}$ |
| **Linear**, $q = 1$ {0 1 1 0}, $\sigma_{inh} = 35\ s^{-1}$ | $A_1 \bullet A_3 \bullet \overline{A_2 + A_4}$ | $\overline{A_1 \bullet A_3} + A_2 + A_4$ | The same as 2nd cell | The same as 1st cell |
| **Linear**, $q = 1$ {1 0 0 1}, $\sigma_{inh} = 35\ s^{-1}$ | $A_1 + A_3 + \overline{A_2 \bullet A_4}$ | $\overline{A_1 + A_3} \bullet A_2 \bullet A_4$ | The same as 2nd cell | The same as 1st cell |
| **Cyclic,** $q = 1$, $q = 1.2$ {0 0 1 1} {0 1 1 0} {1 1 0 0} {1 0 0 1}, $\sigma_{inh} = 35\ s^{-1}$ | $\mathbf{0} \sim A_1 \bullet \overline{A_3} \bullet (A_2 \oplus A_4)$<br>$\mathbf{1} \sim \overline{A_1} + A_3 + \overline{A_2 \oplus A_4}$ | $\mathbf{0} \sim (A_1 \oplus A_3) \bullet A_2 \bullet \overline{A_4}$<br>$\mathbf{1} \sim \overline{A_1 \oplus A_3} + \overline{A_2} \bullet A_4$ | $\mathbf{0} \sim \overline{A_1} \bullet A_3 \bullet (A_2 \oplus A_4)$<br>$\mathbf{1} \sim \overline{A_1} + A_3 + \overline{A_2 \oplus A_4}$ | $\mathbf{0} \sim (A_1 \oplus A_3) \bullet \overline{A_2} \bullet A_4$<br>$\mathbf{1} \sim \overline{A_1 \oplus A_3} + \overline{A_2} \bullet A_4$ |
| **Cyclic**, $q = 1$ {0 0 1 1} {0 1 1 0} {1 1 0 0} {1 0 0 1}, $\sigma_{inh} = 50\ s^{-1}$ | $\mathbf{0} \sim (A_2 \oplus A_3 \oplus A_4) \bullet A_1 \bullet \overline{A_2 \bullet A_3}$<br>$\mathbf{1} \sim \overline{\left[\overline{(A_2 \oplus A_3)} \oplus A_4\right]} + A_1 + \overline{A_2} + \overline{A_3}$ | $\mathbf{0} \sim (A_1 \oplus A_3 \oplus A_4) \bullet A_2 \bullet \overline{A_1 \bullet A_3}$<br>$\mathbf{1} \sim \overline{\left[\overline{(A_1 \oplus A_3)} \oplus A_4\right]} + A_2 + \overline{A_3} + \overline{A_4}$ | $\mathbf{0} \sim (A_1 \oplus A_2 \oplus A_4) \bullet A_3 \bullet \overline{A_1 \bullet A_2}$<br>$\mathbf{1} \sim \overline{\left[\overline{(A_1 \oplus A_2)} \oplus A_4\right]} + A_3 + \overline{A_1} + \overline{A_2}$ | $\mathbf{0} \sim (A_1 \oplus A_2 \oplus A_4) \bullet A_{4\|} \bullet \overline{A_1 \bullet A_2}$<br>$\mathbf{1} \sim \overline{\left[\overline{(A_1 \oplus A_2)} \oplus A_3\right]} + A_4 + \overline{A_1} + \overline{A_2}$ |
| **Cyclic,** $q = 1.2$ {1 1 0 0} {1 0 0 1} {0 1 1 0} {0 0 1 1}, $\sigma_{inh} = 50\ s^{-1}$ | $\mathbf{0} \sim A_1 \bullet \overline{A_3} \bullet (A_2 \oplus A_4)$<br>$\mathbf{1} \sim \overline{A_1} + A_3 + \overline{A_2 \oplus A_4}$ | $\mathbf{0} \sim (A_1 \oplus A_3) \bullet A_2 \bullet \overline{A_4}$<br>$\mathbf{1} \sim \overline{A_1 \oplus A_3} + \overline{A_2} \bullet A_4$ | $\mathbf{0} \sim (A_2 \oplus A_4) \bullet \overline{A_1} \bullet A_3$<br>$\mathbf{1} \sim \overline{A_1} + A_3 + \overline{A_2 \oplus A_4}$ | $\mathbf{0} \sim (A_1 \oplus A_3) \bullet \overline{A_2} \bullet A_4$<br>$\mathbf{1} \sim \overline{A_1 \oplus A_3} + \overline{A_2} \bullet A_4$ |
| **Cyclic**, $q = 1.2$ {1 1 1 0} {1 1 0 1} {1 0 1 1} {0 1 1 1} {1 1 0 0} {1 0 0 1} {0 1 1 0} {0 0 1 1}, $\sigma_{inh} = 30\ s^{-1}$ | $\mathbf{0} \sim \overline{A_2} \bullet A_3 \bullet A_4 \bullet (A_2 + A_3 + A_4) \bullet A_1$<br>$\mathbf{1} \sim \overline{A_2} \bullet A_3 \bullet A_4 \bullet (A_2 \oplus A_3 \oplus A_4) + \overline{A_2} + \overline{A_3} + \overline{A_4} + A_1$ | $\mathbf{0} \sim \overline{A_1} \bullet A_3 \bullet A_4 \bullet (A_1 + A_3 + A_4) \bullet A_2$<br>$\mathbf{1} \sim \overline{A_1} \bullet A_3 \bullet A_4 \bullet (A_1 \oplus A_3 \oplus A_4) + \overline{A_1} + \overline{A_3} + \overline{A_4} + A_2$ | $\mathbf{0} \sim \overline{A_1} \bullet A_2 \bullet A_4 \bullet (A_1 + A_2 + A_4) \bullet A_3$<br>$\mathbf{1} \sim \overline{A_1} \bullet A_2 \bullet A_4 \bullet (A_1 \oplus A_2 \oplus A_4) + \overline{A_1} + \overline{A_2} + \overline{A_4} + A_3$ | $\mathbf{0} \sim \overline{A_1} \bullet A_2 \bullet A_3 \bullet (A_1 + A_2 + A_3) \bullet A_4$<br>$\mathbf{1} \sim \overline{A_1} \bullet \overline{A_2} \bullet \overline{A_3} \bullet (A_1 \oplus A_2 \oplus A_3) + \overline{A_1} + \overline{A_2} + \overline{A_3} + A_4$ |

*0∼–knockout perturbation has value 0 in the respective column resulting to following function.*

*1∼–knockout perturbation has value 1 in the respective column resulting to following function.*

*In order to calculate each function properly, negative operators (NOT, NAND, NOR, NXOR) need to be processed first, otherwise commutative, associative and parenthesis rules apply.*

some of our previously proposed techniques. Specifically, we consider a technique, where 1-bit is stored using perturbation of an array of two cells with the perturbation sequence either |1 0| or |0 1|, details are described in our previous work (Muzika and Schreiber, 2013; Muzika et al., 2014). The advanced cellular assemblage system can work continuously by being perturbed with input perturbation sequences of 1 and 0 ("data input"), while it continuously calculates output stream in a form of 1 and 0. Data stream is conducted through brown channels. Output sequences can be stored in the memory block, used further as "data output" or both operations simultaneously The knockout switch blocks the knockout signal so that only a desired central knockout perturbation sequence will reach the array of cells.

## DISCUSSION AND CONCLUSIONS

We analyzed three coupled cells in a cyclic array and four coupled cells in linear, cyclic, and T-shaped arrays by methods of one-parameter continuation, two-parameter continuation, and dynamic simulation. We constructed and discussed bifurcation diagrams for all the analyzed systems with a focus on stable non-uniform stationary states (discrete Turing patterns). We performed dynamical simulations to determine response to the central knockout perturbation system with the aim of using them for chemical computing tasks.

By comparing three and four coupled cells with equal ratio of transport rate coefficients of both species ATP and ADP for $q = 1$, we found that discrete Turing patterns occur in arrays of four coupled cells in a wider parameter range than in the case of three coupled cells. When comparing different topology of arrays of four coupled cells, the cyclic array has both the widest parameter regions of occurrence of non-uniform stationary states and the largest number of different discrete Turing patterns. Parameter setting for occurrence of discrete Turing patterns for $q = 1$ can only be found under specific conditions, such as increased temperature, increased pH (Deville-Bonne et al., 1991; Tlapak-Simmons and Reinhart, 1998) and the presence of carbonates (Hereng et al., 2014). Under common laboratory conditions (∼25°C, pH∼5.5), discrete Turing patterns can only occur in specific media or using specific membranes, where q >> 1. The complexity of discrete Turing patterns at $q = 100$ [the transport rate coefficient of the inhibitor (ATP) is 100 times higher

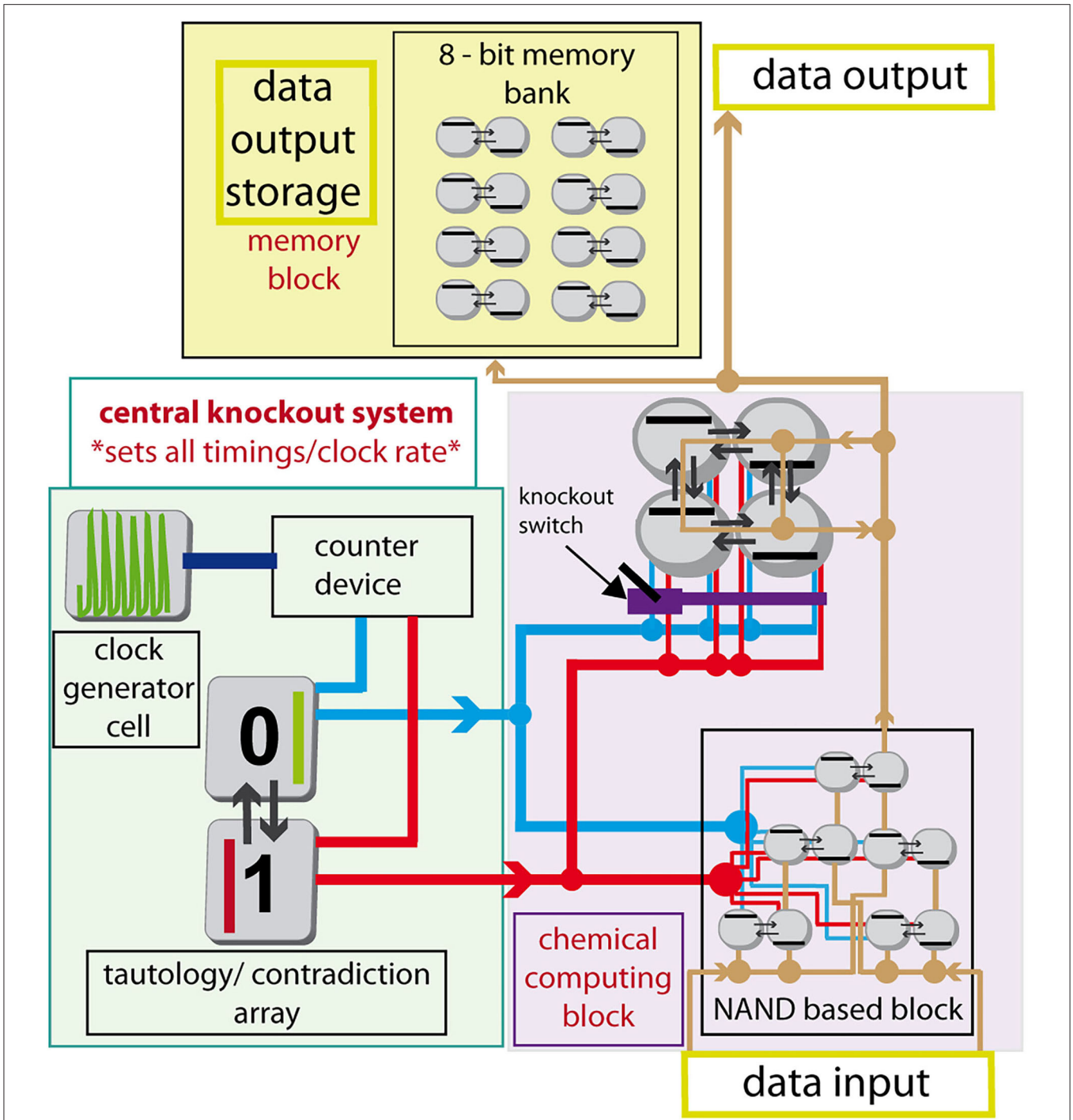


**FIGURE 8 |** Schematic diagram of an advanced cellular assemblage with chemical computing block, memory block, and central knockout system. Red line—knockout channel with signal 1, blue line—knockout channel with signal 0, brown line—data channel conducting signals 1/0, violet structure -knockout switch, counter device –counts 20 times the period 50.3 s, then sends the pulse into tautology/contradiction device. Full circle on data or knockout channels represents a splitting node.

than the transport rate coefficient of the activator (ADP)], is qualitatively similar to discrete Turing patterns at $q = 1$, the difference is in spontaneous vs. non-spontaneous occurrence of patterns, when parameters are varied and also in the range of parameters for which the patterns exist. Another observation we made is that cyclic arrays of cells offer richer selection

of Turing patterns, which might benefit the morphogenesis (Turing, 1952).

Analysis of solutions diagrams of all studied arrays of coupled cells shows parameter ranges of coexistence of multiple discrete Turing patterns. Careful transitions between discrete Turing patterns and uniform oscillations using precisely targeted perturbations can be used to design chemical computing devices (Muzika and Schreiber, 2013; Muzika et al., 2014). Using ATP as a signaling species might seem unconventional, as there is ATP in most of the living cells and it might cause interference. Nevertheless, some parts of human brain utilize ATP as a neurotransmitter (Verderioa and Matteolia, 2011) and there are channels with selective permeability to ATP (Locovei et al., 2006), therefore it makes the use of ATP plausible. Our previous technique for the knockout perturbation was focused on oscillations occurring in a specific array. In this work, we propose a modified technique, which creates knockout signal and sends it periodically to each array of cells in an advanced cellular assemblage. Also, it is only applied when the array is currently oscillating. Using this type of knockout technique, the user can switch between functions, which each array utilizes for chemical computing even during the process. Since it controls the computing rate of the advanced cellular assemblage, we call it the central knockout perturbation system.

In a number of papers Katz et al. proposed techniques based on working with enzymes in microfluidic cells using ATP and $NAD^+$/NADH as input/output signals and measuring their response in cuvettes using a UV-Vis spectrophotometer. The basic reactor technique is the AND gate using ATP (Privman et al., 2013a) followed by a network of AND gates working both with ATP and NADH (Privman et al., 2013b). NADH also allows enzymatic 1-bit memory units (one bit per cell), which can be arranged to groups by 8 to store ASCII table characters (Pita et al., 2009) similarly as shown in our advanced cellular assemblage scheme, where we use two cells to store one bit. Their technique also allows the release of NADH from the enzymatic computing device to trigger DNA computing (Mailloux et al., 2015). More complicated gates [switch gate, Fredkin gate, half bit adder, half bit subtractor (Fratto and Katz, 2016; Fratto et al., 2016)] can be constructed using three or more interconnected microfluidic devices, where the result is read from cuvette as collected solution from the microfluidic devices as a concentration of NADH and ABTS or ferricyanide/ferrocyanide. These techniques are somewhat closer to measuring metabolites, mainly NADH metabolically connected to ATP/ADP through glycolytic reaction chain as in our experimental system (Muzika et al., 2016), where the level of NADH concentrations is not the result of triggering one cascade of enzymes in microfluidic devices over another cascade of enzymes, but it is the result of transitions between non-uniform spatiotemporal patterns caused by synergy of enzymatic reactions and diffusion.

Gorecki et al. proposed a technique based on inorganic excitable channels utilizing various patterns of pathways of excitable channels. They constructed diodes (Gorecka and Gorecki, 2005; Gorecka et al., 2007; Igarashi et al., 2008), memory units (Górecki et al., 2009), clock generators (Gorecka and Gorecki, 2005), distance detectors (Bagyan et al., 2005; Górecki et al., 2009), band filter (Górecka and Górecki, 2003), logic gates (Sielewiesiuk and Górecki, 2001), and neuron-like structures (Górecka and Górecki, 2006). Such techniques have a great potential especially due to their universality. We expect that the excitable channel technique by Gorecki et al. can be combined with our chemical computing technique and some devices supplemented with it, provided that an excitable glycolytic reaction medium is available (Goldbeter and Moran, 1984; Bagyan et al., 2005; Bolyó et al., 2010). The main difference between excitable vs. Turing pattern techniques is that their memory unit requires a spatial disc reactor, where the waves are constantly traveling, while our memory unit holds its pattern as long as the cells are properly fed and temperature and pH conditions are maintained.

Our current logic gate technique can also be compared with techniques by Holley et al. (2011) and Górecki et al. (2014). By operating the BZ reaction in two oscillatory regimes, the signal is transported through connections between adjacent droplets (gel disks) and, based on the signal type in the output gel droplet it is either digital 0 or digital 1. Using this technique, Adamatzky et al. were able to construct a diode, NAND and XOR logic gate and 1-bit adder. Their technique requires a larger number of droplets for a single basic logic function compared to the number of coupled cell used in our parallel thread chemical computing technique. On the other hand, their technique does not require knockout perturbation system.

Our future research will focus on experiments with transitions between oscillations and non-uniform stationary states in two cuvettes coupled by peristaltic reciprocal pumping (Muzika et al., 2016) and on a chemical computing technique that does not require knockout perturbations.

## DATA AVAILABILITY STATEMENT

The raw data supporting the conclusions of this article will be made available by the authors, without undue reservation.

## AUTHOR CONTRIBUTIONS

FM and IS: conceptualization, formal analysis, software, writing—review, and editing. IS: funding acquisition. FM, IS, and LS: investigation and methodology. FM: visualization and writing—original draft. All authors contributed to the article and approved the submitted version.

## FUNDING

This work was supported by the grant 18-24397S from the Czech Science Foundation.

## ACKNOWLEDGMENTS

We thank the University of Chemistry and Technology for laboratory equipment and Czech Science Foundation for support.

## REFERENCES


Adamatzky, A. (1998). Universal dynamical computation in multidimensional excitable lattices. *Int. J. Theor. Phys.* 37, 3069–3108. doi: 10.1023/A:1026604401265

Adamatzky, A., Kitson, S., Costello, B. D. L., Matranga, M. A., and Younger, D. (2011). Computing with liquid crystal fingers: models of geometric and logical computation. *Phys. Rev. E* 84:061702. doi: 10.1103/PhysRevE.84.061702

Asakura, K., Konishi, R., Nakatani, T., Nakano, T., and Kamata, M. (2011). Turing pattern formation by the CIMA reaction in a chemical system consisting of quaternary alkyl ammonium cationic groups. *J. Phys. Chem. B* 115, 3959–3963. doi: 10.1021/jp111584u

Bagudu, A., Kraemer, C., Germann, P., Menshykau, D., and Iber, D. (2012). Digit patterning during limb development as a result of the BMP-receptor interaction. *Sci. Rep.* 2:991. doi: 10.1038/srep00991

Bagyan, S., Mair, T., Dulos, E., Boissonade, J., De Kepper, P., and Müller, S. C. (2005). Glycolytic oscillations and waves in an open spatial reactor: impact of feedback regulation of phosphofructokinase. *Biophys. Chem.* 116, 67–76. doi: 10.1016/j.bpc.2005.02.002

Bánsági, T., and Taylor, A. F. (2015). Helical Turing patterns in the Lengyel-Epstein model in thin cylindrical layers. *Chaos* 25:064308. doi: 10.1063/1.4921767

Bar-Eli, K. (1984). Coupling of chemical oscillators. *J. Phys. Chem.* 88, 3616–3622. doi: 10.1021/j150660a048

Bar-Eli, K., and Reuveni, S. (1985). Stable stationary states of coupled chemical oscillators. experimental evidence. *J. Phys. Chem.* 89, 1329–1330. doi: 10.1021/j100254a002

Bolyó, J., Mair, T., Koncová, G., and Hauser, M. J. B. (2010). Spatiotemporal dynamics of glycolytic waves provides new insights into the interactions between immobilized yeast cells and gels. *Biophys. Chem.* 153, 54–60. doi: 10.1016/j.bpc.2010.10.004

Boole, G. (1854). *An Investigation into the Laws of Thought, on which are founded the Mathematical Theories of Logic and Probabilities*. (Cambridge: Walton and Maberly; London: Macmillian and Co), 424. doi: 10.5962/bhl.title.29413

Castets, V., Dulos, E., Boissonade, J., and De Kepper, P. (1990). experimental evidence of a sustained standing turing type nonequilibrium chemical pattern. *Phys. Rev. Lett.* 64:2953. doi: 10.1103/PhysRevLett.64.2953

Crowley, M. F., and Epstein, I. R. (1989). Experimental and theoretical studies of a coupled chemical oscillator: phase death, multlstability, and in-phase and out-of-phase entrainment. *J. Phys. Chem.* 93, 2496–2502. doi: 10.1021/j100343a052

Deville-Bonne, D., Bourgain, F., and Garel, J. R. (1991). pH dependence of the kinetic properties of allosteric phosphofructokinase from escherichia coli. *Biochemistry* 30, 5750–5754. doi: 10.1021/bi00237a017

Dolník, M., Berenstein, I., Zhabotinsky, A. M., and Epstein, I. R. (2001). Spatial periodic forcing of turing structures. *Phys. Rev. Lett.* 87:238301. doi: 10.1103/PhysRevLett.87.238301

Dolník, M., and Marek, M. (1988). Extinction of oscillations in forced and coupled reaction cells. *J. Phys. Chem.* 92, 2452–2455. doi: 10.1021/j100320a014

Engl, E., and Attwell, D. (2015). Non-signalling energy use in the brain. *J. Physiol.* 593, 3417–3429. doi: 10.1113/jphysiol.2014.282517

Fratto, B. E., and Katz, E. (2016). Controlled logic gates—switch gate and fredkin gate based on enzyme-biocatalyzed reactions realized in flow cells. *ChemPhysChem* 17, 1046–1053. doi: 10.1002/cphc.201501095

Fratto, B. E., Lewer, J. M., and Katz, E. (2016). An enzyme-based half-adder and half-subtractor with a modular design. *ChemPhysChem* 17, 2210–2217. doi: 10.1002/cphc.201600173

Garzón-Alvarado, D. A., Martinez, A. M. R., and Segrera, D. L. L. (2011). A model of cerebral cortex formation during fetal development using reaction–diffusion–convection equations with Turing space parameters. *Comput. Methods Prog. Biomed.* 104, 489–497. doi: 10.1016/j.cmpb.2011.07.001

Giese, W., Eigel, M., Westerheide, S., Engwer, S., and Klipp, E. (2017). Influence of cell shape, inhomogeneities and diffusion barriers in cell polarization models. *Phys. Biol.* 12:066014. doi: 10.1088/1478-3975/12/6/066014

Goldbeter, A., and Moran, F. (1984). Onset of birhytmicity in a regulated biochemical system. *Biophys. Chem.* 20, 149–156. doi: 10.1016/0301-4622(84)80014-9

Górecka, J., and Górecki, J. (2003). T-shaped coincidence detector as a band filter of chemical signal frequency. *Phys. Rev. E* 67:067203. doi: 10.1103/PhysRevE.67.067203

Gorecka, J., and Gorecki, J. (2005). On one dimensional chemical diode and frequency generator constructed with an excitable surface reaction. *Phys. Chem. Chem. Phys.* 7, 2915–2920. doi: 10.1039/b504621a

Górecka, J., and Górecki, J. (2006). Multiargument logical operations performed with excitable chemical medium. *J. Chem. Phys.* 12:084101. doi: 10.1063/1.2170076

Gorecka, J. N., Górecki, J., and Igarashi, Y. (2007). One dimensional chemical signal diode constructed with two nonexcitable barriers. *J. Phys. Chem. A* 111, 885–889. doi: 10.1021/jp0662404

Górecki, J., Górecka, J. N., and Adamatzky, A. (2014). Information coding with frequency of oscillations in belousov-zhabotinsky encapsulated disks. *Phys. Rev. E* 89:042910. doi: 10.1103/PhysRevE.89.042910

Górecki, J., Górecka, J. N., Igarashi, Y., and Yoshikawa, K. (2009). Information processing with structured chemical excitable medium. *Nat. Comput.* 1, 48–68. doi: 10.1007/978-4-431-88981-6_5

Górecki, J., Yoshikawa, K., and Igarashi, Y. (2003). On chemical reactors that can count. *J. Phys. Chem. A* 107, 1664–1669. doi: 10.1021/jp021041f

Hadač, O., Muzika, F., Nevoral, V., Schreiber, I., and Pribyl, M. (2017). Minimal oscillating subnetwork in the huang-ferrell model of the MAPK cascade. *PLoS ONE* 12:e017845. doi: 10.1371/journal.pone.0178457

Hereng, T. H., Elgstøen, K. B. P., Eide, L., Rosendal, K. R., and Skålhegg, B. S. (2014). Serum albumin and HCO3- regulate separate pools of ATP in human spermatozoa. *Hum. Reprod.* 29, 918–930. doi: 10.1093/humrep/deu028

Hjelmfelt, A., and Ross, J. (1993). Mass-coupled chemical systems with computational properties. *J. Phys. Chem.* 97, 7988–7992. doi: 10.1021/j100132a030

Hjelmfelt, A., Schneider, F. W., and Ross, J. (1993). Pattern recognition in coupled chemical kinetic systems. *Sci. N. Ser.* 260, 335–337. doi: 10.1126/science.260.5106.335

Holley, J., Jahan, I., Costello, B. D. L., and Bull, L., Adamatzky, A. (2011). Logical and arithmetic circuits in Belousov-Zhabotinsky encapsulated disks. *Phys. Rev. E* 84:056110. doi: 10.1103/PhysRevE.84.056110

Horvath, J., Szalai, I., and De Kepper, P. (2009). An experimental design method leading to chemical turing patterns. *Science* 324, 772–775. doi: 10.1126/science.1169973

Howard, G., Bull, L., Costello, B. D. L., Gale, E., and Adamatzky, A. (2014). Evolving spiking networks with variable resistive memories. *Evol. Comput.* 22, 79–103. doi: 10.1162/EVCO_a_00103

Hynne, F., Danø, S., and Sørensen, P. G. (2001). Full-scale model of glycolysis in Saccharomyces cerevisiae. *Biophys. Chem.* 94, 121–163. doi: 10.1016/S0301-4622(01)00229-0

Igarashi, Y., Górecki, J., and Gorecka, J. N. (2008). One dimensional signal diodes constructed with excitable chemical system. *Acta Phys. Polonica B* 39:1187–1197. Available online at: https://www.actaphys.uj.edu.pl/R/39/5/1187/pdf

Kerszberg, M., and Wolpert, L. (1998). Mechanisms for positional signalling by morphogen transport a theoretical study. *Theor J. Biol.* 191, 103–114. doi: 10.1006/jtbi.1997.0575

Kim, J., and Winfree, E. (2011). Synthetic *in vitro* transcriptional oscillators. *Mol. Syst. Biol.* 7:465. doi: 10.1038/msb.2010.119

Kohout, M., Schreiber, I., and Marek, M. (2002). A computational tool for nonlinear dynamical and bifurcation analysis of chemical engineering problems. *Compt. Chem. Eng.* 26, 517–527. doi: 10.1016/S0098-1354(01)00783-9

Kondo, S., and Miura, T. (2010). Reaction-diffusion model as a framework for understanding biological pattern formation. *Science* 329, 1616–1620. doi: 10.1126/science.1179047

Kozubowski, L., Saito, K., Johnson, J. M., Howell, A. S., Zyla, T. R., and Lew, D. J. (2008). Symmetry-breaking polarization driven by a Cdc42p GEF-PAK complex. *Curr. Biol.* 18, 1719–1726. doi: 10.1016/j.cub.2008.09.060

Kubíček, M., and Marek, M. (1983). *Computational Methods In Bifurcation Theory And Dissipative Structures*. (New York, NY: Springer Verlag), 243. doi: 10.1007/978-3-642-85957-1

Locovei, S., Wang, J., and Dahl, G. (2006). Activation of pannexin 1 channels by ATP through P2Y receptors and by cytoplasmic calcium. *FEBS Lett.* 580, 239–244. doi: 10.1016/j.febslet.2005.12.004

Lue, J. C., and Fang, W. C. (2008). Bio-inspired microsystem for robust genetic assay recognition. *J. Biomed. Biotechnol.* 2008:259174. doi: 10.1155/2008/259174

Mailloux, S., Gerasimova, Y. V., Guz, N., Kolpashchikov, D. M., and Katz, E. (2015). Bridging the two worlds: a universal interface between enzymatic and DNA computing systems. *Angew. Chem. Int. Ed. Engl.* 54, 6562–6566. doi: 10.1002/anie.201411148

Majaj, N. J., Hong, H., Solomon, E. A., and Dicarlo, J. J. (2015). Simple learned weighted sums of inferior temporal neuronal firing rates accurately predict human core object recognition performance. *J. Neurosci.* 35, 13402–13418. doi: 10.1523/JNEUROSCI.5181-14.2015

McMurtrey, R. J. (2016). Analytic models of oxygen and nutrient diffusion, metabolism dynamics, and architecture optimization in three-dimensional tissue constructs with applications and insights in cerebral organoids. *Tissue Eng.* 22, 221–249. doi: 10.1089/ten.tec.2015.0375

Mediavilla, D., Metón, I., and Baanate, I. V. (2007). Purification and kinetic properties of 6-phosphofructo-1-kinase from gilthead sea bream muscle. *Biochim. Biophys. Acta* 1770, 706–715. doi: 10.1016/j.bbagen.2006.11.014

Meinhardt, M., and Gierer, A. (1974). Application of a theory of biological pattern formation based on lateral inhibition. *J. Cell Sci.* 15, 321–346.

Meinhardt, M., and Gierer, A. (2000). Pattern formation by local self-activation and lateral inhibition. *BioEssays* 22, 753–760. doi: 10.1002/1521-1878(200008)22:8<753::AID-BIES9>3.0.CO;2-Z

Monod, J., Wyman, J., and Changeux, J. P. (1965). On the nature of allosteric transition: a plausible model. *J. Mol. Biol.* 12, 88–118. doi: 10.1016/S0022-2836(65)80285-6

Muzika, F., and Schreiber, I. (2013). Control of turing patterns and their usage as sensors, memory arrays, and logic gates. *J. Chem. Phys.* 139:164108. doi: 10.1063/1.4825379

Muzika, F., Schreiberová, L., and Schreiber, I. (2014). Chemical computing based on turing patterns in two coupled cells with equal transport coefficients. *RSC Adv.* 4, 56165–56173. doi: 10.1039/C4RA08859J

Muzika, F., Schreiberová, L., and Schreiber, I. (2016). Discrete turing patterns in coupled reaction cells in a cyclic array. *Reac. Kinet. Mech. Cat.* 118, 99–114. doi: 10.1007/s11144-016-1004-y

Ouyang, Q., Li, R., Li, G., and Swinney, H. L. (1995). Sustained patterns in chlorite–iodide reactions in a onedimensional reactor. *J. Chem. Phys.* 102:2551–2555. doi: 10.1063/1.468684

Pita, M., Strack, G., MacVittie, K., Zhou, J., and Katz, E. (2009). Set–reset flip-flop memory based on enzyme reactions: toward memory systems controlled by biochemical pathways. *J. Phys. Chem. B* 113, 16071–16076. doi: 10.1021/jp908291f

Privman, V., Fratto, B. E., Zavalov, O., Halámek, J., and Katz, E. (2013a). Enzymatic AND logic gate with sigmoid response induced by photochemically controlled oxidation of the output. *J. Phys. Chem. B* 117, 7559–7568. doi: 10.1021/jp404054f

Privman, V., Zavalov, O., Halámková, L., Moseley, F., Halámek, J., and Katz, E. (2013b). Networked enzymatic logic gates with filtering: new theoretical modeling expressions and their experimental application. *J. Phys. Chem. B* 117, 14928–14939. doi: 10.1021/jp408973g

Qian, L., Winfree, E., and Bruck, J. (2011). Neural network computation with DNA strand displacement cascades. *Nature* 475, 368–372. doi: 10.1038/nature10262

Roy, K., Sharad, M., Fan, D., and Yogendra, K. (2014). "Brain-inspired computing with spin torque devices," in *DATE '14: Proceedings of the Conference on Design, Automation & Test in Europe* (Dresden), 1–6. doi: 10.7873/DATE.2014.245

Rudovics, B., Barillot, E., Davies, P. W., Dulos, E., Boissonade, J., and De Kepper, P. (1999). Experimental studies and quantitative modeling of turing patterns in the (chlorine dioxide, iodine, malonic acid) reaction. *J. Phys. Chem. A* 103, 1790–1800. doi: 10.1021/jp983210v

Sanz-Anchelergues, A., Zhabotinsky, A. M., Epstein, I. R., and Mañuzuri, A. P. (2001). Turing pattern formation induced by spatially correlated noise. *Phys. Rev. E* 63:056124. doi: 10.1103/PhysRevE.63.056124

Sauro, H. M., and Kholodenko, B. N. (2004). Quantitative analysis of signaling networks. *Prog. Biophys. Mol. Biol.* 86, 5–44. doi: 10.1016/j.pbiomolbio.2004.03.002

Shen, J., Ma, D., Gu, Z., Zhang, M., Zhu, X., Xu, X., et al. (2016). Darwin: a neuromorphic hardware co-processor based on spiking neural networks. *Sci. China Inf. Sci.* 59:023401. doi: 10.1007/s11432-015-5511-7

Sielewiesiuk, J., and Górecki, J. (2001). Logical functions of a cross junction of excitable chemical media. *Phys. Chem. A* 105, 8189–8195. doi: 10.1021/jp011072v

Snowdon, C., and Johnston, M. (2016). A novel role for yeast casein kinases in glucose sensing and signaling. *Mol. Biol. Cell* 27, 3369–3375. doi: 10.1091/mbc.E16-05-0342

Tlapak-Simmons, V. L., and Reinhart, G. D. (1998). Obfuscation of allosteric structure–function relationships by enthalpy–entropy compensation. *Biophys. J.* 75, 1010–1015. doi: 10.1016/S0006-3495(98)77589-7

Turing, A. (1952). The chemical basis of morphogenesis. *Phil. Trans. R. Soc. Lond. B* 237, 37–72. doi: 10.1098/rstb.1952.0012

Vanag, V. K., and Epstein, I. R. (2001). Pattern formation in a tunable medium: the belousov-zhabotinsky reaction in an aerosol OT microemulsion. *Phys. Rev. Lett.* 87:228301. doi: 10.1103/PhysRevLett.87.228301

Vastano, J. A., Pearson, J. E., Horsthemke, W., and Swinney, H. L. (1987). Chemical pattern formation with equal diffusion coefficients. *Phys. Lett. A* 124, 320–324. doi: 10.1016/0375-9601(87)90019-3

Verderioa, C., and Matteolia, M. (2011). ATP in neuron–glia bidirectional signaling. *Brain Res. Rev.* 66, 106–114. doi: 10.1016/j.brainresrev.2010.04.007

Wolpert, L. (1969). Positional information and the spatial pattern of cellular differentiation. *J. Theoret. Biol.* 25, 1–47. doi: 10.1016/S0022-5193(69)80016-0

Yoshimoto, M., Yoshikawa, K., and Mori, Y. (1993). Coupling among three chemical oscillators: synchronization, phase death, and frustration. *Phys. Rev. E* 47, 864–874. doi: 10.1103/PhysRevE.47.864

**Conflict of Interest:** The authors declare that the research was conducted in the absence of any commercial or financial relationships that could be construed as a potential conflict of interest.

*Copyright © 2020 Muzika, Schreiberová and Schreiber. This is an open-access article distributed under the terms of the Creative Commons Attribution License (CC BY). The use, distribution or reproduction in other forums is permitted, provided the original author(s) and the copyright owner(s) are credited and that the original publication in this journal is cited, in accordance with accepted academic practice. No use, distribution or reproduction is permitted which does not comply with these terms.*

frontiers in Chemistry

ORIGINAL RESEARCH
published: 09 November 2020
doi: 10.3389/fchem.2020.580703

# How Does a Simple Network of Chemical Oscillators See the Japanese Flag?

*Jerzy Gorecki* and Ashmita Bose*

*Department of Complex Systems and Chemical Processing of Information, Institute of Physical Chemistry, Polish Academy of Sciences, Warsaw, Poland*

Chemical computing is something we use every day (e.g., in the brain), but we can still not explore and master its potential in human-made experiments. It is expected that the maximum computational efficiency of a chemical medium can be achieved if information is processed in parallel by different parts of the medium. In this paper, we use computer simulations to explore the efficiency of chemical computing performed by a small network of three coupled chemical oscillators. We optimize the network to recognize the white and red regions of the Japanese flag. The input information is introduced as the inhibition times of individual oscillators, and the output information is coded in the number of activator maxima observed on a selected oscillator. We have used the Oregonator model to simulate the network time evolution and the evolutionary optimization to find the best network for the considered task. We have found that even a network of three interacting oscillators can recognize the color of a randomly selected point with 95% accuracy.

**Keywords: chemical oscillating reaction, Belousov-Zhabotinsky, Oregonator model, mutual information, evolutionary optimization, network, chemical computation**

OPEN ACCESS

***Edited by:***
*Annette F. Taylor, The University of Sheffield, United Kingdom*

***Reviewed by:***
*Vladimir Karl Vanag, Immanuel Kant Baltic Federal University, Russia*
*Pier Luigi Gentili, University of Perugia, Italy*

****Correspondence:***
*Jerzy Gorecki*
*jgorecki@ichf.edu.pl*

***Specialty section:***
*This article was submitted to Physical Chemistry and Chemical Physics, a section of the journal Frontiers in Chemistry*

***Received:*** *06 July 2020*
***Accepted:*** *31 August 2020*
***Published:*** *09 November 2020*

***Citation:***
*Gorecki J and Bose A (2020) How Does a Simple Network of Chemical Oscillators See the Japanese Flag? Front. Chem. 8:580703. doi: 10.3389/fchem.2020.580703*

## 1. INTRODUCTION

The success of semiconductor technology in machine information processing is the consequence of a highly efficient realization of logic gates characterized by a long time of error-free operation. The gates can be downsized to the nanoscale and concatenated to make more complex information processing devices. The semiconductor technology perfectly matches the bottom-up design scenario of information processing systems according to which more complex operations are represented by the combination of simpler tasks for which constructions of corresponding circuits have already been developed (Feynman et al., 2000).

The usefulness of logic gates and binary information coding demonstrated by semiconductor devices has strongly influenced other fields of unconventional computation including the chemical one (Adamatzky, 2018). Many studies have focused on strategies for the use of binary information coding in a computing medium and on realization of the logic gates or binary operations (Hjelmfelt et al., 1992; Adamatzky and De Lacy Costello, 2002; Magri et al., 2006; de Silva and Uchiyama, 2007; Gorecki et al., 2009). In some cases, molecular logic gates used as molecular probes offer an interesting alternative to the standard techniques (McKinney et al., 2017). However, most proposed chemical gates were much less efficient and were slower than the equivalent operations performed using semiconductors. The fact that a medium allows us to generate all logic gate proofs that the universal computation with this medium is theoretically possible. However, usually, the gates made of a chemical computing medium have limited potential applications. In the case of the Belousov-Zhabotinsky (BZ) reaction (Belousov, 1959; Zhabotinsky, 1964), the output signal

appears a few seconds after the input is introduced (Toth and Showalter, 1995; Steinbock et al., 1996). For other media, this time can be longer. For example, for gates with information coded in DNA molecules, it may take a few hours before the gate answer is obtained (Lin et al., 2018). The bottom-up construction of chemical information processing devices does not therefore seem to lead to an efficient realization of algorithms.

On the other hand, living organisms use chemistry for information processing and do so with significant efficiency for various classes of algorithms, including sound and image recognition, orientation in space, or navigation in crowded environments. This observation demonstrates that a chemical medium can be efficiently applied for specific computing tasks and presumably solve them using a highly parallel approach. Applications of parallel chemical computation have been reported in the literature. The classic example is the Adleman demonstration that the Hamiltonian path problem can be solved with DNA molecules (Adleman, 1994; Calude, 2002). Another example is the so-called prairie-fire algorithm for verification if there is a path linking two randomly selected points in a labyrinth. This problem can be solved by a labyrinth formed of an excitable medium where stable pulses of excitation can propagate (Steinbock et al., 1995; Agladze et al., 1997). If there is a path linking two points, an excitation generated at one of the points will then appear at the other, and the time difference between excitation and detection gives the estimation for the shortest path linking these points. Yet another famous computing application of a chemical medium working in parallel is the image processing of black and white photos performed using a photosensitive variant of BZ-reaction proceeding in a uniform, spatially distributed system (Kuhnert, 1986, 1989; Rambidi and Maximychev, 1997). In such medium, image processing is the consequence of a non-homogeneous initial state generated by initial illumination with intensity proportional to the grayscale of pixels of the processed image. In all methods mentioned above, the output information is coded in the time evolution of the computing medium.

The number of examples where a chemical medium can be efficiently used for computing is, however, limited. A top-down design strategy offers a promising method for the identification of the new ones. The strategy can be summarized as follows. In the beginning, we select a problem we want to solve and the computing medium that is supposed to do it. Next, we define how the input information is introduced and how the output is extracted from the observation of medium evolution. The top-down approach can be applied if the properties of the medium—and thus of the medium evolution—can be controlled by a number of adjustable parameters. Within this strategy, we are supposed to find the values of parameters for which the medium answer (the output) gives the most accurate solution of the considered problem. To do this, we need a number of examples (the training dataset) that can be used to verify the accuracy of computation performed by the medium.

In this paper, we concentrate on the geometrically oriented problem illustrated in **Figure 1A**. The object of our research is the Japanese flag with slightly rescaled proportions. We consider a red disk (sun) located in the mid of a white square (here represented by the Cartesian product $[0, 1] \times [0, 1]$). We postulate that a chemical computer can answer if a randomly selected point $(x, y) \in [0, 1] \times [0, 1]$ is located in the red or in the white region. To make the problem difficult, the disk radius $r = (\sqrt{2\pi})^{-1}$ is selected such that the areas of the sun and the white region are equal. A device that gives a random answer or a device that gives the same answer (red, white) to all inputs thus solves the problem with 50% accuracy (or with 50% chance to obtain the wrong answer). We show below that a chemical medium can solve the problem with much higher accuracy.

We postulated that the chemical medium composed of three coupled oscillators, illustrated in **Figure 1B**, was able to produce an accurate solution to the problem. The two-variable Oregonator model (Field and Noyes, 1974; Jung et al., 1998) of the Belousov-Zhabotinsky reaction (cf. Equations 1, 2) was used to describe the time evolution of individual oscillators. The interactions between individual oscillators were represented by reactions involving activators of individual oscillators. The choice of model has been motivated by the broad interest in applications of BZ-reaction for chemical information processing. The BZ-reaction is a complex, catalytic oxidation of an organic substrate (usually malonic acid) in an acidic environment (Field and Burger, 1985; Epstein and Pojman, 1998). Two stages of BZ reaction can be identified. One is fast oxidation of the catalyst, and the other is a slow reduction of the catalyst by an organic substrate. The solution color reflects concentrations of catalyst in the oxidized and reduced forms, and such types of non-linear evolution of the medium as oscillations, wave propagation, or the appearance of spatio-temporal patterns can therefore be easily observed. If the ruthenium complex $(Ru(bpy)_3^{2+})$ is used as the reaction catalyst, the BZ-reaction then becomes photosensitive (Kádár et al., 1997) and can be externally controlled by illumination. For the same initial concentrations of reagents, the medium can oscillate at dark, show an excitable behavior at a low light intensity, and have a steady state when it is strongly illuminated. At specific conditions, a spatially distributed medium can be locally excited, and the excitation can propagate in space. This type of behavior resembles the propagation of nerve impulses in living organisms. As a result, the BZ reaction has attracted attention as an inexpensive medium for experiments with neuron-like chemical computing (Adamatzky et al., 2005; Gorecka and Gorecki, 2006; Gentili et al., 2017). A moving pulse of excitation can be interpreted as a propagating bit of information. The Oregonator model used below to simulate *in-silico* the time evolution of the medium (see Equations 1, 2) correctly describes this phenomenon (Holley et al., 2011). However, such an approach requires a spatially distributed medium with a complex structure and precisely controlled reaction parameters, which seems complicated in real applications (Adamatzky et al., 2011).

In a number of recent papers, we considered flow of information (Grüunert et al., 2015) and the computational potential of coupled oscillator networks (Gizynski and Gorecki, 2016, 2017b; Gizynski et al., 2017). It was demonstrated that network parameters could be adjusted such that it can solve selected problems, e.g., recognizing a sphere in a multidimensional space or concluding on the type of cancer on

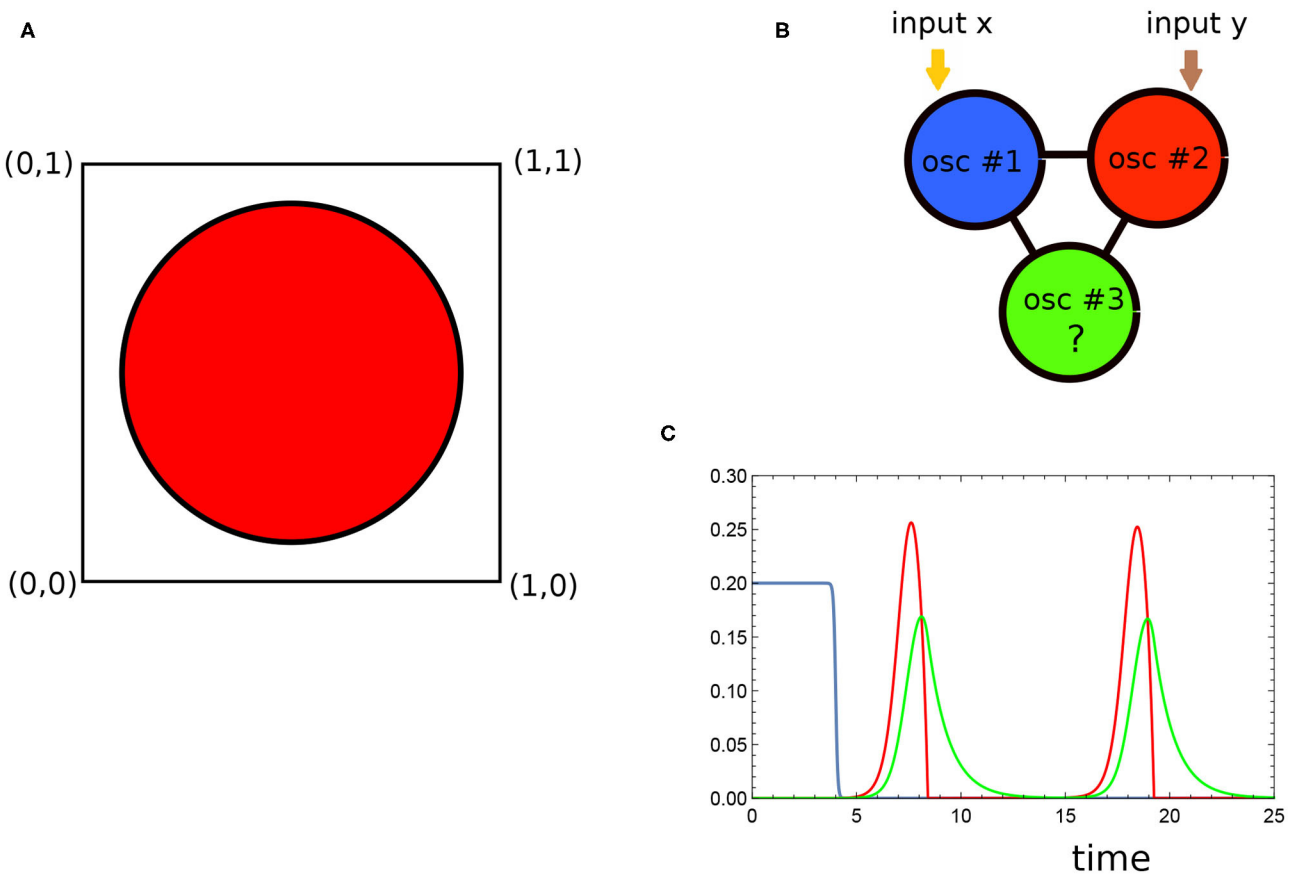


**FIGURE 1 | (A)** The graphical illustration of the problem that is solved by the optimized network. The disk is located at the square center. Its radius was selected such that the areas of the red sun and the white surrounding are equal. The network is supposed to answer if a randomly selected point $(x, y) \in [0, 1] \times [0, 1]$ belongs to the red or to the white regions. **(B)** The structure of the considered chemical oscillator network. The black line indicates interactions between oscillators. The type of oscillator #3 was optimized to achieve the maximum mutual information between locations of points and the number of activator maxima. **(C)** The time evolution of the activator (the red curve) and the inhibitor (the green line) for the Oregonator model with the activator decay corresponding to that of the optimized network ($\alpha = 0.849$). The blue line represents the external illumination (cf. Equation 4, $t_{illum} = 4$).

the basis of results of medical tests, with high accuracy. However, numerical simulations leading to these conclusions were based on oversimplified event-based-model reflecting only the basic features of the time evolution of a chemical oscillator and interactions between oscillators coupled with mutual activations. The event-based-model assumes sharp boundaries between three phases of the oscillation cycle: excitation, refractory, and responsive phases. It takes interactions into account as the condition for the excitation of an oscillator in the responsive phase in contact with an excited oscillator. Here, we present simulation results using the Oregonator model for a single oscillator and a model for oscillator interactions based on reactions involving their activators. We therefore believe the current model is more realistic than the one previously used and gives more information for potential experiments on the chemical computation.

The paper is organized as follows. The description of the mathematical model of the network time evolution and the optimization procedure are described in the next section. Section 3 contains obtained results and their discussion. The conclusions summarize obtained results and present suggestions for the future studies.

## 2. THE MODEL OF THE OSCILLATOR NETWORK AND ITS OPTIMIZATION PROCEDURE

### 2.1. The Network

We postulate that the problem of attributing color to a point on the Japanese flag defined by its coordinates can be approximately solved by a network of interacting chemical oscillators (cf. **Figure 1B**). The time evolution of each individual oscillator is described by two-variable Oregonator model (Field and Noyes, 1974; Jung et al., 1998) combined with additional reaction (cf. Equation 3) that reduces the concentration of activator. Let us assume that the variables $u_j$ and $v_j$ represent concentrations of the activator ($U_j$) and the inhibitor ($V_j$) for reactions proceeding

in the oscillator #j. The equations describing the time evolution of $u_j$ and $v_j$ read:

$$\frac{\partial u_j}{\partial t} = \frac{1}{\varepsilon}(u_j - u_j^2 - (fv_j + \phi_j(t))\frac{u_j - q}{u_j + q}) - \alpha u_j \quad (1)$$

$$\frac{\partial v_j}{\partial t} = u_j - v_j \quad (2)$$

The parameter $\varepsilon$ sets up a ratio of time scales of variables $u_j$ and $v_j$, and $q$ is a scaling constant and $f$ is the stoichiometric coefficient. In our simulations we used the following values of Oregonator model parameters for all oscillators ($1 \leq j \leq 3$): $\varepsilon = 0.2, q = 0.0002$ and $f = 1.1$. These values are similar to those reported in the literature (Holley et al., 2011). We assumed that the parameters of the Oregonator model were fixed and did not undergo optimization when we searched for the network with the highest ability to relate point position with its color.

The last term in Equation (1) describes the additional decay of activator with the reaction rate $\alpha$, which can be represented by the following reaction:

$$U_j + D_j \rightarrow products \quad (3)$$

The time dependent function $\phi_j(t)$ describes the influence of illumination on a photosensitive BZ-reaction and it is proportional to the light intensity. We considered $\phi_j(t)$ in the following form:

$$\phi_j(t) = 0.1 \cdot (1.001 + \tanh(-10(t - t_{ilum}(j))) \quad (4)$$

In this definition, the parameter $t_{ilum}(j)(> 0)$ defines the moment at which the illumination of the *jth* oscillator is switched off. At the beginning, the value of $\phi_j(t) \sim 0.2$ and the Oregonator model, with parameters given above and without the additional decay of the activator, predicts a stable steady state corresponding to $u_j = 0.0002$ and $v_j = 0.0002$. For long durations, $\phi_j(t)$ approaches 0.0001, which corresponds to an oscillation with a period of approximately 10.8 time units. The time evolution of the activator (the red curve) and inhibitor (the green line) for the Oregonator model for $\alpha = 0.849$ is illustrated in **Figure 1C**. The blue line represents the external illumination for $t_{illum} = 4$.

We assumed that oscillators in the network are coupled via the transport of the activator. This type of coupling was observed in our experiment on BZ-droplets stabilized by a solution of lipids in decane (Szymanski et al., 2011; Gizynski and Gorecki, 2017a). However, the network optimization method discussed below is general and can be applied to other couplings, such as the inhibitory coupling via transport of bromine studied by Vanag and his co-workers (Vanag and Epstein, 2004; Kaminaga et al., 2005, 2006; Smelov and Vanag, 2017). In such a case, a more complex model of oscillator dynamics should be applied (Vanag and Yasuk, 2018).

The interactions between oscillations in the considered network are indicated by the linking lines shown in **Figure 1B**. The pairs oscillators that interacted were fixed, and we did not modify the interactions during the network optimization. The coupling between the oscillators #k and #j was described by additional reactions involving the activators $U_k$ and $U_j$ of these oscillators:

$$U_j + B_j \rightarrow U_k + C_k \quad (5)$$

$$U_k + B_k \rightarrow U_j + C_j \quad (6)$$

with the identical reaction rate $\beta$. In reactions (3,5,6) $B, C$, and $D$ denote other molecules involved. We assume their concentrations were high with respect to concentrations of activators involved. The concentrations of $B$ and $D$ were thus assumed to be constant during the network evolution, and they are consequently not included in the model. Such an approach reflects the idea that reactions in individual oscillators are independent, and their coupling occurs as the result of processes 5 and 6 only.

Within our model the time evolution of the network is described by the following set of kinetic equations:

$$\frac{\partial u_j}{\partial t} = \frac{1}{\varepsilon}(u_j - u_j^2 - (fv_j + \phi_j(t))\frac{u_j - q}{u_j + q}) - (\alpha + 3\beta)u_j + \beta(u_1 + u_2 + u_3) \quad (7)$$

$$\frac{\partial v_j}{\partial t} = u_j - v_j \quad (8)$$

Let us notice that for each index $j$ the contributions $\beta u_j$ in the last two terms in Equation (7) cancel out reduce to $-(\alpha + 2\beta)u_j + \sum_{i \neq j} \beta u_i$, which reflects the kinetics of processes (3), (5), and (6).

Mathematically, the terms resulting from processes (5) and (6) have a similar form to those describing the coupling between CSTRs resulting from the exchange of equal volumes of reagents (and assuming that the is no transport of inhibitor). For the considered parameters of the Oregonator model (as well as a few other we tried), we found the interactions between oscillators described by reactions (5,6) were difficult to control without the process (3) because the model, depending on the value of $\beta$, gave too weak or too strong coupling between oscillators. The introduction of reaction (3) allowed us to control the value of activator concentration around its maximum and to moderate these interactions without the need to optimize all parameters of the Oregonator model.

Following our previous studies, we assume that an oscillator in the network can perform one of two functions (Gizynski and Gorecki, 2016, 2017b; Gizynski et al., 2017). There are input oscillators used to introduce the input values into the network. The activity of an oscillator assigned as the input of $x$ or $y$ is suppressed for time related to the input value. We assume that the relationship is described by an affine function. If the *jth* oscillator functions as the input one for the coordinate $x \in [0, 1]$, then

$$t_{ilum}(j) = t_{start} + (t_{end} - t_{start}) \cdot x \quad (9)$$

Keep in mind the symmetry of the problem the input oscillator #k for the $y$ value is inhibited for time:

$$t_{ilum}(k) = t_{start} + (t_{end} - t_{start}) \cdot y, \quad (10)$$

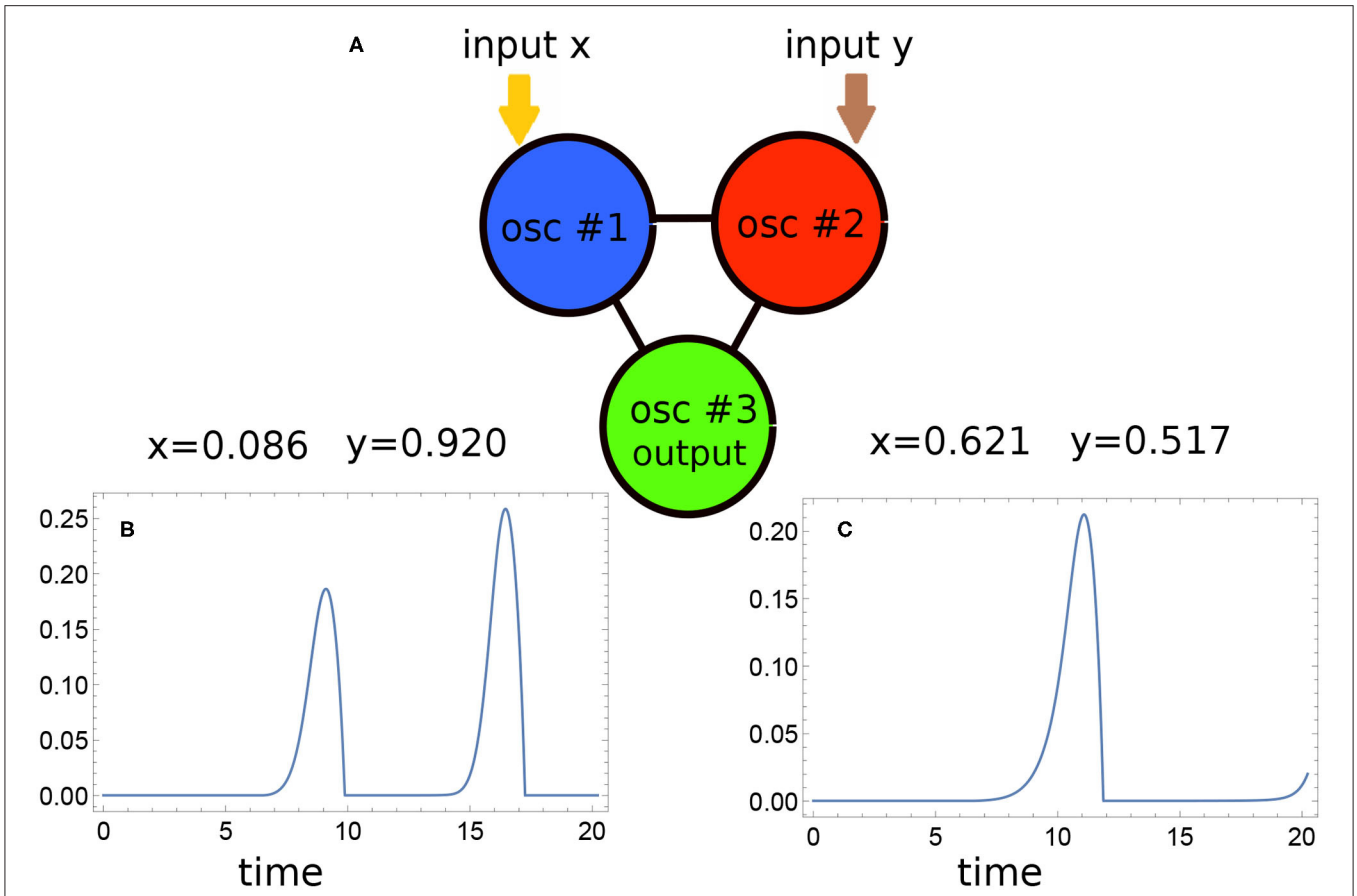


**FIGURE 2 | (A)** The idea of information processing with a network of oscillators illustrated using the parameters of the optimized network. Oscillators #1 and #2 are inhibited by times related to the values of $x$ and $y$ respectively. The output information is coded in the number of activator maxima observed on the oscillator #3. The time evolution of activator observed on this oscillator for points located in the white and red regions are shown in **(B,C)**, respectively. The evolution was calculated using the parameters of the optimized network: the oscillator #3 is the normal one with $t_{ilum}(3) = 6.37$, $t_{max} = 20.23$, $t_{start} = 3.78$, $t_{end} = 12.10$, $\alpha = 0.849$, $\beta = 0.251$.

and the values of parameters $t_{end}$ and $t_{start}$ in Equations (9) and (10) are identical. The values of $t_{end}$ and $t_{start}$ were the subject of network optimization procedure. The relationship between $t_{ilum}$ and the input value, obtained for the Japanese flag problem, is illustrated in **Figure 3B**.

The network can also include so-called normal oscillators inhibited for a fixed time that is not related to the values of $x$ and $y$. These normal oscillators moderate interactions in the medium and optimize it for a specific problem. Here, the type of oscillator #3 was not fixed, and the optimization procedure decided it.

We also assumed that the output information is coded in the number of activator maxima observed on one of the network oscillators within the time interval $[0, t_{max}]$. As we show later, the choice of the output oscillator results directly from the network optimization. The full definition of a computing network therefore includes the number of oscillators in the network, their types, the method of inputting $x$, $y$ values, and the interactions between oscillators.

The parameters that were modified during the network optimization procedure were:

- The type of oscillator #3 and, in the case it was a normal oscillator, its illumination time $t_{ilum}(3)$,
- The length of time interval $t_{max}$, within which the network evolution was observed,
- The times $t_{start}$ and $t_{end}$,
- The reaction rates $\alpha$ and $\beta$.

The values of network parameters and the parameters describing the relationship between the input values and the time-dependent illuminations of input oscillators determine the medium evolution. For each set of parameters, we solved the set of Equations (7, 8) numerically and studied the time evolution of the network for any values of $x$ and $y$. We used the explicit fourth-order Runge-Kutta algorithm (Press et al., 2007) with $h = 10^{-4}$ time step. The output information corresponding to a specific input was extracted from the numerical solution as the number of activator maxima observed at the selected oscillator within the time interval $[0, t_{max}]$. **Figures 2B,C** show such evolution for two selected points, one outside the sun and the other inside it. In the first case, the output oscillator produced two maxima of activator. In the second, we observed just a single one.

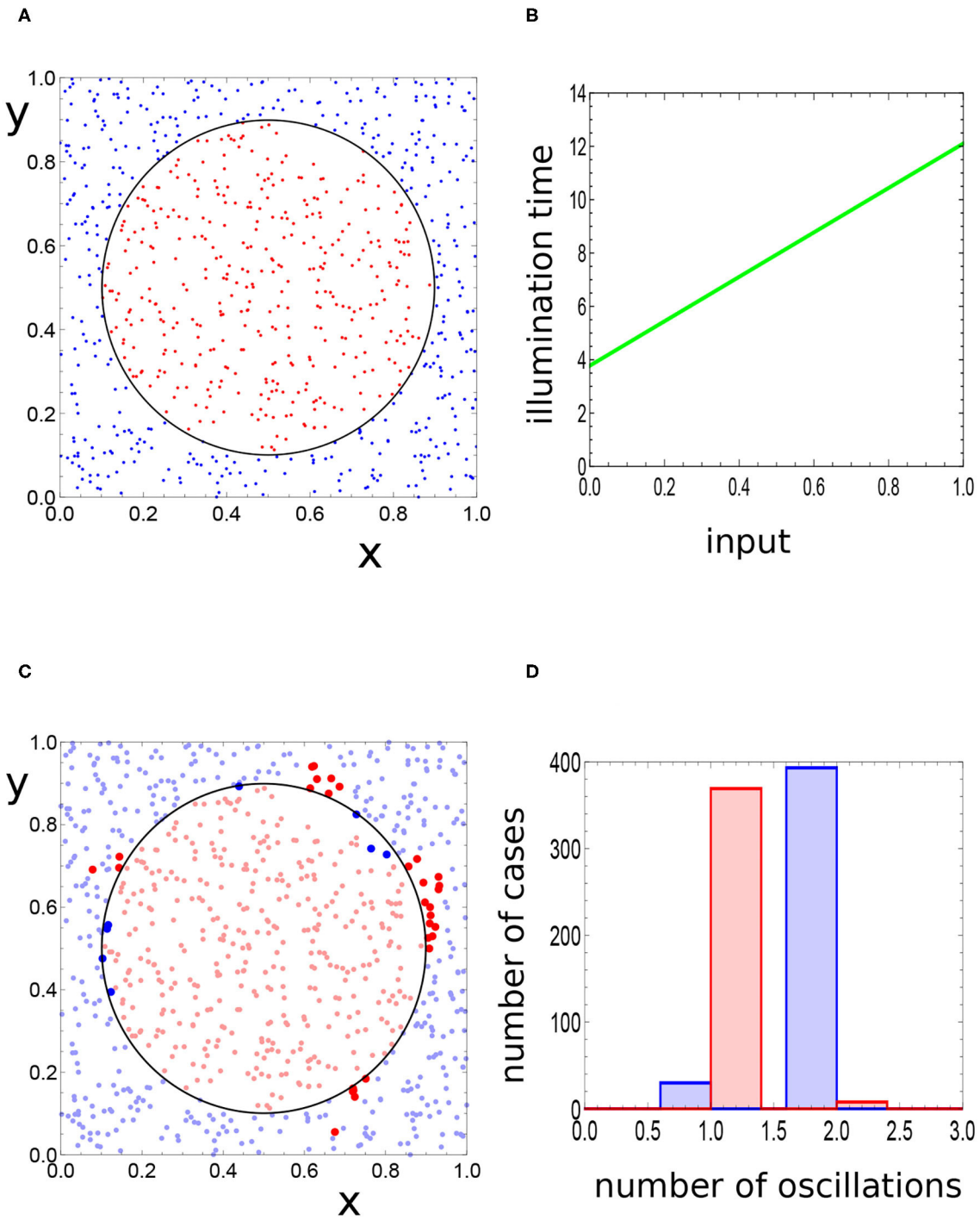


**FIGURE 3 | (A)** Locations of 800 points representing the records of the training dataset $D_S$. The red points are in the sun area, the blue ones outside it. **(B)** The relationship between $t_{ilum}$ and the input value, obtained for the optimized network solving the Japanese flag problem. **(C)** The response of the optimized network to inputs from the training dataset. The dark red points are located outside the sun area and generate a single maximum of activator at the output oscillator. The dark blue points are in the sun area and generate two maxima of activator. **(D)** The red and blue bars correspond to the red and blue points in **(A)**. The majority of red points produce a single maximum of the activator on oscillator #3, whereas most of the records corresponding to blue points generate two maxima.

## 2.2. Network Optimization

The method of the top-down optimization of a computing network has been described in details in our previous papers (Gizynski and Gorecki, 2016, 2017b), and we thus present it here shortly. In order to apply the method, we need a training dataset $D_S = \{(x_n, y_n, g_n), n = 1, N\}$ of the records in the form $(x, y, g)$

where $x, y \in [0, 1]$ and $g \in \{0, 1\}$. The numbers $x, y$ denote the point coordinates and $g$ is the record type; $g = 1$ for points located in the red disk and $g = 0$ for points outside it. Here, we used $D_S$ of $N = 800$ records with randomly generated points inside $[0, 1] \times [0, 1]$ located as illustrated in **Figure 3A**. Let us also introduce the discrete random variable of record types $G$, defined as: $G = \{g_n, n = 1, N\}$.

We postulate that information about the point color can be extracted from the number of activator maxima recorded on a selected oscillator of the network during the time interval $[0, t_{max}]$. The quality of an oscillator network for solving a specific problem can be estimated in the following way. Let us consider a record $(x_n, y_n, g_n) \in D_S$ and study the network evolution for the input $(x_n, y_n)$. Assume that $o_1(n)$, $o_2(n)$ and $o_3(n)$ are the numbers of activator maxima observed on oscillators #1, #2, and #3, respectively. Now, let us combine the results obtained for all inputs from the training dataset together and introduce the random variables $O_j = \{o_j(n), n = 1, N\}$ for $j \in \{1, 2, 3\}$. The mutual information between the random variables $G$ and $O_j$ is defined as (Cover and Thomas, 2006)

$$I(G; O_j) = H(G) + H(O_j) - H(G, O_j), \tag{11}$$

and it measures the usefulness of the oscillator #j to give information on the problem output. In general, the mutual information is the amount of information (in bits) that one random variable contains about another random variable. In Equation (11), $H(A)$ is the Shannon information entropy of the discrete random variable $A$ (Shannon, 1948) and the random variable $G, O_j$ is defined as $G, O_j = \{(g_n, o_j(n)), n = 1, N\}$. Obviously, the oscillator for which $I(G; O_j)$ is maximal was selected as the network output. The maximum $I(G; O_j)$ was used as the measure of network fitness in our optimization program.

The use of mutual information gives the quantitative measure of the network usefulness without the need to specify how to translate the number of activator maxima into the output. On the other hand, it has been shown that there is no monotonic relationship between the accuracy and mutual information (Gorecki, 2020), and a classifier optimized for the highest mutual information may therefore be less accurate than another one with lower mutual information. However, we believe this does not lead to a significant reduction in accuracy.

The network parameters, such as the type of oscillator #3, its inhibition time, the method for inputting the predictor values, or the type of interactions between oscillators, undergo optimization to achieve the highest mutual information on a representative dataset of cases. Both systematic methods of optimization and random trial and error ones can be applied. We have found (Gizynski and Gorecki, 2016, 2017b; Gizynski et al., 2017) that evolutionary optimization (Goldberg, 1989) oriented on obtaining the best classifier for a representative training dataset of the problem can lead to a computing network that performs the anticipated task with reasonable accuracy. At the beginning of the optimization procedure, we generated a population of $K = 200$ networks and selected a random training dataset illustrated in **Figure 3A**. The training dataset contained 377 points in the sun area (red) and 423 points in the surrounding region (blue). The adjustable parameters defining each network [type of oscillator #3, $t_{ilum}(3)$, $t_{max}$, $t_{start}$, $t_{end}$, $\alpha$ and $\beta$] were randomly generated. The fitness of each network was calculated using the whole training dataset. The next generation comprised of 20% of most fit networks of the previous population and of 80% of offspring generated by recombination and mutation operations applied to oscillators from top 50% networks of the previous population. We randomly selected two parents from 50% of the fittest networks and next recombined randomly their parameters to obtain an offspring. After recombination, we applied mutations to randomly selected parameters. The probability of this operation was selected, such that on average, a single parameter of the network was mutated. The maximum change in the chosen parameter value was restricted to 10% of the original one. Next, the fit of networks belonging to the new generation were calculated, and the procedure was repeated. The optimization procedure was continued for 1,000 generations.

## 3. RESULTS

The optimization procedure returned the network illustrated in **Figure 2A** in which the oscillator #3 is of the normal type and $t_{ilum}(3) = 6.37$. The other parameters of the network are the following: $t_{max} = 20.23$, $t_{start} = 3.78$, $t_{end} = 12.10$, $\alpha = 0.849$, and $\beta = 0.251$. The oscillator #3 is also the output one. For each input, we observed one or two activator maxima at the output oscillator. **Figure 3C** illustrates the relationship between the point location and the number of activator maxima. The statistic of the network outputs for all inputs from the training dataset is illustrated in **Figure 3D**. For most cases located in the sun area, we observed a single maximum (369 cases) and two maxima for only eight points (marked by dark blue dots in **Figure 3C**). On the other hand, for most of the background points, two activator maxima were observed (393 cases), whereas only 30 cases produced a single maximum (dark red points in **Figure 3C**). We can use the majority rule and declare that all points for which the network outputs a single maximum correspond to the sun, and all points for which two maxima are observed correspond to the surrounding white area. For the training dataset $D_S$, such a majority rule leads to $(369 + 393)/800 \sim 0.95$ accuracy. It is interesting that the distribution of incorrectly attributed cases is not rotationally symmetric.

For more objective evaluation of the accuracy of the optimized network we considered a large test dataset $D_T$ of 100,000 random, uniformly distributed points in the square $[0, 1] \times [0, 1]$. **Figure 4** shows the comparison between the location of a point from $D_T$ and the number of activator maxima observed on the output oscillator within the time interval $[0, t_{max}]$. The red light points are located inside the sun disk and produced a single maximum (48,028 cases). The light blue points are located in the surrounding area, and they forced two maxima of the output oscillator (47,117 cases). Using the majority rule introduced for the training dataset $D_S$ we can say that the total number of correctly located points was 95,145 thus the classifier accuracy is ∼95%. The dark colors mark points that are incorrectly attributed. The dark red points are located outside the sun,

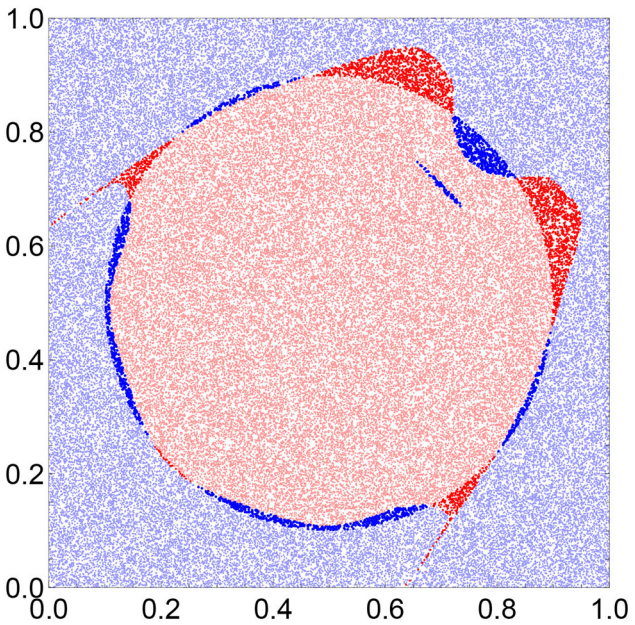


**FIGURE 4 |** The figure shows how the optimized network sees the Japanese flag. Each dot corresponds to a record from the testing dataset that contains 100,000 records. The red points produce a single activator maximum and are thus considered to be sun. For the records represented by the blue points, two maxima are observed, and they are thus classified as the surrounding white area. The light red and light blue points are those that are classified correctly. The dark red points belong to the white region in **Figure 1A**, but the network thinks they belong to the sun. The dark blue points are the points belonging to the sun, but the network incorrectly classifies them as the points of the white surrounding area.

but they force a single activator maximum (2,967 cases). The dark blue points produced two activator maxima, but they were located in the sun area (1,888 cases).

The red points in **Figure 4** (both light and dark) can be regarded as the image of the sun area seen by the optimized network. Instead of the disk, the network senses a complex, two-horned shape. In order to describe it more precisely we introduce new coordinates: $p = x - y$ and $q = x + y$. In these coordinates, the points producing a single activator maximum on the output oscillator are located, as shown in **Figure 5A**. The upper fitting curve (blue) is described:

$$F_U(p) = 1.49928 + 5.56776p^2 - 81.5484p^4 + 503.745p^6 - 2275.64p^8 + 7512.65p^{10} - 14690.6p^{12} + 11764.8p^{14} \quad (12)$$

and the lower fitting curve (green) is:

$$F_D(p) = 0.432601 + 1.65454p^2 - 2.0677p^4 - 107.24p^6 + 1120.59p^8 - 3887.3p^{10} + 5377.69p^{12} - 2552.69p^{14} \quad (13)$$

Now we can forget about the original problem and consider the question if a chemical computer can correctly distinguish the points of the unit square that are located between the curves $F_D(x - y)$ and $F_U(x - y)$. Such a problem looks rather difficult, but the answer is simple: a good candidate for such a chemical computer is the optimized network described above. Its accuracy is around 99%. The incorrectly attributed points are marked in **Figure 5B**. Most of them are located at the boundary, and the error may be connected with oversimplified fitting. There are also some points for which the attribution error is hard to explain (the blue horizontal line at $q \sim 1.4$ on **Figure 5B**), It would be interesting to verify if the number of such points can be reduced by changing the parameters of Oregonator.

## 4. DISCUSSION AND CONCLUSIONS

In this paper, we investigated whether a chemical computer can solve the color determination problem for a point on the Japanese flag. We considered the flag of Japan because it represents more complex geometrical structure than the striped pattern common for many flags like the Polish or the French ones. For example the flag of France can be represented by a unit square with the blue points for $(x, y), x \in [0, 1/3)$, the white area for $(x, y), x \in [1/3, 2/3)$, and the red region defined as $(x, y), x \in [2/3, 1]$. In such a case, the point color can be easily determined by a single oscillator that is also the input of x-coordinate. Let us consider $t_{start} = 0$. The inhibition time of input oscillator $[t_{illum}(1)]$ is proportional to the value of $x$ $[t_{illum}(1) = xt_{end}]$, and we can thus select $t_{end}$ such that a small number of oscillations appear in the red area, more of them are seen for the white points, and the largest number of oscillations is observed if the input represents coordinates of a blue point. For example, if $t_{end} = 32.4$, then the oscillator with parameters given in this paper observed for $t_{max} = 47$ shows 4, 3, and 2 maxima of activator for blue, white and red regions respectively.

The idea of a neural network has inspired the considered medium structure, composed as it is of interacting, individual units. Classical image recognition methods are based on multilayered neural networks in which the output of an artificial neuron is a single number (MacKay, 2003). In our approach, the time evolution of a neuron (oscillator) is more complex. The output of a separated artificial neuron remains constant, whereas, in our medium, the activator concentration in a non-interacting oscillator periodically changes in time. The output also depends on the time $t_{max}$ it was observed. It seems that to determine the color of a point on the Japanese flag with a given accuracy with a standard neural network, one needs more nodes than the number of oscillators used by our medium (Zammataro, 2010).

We have demonstrated that a simple network of just three coupled chemical oscillators can predict the color of a randomly selected point on the Japanese flag with 95% accuracy. Another interesting result is that the network delivers a fast answer. The output information if a point belongs to the white or the red region on the flag appears just within two oscillation periods. Our simulations were based on the Oregonator model that is more realistic than the event-based model previously used in papers on chemical classifiers (Gizynski and Gorecki, 2016, 2017b; Gizynski et al., 2017; Gorecki, 2020). The results of both models were

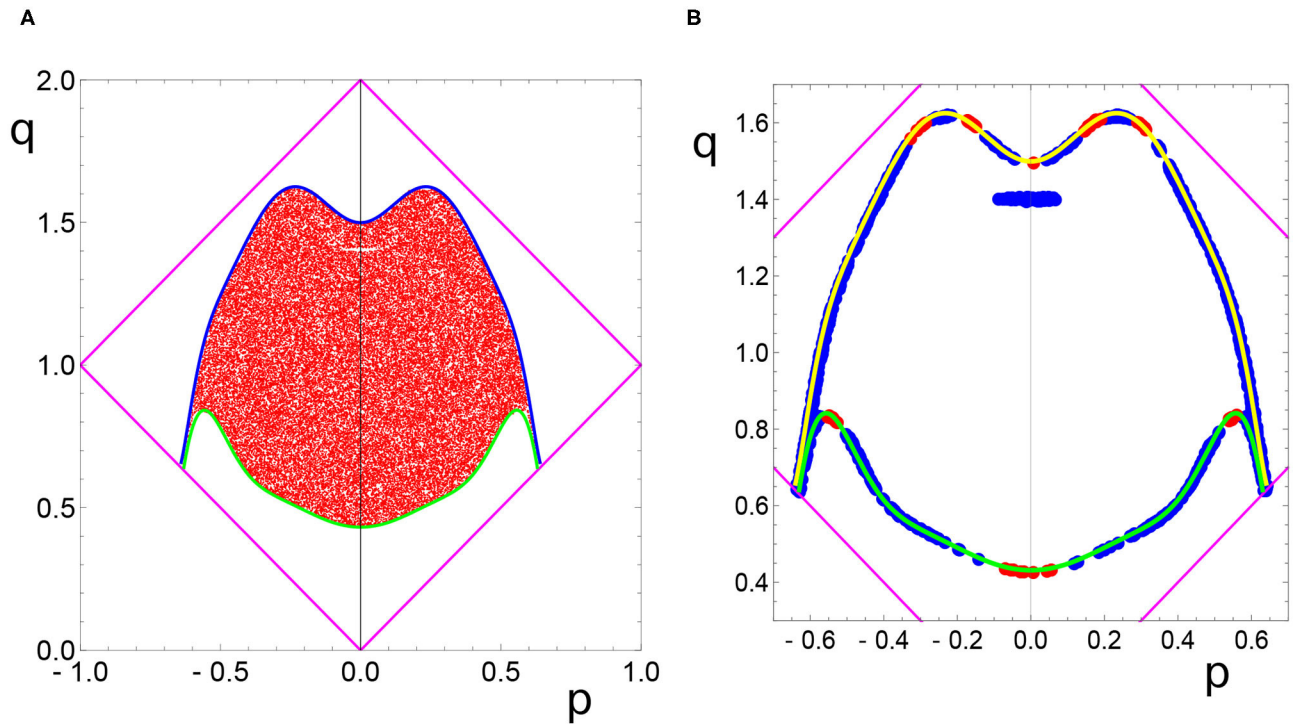


**FIGURE 5 | (A)** The shape of the sun area, as seen by the optimized network in the $p, q$ coordinates. The blue and green lines are the fits of the sun boundaries (cf. Equations 12, 13). **(B)** The positions of incorrectly classified points that are located in the region between the fitting lines. The blue points are classified as belonging to the region outside, but they should be inside. The red points are classified as belonging to the red region, but they fail outside the fitting lines. In **(B)** for better visibility, the upper fitting line is represented by a yellow curve.

qualitatively similar. It confirms that even small networks of interacting oscillators can perform complex computations. It can be expected that a more accurate location of point color can be achieved when more oscillators are taken into account. However, the numerical complexity of optimization rapidly increases with the number of parameters. We are working on the optimization method for large networks that would include previously accumulated results for smaller ones.

It is worth noticing that the points classified as belonging to the sun area group into an interesting, horned shape illustrated in **Figure 4A**. The boundaries of this shape can be described by complex polynomials of a high order. The problem of finding whether a point is located inside a horn-shaped area is more complex than the determination of point location with respect to a disk located at the center of the unit square. If a point belongs to the horned region, a high accuracy algorithm (∼99% accuracy) is given by the network of three oscillators we optimized to see the Japanese flag. We doubt whether any multilayered neural network can produce equally simple algorithm of finding a point in the horn-shaped area. An interesting problem for future studies is whether or not the shape of the correctly classified region can be regulated by the network parameters.

Results presented in the paper were obtained based on computer simulations, but the Oregonator model can qualitatively describe BZ-reaction and therefore brings information for potential experiments on the chemical computation. Systems of interacting oscillators have been studied experimentally using a few techniques (Vanag and Epstein, 2004; Kaminaga et al., 2005, 2006; Gentili et al., 2017). Interacting droplets containing reagents of BZ-reaction can be stabilized by a solution of lipids in the organic phase (Szymanski et al., 2011). If the photosensitive variant of BZ-reaction is used, then oscillations in droplets can be individually controlled. Experiments on the control of three coupled droplets mechanically stabilized inside a plastic cage were reported in Gizynski and Gorecki (2017a). Precisely the same system can be used as the classifier of a point in the Japan flag. The droplets acting as normal oscillators in the network are inhibited by illumination within the time interval that does not depend on the input values. The illumination times of input droplets depend on $x$ and $y$, as described by Equations (9) and (10). However, the experiments have demonstrated (Gizynski and Gorecki, 2017a) that it is rather difficult to stabilize even three droplets if a standard variant of BZ-reaction with the malonic acid is used. The bubbles of gas can appear between droplets, deform them, and change interactions between oscillators. We therefore believe that solid objects loaded with the catalyst, like DOWEX beads (Kuze et al., 2019) or silica gel beads (Mallphanov and Vanag, 2020), seem to be more suitable for experiments with information processing using a network of oscillators. Also, the

strategy of optical communication described by Gentili et al. (2017) can be applied to control interactions between oscillators and the inflow of input data.

We believe the maximization of information processing functionality based on optimization of the mutual information can be combined with other types of complex chemical dynamics, such as excitability or multistability. However, in typical experiments, oscillations are robust, whereas other types of non-linear behavior are more difficult to control, stabilize, and repeat. Additionally, our results illustrate that even a small network of oscillators can have significant information processing potential.

## DATA AVAILABILITY STATEMENT

All datasets presented in this study are included in the article.

## AUTHOR CONTRIBUTIONS

JG was responsible for the idea of the presented study, network optimization, and presentation of results. AB helped to develop the model for interactions between oscillators and verified the obtained results using her own simulation code. All authors contributed to the article and approved the submitted version.

## FUNDING

This publication was part of a project that has received funding from the European Union's Horizon 2020 (H2020-EU.1.3.4.) research and innovation program under the Marie Skłodowska-Curie Actions (MSCA-COFUND ID 711859) and from the Polish Ministry of Science and Higher Education for the implementation of an international co-financed project.

## REFERENCES

Adamatzky, A. (ed.). (2018). *Advances in Uncnoventional Computing*. Vol. 2. Springer.

Adamatzky, A., and De Lacy Costello, B. (2002). Experimental logical gates in a reaction diffusion medium: the XOR gate and beyond. *Phys. Rev. E* 66:046112. doi: 10.1103/Phys RevE.66.046112

Adamatzky, A., De Lacy Costello, B., and Asai, T. (2005). *Reaction-Diffusion Computers*. New York, NY: Elsevier.

Adamatzky, A., De Lacy Costello, B., Bull, L., and Holley, J. (2011). Towards arithmetic circuits in subexcitable chemical media. *Isr. J. Chem.* 51, 56–66. doi: 10.1002/ijch.201000046

Adleman, L. M. (1994). Molecular computation of solutions to Combinatorial Problems. *Science* 266, 1021–1024.

Agladze, K., Magome, N., Aliev, R., Yamaguchi, T., and Yoshikawa, K. (1997). Finding the optimal path with the aid of chemical wave. *Phys. D* 106, 247–254. doi: 10.1016/S0167-2789(97)00049-3

Belousov, B. P. (1959). "Periodically acting reaction and its mechanism (in Russian)," in *Collection of Short Papers on Radiation Medicine* (Medgiz), 145–152.

Calude, C. S. (2002). *Computing with Cells and Atoms*. London: Taylor & Francis Publishers.

Cover, T. M., and Thomas, J. A. (2006). *Elements of Information Theory*. New York, NY: Wiley-Interscience.

de Silva, A. P., and Uchiyama, S. (2007). Molecular logic and computing. *Nat. Nanotechnol.* 2, 399–410. doi: 10.1038/nnano.2007.188

Epstein, I. R., and Pojman, J. A. (1998). *An Introduction to Nonlinear Chemical Dynamics: Oscillations, Waves, Patterns, and Chaos*. New York, NY: Oxford University Press.

Feynman, R. P., Hey T., and Allen R. (2000). *Feynman Lectures on Computation*. Boulder, CO: CRC Press.

Field, R. J., and Burger, M. (eds.). (1985). *Oscillations and Traveling Waves in Chemical Systems*. New York, NY: Wiley.

Field, R. J., and Noyes, R. M. (1974). Oscillations in chemical systems. IV. Limit cycle behavior in a model of a real chemical reaction. *J. Chem. Phys.* 60, 1877–1884.

Gentili, P. L., Giubila, M. S., Germani, R., Romani, A., Nicoziani, A., Spalletti, A., et al. (2017). Optical communication among oscillatory reactions and photo-excitable systems: UV and visible radiation can synchronize artificial neuron models. *Angew. Chem. Int. Ed.* 56, 7535–7540. doi: 10.1002/anie.201702289

Gizynski, K., and Gorecki, J. (2016). A chemical system that recognizes the shape of a sphere. *Comput. Methods Sci. and Technol.* 22, 167–177. doi: 10.12921/cmst.2016.0000057

Gizynski, K., and Gorecki, J. (2017a). Chemical memory with states coded in light controlled oscillations of interacting Belousov-Zhabotinsky droplets. *Phys. Chem. Chem. Phys.* 19, 6519–6531. doi: 10.1039/C6CP07492H

Gizynski, K., and Gorecki, K. (2017b). Cancer classification with a network of chemical oscillators. *Phys. Chem. Chem. Phys.* 19, 28808–28819. doi: 10.1039/C7CP05655A

Gizynski, K., Gruenert, G., Dittrich, P., and Gorecki, J. (2017). Evolutionary design of classifiers made of oscillators containing a nonlinear chemical medium. *MIT Evol. Comput.* 25, 643–671. doi: 10.1162/EVCO_a_00197

Goldberg, D. E. (1989). *Genetic Algorithms in Search, Optimization and Machine Learning*. Boston, MA: Addison-Wesley Longman Publishing Co., Inc.

Gorecka, J., and Gorecki, J. (2006). Multi-argument logical operations performed with excitable chemical medium. *J. Chem. Phys.* 124:084101. doi: 10.1063/1.2170076

Gorecki, J. (2020). Applications of information theory methods for evolutionary optimization of chemical computers. *Entropy* 22:313. doi: 10.3390/e22030313

Gorecki, J., Gorecka, J. N., and Igarashi, Y. (2009). Information processing with structured excitable medium. *Nat. Comput.* 8, 473–492. doi: 10.1007/s11047-009-9119-y

Grüunert, G., Gizynski, K., Escuela, G., Ibrahim, B., Gorecki, J., and Dittrich, P. (2015). Understanding networks of computing chemical droplet neurons based on information flow. *Int. J. Neur. Syst.* 25:1450032. doi: 10.1142/S0129065714500324

Hjelmfelt, A., Weinberger, E. D., and Ross, J. (1992). Chemical implementation of finite-state machines. *Proc. Natl. Acad. Sci. U.S.A.* 89, 383–387.

Holley, J., Jahan, I., De Lacy Costello, B., Bull, L., and Adamatzky, A. (2011). Logical and arithmetic circuits in Belousov-Zhabotinsky encapsulated disks. *Phys. Rev. E* 84:056110. doi: 10.1103/PhysRevE.84.056110

Jung, P., Cornell-Bell, A., Moss, F., Kadar, S., Wang, J., and Showalter, K. (1998). Noise sustained waves in subexcitable media: from chemical waves to brain waves. *Chaos* 8, 567–575. doi: 10.1063/1.166338

Kádár, S., Amemiya, T., and Showalter, K. (1997). Reaction Mechanism for Light Sensitivity of the $Ru(bpy)_3^{2+}$ -Catalyzed Belousov-Zhabotinsky Reaction. *J. Phys. Chem. A* 101, 8200–8206.

Kaminaga, A., Vanag, V.K., and Epstein, I. R. (2006). A reaction-diffusion memory device. *Angew. Chem. Int. Ed.* 45, 3087–3089. doi: 10.1002/anie.200600400

Kaminaga, A., Vanag, V. K., and Epstein, I. R. (2005). "Black spots" in a surfactant-rich Belousov-Zhabotinsky reaction dispersed in a water-in-oil microemulsion system. *J. Chem. Phys.* 122:174706. doi: 10.1063/1.1888386

Kuhnert, L. (1986). A new optical photochemical memory device in a light-sensitive chemical active medium. *Nature* 319, 393–394. doi: 10.1038/319393a0

Kuhnert, L., Agladze, K. I., and Krinsky, V. I. (1989). Image processing using light-sensitive chemical waves. *Nature* 337, 244–247. doi: 10.1038/337244a0

Kuze, M., Horisaka, M., Suematsu, N. J., Amemiya, T., Steinbock, O., and Nakata S. (2019). Chemical wave propagation in the Belousov-Zhabotinsky reaction controlled by electrical potential. *J. Phys. Chem. A* 123, 4853–4857. doi: 10.1021/acs.jpca.9b02636

Lin, X., Liu, Y., Deng, J., Lyu, Y., Qian, P., Lia, Y., et al. (2018). Multiple advanced logic gates made of DNA-Ag nanocluster and the application for intelligent detection of pathogenic bacterial genes. *Chem. Sci.* 9, 1774–1781. doi: 10.1039/C7SC05246D

MacKay, D. J. C. (2003). *Information Theory, Inference and Learning Algorithms*. Cambridge, UK: Cambridge University Press.

Magri, D. C., Brown, G. J., McClean, G. D., and de Silva, A. P. (2006). Communicating chemical congregation: a molecular AND logic gate with three chemical inputs as a "lab-on-a-molecule" prototype. *J. Am. Chem. Soc.* 128, 4950–4951. doi: 10.1021/ja058295+

Mallphanov, I. L., and Vanag, V. K. (2020). Fabrication of new Belousov-Zhabotinsky micro-oscillators on the basis of silica gel beads. *J. Phys. Chem. A* 124, 272–282. doi: 10.1021/acs.jpca.9b09127

McKinney, B. O. F., Daly, B., Yao, C., Schroeder, M., and de Silva, A. P. (2017). Consolidating molecular logic with new solid-bound YES and PASS 1 gates and their combinations. *ChemPhysChem* 18:1760. doi: 10.1002/cphc.201700120

Press, W. H., Teukolsky, S. A., Vetterling, W. T., and Flannery, B. P. (2007). *Numerical Recipes: The Art of Scientific Computing*. New York, NY: Cambridge University Press.

Rambidi, N. G., and Maximychev, A. V. (1997). Towards a biomolecular computer. Information processing capabilities of biomolecular nonlinear dynamic media. *Biosystems* 41, 195–211. doi: 10.1016/S0303-2647(96)01678-4

Shannon, C. E. (1948). A mathematical theory of communication. *Bell Syst. Tech. J.* 27, 379–423. doi: 10.1002/j.1538-7305.1948.tb01338.x

Smelov, P. S., and Vanag, V. K. (2017). Experimental investigation of a unidirectional network of four chemical oscillators pulse-coupled through an inhibitor. *Russ. J. Phys. Chem. A* 91, 1015–1020. doi: 10.1134/S003602441706022X

Steinbock, O., Kettunen, P., and Showalter, K. (1996). Chemical wave logic gates. *J. Phys. Chem.* 100, 18970–18975. doi: 10.1021/jp961209v

Steinbock, O., Toth, A., and Showalter, K. (1995). Navigating complex labyrinths-optimal paths from chemical waves. *Science* 267, 868–871. doi: 10.1126/science.267.5199.868

Szymanski, J., Gorecka, J. N., Igarashi, Y., Gizynski, K., Gorecki, J., Zauner, K. P., et al. (2011). Droplets with information processing ability. *Int. J. Unconv. Comput.* 7, 185–200.

Toth, A., and Showalter, K. (1995). Logic gates in excitable media. *J. Chem. Phys.* 103, 2058–2066. doi: 10.1063/1.469732

Vanag, V. K., and Epstein, I. R. (2004). Stationary and oscillatory localized patterns, and subcritical bifurcations. *Phys. Rev. Lett.* 92:128301. doi: 10.1103/physrevlett.92.128301

Vanag, V. K., and Yasuk, V. O. (2018). Dynamic modes in a network of five oscillators with inhibitory all-to-all pulse coupling. *Chaos* 28:033105. doi: 10.1063/1.5004015

Zammataro, L. (2010). *Solving the Hole in the Square Problem with a Neural Network*. Available online at: http://demonstrations.wolfram.com/SolvingTheHoleInTheSquareProblemWithANeuralNetwork/

Zhabotinsky, A. M. (1964). Periodic oxidizing reactions in the liquid phase. *Dokl. Akad. Nauk SSSR* 157, 392–395.

**Conflict of Interest:** The authors declare that the research was conducted in the absence of any commercial or financial relationships that could be construed as a potential conflict of interest.

*Copyright © 2020 Gorecki and Bose. This is an open-access article distributed under the terms of the Creative Commons Attribution License (CC BY). The use, distribution or reproduction in other forums is permitted, provided the original author(s) and the copyright owner(s) are credited and that the original publication in this journal is cited, in accordance with accepted academic practice. No use, distribution or reproduction is permitted which does not comply with these terms.*

frontiers in Chemistry

REVIEW
published: 11 May 2021
doi: 10.3389/fchem.2021.611120

# Native Chemical Computation. A Generic Application of Oscillating Chemistry Illustrated With the Belousov-Zhabotinsky Reaction. A Review

*Marta Dueñas-Díez*[1,2] *and Juan Pérez-Mercader*[1,3]*

[1] Department of Earth and Planetary Sciences and Origins of Life Initiative, Harvard University, Cambridge, MA, United States, [2] Repsol Technology Lab, Madrid, Spain, [3] Santa Fe Institute, Santa Fe, NM, United States

Computing with molecules is at the center of complex natural phenomena, where the information contained in ordered sequences of molecules is used to implement functionalities of synthesized materials or to interpret the environment, as in Biology. This uses large macromolecules and the hindsight of billions of years of natural evolution. But, can one implement computation with small molecules? If so, at what levels in the hierarchy of computing complexity? We review here recent work in this area establishing that all physically realizable computing automata, from Finite Automata (FA) (such as logic gates) to the Linearly Bound Automaton (LBA, a Turing Machine with a finite tape) can be represented/assembled/built in the laboratory using oscillatory chemical reactions. We examine and discuss in depth the fundamental issues involved in this form of computation exclusively done by molecules. We illustrate their implementation with the example of a programmable finite tape Turing machine which using the Belousov-Zhabotinsky oscillatory chemistry is capable of recognizing words in a Context Sensitive Language and rejecting words outside the language. We offer a new interpretation of the recognition of a sequence of chemicals representing words in the machine's language as an illustration of the "Maximum Entropy Production Principle" and concluding that word recognition by the Belousov-Zhabotinsky Turing machine is equivalent to extremal entropy production by the automaton. We end by offering some suggestions to apply the above to problems in computing, polymerization chemistry, and other fields of science.

**Keywords: oscillatory chemical systems, chemical computing languages, computing automata, thermodynamics of computation, Turing machine, maximum entropy principle, chemical computing paradigm, Belousov-Zhabotinsky oscillatory reaction**

OPEN ACCESS

***Edited by:***
*Marek Orlik,*
*University of Warsaw, Poland*

***Reviewed by:***
*Kenichi Yoshikawa,*
*Doshisha University, Japan*
*Pier Luigi Gentili,*
*University of Perugia, Italy*

***Correspondence:**
*Juan Pérez-Mercader*
*jperezmercader@fas.harvard.edu*

***Specialty section:***
*This article was submitted to Physical Chemistry and Chemical Physics, a section of the journal Frontiers in Chemistry*

***Received:*** *28 September 2020*
***Accepted:*** *17 March 2021*
***Published:*** *11 May 2021*

***Citation:***
*Dueñas-Díez M and Pérez-Mercader J (2021) Native Chemical Computation. A Generic Application of Oscillating Chemistry Illustrated With the Belousov-Zhabotinsky Reaction. A Review. Front. Chem. 9:611120. doi: 10.3389/fchem.2021.611120*

## INTRODUCTION. WHAT IS A COMPUTATION? AND HOW DOES CHEMISTRY DO IT?

Computation is about information and its transformation. Given (Evans, 2011) some input information during a computation this information is suitably transformed and output in a way that can be used for some functional purpose. We can input into some machine the number of hours worked by employees, input information for an hourly rate and, if so instructed, the machine

will give the dollar amount for each employee which is then communicated to payroll … which, hopefully, will issue a funded paycheck! In a general sense a computation consists of the (a) input, (b) transformation, and (c) output of information that can then be used for some useful purpose (Feynman, 2000; Evans, 2011). For the above to take place, one needs to have some available information and a means of transforming it into some different form which is then output.

The "transformation" of the information must be (Feynman, 2000) "mechanical," i.e., same input information gives same output information. "Information" above is understood as "what is conveyed or represented by a particular arrangement or sequence of things" (Simpson and Weiner, 1994). The "things" can be any collection of objects, letters, numbers, or shapes, to mention just a few instances. Information, therefore, can be encoded into a sequence of symbols.

Let us now consider the general features of chemical reactions (Pauling, 1947, pp. 12, 95) in parallel to the previous description of a computation. In a chemical reaction, substances in the correct proportions get together, react according to a reaction mechanism, and generate a particular output. We can think of the reactants and the sequence in which they are brought into the reaction as input information. If we are at a scale where we can ignore the effects of fluctuations, we can think of the reaction mechanism as a means for mechanically transforming the reactants into some output products. We can immediately see that there is a clear parallel between a computation and a chemical reaction.

Therefore, in principle we can establish an analogy between chemistry and computation and unlock the power of chemistry to do some form of computational work. This, however, requires that we understand how to represent information in a form that can be (mechanically) processed by chemistry.

In chemistry, information resides in the relative positions of atoms in molecules, in the bonds, electron densities, and a long etc. of the properties of molecules and atoms (Sienko and Lehn, 2003). We can also take inspiration from natural life and represent information using chemistry following the way in which genetic information is represented with DNA: by means of an alphabet constructed with the purine and pyrimidine molecular bases, arranged in a certain order to represent and carry information which is (mechanically, i.e., systematically) processed in the cell's ribosomes. By analogy we can think of using a sequence of chemicals as a means to represent information with chemistry. The chemicals in the sequence could be the reactants for some reaction; the chemical transcription of the symbols would consist of the assignment of specific aliquots of the reactants to each symbol. Then the sequence in which the aliquots are fed to the reaction would represent the chemical transcription of the original symbolic sequence (cf. **Figure 1**).

The various aliquots of the reactants could represent "letters" in an abstract alphabet and some of their ordered sequential groupings would represent "words" in a language which is generated by an underlying grammar. If the aliquots correspond to chemical substances that react, we then have a parallel between letters/symbols, words in a language, and a "mechanical" processor of their information which is the chemical reaction (and the pathways contained in its mechanism). The products of the reaction in quantity and quality (including radicals) and the corresponding values of the state functions of the chemical system after it reaches some stable regime (not necessarily equilibrium) are the (chemically autonomous) material and physico-chemical "result" of the computation! We call this form of computation "native chemical computation" to emphasize the fact that it is only unassisted chemistry carrying out all the computation autonomously once the information has been input to the "machine." All the computation is done by molecules and atoms participating in the reaction. Note that "chemical computation" is a very broad topic and there are different approaches, most of them making use of reaction-diffusion, geometrical aids, and other types of hybrid approaches (Tóth and Showalter, 1995; Adamatzky and Costello, 2002; Gorecki et al., 2003; Ross et al., 2006; Wang et al., 2016). For an excellent review see Adamatzky (2019). Another interesting form of chemical computation uses chemical reactions to implement Fuzzy logic (a form of logic that deals with approximate modes of reasoning) and provides an approach to applications of chemical computation related to those of Fuzzy logic (Gentili, 2018 and references therein). Here, however, our focus is strictly on the "Native Chemical Computation" approach as defined above (In the remainder of the text whenever we talk of chemical computation we thus refer to Native Chemical Computation).

A chemical computation can involve of the order of Avogadro's number of molecules all of which contribute to the computation taking place in the reactor. This is indeed a very large level of parallelism but, unfortunately, it is offset by the huge level of correlation and synchronization of the molecules, so that effectively there seems to be a waste of the potentially available computational power in the molecules. In this paper, we will review some steps taken recently in the direction of harnessing this "waste" by making it more efficient.

After this brief Introduction, we will continue with a discussion of "How computations are performed," followed by a discussion of "What chemistry brings to computing;" these will be followed by sections devoted to "How Chemistry Computes," to a discussion of "Oscillatory Chemistry and Native Chemical Computation" then there is a section devoted to "The Interpretation of word acceptance in a native chemical Turing Machine" and on to a final section covering the necessary details for "Building a Turing machine using the BZ reaction Chemistry." We finalize with a brief Discussion and Conclusions section. The review is complemented by a basic bibliography where further references can be found, a list of Nomenclature and Definitions used in the review and four more technical **Appendices**.

## HOW COMPUTATIONS ARE PERFORMED

We can imagine a computation (in a mathematical sense) as the application of a sequential series of operations, or procedure, on some data which are carried out in order to solve some mathematical problem. For example, to solve a differential equation describing the time evolution of some substance

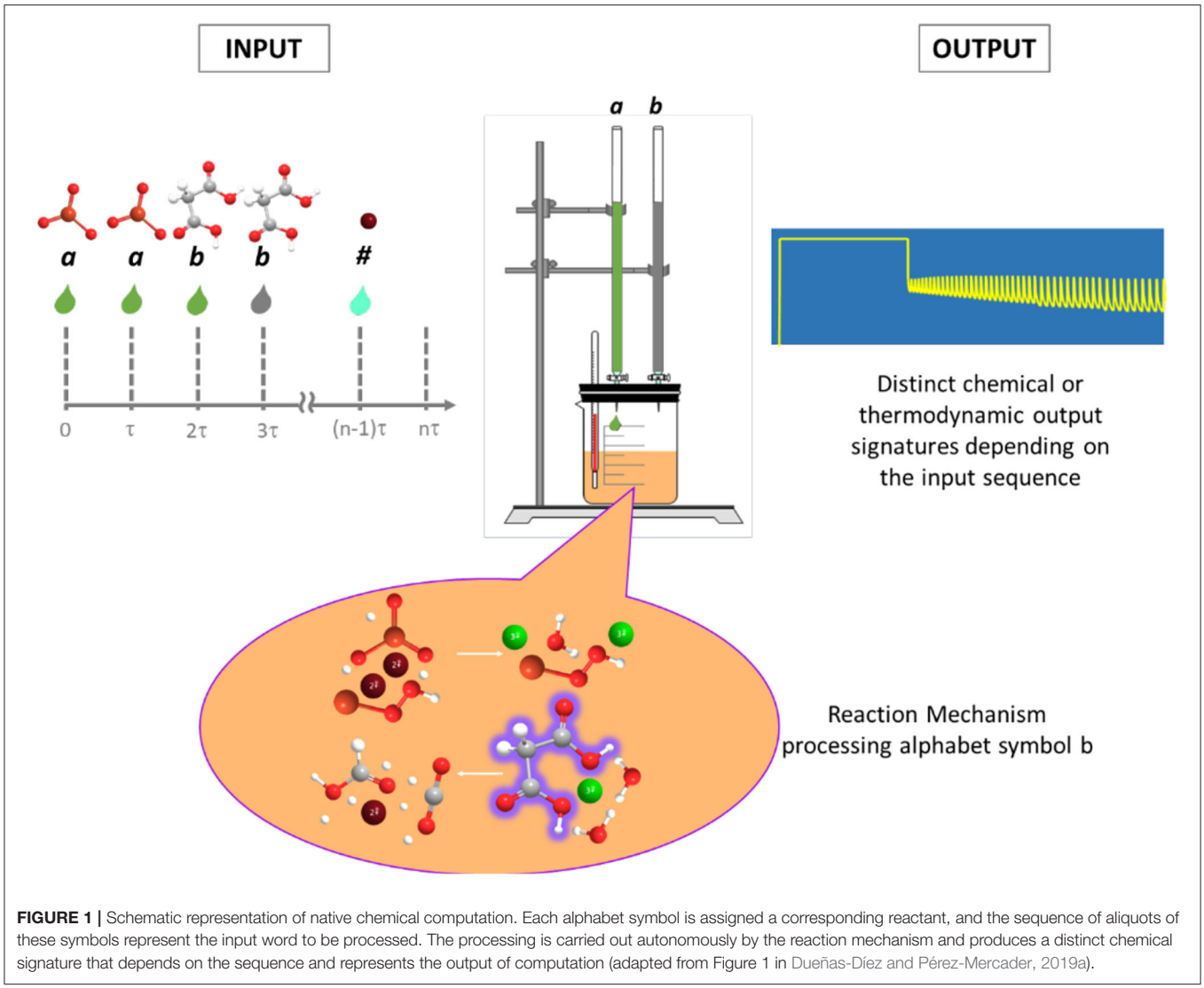


**FIGURE 1 |** Schematic representation of native chemical computation. Each alphabet symbol is assigned a corresponding reactant, and the sequence of aliquots of these symbols represent the input word to be processed. The processing is carried out autonomously by the reaction mechanism and produces a distinct chemical signature that depends on the sequence and represents the output of computation (adapted from Figure 1 in Dueñas-Díez and Pérez-Mercader, 2019a).

participating in a chemical reaction. Such a systematic procedure is called an algorithm, and the execution of an algorithm by a human "computer" was essentially the way in which Turing (1936) envisaged the "mechanization" of a computation back in the 1930s. The result of these studies was the introduction of an automaton[1] capable of implementing any algorithm, even though the automaton might take a very long time to solve the problem. The class of automata capable of doing any computation constitute the class of "Turing Machine" automata. In this latter class there are automata which require an infinitely long tape and are therefore not accessible to representations with real material components, which can only use a bounded amount of energy and translates into a class of finite tape-length automata (Minsky, 1967; Linz, 2012). In what follows, we will restrict ourselves to automata which do not require any infinitely long tapes or unbounded amounts of energy for their operation.

[1]An "automaton" is an abstract computing machine. Its plural is "automata".

The idea behind these automata is that a mathematical problem involving computations can be reduced to a (perhaps very large, but always finite) number of steps involving linear and non-linear (Sheffer, 1913; Lloyd, 1992) operations. The linear and non-linear operations can be performed using various approaches: analogical and digital, sequential or in parallel, and combinations thereof. The computing machinery can be of many types: geometrical, mechanical, electronic, or chemical.

In the case of analog computation numbers are represented by some continuous property, for example, lengths in a slide rule (Stoll, 2006) or chemical concentrations, and we measure another length to obtain the "result." For example, in the case of the slide rule, there is an analogy (or correspondence) between adding lengths and the addition of the logarithm of numbers. In this way we can represent the basic arithmetic operations on numerical quantities by analogy: we input some continuous physical quantities and measuring another (analog) physical quantity gives us the result of some operation. Analog computation

depends specifically on the analogy between a physical property and its mathematical formulation, which therefore limits the application of an analog machine. Another incarnation of analog computation considers a particular physical phenomenon and the differential equations that represent it. Then, by physically implementing one instance of the phenomenon whose differential equations are known one can, in principle, establish an analogy with any other phenomenon that follows the same differential equation. A standard example of this is the relationship between RCL electrical circuits and damped springs (Truitt and Rogers, 1960).

Alternatively, we could operate directly with numbers (digits) in the same way we do with pencil and paper, and therefore generate an approach that can be used to tackle any problem solvable by arithmetic procedures. Digital computation is of course closely connected to Boolean logic and the immensely important (unpublished) 1880's work by Peirce on the functional completeness of the NOR Boolean function (see Nahin, 2013) and the completely independent 1913 Sheffer's (Sheffer, 1913) result that the NAND Boolean function is also functionally complete (i.e., any of the other Boolean functions can be represented with combinations of the NAND or the NOR gates). This together with the representation of data using a binary system, the fast switching capabilities available with electrons in electronic devices, especially solid state, and the direct electrical interconnectability of logic gates are some of the fundamental bases for today's dominance of electronic computers. Indeed, using this approach one can carry out both linear and non-linear operations in general and, sometimes, also energetically efficiently.

But there are many other equivalent possibilities for digital computing. For example (Lloyd, 1992), if one has only gates that produce a constant output, that multiply their input by constants, plus gates that add these inputs together and which can be interconnected by wires and fanouts then one can carry out any linear operation. However, to be able to do general computation which involves both linear and non-linear operations, one needs to supplement the above with a means to perform non-linear operations. Indeed, it can be seen that any non-linearity on top of the above linear gates is sufficient to enable non-linear general computation (Lloyd, 1992). That is, the presence of a switch is a fundamental enabler of general computation.

In summary then, to carry out a general digital computation using logic gates we need input information which must be fed in a timely fashion to some appropriate array of linear gates, non-linear switches and fan outs and, finally, in the end presented as the result of the computation. In other words, if we are computing with gates we will need to be able to transport information from the location of the output of a gate at one particular spatial location, to another location where the input to the next gate is located. The process of switching and feeding of the digital sequence to the gates must be timed very precisely. This information transportation process requires that the traveling information be unaffected during the actual travel of the information carriers (electrons in electronic computing). Otherwise, noise will reduce the accuracy of the computation, perhaps to intolerable levels.

For any interesting computation this implies that the information must be shuttled between interconnected gates and the various events and their timing carefully synchronized. Except because of thermal dissipations this is, in general, not a problem for electronic computers, where the digital information (written in 0 and 1 s) is carried by electrons moving at speeds close to 30,000 km/s, and can be directed by means of cables and multiplexing circuits. This state of affairs of course changes dramatically when one needs to deal with millions of gates and the computation is not reversible (Landauer, 1961).

Unfortunately, when using gates for chemical computation this becomes a serious problem because the shuttling of information by mass transport necessarily involves molecular transport by diffusion, convection, or molecular migration all of which degrade information. For example, diffusion in chemistry not only brings into play the "Arithmetic demon" (Ireland, 1969; Serratosa, 1990; Gilbert and Martin, 2016) of chemistry hindering conversion, selectivity, and reaction yields but diffusion, *per se*, increases entropy and consequently efficiently and irreversibly information is destroyed as it travels and time elapses (Similar statements can be made about convection or unguided molecular migration). Separately or together due to the rapid and prohibitive accumulation of errors during these processes, the above makes very difficult (if not quickly impossible) the use of gates when both the information carrier and the information processing machine are chemical in nature. This makes the strategy of using gates in native chemical computation even more difficult if one intends to use chemistry for relevant computations and information processing at any level of meaningful complexity.

However, not all is lost, as there is another way to solve computational problems and implement the mechanics of the computation required by the algorithm which does not require the use of arrays of linked Boolean logic gates. Other automata exist in computer science which are more advanced than gates and are capable of performing the computational equivalent of many gates together and classifying the results of the input information as either Accepted or Rejected (Adamatzky and Costello, 2002; Rich, 2008). This provides a powerful workaround to the problems with gates in chemistry and enables chemical computation in a framework where chemistry is both carrier and processor of the information. Interestingly, the resulting computing architecture inextricably integrates both processor and memory via the chemical reaction (i.e., it is a non-von Neumann architecture).

## COMPUTING WITH AUTOMATA

As mentioned in the Introduction, a basic element in a computation is the matching of information, just as it happens with molecules in a chemical reaction when under certain conditions some molecules react (the information in the reacting molecules matches) or do not react (the information in the molecules does not match). The fact that anything can be represented by a string of symbols is a very powerful concept and it is because of this that sequence recognition can be naturally

translated into chemistry. Of course, this requires a particular encoding of the object (the "thing") using symbols belonging to an alphabet. And to be successful one needs to encode the problem to be solved we wish to solve as a string which would then be presented as a "word" in some language that an automaton could recognize as belonging to this language. At first sight the above sounds like an intractable problem: there could be so many languages! But today the important question of defining the right language for a problem is a standard task in Computer Science and is discussed in many modern textbooks (e.g., Sudkamp, 2006; Rich, 2008).

Work on languages and computation done during the 1950s and 1960s proved the remarkable fact that all languages could be classified according to their complexity into a four-level hierarchy of languages. This hierarchy of languages is known as the Chomsky Hierarchy of Languages (Chomsky, 1956) after the linguist Norman Chomsky who proposed it and made major contributions to its development. The hierarchy is shown and described in **Table 1** (cf. Dueñas-Díez and Pérez-Mercader, 2019a, 2020). Equally remarkably, accompanying this classification and hierarchy of languages, there is a parallel hierarchy of automata which have the appropriate structures to identify one or more languages at their level in the hierarchy and languages at all the levels below its own. Because of this, the hierarchy of automata and languages is inclusive, which is a fundamental property of the hierarchy and has deep implications for programmability. Furthermore, languages and automata go up in complexity as we go to higher orders in the hierarchy. That is members at lower levels are simpler constructs.

The simplest languages are called "Regular Languages" and they are accepted also by the simplest automata, the Finite Automata (FA) class which includes all the Boolean logic gates. These automata do not have memory. The FA can be extended by incorporating in them a memory of the last-in-first-out type (LIFO) so that the automaton can store and retrieve information. This memory is called the stack. The class of FA endowed with the rules necessary to operate the memory are called the 1-stack Push Down Automata (1-stack PDA) because they have one memory stack of the LIFO type: information can be stored by putting it at the top of the stack while pushing down the stack any previously stored information items.

So, one may ask, can we give more power to the 1-stack PDA by adding more stacks? The answer is yes, but surprisingly 2-stacks is all one needs in order to achieve maximum physical computing power (Hopcroft et al., 2007). That is, these systems will be limited in their computational power by the amount of memory (which obviously cannot be infinite for any physical or for that matter, chemical realization) available to them. With just two stacks and appropriate calls to them as a memory, one can do a lot. These 2-stack PDAs are called Linearly Bounded Automata (LBA) and can, in principle, resolve all strings of bounded length in the Chomsky Hierarchy of Languages. They belong in the class of the Turing machines (Harrison, 1978).

The above implies that in addition to computations performed with gates there is an alternative approach to computation which uses non-trivial generalizations of the Boolean gates. This alternative is based on the fact that any computation can be posed as statements of Acceptance/Rejection of a string of symbols representing words in a language. The language will be a member of one of the language classes in the Chomsky hierarchy. This, combined with the knowledge that anything can in principle be represented by a string (Rich, 2008) gives us the possibility of recasting any computational problem soluble with many gates as a collection of problems soluble with fewer but more advanced automata. The automata, however, are more complex than the Boolean gates [An actual example of the latter is provided in a very complex fashion and in ways that still are not fully understood (Searls, 2002, 2012) by natural life and its central use of genetic information].

In the case of chemistry where the use of Boolean gates, even for reasonably error-tolerant computational problems is prohibitive, having access to automata provides a clear advantage. Thus, access to chemical automata then offers the potential to open new horizons for chemical computing. Recent breakthroughs along these lines demonstrate that there exists a direct correspondence between chemical reactions and the automata in the Chomsky hierarchy in **Figure 2** (Pérez-Mercader et al., 2017; Dueñas-Díez and Pérez-Mercader, 2019a).

Any materially realizable automaton with a tape is bounded in tape length, as any infinite tape requires an infinite amount of energy to operate. Because of this, the top automaton that can be physically realized with actual matter (chemical or otherwise) is the class of the finite tape-length Turing machines (the LBAs). Furthermore, for an automaton to be configurable and used as a finite tape-length Turing machine the automaton must be capable of handling non-linearity and have access to at least two memory stacks. These requirements are satisfied in chemistry by oscillatory chemical reactions and bring us to the subject of non-linear chemical oscillators (Epstein and Pojman, 1998) which will play a major role in native chemical computation and allow us to take full advantage of the above in chemical computation.

## OSCILLATORY CHEMISTRY AND NATIVE CHEMICAL COMPUTATION

As we have seen, to implement the most powerful (physically realizable) automaton we need to have access to non-linearity, for example as provided by a switch, and at least two memory stacks. To translate the above into a chemical computing automaton, we have to ask which chemical reactions offer those two capabilities. If correctly implemented we should then be able to build a chemically operated LBA-Turing machine automaton for the rest of this introductory review, and in the interest of conciseness, we will not consider examples of chemical FA or 1-stack PDAs; for full details on these chemical automata, the interested reader can consult (Pérez-Mercader et al., 2017; Dueñas-Díez and Pérez-Mercader, 2019a,b; Dueñas-Díez and Pérez-Mercader, 2020).

A chemistry where the presence of a switch is essential is oscillatory chemistry: a chemical switch, together with autocatalysis and feedback, is a basic component of the mechanism that underlies oscillatory behavior in chemical reactions (Volkenshtein, 1983; Epstein and Pojman, 1998). We can then think of chemical oscillations as adequate providers

**TABLE 1 |** The Chomsky hierarchy.

| Grammars | Languages | Accepting automata |
|---|---|---|
| Type 0 grammars, phase-structure grammars, unrestricted grammars | Recursively enumerable | Turing machine, non-deterministic Turing machine |
| Type 1 grammars, context-sensitive grammars | Context-sensitive | Linear-bounded automata (bounded tape-length Turing machine) |
| Type 2 grammars, context-free grammars | Context-free | 1-Stack pushdown automata |
| Type 3 grammars, regular grammars, left-linear grammars, right-linear grammars | Regular | Deterministic finite automata, non-deterministic finite automata |

*Languages are generated by grammars. By gradually imposing restrictions on them (Hopcroft et al., 2007), grammars are categorized into an inclusive four level hierarchy, the Chomsky hierarchy. Type-0 are unrestricted grammars and Type-3 the most restricted. Type-1 grammars correspond to Type-1 Languages which are also called Context Sensitive Languages (CSL). Type-2 and Type-3 correspond to Context Free (CFL) and Regular (RL) languages, respectively. Each class of languages in the Chomsky hierarchy has been characterized as the languages generated by a family of grammars and accepted by a type of machine. The relationships developed between generation and recognition are summarized in this table which is adapted from p. 338 of Sudkamp (2006). Type 0 and Type 1 grammars are accepted by Turing machines, hence the horizontal line in the Table that separates them from Types 2 and 3. Reprinted from Dueñas-Díez and Pérez-Mercader (2019a) Copyright (2019) with permission from Cell Press.*

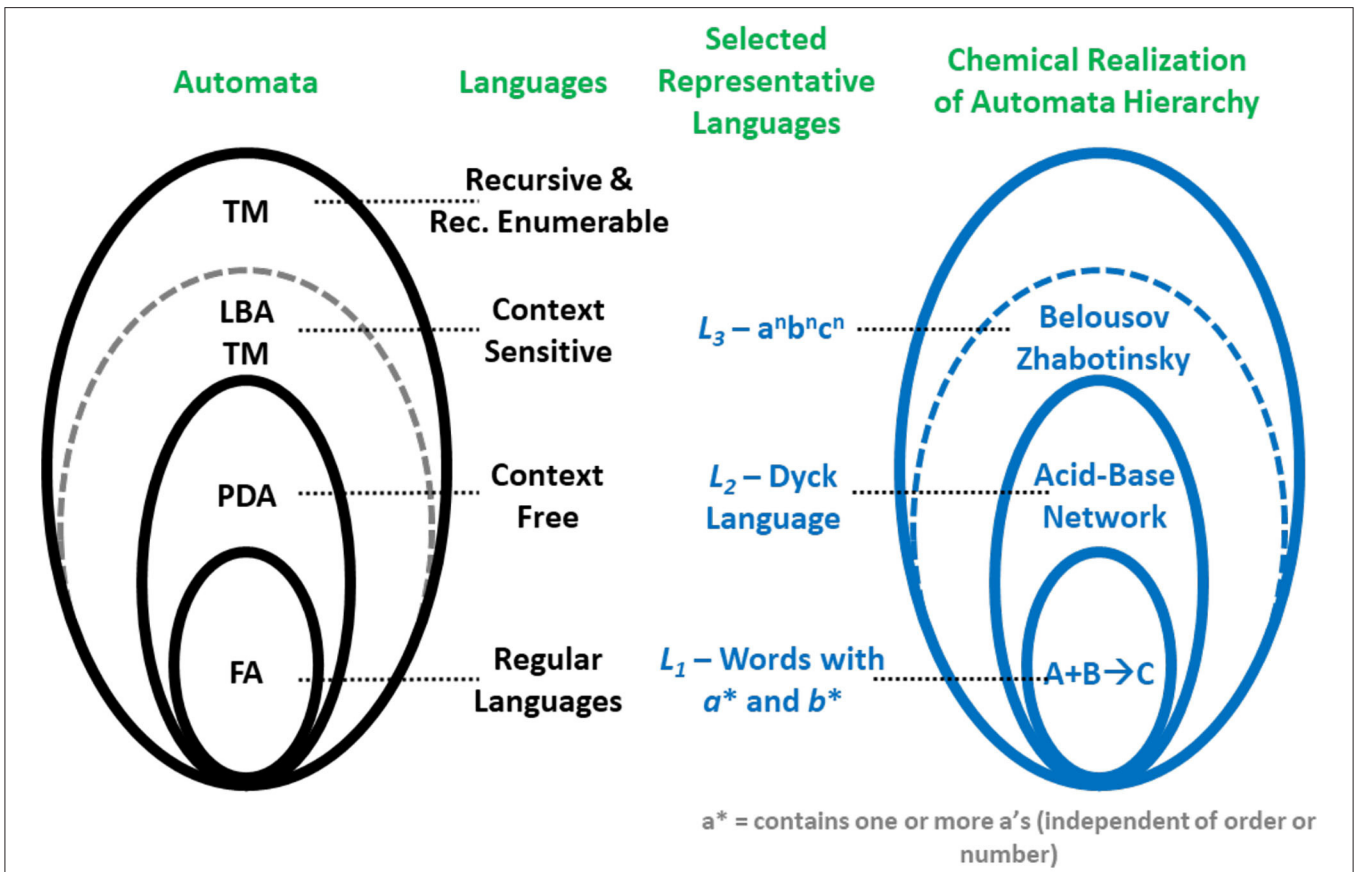


**FIGURE 2 |** Correspondence between the automata hierarchy, the Chomsky hierarchy of languages on the left, and the experimental realizations of native chemical automata on the right side of the figure. All these hierarchies are inclusive, e.g., the BZ reaction can be shown (Dueñas-Díez and Pérez-Mercader, 2019a, 2020) to recognize not only a context sensitive language ($L_3$) but also a context-free language ($L_2$) and a regular language ($L_1$). Reprinted from Dueñas-Díez and Pérez-Mercader (2020) Copyright (2020) with permission from Nature Scientific Reports.

of the non-linearity required by fully fledged computation. But, remarkably, chemical oscillations bring with them another feature useful for enabling chemical computation. Indeed, chemical oscillations, like any other oscillatory phenomena, are characterized by two interdependent (which for the particular case of linear oscillators are independent) physical variables: the

frequency and the amplitude of oscillations. Furthermore, since the instantaneous state of a chemical reaction taking place in a reactor is the result of adding aliquots of the reacting substances to the reaction, we see that one can think of the frequency and amplitude and their value in the reactor at a given time as directly related to two stacks of memory. These "stacks" are of course dynamically interconnected by the non-linear oscillatory reaction, and their time dependent values are correlated with the internal reaction pathways visited in the course of the reaction. These will change upon addition of reactants or other modifiers of reaction intermediates, such as changing the pH or the concentrations of reaction catalysts in the reactor.

The above indicate that oscillatory chemical reactions contain the necessary components for the native chemical representation of a 2-stack Push-Down Automaton: the 2-stacks and the on-off switch which control the pathways that are visited upon the addition of substrates to the reactor. That is, the oscillatory behavior that would start upon the addition of substrates in the adequate order and concentrations, is the manifestation of the internal state and rules for the operation of the chemical automaton (cf. **Figure 3**).

The operation of a chemical oscillator brings with it another basic ingredient of chemical computation: aliquots of the substrates and the modifiers of the reaction conditions can be used to translate abstract symbols in a symbolic alphabet. Additionally, the order in which the aliquots are fed to the reactor matters, which is a direct consequence of the non-linear nature of the chemical reaction [non-linear operations do not commute, exp (sin x) is not the same as sin (exp x)]. Therefore, it follows that we can represent meaningful information using aliquots of these substances as the letters of an alphabet. In other words, just as we can represent anything by strings of symbols we can represent information by means of a sequence of aliquots fed to the core, i.e., the chemicals not entering into the above mentioned category of "substrates" and modifiers of an oscillatory reaction.

All the canonical languages and their grammars that enter in the Chomsky hierarchy can be represented by finite size alphabets. And they can be further transformed (without getting out of their level in the hierarchy) by means of some encoding.

The languages that can be handled by oscillatory chemistry are all the languages at the level of the LBA-TM in the Chomsky hierarchy and below (cf. **Table 1**, The Chomsky hierarchy). These are the Regular Languages (RL), the Context Free Languages (CFL), and the Context Sensitive Languages (CSL).

Useful examples of the simpler languages in the hierarchy are provided by the following languages. A particularly simple RL is the language $L_1$ of all words using a two symbol alphabet, a and b, with the words containing at least one instance of symbol a and at least one instance of symbol b. Words in this language would be "ab," "aab," "baa," or "aaabbbb" sequentially fed to the automaton from left to right. This language [like any regular language (Hopcroft et al., 2007)] does not require counting or memory in order to identify its words. Regular languages are recognized by FA and other automata above them in the Chomsky hierarchy.

For a CFL there is the need for counting and a prototype language is $L_2$, the language of well-balanced pairs of brackets. The symbols here are "(" and ")" which brings with it a notion of order: while the sequence "()" is well-balanced, the sequences ")("or "))" or "((" are not well-balanced. The words in this language are called Dyck words (Weisstein, 2009), examples of which are "(())" or "(()())" etc. To implement this language, one needs one memory stack, and its accepting automata belong to the 1-stack PDA class or above in the Chomsky hierarchy.

In a CSL the grammar is more structured than for a CFL (note the "S" for sensitive and the "F" for free in the language type) and this requires the presence of two stacks in the automata that can identify CSLs, one more stack than what is necessary in the cases of CFLs. A typical example of a CSL is $L_3$, made up of words of the form $a^n b^n c^n$ which require at least a 3-symbol alphabet. These words are strings containing n a's followed by n b's and then by n c's. A few examples of words in $L_3$ are "abc," "aabbcc," or "aaaaabbbbbccccc." The reader can easily check that by grouping letters one can restrict the more complex languages to provide instances of languages with a lower complexity. The physically realizable automata in the Chomsky hierarchy that recognize CSLs are the LBAs. There is no 1-stack PDA or FA that can recognize them.

Of course, to perform a "native chemical computation" the letters in the alphabet themselves must be chemically represented. This is achieved by the translation of the letter symbol say, a, b, or c into an aliquot of a suitably chosen and reacting chemical species. The aliquot corresponding to each letter in the word is sequentially added to a one pot reactor which will process each letter during a fixed time $\tau$. This time must be long enough so as to get the aliquot thoroughly mixed with the rest of the chemicals already in the reactor.

The result of the computation, that is, whether the input word is or is not in the language for whose recognition the automaton (chemical reaction) was engineered, can be a physico-chemical signature produced by the reaction at the end of the computation. In this context, it is important to notice that, just as in the theory of abstract automata, we need a beginning and end of word symbol, which following the tradition of automata theory we will denote by "#." For example, in the LBA-Turing machine described in Section **Building a Chemical Turing Machine Using the BZ Reaction Chemistry**, this symbol is chemically translated as an aliquot of the BZ ruthenium catalyst. The # symbol is fed to the automaton before the first and also after the last symbol in the word being processed. After the # is processed the two oscillator variables $D$ and $f$ (see at the end of this review a list with Nomenclature and Definitions for their definitions) will have specific values. These values reflect the state of the reactor after the preceding symbols have been chemically processed in the course of the computation.

That is, once the aliquots for the symbols and the composition of the rest of the reaction components are formulated, the result of processing any words (in the language accepted by the automaton or not in that language) is represented by the values of the system's state variables at the end of the computation. The values of these variables characterize the relationships between automaton, language, chemical representation of the alphabet, and details of the word processing carried out by the automaton. There is a characteristic and systematic response for the words in the language recognized by the automaton. It is experimentally

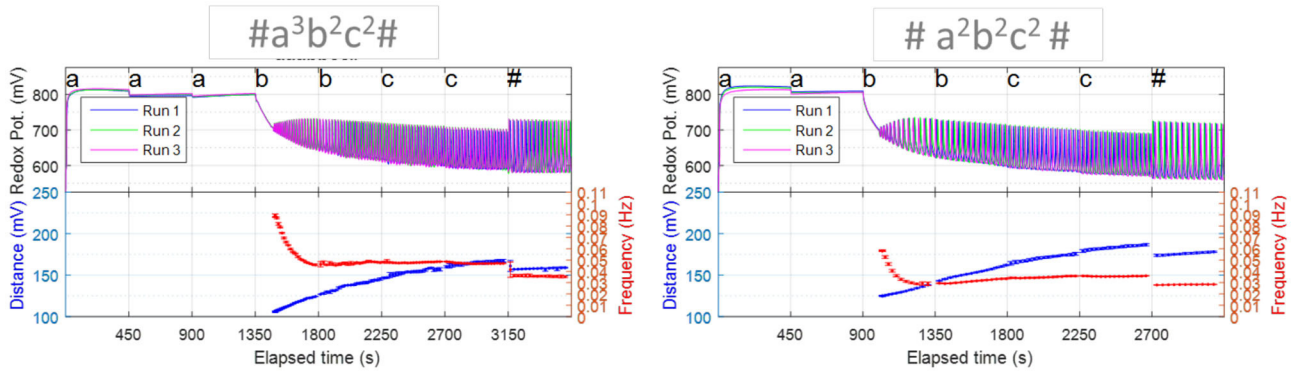


**FIGURE 3 |** Oscillatory reactions contain the necessary components for computation. These relaxation chemical oscillations not only show the key non-linearity, but also have two stacks, i.e., two oscillatory features (e.g., frequency and amplitude or equivalent measure). Note that the oscillatory features vary depending on the order of the sequence. Each sequence experiment was repeated three times, from whose results the plotted error bars were calculated. Reprinted from Dueñas-Díez and Pérez-Mercader (2019a) Copyright (2019) with permission from Cell Press.

verified that the locus of these values is a smooth convex upwards curve that connects words in the language and discriminates the words not in the language by dividing the *(D,f)*-plane into two disjoint regions of rejected words. How do we interpret these? What "state variable" can be associated with the sequence recognition process and its physical interpretation? Answering these questions will lead us to identify some profound properties of native chemical computation, its use and about the similarities and some differences between chemical computation and other forms of general computation.

It should not come as a surprise that a chemical automaton will produce correlated values of some physical variable for a computation ending in acceptance. This is so because the result of the computation of a submitted sequence will be either acceptance or rejection, and whereas in general there could be many types of rejection, the acceptance only happens for sequences sharing the pattern (order) of words belonging to the identified language. Since a computation is a process of molecular recognition, we expect that recognition would entail some form of "optimization" or reduction in uncertainty. That is, a reduction in the entropy of the system. Therefore, given an automaton with its chemical recipe for language recognition (including the recipe for the symbols), in chemical space the recognition process will be equivalent to following "paths" in the reaction mechanism for free-energy dissipation during the computation (Landauer, 1961; Notice that this implies that a chemical computation of sufficient complexity can enable, for example, "if-then-else" rules and other basic constructs related to programmability. In this regard, cf. also Landauer, 1961).

Thus, we expect that (as is actually observed) for words in the language recognized by the automaton, accepted words, there will be a locus connecting the automaton's outputs for the words once all the symbols in the words have been fully processed. Depending on the actual details of the sequence of letters making up the rejected words, the words will fall into one or the other disjoint areas (subspaces). That is, the particular order of the symbols in the sentence being computed determines the manifold on which they will "land" at the end of the computation. Mathematically this can be related to the non-commutativity of non-linear operations, but chemically this is a manifestation of the fact that each aliquot will excite a particular subset of pathways within the reaction mechanism (**Figure 4**). In other words, thinking of aliquots as "chemical fuels" for these non-equilibrium systems, the total energy dissipated (or consumed) by the system in recognizing or rejecting words will depend on both the internal reaction pathways excited in a particular order by the chemicals representing the word sequence, and on the total length of time these specific pathways are visited and remain excited. In fact, we can follow the kinetics and roughly trace the pathways within the reaction mechanism that are visited by the substrates in the course of a computation (This, of course, leads to the notion that word recognition by a chemical automaton is associated to some kind of optimization).

For example, in the extended FKN model of the Belousov-Zhabotinsky redox reaction (Field et al., 1972; Dueñas-Díez and Pérez-Mercader, 2019a), **Figure 4**, we display the "traffic" patterns in the reaction pathways that are generated when each of the species $BrO_3^-$, MA, Ru catalyst, or $H^+$ are added. (In what follows we will be using the stoichiometry and level of chemical mechanism fine-graining described by the FKN model of the BZ reaction). One can then understand how there may exist energy optimized pathways and how certain combinations of the pathways (i.e., sequence of # followed by a's, b's, and c's and ending with #) would be more suitable than others to balance the respective contributions of the oxidized and reduced states of the reaction. These, in turn, are connected to the previously introduced physical variables $D$ and $f$ which in the case of the TM are stored in the two stacks. For later reference, we note that their respective dimensionalities are inverse time and energy per unit charge as they are a voltage and a frequency.

The final values of these variables are at the top of the stacks at the end of the computations. As argued above, their values are remarkably correlated (cf. **Figure 5**) at the end of the computations for words in the accepted language.

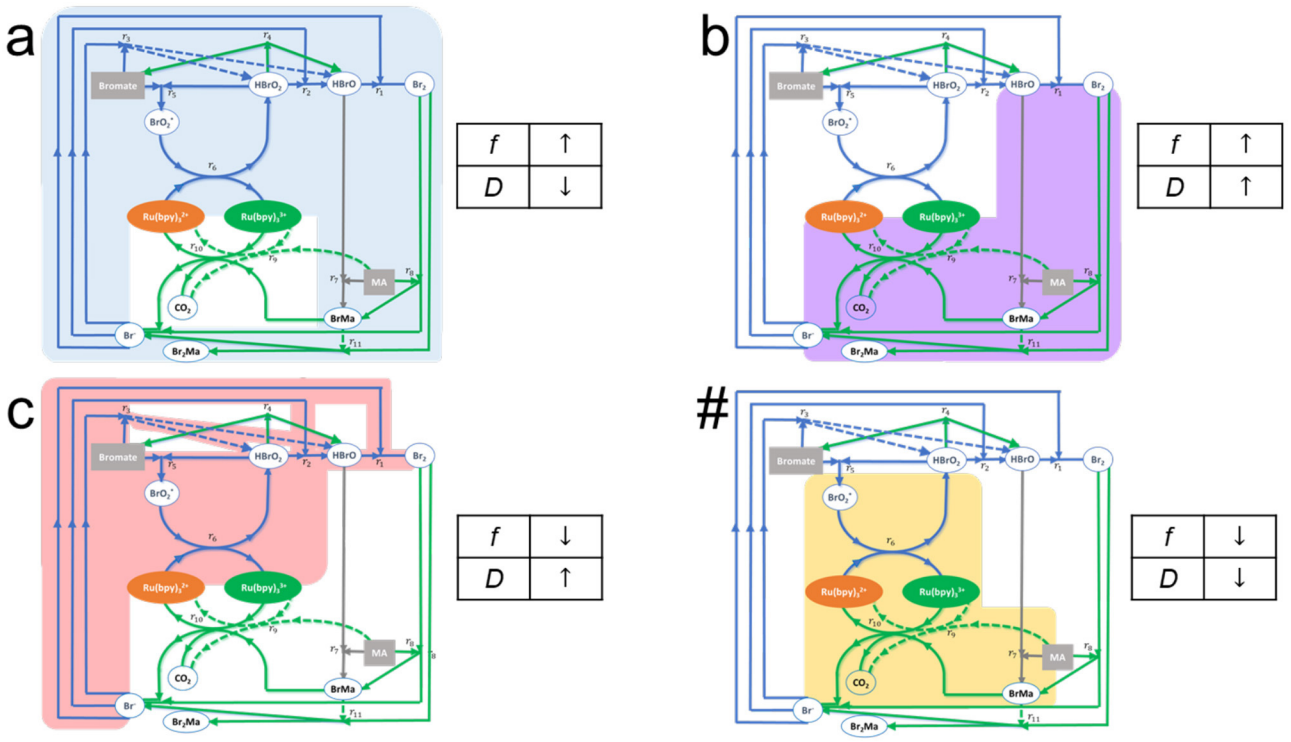


**FIGURE 4 |** Effects on the dominant pathways in the extended FKN model of the BZ reaction mechanism, as well as on the oscillatory metrics *f* and *D* due to the specific assignment of alphabet symbols in the implementation of a chemical Turing machine built using the BZ oscillatory chemistry, Here the aliquots for the symbols are **(a)** Sodium Bromate, **(b)** Malonic Acid, **(c)** NaOH, and **(#)** Catalyst Ru(II). The colored areas represent the set of reaction pathways affected by each of the alphabet symbols. In the case of **(a,b,#)** the highlighted reactions are enhanced, whereas in the case of **(c)** the highlighted reactions are slowed down. Reprinted from Dueñas-Díez and Pérez-Mercader (2019a). Copyright (2019) with permission from Cell Press.

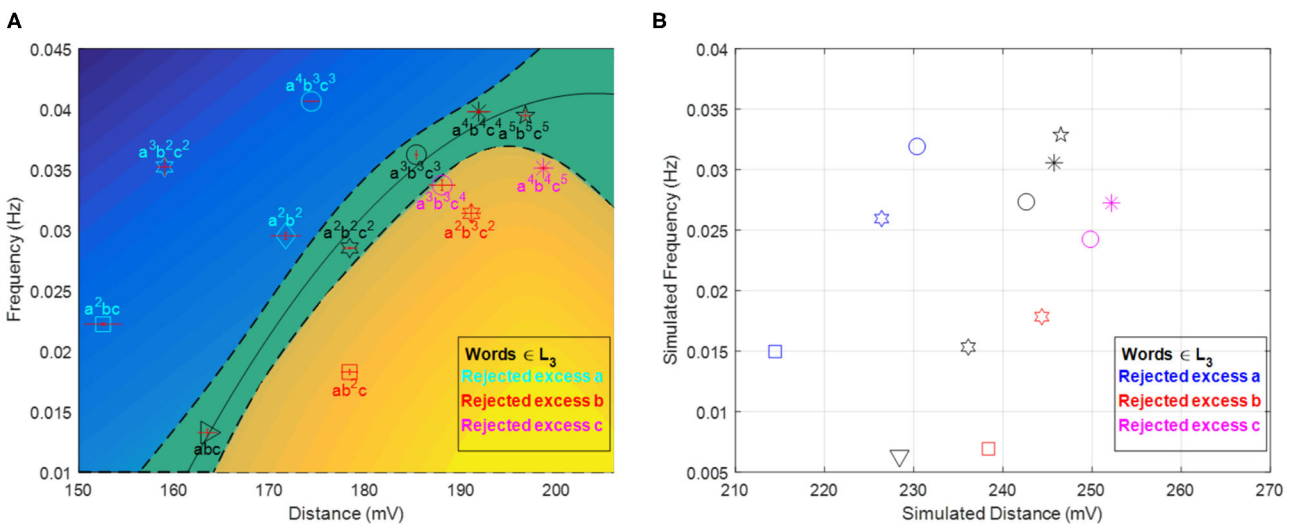


**FIGURE 5 |** [*D, f*] plot at the end of computation. Panel **(A)** shows experimental results (each sequence experiment was repeated three times from which the plotted error bars were calculated) while panel **(B)** shows simulation results based on a modified FKN model (cf. **Appendices 1** and **2**). The locus of accepted words divides the plane in two disjoint regions of rejected words. The relative position of accepted and rejected sequences is reproduced qualitatively by the simulations. Panel **(A)** is Reprinted from Dueñas-Díez and Pérez-Mercader (2019a) Copyright (2019) with permission from Cell Press.

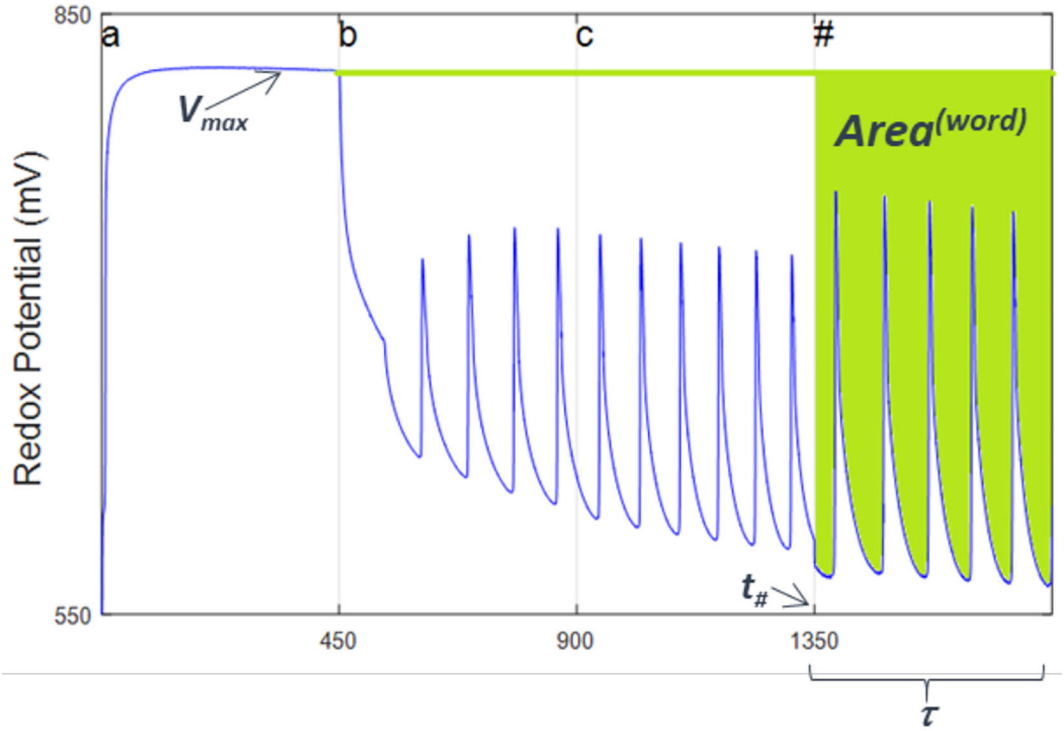


**FIGURE 6 |** Experimental readout of $Area^{(word)}$ from the redox potential plot from a given processed word in a native automaton based on Belousov-Zhabotinsky oscillatory chemistry. Shown in this figure is the plot for a word made up by the sequence of one aliquot of **(a)**, followed by one aliquot of **(b)**, then one of **(c)** and finally the end of word symbol, **(#)**. Note how the frequency and amplitude of oscillations vary depending on the sequence, thus in turn determining the value of $Area^{(word)}$. Time is in seconds. Reprinted from Dueñas-Díez and Pérez-Mercader (2019a) Copyright (2019) with permission from Cell Press.

Of course the values of $D$ and $f$ have evolved as we added the chemical realization of the symbols (letters) making up the words. This means that they are a function (actually a functional) of the reaction extents, $\xi^{(i)}$, of the various reactions that have been visited during the processing of the words. This suggests that instead of looking directly at the values of $D$ and $f$, we look at them in a way where the use of the extents is explicit, while we still examine the final state of the reaction (Experimental numerical values for the process can be obtained if we consider the evolution of the reaction redox profile as a function of time). The processing of the beginning-of-sequence and end-of-sequence symbol, #, will give us a read out of the relative weights of the reduced and oxidized extents of reaction at the end of the computation. To implement experimentally the above procedure, we consider in a $V_{redox}$ vs. $t_{seq}$ plot the fraction of the initial area that has remained during the computation in the oxidized state after the addition of the first symbol to the Turing machine reactor. This fraction is equal to the area in the $V$–$t$ (voltage vs. time) plane representing the evolution of the redox potential after processing of the first symbol has taken place $\sim V_{max} \times t$, minus the area below the redox voltage spanned by the experimental trace of the $V_{redox}$ $(t)$ curve during the processing of the final # (see **Figure 6**). Time units are seconds. We will call this difference the processed word's "area," $A^{(Word)}$. It is given by

$$A^{(Word)} \equiv V_{\max} \cdot (\tau - 30) - \int_{t_{\#}+30}^{t_{\#}+\tau} V_{osc}\,(t)\,dt \qquad (1)$$

where $V_{osc}$ has dimensions of energy divided by electric charge and the 30 s added to the lower limit of the integral are introduced to allow for any potential transients to settle. If multiplied by $e$, the charge of the electron, this quantity [i.e., $e$ times $A^{(word)}$] has the dimensions of the action in physics which, as we will describe below, plays an important role providing a physico-chemical interpretation of a native chemical computation.

Using Nernst's law and a model for the kinetics of the oscillating reaction one can readily compute the integrand of Equation (1) which can then be used (see Section Building a Chemical Turing Machine Using the BZ Reaction Chemistry describing the construction and formulation of the BZ TM) to calculate the values of the area for the word processed by the chemical automaton. Remarkably, one finds that the area for words in the language accepted by the Turing Machine, plotted as a function of the total time it takes to process all the symbols in the word (including the two instances of the end of sequence symbol # at the beginning of the word and at word end), follows a straight line in the $A^{(Word)}$ vs. $t$ plane. We also see that the words not in the language follow different paths which depend on how or when in their symbol sequence they come out of the automaton's accepted language. They are not on the same straight line as the words in the language, which indicates that some (global, internal, and autonomous) optimization takes place during the course of the native chemical computation being carried out by the automaton. Moreover, the slope of this straight

line can be made to vanish by suitably adjusting the molarity of the aliquots representing some of the alphabet symbols. This implies[2] that for words in the language, the quantity $A^{(Word)}$ does not change (is invariant) under changes in the total time spent by the automata performing the computation (Dueñas-Díez and Pérez-Mercader, 2019a). That is,

$$\delta A^{(Word)}|_{Word\ in\ Language} = 0 \tag{2}$$

But $A^{(Word)}$ is a integral over time, and therefore Equation (2) represents at least a piece for the formulation of a variational "principle," as in the cases of the principle of least action in mechanics (cf. Feynman et al., 1965; Goldstein et al., 2002; Lanczos, 2012) or of entropy generation in chemistry (cf. Prigogine, 1955; Yourgrau and Raw, 1957). Paraphrasing Feynman, we can say that words in the language follow paths in the area-sequence length plane that keep $A^{(Word)}$ at a constant value.

Let us further explore what is at work behind these observations. From Nernst's law we have that for a redox reaction

$$V_{osc} = V_0 + \frac{RT}{\nu F}\ln\left(\frac{\left[Ru(bpy)_3^{3+}\right]}{\left[Ru(bpy)_3^{2+}\right]}\right) \tag{3}$$

where $V_o$ is a reference voltage $\left[Ru\left(bpy\right)_3^{3+}\right]$ and $\left[Ru\left(bpy\right)_3^{2+}\right]$ are the (instantaneous or time dependent) concentrations of catalyst in the oxidized and reduced states, $\nu$ is the number of electrons involved in the redox reaction, and $F$ is Faraday's constant. Equation (3) multiplied by $\nu$ and Faraday's constant, is the Gibbs free-energy $G(t)$ for the oscillating redox reaction (Kuhn and Försterling, 2000), which inserted into Equation (1) tells us that for isothermal and isobaric conditions

$$\delta A^{(Word)} = \delta \int_{t_\#+30}^{t_\#+\tau} G(t)\, dt \tag{4}$$

The function $G(t)$ has a support restricted to the substances involved in the electrochemical sector of the redox reaction, $Ru^{3+}$ and $Ru^{2+}$. It is a functional of the extents of reaction, $\xi^{(i)}(t)$, for the reactions $i$ involved in the changes in concentrations between the two redox states of the catalyst. In the FKN model of the BZ reaction (Dueñas-Díez and Pérez-Mercader, 2019a; see also **Appendices 1** and **2** in this review) we have that

$$\left[Ru\left(bpy\right)_3^{3+}\right] = \left[Ru\left(bpy\right)_3^{3+}\right]_{input} + \xi^{(6)} - 6\xi^{(9)} - 4\xi^{(10)} \tag{5}$$

and

$$\left[Ru\left(bpy\right)_3^{2+}\right] = \left[Ru\left(bpy\right)_3^{2+}\right]_{input} - \xi^{(6)} + 6\xi^{(9)} + 4\xi^{(10)} \tag{6}$$

From Equations (2)–(5) we see explicitly that the Gibbs free energy can be a function of the form

$$G(t) \equiv G\left(\xi^{(i)}(t),\, d\xi^{(i)}/dt; t\right) \tag{7}$$

[2]It also implies that the two-dimensional distance between points in the area vs. time plane that represent words in the language is the shortest (minimum) distance.

And the area variation becomes,

$$\delta A^{(Word)} = \delta \int_{t_\#+30}^{t_\#+\tau} G\left(\xi^{(i)}(t),\, d\xi^{(i)}/dt, t\right) dt. \tag{8}$$

## INTERPRETATION OF WORD-ACCEPTANCE IN A NATIVE CHEMICAL TURING MACHINE

We have seen above that an appropriate phenomenological reformulation of the aliquots for the symbols representing the words in the language accepted by the native chemical Turing Machine reveals three important aspects of the chemical computation. First that for every word not in the language recognized by the TM, the TM automaton classifies them in the amplitude-frequency plane as being either below or above a path in that plane which connects the machine's response points corresponding to words in the language for which it was programmed. Secondly, that one can transform the previous response in the *(D,f)* plane into an equivalent response in an "$A^{(Word)}$" vs. word-symbol count plane where the words in the language fall in a straight line. And thirdly, that this straight line can be rotated into a horizontal straight line in the *(D,f)* plane by an additional chemical concentration adjustment of the aliquots translating the word in the language of the automaton to new (chemical concentration reformulated) alphabet symbols. It is important to note that these reformulations involve the concentrations but not, necessarily, changing the nature of their molecules [The latter can be shown to be due to some invariance or symmetry in the chemical kinetics (cf. Noether, 1918; Nicolis and Prigogine, 1977; De Groot and Mazur, 2011) which will not be discussed in this review].

Let us concentrate on the third remark above. Put succinctly, it is saying that there is a chemical equivalent of the "action" in physics which can be used to account for the evolution of the state of the chemical automaton as it processes symbols, and that this equivalence is such that (1) gives the same value of the action (area) for any accepted word, (2) this value is independent of the word length so long as it accepted, (3) the distance between consecutive accepted words is a constant, and (4) that after a "rotation" in chemical space, the distance between consecutive accepted words is the shortest possible in a two dimensional space [i.e., the brachistochrone, or "curve down which a bead sliding from rest and accelerated by gravity will slip (without friction) from one point to another in the least time" (cf. Goldstein et al., 2002) in this action vs. time plane is a straight line].

Indeed, the value of the area after processing the # symbol provides a direct measure of how much the extents of reaction have progressed during their visits to the oxidized and reduced states. That is, this action gives us information on how the changes in the concentrations of $Ru^{3+}$ and $Ru^{2+}$ have evolved during the full course of the computation. Its values and functional evolution clearly involve the Gibbs relationship for entropy production (cf. Baierlein, 1999) with the reaction extents $\xi(t)$ (which reflect changes in concentrations as a function of time) as reaction coordinates. It is interesting to note that the constant area/action functional harkens the presence of some optimal dynamical evolution of the BZ chemistry when

configured to operate as a TM and fed with words in the language it recognizes. In other words: some physical quantity must be optimal when the TM processes and accepts words in its language.

As motivated earlier in the review, a quantity that can naturally reflect what occurs during a chemical computation is the non-equilibrium entropy which is produced by the "flow" of the *i*-th reaction, $d\xi^{(i)}/dt$, driven by its conjugate force, the activity for that reaction $A^{(i)}$ (cf. Aris, 1999; De Groot and Mazur, 2011; Yourgrau et al., 2013). One expects that the events of molecular recognition taking place in a chemical automaton will translate into corresponding out-of-equilibrium changes in the entropy. These cannot be arbitrary and will depend on the sequence of chemicals (word) fed to the automaton for its computation. They are constrained by the entropy balance for an out-of-equilibrium system (cf. Martyushev and Seleznev, 2006; De Groot and Mazur, 2011; Yourgrau et al., 2013; Kondepudi and Prigogine, 2014), given by the equality

$$\frac{\partial s}{\partial t} + \nabla \cdot \mathbf{J}_s = \sigma \tag{9}$$

Here, $s$ is the specific entropy, $\frac{\partial s}{\partial t}$ represents the net entropy production, $\mathbf{J}_s$ is the flow of entropy across system boundaries, and $\sigma$ is the entropy production density. At constant pressure and temperature the above becomes

$$\frac{ds}{dt} = \sigma + \frac{1}{T}\frac{dQ}{dt}. \tag{10}$$

Upon using the first law of thermodynamics together with the definition of the Gibbs free energy $G = U + PV$ - $TS$ Equation (10) implies that

$$\sigma = -\frac{1}{T}\frac{dG}{dt}. \tag{11}$$

In other words, the entropy production in the above conditions is the negative of the change in time of the Gibbs free energy [Furthermore, Equation (11) also says that if d$G/dt$ is a minimum, $\sigma$ is a maximum, and vice versa, that is if $\sigma$ is a minimum then d$G/dt$ is a maximum].

Our *in vitro* experimental measurements (made at constant pressure and temperature) together with Equations (8) and (2) imply that for words in the language accepted by the Turing machine using the realization where the composition of aliquots is such that $\delta A^{(word)} = 0$ and the distance is the shortest between words in the language,

$$\frac{\partial G}{\partial t} = 0 \tag{12}$$

and (after using the techniques of the calculus of variations) this implies that

$$\frac{\partial G}{\partial \xi} = 0 \tag{13}$$

We conclude from Equation (11) (cf. Yourgrau and Raw, 1957) that when processing those words, the entropy production by the Turing machine is zero. That is,

$$\delta\sigma|_{Word\ in\ Language} = 0 \tag{14}$$

Applied to the results of our experiments concerning the area for accepted and not accepted words, this expression tells us that words in the language for which the Turing Machine was designed, generate a constant entropy in the redox sector of the reaction. In other words, the process of word acceptance in a chemical Turing machine brings its entropy to an extremum.

Since the path joining the words in the [*Sequence Length,* $A^{(word)}$]-plane is a horizontal straight line, we can also say that the paths for words in the Turing machine all occur for their minimum separation, i.e., they are processed by the Turing machine following the shortest path. Chemically, these $\sigma = 0$ paths are accompanied by the presence of specific quantities of radicals and reaction intermediates produced during the process of word recognition. Since these radicals can be used, for example, to induce RAFT polymerization of amphiphilic block copolymers (ABC) followed by their out-of-equilibrium self-assembly (cf. Bastakoti and Pérez-Mercader, 2017a,b; Hou et al., 2019), we infer that the self-organization and dynamical self-assembly properties of such amphiphiles can be linked to the collective properties of the ABC dissipative self-assembly. The above, in turn implies that these properties can be controlled/programmed by a chemical automaton and in particular by a chemical Turing machine. Such applications showcase interesting and suggestive scenarios where the hybrid analog-digital nature of the computation plays an intriguing and suggestive role. For example, one can think of autonomous programmed dynamical self-assembly of functional materials or supramolecular structures (Pearce and Perez-Mercader, 2020).

The experimental and analytical results presented above can be recast as the statement of a variational principle just as in classical mechanics or in non-equilibrium thermodynamics (cf. Goldstein et al., 2002; Lebon et al., 2008) where the action functional (cf. Goldstein et al., 2002; Lanczos, 2012) integrated along the paths of actual physical motion are extremal, and a minimum in the case of Hamilton's principle. The above translates to our case by simply substituting action for our "area" and the extremal path corresponds to paths that include only words in the language of the Turing machine. Applying Prigogine's result on entropy production in the course of a chemical reaction we then conclude that language recognition in the chemical automaton generates, cf. Equation (11), a minimum amount of entropy if the change of the free energy is a maximum and viceversa.

The above provides an interesting view of acceptance states in chemical Turing machines (and arguably for other automata). Interestingly this extremum can be adjusted in the interest of efficiency by making use of the digital-analog nature of native chemical computation and selecting an appropriate aliquot recipe for the symbols. Theoretically, this adjustment can be done with a precision of a few parts in $10^{21-23}$ and opens an intriguing set of questions related to the reversibility of computations done by chemical automata.

In summary, we have seen that a native chemical computation at the Turing machine level can be understood in terms of extremal entropy production. This is accompanied by the release of radicals by the TM in specific proportions which can then be used as chemical inputs to subsequent chemical processes and,

therefore, enable the fully chemical and autonomous control of complex systems. This we will explore in the following section which is devoted to the specific example of a BZ-based native chemical Turing machine in the LBA-class.

# BUILDING A CHEMICAL TURING MACHINE USING THE BZ REACTION CHEMISTRY

We are now ready to discuss how an actual chemical Turing machine is built using the oscillatory Belousov-Zhabotinsky reaction to recognize CSL $L_3$ (Dueñas-Díez and Pérez-Mercader, 2019a). We will discuss the design and operation of the Turing Machine in both batch mode and flow mode, specifically in a continuously stirred tank reactor (CSTR) mode.

## Chemical Turing Machine in a Batch Reactor

First, the alphabet symbols in the language to be recognized need to be assigned to their counterpart chemical species. Language $L_3$ has **a**, **b**, **c,** and **#** as symbols. Therefore, four different chemical species need to be identified that affect in distinct ways the dominant pathways in the reaction mechanism, and, in turn, the observed oscillatory features. The assignment can be done empirically, or preferably, guided by the knowledge on the reaction mechanism and kinetics (cf. Dueñas-Díez and Pérez-Mercader, 2019a, and **Appendices 1** and **2**). As a rule of thumb, the reactants, the catalysts, and the most interconnected intermediates or chemical species interacting with them, are the best candidates for assignment. Here, the reactants sodium bromate and malonic acid were successfully assigned to **a** and **b**, respectively, and sodium hydroxide, a species affecting the most interconnected intermediate $H^+$, to **c**. The catalyst was assigned to **#**. The mapping between the symbols and their effects on the oscillatory features ($f$ and $D$) and dominant pathways in the FKN model is discussed in the previous reference.

Next, we need to quantify the alphabet recipes and initial conditions that ensure a proper operation envelope of the automaton, i.e., keeping the reaction mixture within the oscillatory regime and simultaneously leading to observable/measurable changes in the oscillatory features whenever a symbol is read and processed. Recipe quantification typically involves optimization, which can be carried out experimentally or aided by kinetic simulations (cf. **Appendices 2** and **3**). In the first experimental realization, the recipe was optimized experimentally to minimize the gas production that interferes with the redox potential monitoring, and to ensure reliable accept/reject outputs for sequences up to $n = 5$ both in the $[D, f]$ (cf. **Figure 5**) and $A^{(word)}$ accept/reject criteria (cf. **Figure 7**). The time interval between aliquots is a design parameter of the chemical automaton that influences the speed and performance of the machine. It was chosen long enough to ensure that the system gives two full oscillations (after the induction period) once both an **a** and **b** are in the system.

The $[D, f]$ accept/reject criterion is non-linear, while the $A^{(word)}$ shows a linear dependence with respect to the sequence length. Such linearity motivated the further optimization of the recipes to achieve a simpler accept/reject criterion: a constant $A^{(word)}$ regardless of sequence length (for words in the language). This was implemented using model-based mathematical optimization and a subsequent experimental fine-tuning (cf. **Appendix 3** and **Figure 8**).

The inclusiveness of chemical automata and their reconfigurability have been proven experimentally (cf. Dueñas-Díez and Pérez-Mercader, 2020 and **Appendix 4** of this review). Indeed, the batch chemical Turing machine was reconfigured to recognize the context-free language of balanced parentheses $L_2$ (Dyck Language) by adjusting the recipe of aliquot **b.** It was also reconfigured to recognize a simple regular language $L_1$, the language of all sequences that contain at least one **a** and one **b**. The choice of time interval guarantees adequate performance without requiring further recipe adjustment.

## Extension of Chemical Turing Machine to CSTR Operation

The extension to continuous operation (CSTR) is appealing for several reasons: the autonomous resetting of the machine to process a new input, the potential for faster computations since the machine is already in an oscillating regime at the onset of computation, the availability of a wider range of periodic and aperiodic oscillatory regimes (cf. Hou et al., 2019) to be eligible for accept/reject signatures, and the straightforward ability to reconfigure and to connect several automata such that new computations can be carried out (cf. Cohen, 1991; Hopcroft et al., 2007).

The autonomous resetting of the automaton for running a new input means that the input is "erased" from the reactor after a certain resetting time $T_{resetting}$ that can be estimated from the residence time distributions (RTD) mean $\mu_{RTD}$ and standard deviation $\sigma_{RTD}$, which for an ideal CSTR combine to give (Levenspiel, 1999):

$$T_{resetting} \sim \mu_{RTD} + 2 \cdot \sigma_{RTD} \sim 3 \cdot \tau_{res} \tag{15}$$

Which aspects of the design remain the same, and what additional conditions need to be considered when extending native chemical computation in CSTR mode? The choice of alphabet assignment would still be based on the same principles, and the aliquot amount design would follow the same considerations of keeping the system within the oscillatory regime while simultaneously providing a measurable change in the oscillatory features whenever an alphabet symbol is read. The time interval would still be limited by the slowest symbol-pathway pairing, but the effect of flow in reaction needs to be considered as well. The ratio between the resetting time $T_{resetting}$ and the computational time interval $\tau$ influences the maximum length of input sequence that can be processed without erasure of information during the processing of the sequence:

$$l_{\max} \sim \frac{T_{resetting}}{\tau} \sim \frac{3 \cdot \tau_{res}}{\tau}. \tag{16}$$

Hence, $\tau$ and $\tau_{res}$ would need to be carefully chosen to try to maximize the processable sequence length.

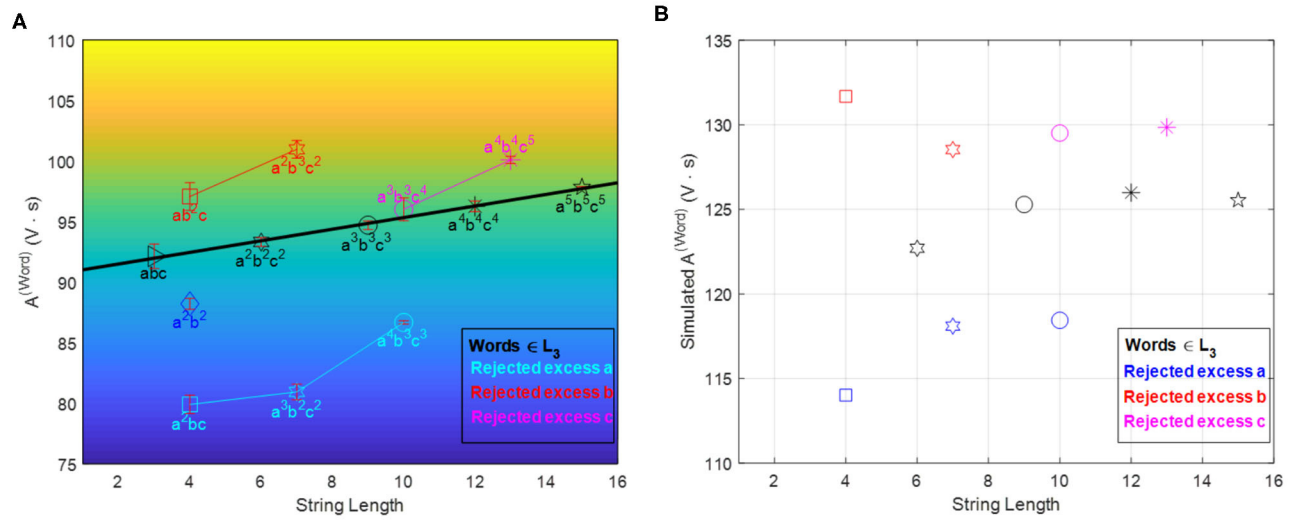


**FIGURE 7 |** $A^{(Word)}$ vs. word-symbol count accept/reject criteria. Panel **(A)** shows experimental results (error bars are based on three repetitions of each sequence experiment) while panel **(B)** shows simulation results based on a modified FKN model (cf. **Appendices 1** and **2**). The locus of accepted words is now linear (in experimental results) and divides the plane in two disjoint regions of rejected words. The relative position of accepted and rejected sequences is reproduced qualitatively by the simulations. Reprinted from Dueñas-Díez and Pérez-Mercader (2019a) Copyright (2019) with permission from Cell Press.

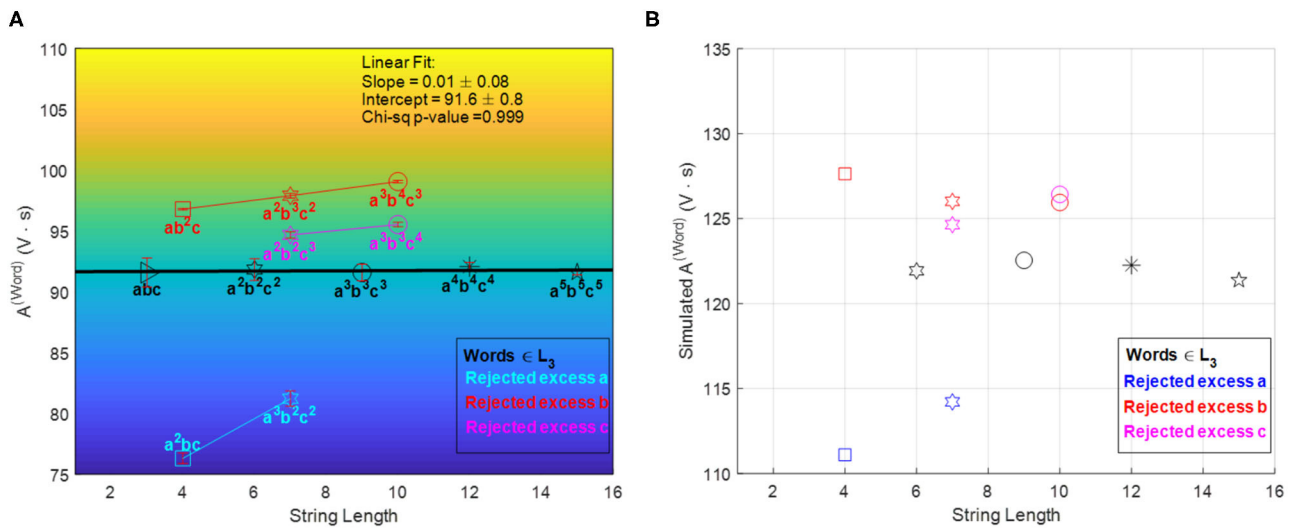


**FIGURE 8 |** $A^{(Word)}$ vs. word-symbol count accept/reject criteria after model-based optimization (cf. **Appendix 3**) and experimental fine tuning. Panel **(A)** shows the experimental results achieving a linear criterion with zero slope with the fine-tuned recipe (error bars are based on three repetitions of each sequence experiment), and panel **(B)** shows the simulation results for the recipe given by the mathematical optimization (prior to fine tuning). The relative position of accepted and rejected sequences is reproduced qualitatively by the simulations. Reprinted from Dueñas-Díez and Pérez-Mercader (2019a) Copyright (2019) with permission from Cell Pres.

The experimental setup for running a native computation in CSTR is more complex than that for a native batch computation, but the only additional required equipment would all be standard to continuous operation.

Another difference with the batch implementation is the initial conditions. In CSTR, the reactor would be in a stationary out-of-equilibrium oscillatory regime before processing the input, and once the sequence is fully processed the oscillations would evolve toward the initial oscillatory features, thus automatically resetting the automaton for a new computation.

Finally, since the machine's operation would start in an oscillatory regime, $V_{max}$ would never be reached in the CSTR, thus the $A^{(word)}$ criterion needs modification. A possible extension of the previous definition of the area for

a batch reactor is

$$A^{(word)} = \int_{2\ oscillations} V_{CSTR} dt - \int_{2\ oscillations} V_{\#\ interval} dt \quad (17)$$

where the first term integrates the area below the two last complete oscillations before the beginning-of-sequence # (in the stationary CSTR regime) and the second integral gives the area below the two last complete oscillations within the time interval corresponding to the end-of-sequence #.

## CONCLUSIONS

In this paper, we have reviewed recent work on native chemical computation: computations performed exclusively by the molecules involved in chemical reactions without involving constructs external to the chemical reaction mechanism. Oscillatory reactions turn out to play a central role in this area of computation.

A computation is a process in which some available information is input, systematically ("mechanically") transformed in prescribed ways and output into a form suitable for the implementation of some function. Computations are carried out by computing automata. Abstractly, these are machines that do some computations. Some of these abstract automata require access to infinite lengths of tape for their operation and cannot therefore be practically realized. For the practically realizable automata, both a conceptual and technical parallel can be established with the way in which chemical reactions occur. The information to be processed can be transcribed into aliquots of the reactants for a chemical reaction, translated (transformed) by the reaction and output as the molecular products of the reaction or as the values of some physico-chemical quantities which include entropy, redox potential, or pH. Thus, chemical reactions can be viewed as a kind of chemical automata which operate on information represented with chemistry.

Computation with chemistry is central to biology enabling the beautiful phenomena of life, from the synthesis of proteins, to the life cycle of bacteria, to the workings of the human brain. During the last 50 years or so, many workers (Adamatzky and Costello, 2002; Adamatzky, 2019) have worked on the implementation of computation with chemistry but whenever automata were used in laboratory realizations, they used only a few Boolean gates and, due to the intrinsically noisy nature of the transport of information in chemical form, the computations relied on external constructs to take advantage of effects induced by molecular transport, such as waves or externally made shapes to guide the appropriate chemicals during the computation. With native chemical computation, the information processing takes place within the reaction itself making available for the computation the full reaction mechanism. Not surprisingly, this enables the application of chemical computation to more complex problems. These additional potential applications include the interconnection of automata into networks or architectures such as chemical perceptrons and neural networks which, due to the access of chemistry to more complex automata in the various layers of these neural processors, can see enhancements of their capabilities and the nature of the problems that can be tackled with them when using native chemical computation and other forms of chemical computation or their combination.

It is a well-established notion in computer science that any computing problem can be cast as a sequence of language recognition problems. Computer languages can be classified according to their complexity into an inclusive hierarchy known as the Chomsky hierarchy. In parallel with the language hierarchy there is a hierarchy of automata; that is automata capable of recognizing languages according to their complexity. It can be seen that for the case of chemical computation there is a parallel correspondence of computing automata with classes of chemical reactions. At the top of the materially implementable (i.e., not requiring infinite amounts of energy for their operations) are the Linear Bounded Automata (LBA) which correspond to bounded (finite) tape length Turing machines. These automata require their memory to hold at least two variables and are represented by (non-linear) oscillatory chemical reactions, such as the Belousov-Zhabotinsky reaction, where the two variables correspond to the frequency and amplitude of the redox oscillations. These two observables are non-linearly interrelated in a way that depends on the nature and order of the sequence of reactants being fed to the reaction. The reaction recipe can be formulated so as to recognize languages that only LBAs and automata at their level in the Chomsky hierarchy can recognize.

We have also seen how these LBAs can be reprogrammed and how they recognize other languages below their level in the hierarchy. This opens a window for the simulation of chemistry with chemistry, i.e., without any intermediary translation (cf. Feynman, 1982) and brings us closer to attempt unlocking the power of $10^{23}$ processor per mol, but whose effectiveness is seriously hindered by the very strong correlation among the computing molecules in the bulk reaction solution at room temperature.

The results of the computation, for example, in the case of the BZ-finite tape length Turing machine, are in the form of radicals, relative concentrations of reaction products, and physico chemical signatures. These can be used to connect with other automata down the line and enable more complex operations, or to use in other chemical processes such as in polymerization reactions (Washington et al., 1999) and even enable the chemically controlled, out-of-equilibrium synthesis of complex molecules from small molecules to self-assembled amphiphilic structures, such as micelles or vesicles (Bastakoti and Pérez-Mercader, 2017a,b). The physico-chemical signatures associated with language acceptance offer an experimental glimpse into the implications of native chemical computing for the implementation of the predictions of the Maximum Entropy Production Principle and its connection with the efficiency of computing processes.

Many questions remain open: from the extension of the above framework to other oscillating reactions, to their application to "computer controlled" molecular and supramolecular architectural assembly from the subnanometer to the micrometer scales, to the study of their implications in non-equilibrium thermodynamics and efficient computation, their direct use

in the simulation of chemistry by chemistry, including the development of such processors or their use in the construction of mimics of life without using biochemistry.

## AUTHOR CONTRIBUTIONS

MD-D wrote the BZ Turing machine section, the appendices and made all the figures. JP-M wrote the rest of the manuscript and created the outline. All authors contributed to the article and approved the submitted version.

## FUNDING

This work was funded by REPSOL, S.A., an energy company from Spain.

## ACKNOWLEDGMENTS

We thank REPSOL S.A. for their continued support. JP-M thanks Andrew Adamatzky, Jeremy England, Irving Epstein, Seth Fraden, Stein Jacobsen, Greg Kovacs, Scott Hubbard, the late Murray Gell-Mann, Seth Lloyd, Stephen Mann, Mark Ritter, and Dimitar Sasselov for many useful conversations related to the work we have summarized here.

## SUPPLEMENTARY MATERIAL

The Supplementary Material for this article can be found online at: https://www.frontiersin.org/articles/10.3389/fchem.2021.611120/full#supplementary-material

## REFERENCES

Adamatzky, A. (2019). A brief history of liquid computers. *Philos. Trans. R. Soc. B* 374:20180372. doi: 10.1098/rstb.2018.0372

Adamatzky, A., and Costello, B. D. L. (2002). Experimental logical gates in a reaction-diffusion medium: the XOR gate and beyond. *Phys. Rev. E* 66:046112. doi: 10.1103/PhysRevE.66.046112

Aris, R. (1999). *Elementary Chemical Reactor Analysis*. New York, NY: Dover Books.

Baierlein, R. (1999). *Thermal Physics*. Cambridge, UK; New York, NY: Cambridge Press.

Bastakoti, B., and Pérez-Mercader, J. (2017a). Facile one pot synthesis of functional giant polymeric vesicles controlled by oscillatory chemistry. *Angew. Chem. Int. Ed. Engl.* 56, 12086–12091. doi: 10.1002/anie.201703816

Bastakoti, B., and Pérez-Mercader, J. (2017b). Autonomous *ex-novo* chemical assembly with blebbing and division of functional polymer vesicles from a "homogeneous mixture". *Adv. Mater.* 29:1704368. doi: 10.1002/adma.201704368

Chomsky, N. (1956). Three models for the description of language. *IRE Trans. Inform. Theory* 2, 113–124. doi: 10.1109/TIT.1956.1056813

Cohen, D. (1991). *Introduction to Computer Theory, 2nd Edn*. New York, NY: John Wiley and Sons, Inc.

De Groot, S., and Mazur, P. (2011). *Nonequilibrium Thermodynamics*. New York, NY: Dover Books.

Dueñas-Díez, M., and Pérez-Mercader, J. (2019a). "How chemistry computes: language recognition by non-biochemical chemical automata. From finite automata to Turing machines." *iScience* 19, 514–526. doi: 10.1016/j.isci.2019.08.007

Dueñas-Díez, M., and Pérez-Mercader, J. (2019b). "Native chemical automata and the thermodynamic interpretation of their experimental accept/reject responses," in *The Energetics of Computing in Life and Machines*, eds D. H. Wolpert, C. Kempes, J. A. Grochow, and P. F. Stadler (Santa Fe, NM: SFI Press), 119–139. doi: 10.37911/9781947864078.04

Dueñas-Díez, M., and Pérez-Mercader, J. (2020). *In-vitro* reconfigurability of native chemical automata, the inclusiveness of their hierarchy and their thermodynamics. *Sci. Rep.* 10, 1–12. doi: 10.1038/s41598-020-63576-6

Epstein, I. R., and Pojman, J. A. (1998). *An Introduction to Nonlinear Chemical Dynamics: Oscillations, Waves, Patterns, and Chaos*. New York; Oxford: Oxford University Press. doi: 10.1093/oso/9780195096705.001.0001

Evans, D. (2011). *Introduction to Computing: Explorations in Language, Logic and Machines*. Creative Commons. Available online at: http://www.computingbook.org/

Feynman, R. P. (1982). Simulating physics with computers. *Int. J. Theor. Phys*. 21, 467–488. doi: 10.1007/BF02650179

Feynman, R. P. (2000). *Feynman Lectures on Computation*. Boca Raton, FL: CRC Press.

Feynman, R. P., Leighton, R. B., and Sands, M. (1965). *The Feynman Lectures on Physics*, Vol. 2. San Francisco, CA: Addison-Wesley. doi: 10.1119/1.1972241

Field, R. J., Körös, E., and Noyes, R. M. (1972). Oscillations in chemical systems: thorough analysis of temporal oscillation in the bromate-cerium-malonic acid system. *J. Am. Chem. Soc*. 94, 8649–8664. doi: 10.1021/ja00780a001

Gentili, P. L. (2018). The fuzziness of the molecular world and its perspectives. *Molecules* 23:2074. doi: 10.3390/molecules23082074

Gilbert, J. C., and Martin, S. F. (2016). *Experimental Organic Chemistry, 6th Edn*. Boston, MA: Cengage Learning.

Goldstein, H., Poole, C., and Safko, J. (2002). *Classical Mechanics, 3rd Edn*. Boston, MA: Addison-Wesley. doi: 10.1119/1.1484149

Gorecki, J., Yoshikawa, K., and Igarashi, Y. (2003). On chemical reactors that can count. *J. Phys. Chem. A* 107, 1664–1669. doi: 10.1021/jp021041f

Harrison, M. A. (1978). *Introduction to Formal Language Theory, 1st Edn*. Boston, MA: Addison-Wesley Longman Publishing Co., Inc.

Hopcroft, J. E., Motwani, R., and Ullman, J. D. (2007). *Introduction to Automata Theory, Languages, and Computation, 3rd Edn*. Pearson Education Inc.

Hou, L., Dueñas-Díez, M., Srivastava, R., and Pérez-Mercader, J. (2019). Flow chemistry controls self-assembly and cargo in Belousov-Zhabotinsky driven polymerization-induced self-assembly. *Commun. Chem.* 2, 1–8. doi: 10.1038/s42004-019-0241-1

Ireland, R. E. (1969). *Organic Synthesis*. Englewood Cliffs, NJ: Prentice-Hall.

Kondepudi, D., and Prigogine, I. (2014). *Modern Thermodynamics: From Heat Engines to Dissipative Structures*. Hoboken, NJ: John Wiley and Sons. doi: 10.1002/9781118698723

Kuhn, H., and Försterling, H.-D. (2000). *Principles of Physical Chemistry*. Hoboken, NJ: John Wiley and Sons.

Lanczos, C. (2012). *The Variational Principles of Mechanics*. New York, NY: Dover Books.

Landauer, R. (1961). Irreversibility and heat generation in the computing process. *IBM J. Res. Dev.* 5, 183–191. doi: 10.1147/rd.53.0183

Lebon, G., Jou, D., and Casas-Vázquez, J. (2008). *Understanding Non-Equilibrium Thermodynamics*, Vol. 295. Berlin: Springer. doi: 10.1007/978-3-540-74252-4

Levenspiel, O. (1999). Chemical reaction engineering. *Ind. Eng. Chem. Res.* 38, 4140–4143. doi: 10.1021/ie990488g

Linz, P. (2012). *An Introduction to Formal Languages and Automata, 5th Edn*. Burlington, MA: Jones and Bartlett Learning.

Lloyd, S. (1992). Any nonlinear gate, with linear gates, suffices for computation. *Phys. Lett. A* 167, 255–260. doi: 10.1016/0375-9601(92)90201-V

Martyushev, L. M., and Seleznev, V. D. (2006). Maximum entropy production principle in physics, chemistry and biology. *Phys. Rep*. 426, 1–45. doi: 10.1016/j.physrep.2005.12.001

Minsky, M. L. (1967). *Computation: Finite and Infinite Machines*. Englewoods Cliff, NJ: Prentice Hall.

Nahin, P. J. (2013). *The Logician and the Engineer*. Princeton, NJ: Princeton University Press. doi: 10.1515/9781400844654

Nelder, J. A., and Mead, R. (1965). A simplex method for function minimization. *Comput. J*. 7, 308–313. doi: 10.1093/comjnl/7.4.308

Nicolis, G., and Prigogine, I. (1977). *Self-Organization in Non-Equilibrium Systems*. New York, NY: Wiley.

Noether, E. (1918). *Invariante Variations Probleme*. Nachr. Akad. Wiss. Göttingen, Math. Kl. II, 235–257.

Pauling, L. (1947). *General Chemistry*. Garden City, NY: Dover Publications.

Pearce, S., and Perez-Mercader, J. (2020). PISA: construction of self-organized and self-assembled functional vesicular structures. *Polym. Chem*. 12, 29–49. doi: 10.1039/D0PY00564A

Pérez-Mercader, J., Dueñas-Diez, M., and Case, D. (2017). *Chemically-Operated Turing Machine, US Patent 9,582,771 B2, February 28, 2017*. Repsol SA: Harvard College.

Prigogine, I. (1955). *Thermodynamics of Irreversible Processes, 3rd Edn*. New York, NY: Interscience.

Rich, E. (2008). *Automata, Computability, and Complexity. Theory and Applications*. Prentice-Hall, NJ: Pearson.

Ross, J., Schreiber, I., and Vlad, M. O. (2006). *Determiation of Complex Reaction Mechanisms. Analysis of Chemical, Biological, and Genetic Networks*. Oxford: Oxford University Press. doi: 10.1093/oso/9780195178685.001.0001

Searls, D. B. (2002). The language of genes. *Nature* 420, 211–217. doi: 10.1038/nature01255

Searls, D. B. (2012). A primer in macromolecular linguistics. *Biopolymers* 99, 203–217. doi: 10.1002/bip.22101

Serratosa, F. (1990). *Organic Chemistry in Action: The Design of Organic Synthesis (Studies in Organic Chemistry)*. Amsterdam: Elsevier.

Sheffer, H. M. (1913). A set of five independent postulates for *Boolean algebras*, with application to logical constants. *Trans. Am. Math. Soc.* 14, 481–488. doi: 10.1090/S0002-9947-1913-1500960-1

Sienko, T., and Lehn, J. M. (2003). "Molecular recognition: storage and processing of molecular information," in *Molecular Computing,* eds T. Sienko, A. Adamatzky, N. G. Rambidi, and M. Conrad (Cambridge, MA: MIT Press). doi: 10.7551/mitpress/4739.001.0001

Simpson, J. A., and Weiner, E. S. C. (1994). *Oxford English Dictionary, 2nd Edn*. Oxford: Clarendon Press.

Stoll, C. (2006). When slide rules ruled. *Sci. Am*. 294, 80–87. doi: 10.1038/scientificamerican0506-80

Sudkamp, T. A. (2006). *Languages and Machines: An Introduction to the Theory of Computer Science, 3rd Edn.* Boston, MA: Pearson Education, Inc.

Tóth, A., and Showalter, K. (1995). Logic gates in excitable media. *J. Chem. Phys*. 103, 2058–2066. doi: 10.1063/1.469732

Truitt, T. D., and Rogers, A. E. (1960). *Basics of Analog Computers*. New York, NY: J. F. Ritter, Inc.

Turing, A. M. (1936). On computable numbers with an application to the entscheidungs-problem. *Proc. Lond. Math. Soc.* 2, 230–265. doi: 10.1112/plms/s2-42.1.230

Volkenshtein, M. V. (1983). *Biophysics*. Moscow: Mir Publishers.

Wang, A. L., Gold, J. M., Tompkins, N., Heymann, M., Harrington, K. I., and Fraden, S. (2016). Configurable NOR gate arrays from Belousov-Zhabotinsky micro-droplets. *Eur. Phys. J. Spec. Top*. 225, 211–227. doi: 10.1140/epjst/e2016-02622-y

Washington, R. P., West, W. W., Misra, G. P., and Pojman, J. A. (1999). Polymerization coupled to oscillating reactions: (1) A mechanistic investigation of acrylonitrile polymerization in the Belousov–Zhabotinsky reaction in a batch reactor. *J. Am. Chem. Soc*. 121, 7373–7380. doi: 10.1021/ja990743o

Weisstein, E. W. (2009). *CRC Encyclopedia of Mathematics, 3rd Edn*. Boca Raton, FL: CRC Press.

Yourgrau, W., and Raw, C. J. G. (1957). Variational principles and chemical reactions. *Il Nuovo Cimento (1955-1965)* 5, 472–478. doi: 10.1007/BF02743932

Yourgrau, W., Van der Merwe, A., and Raw, G. (2013). *Treatise on Irreversible and Statistical Thermodynamics: An Introduction to Nonclassical Thermodynamics*. Mineola, NY: Dover Publications.

**Conflict of Interest:** The authors declare that this study received funding from Repsol, S.A. The funder was not involved in the study design, collection, analysis, interpretation of data, the writing of this article or the decision to submit it for publication.

*Copyright © 2021 Dueñas-Díez and Pérez-Mercader. This is an open-access article distributed under the terms of the Creative Commons Attribution License (CC BY). The use, distribution or reproduction in other forums is permitted, provided the original author(s) and the copyright owner(s) are credited and that the original publication in this journal is cited, in accordance with accepted academic practice. No use, distribution or reproduction is permitted which does not comply with these terms.*

## NOMENCLATURE AND DEFINITIONS

**a:** alphabet symbol in abstract language (in the Chomsky hierarchy). For the experimental Turing machine recognizing $L_3$, this symbol is transcribed by an aliquot of sodium bromate.
**b:** alphabet symbol in abstract language (in the Chomsky hierarchy). For the experimental Turing machine recognizing $L_3$, this symbol is transcribed by an aliquot of malonic acid.
**c:** alphabet symbol in abstract language (in the Chomsky hierarchy). For the experimental Turing machine recognizing $L_3$, this symbol is transcribed by an aliquot of sodium hydroxide.
$A^{(word)}$ : Thermodynamic accept-reject metric, based on integrating in the redox potential vs. time plane, defined as: $A^{(Word)} \equiv V_{\max} \cdot (\tau - 30) - \int_{t_{\#}+30}^{t_{\#}+\tau} V_{osc}(t)\, dt$. Times are in seconds.
***D*:** The (oscillation) distance $D$ between the maximum redox potential value $V_{\max}$ and the redox potential value corresponding to the center of a given oscillation:

$$D = V_{\max} - \left( V_T + \frac{V_P - V_T}{2} \right)$$

$\boldsymbol{D_{\#}}$**:** Value of $D$ corresponding to the last oscillation when one time interval has elapsed after the end-# was added.
***f*:** The (oscillation) frequency $f$, as the inverse of the period. The period is taken to be the time elapsed between two consecutive peaks.
$\boldsymbol{f_{\#}}$**:** Value of $D$ corresponding to the last oscillation once one time interval has elapsed after the end-# was added.
**F**: Faraday Constant.
**G** (**t**) : Gibbs free energy.
**Q** : Heat.
**R** : Universal Gas Constant.
$\left[\mathbf{Ru}\left(\mathbf{bpy}\right)_3^{3+}\right]$: Molar Concentration of oxidized catalyst [Ru(III)].
$\left[\mathbf{Ru}\left(\mathbf{bpy}\right)_3^{2+}\right]_{\mathbf{input}}$ : Total Molar Concentration of oxidized catalyst [Ru(III)] added with the input.
$\left[\mathbf{Ru}\left(\mathbf{bpy}\right)_3^{2+}\right]$: Molar Concentration of reduced catalyst [Ru(II)].
$\left[\mathbf{Ru}\left(\mathbf{bpy}\right)_3^{2+}\right]_{\mathbf{input}}$ : Total Molar Concentration of oxidized catalyst [Ru(II)] added with the input.
**s** : Specific Entropy.
**T** : Temperature.
$\mathbf{T_{resetting}}$ : Resetting time in chemical automata in CSTR mode. Time needed to erase a computation and set back to the steady oscillations.
$\mathbf{V}_{\max}$ : Maximum redox potential value, when all catalyst is in the oxidized form.
$\mathbf{V_P - V_T}$ : Trough-to-peak amplitude of the redox oscillation.
$\mathbf{V_T}$**:** Redox potential value of the trough of the oscillation.
#: beginning and end-of-sequence symbol. For the experimental Turing machine recognizing $L_3$, this symbol is transduced by an aliquot of ruthenium(II) catalyst.
$\mu_{\mathbf{RTD}}$: Residence time distribution mean (CSTR operation).
$\nu$ : Number of electrons exchanged in the redox reaction.
$\xi^{(\mathbf{i})}$ : Reaction extent corresponding to reaction $i$ in the FKN kinetic mechanism of the Belousov-Zhabotinsky reaction.
$\sigma$ : Entropy production density.
$\sigma_{\mathbf{RTD}}$ : Residence time distribution standard deviation (CSTR operation).
$\tau$: Time Interval between aliquots in native chemical automata.
$\tau_{\mathbf{res}}$ : Nominal Residence time (in CSTR operation).

# Advantages of publishing in Frontiers

**OPEN ACCESS**
Articles are free to read for greatest visibility and readership

**FAST PUBLICATION**
Around 90 days from submission to decision

**HIGH QUALITY PEER-REVIEW**
Rigorous, collaborative, and constructive peer-review

**TRANSPARENT PEER-REVIEW**
Editors and reviewers acknowledged by name on published articles

**Frontiers**
Avenue du Tribunal-Fédéral 34
1005 Lausanne | Switzerland

**Visit us:** www.frontiersin.org
**Contact us:** frontiersin.org/about/contact

**REPRODUCIBILITY OF RESEARCH**
Support open data and methods to enhance research reproducibility

**DIGITAL PUBLISHING**
Articles designed for optimal readership across devices

**FOLLOW US**
@frontiersin

**IMPACT METRICS**
Advanced article metrics track visibility across digital media

**EXTENSIVE PROMOTION**
Marketing and promotion of impactful research

**LOOP RESEARCH NETWORK**
Our network increases your article's readership